INVESTIGATION ON CIRRUS CLOUDS BY THE CLOUD-AEROSOL LIDAR AND INFRARED PATHFINDER SATELLITE OBSERVATION DATA

By

Jiang Zhu

RECOMMENDED:

_____

_____

_____

_____

Advisory Committee Chair

_____

Chair, Department of Atmospheric Sciences

APPROVED:

_____

Dean, College of Natural Science and Mathematics

_____

Dean of the Graduate School

_____

Date

INVESTIGATION ON CIRRUS CLOUDS BY THE CLOUD-AEROSOL LIDAR AND INFRARED PATHFINDER SATELLITE OBSERVATION DATA

A

Dissertation

Presented to the Faculty

of the University of Alaska Fairbanks

in partial Fulfillment of the Requirements

for the Degree of

DOCTOR OF PHILOSOPHY

By

Jiang Zhu, B.E., M.E.

Fairbanks, Alaska

August 2011

Abstract

Understanding and describing the role of clouds in the climate system need intensive and extensive research on cloud properties. The albedo and greenhouse effects of clouds and their relations with the physical properties of clouds are analyzed. Cloud-top height and ice water content are key factors in impacting the longwave and shortwave radiation, respectively. Lidar and infrared radiometer measurement technologies are introduced. Cloud-Aerosol Lidar and Infrared Pathfinder Satellite Observation (CALIPSO) level 1 Lidar profile, level 2 cloud layer, and level 2 Lidar/IIR track products are briefly reviewed. The algorithms for identification of cirrus clouds, Linear Depolarization Ratio (LDR), and effective diameter are presented. An average LDR profile is calculated by using the sum of total attenuated backscattering profiles and the sum of perpendicular attenuated backscattering profiles. A weight-average method is applied to calculate the average LDR. A split-window method is applied to estimate the effective diameters of clouds. A set of bulk ice crystal models and a radiative transfer model are applied to produce a look-up table that includes the radiative transfer simulation results. The macro-physical properties of cirrus clouds are analyzed. The frequency of occurrence of cirrus clouds varies with latitude, and strongly relates to the atmospheric circulation. Cirrus clouds are few in high-pressure zones and abundant where seasonal monsoonal circulation occurs. Cloud-top height decreases with increasing latitude. Cloud-top temperature is lower in the tropical regions than in the midlatutude and the polar regions. The measured cloud thickness shows a great diurnal variation.

CALIPSO lidar detects more cirrus clouds than satellite-based passive measurement. LDR values of cirrus clouds vary with latitude and location, and are higher during nighttime than during daytime. The 0.32 and 0.37 annual average LDRs derived by nadir and off-nadir measurements, respectively, indicate that substantial amounts of horizontal orientated ice crystals exist in cirrus clouds. The global distribution of effective diameter of cirrus clouds varies with latitude and season, and the effective diameter has relationship with the LDR.

Table of Contents

Page

List of Figures

Page

List of Tables

Page

List of Appendices

Page

Acknowledgments

To my advisor, Dr. Kenneth Sassen, thanks for over ten years of support and encouragement. He gave me many significant advisories in my thesis work. Thanks also my committee members, Drs. Richard Collins, Nicole Mölders, William A. Bristow and David E. Atkinson, for their constructive criticisms and suggestions. Thanks also Drs. Uma Bhatt and James Campbell for their assistance, Drs. Xiangdong Zhang and Jing Zhang for their help, and Ken Sassen's research group members for their cooperation in the research work.

To my wife, Songzhen Lang, thank you for your consistent understanding and love. To my daughter, Mingjun Zhu, thank you for your wonderful editing work. Finally, to my parents, thank you for your raising and support.

This research was supported by grants from the National Science Foundation (NSF ATM-0630506) and the National Aeronautics and Space Administration (NASA NNX08A056G).

Chapter 1 Introduction

In the atmosphere of the Earth, clouds always exist. They play critical roles in the climate system. Clouds affect the energy budget by reflecting incoming solar radiation and inhibiting the radiation of heat from the Earth. Clouds distribute energy by motion and exchange of energy with the atmospheric environment. Clouds release latent heat as they form, and consume latent heat as they evaporate. Latent heating and cooling associated with clouds modify atmospheric circulation. Clouds regulate the atmospheric hydrological cycle by transporting water vapor evaporated from oceans and lands, redistributing the water vapor through the atmosphere and back to the surface through precipitation. Clouds also play a role in the chemical reaction processes that occur in the atmosphere.

1.1 Radiative Effects of Clouds and Cloud-Climate Feedback Mechanics

Clouds reflect solar radiation, keep the earth cool, and protect what is underneath from overheating. This phenomenon is called the cloud albedo effect. Clouds also trap the long-wave radiation from the earth, and keeping the earth warm, which is called the cloud greenhouse effect. Figure 1.1 (Kiehl and Trenberth, 1997) gives a clear idea of how the albedo and greenhouse effects of clouds affect the earth's energy budget. The sun emits solar radiation to the top of the atmosphere (342 Wm^{-2}). Some (67 Wm^{-2}) is absorbed by molecules, aerosols, and clouds in the atmosphere; some (77 Wm^{-2}) is

reflected by clouds, aerosols and atmospheric gases, and others (168 Wm^{-2}) arrives at the surface of the earth. Because of the partial reflection of incoming solar radiation from clouds, incoming solar radiation to the earth's surface decreases. The earth absorbs the incoming solar radiation and emits longwave radiation (390 Wm^{-2}) to the atmosphere. Clouds and other greenhouse gases absorb the longwave radiation from the surface and re-emit longwave radiation back to the surface (324 Wm^{-2}).

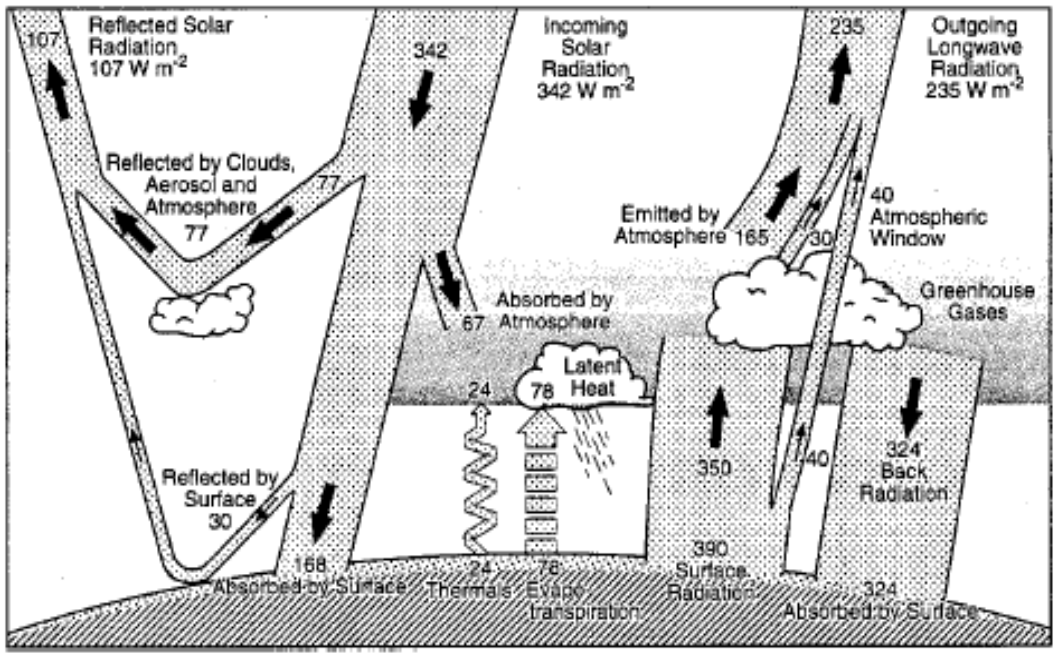

Figure 1.1 The earth's annual global mean energy budget (W m^{-2})
(from Kiehl and Trenberth, 1997)

Cloud radiative forcing (CRF) is defined as the radiation budget difference between clear-sky flux (F_{clr}) and all-sky-measured flux (F_{obs}) at top of the atmosphere (Charlock and Ramanathan, 1985).

$$CRF = F_{clr} - F_{obs}\,. \tag{1.1}$$

The clear-sky and all-sky-measured flux can be interpreted in the following ways: Ellis and VonderHaar (1976) proposed that

$$F_{obs} = (1-N)F_{clr} + NF_{cld} \tag{1.2}$$

represents the all-sky flux observed in a cloudy scene, where N is the fractional cloud amount, F_{cld} is the flux associated with overcast portion of the scene, and F_{clr} is the flux in the clear sky condition. For research purposes, we separate CRF into longwave cloud radiative forcing (C_{LW}) and shortwave cloud radiative forcing (C_{SW}). After plugging the Eq. (1.2) into the Eq. (1.1), we obtain

$$CRF = F_{clr} - F_{obs} = N[F_{clr} - F_{cld}]\,, \tag{1.3}$$

$$C_{LW} = F_{clr,LW} - F_{obs,LW} = N\left[F_{clr,LW}(\varepsilon_s, T_s) - F_{cld,LW}(\varepsilon, T_c)\right], \tag{1.4}$$

$$C_{SW} = F_{clr,SW} - F_{obs,SW} = N\frac{S}{4}(\alpha_{clr} - \alpha_{cld})\,, \tag{1.5}$$

where S/4 is the incident solar flux at the top of Atmosphere (TOA), and T_s and T_c are temperatures of the surface and clouds, respectively. From equations (1.4) and (1.5), we can infer clearly the cloud radiative effects on the earth's energy budget. Normally cloud temperature is lower than the surface temperature, so that the cloud longwave radiative forcing is positive, i.e., the cloud greenhouse effect increases the energy budget. Changes in the height of clouds affect the cloud longwave radiative forcing. High clouds have strong longwave cloud radiative forcing. Emissivity of clouds also influences cloud longwave radiative flux with the longwave radiative flux being proportional to the emissivity of the clouds. Cloud albedo is normally larger than that of surface, so that the

cloud shortwave radiative forcing is negative, which means that the cloud albedo effect decreases the earth's energy budget. The formation and change of clouds in response to the atmospheric conditions is referred to as cloud-climate feedback. Because of the constant change of the atmospheric environment, clouds appear in seemingly endless variety.

Cloud classification is based on cloud height and cloud phase. Under this standard, clouds are classified as low, middle, and high clouds. They are also classified as water clouds, ice clouds, or mix-phase clouds.

Clouds and climate have a strong interaction. The so-called clouds-climate feedback mechanism is complicated. This feedback can be exemplified demonstrated by the cloud's change in response to the surface temperature perturbation.

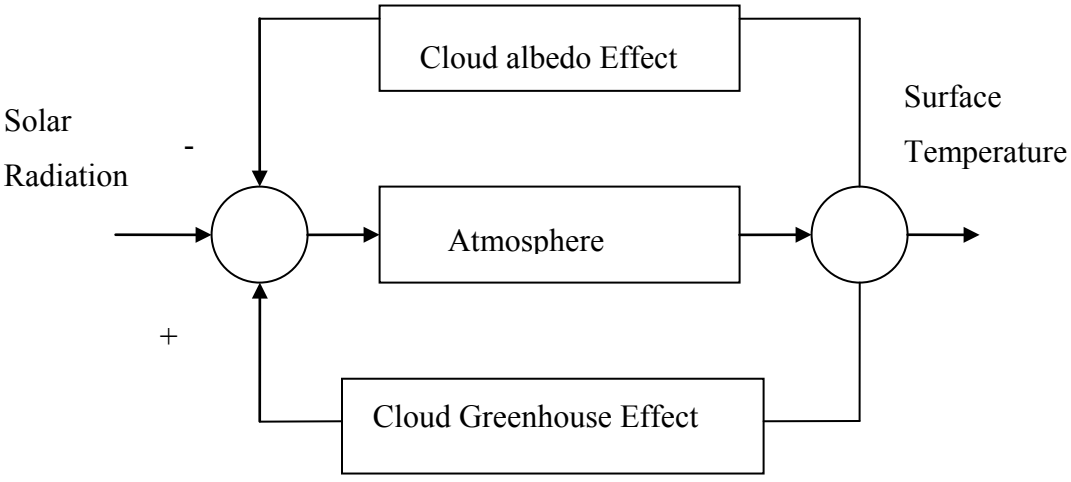

Figure 1.2 Cloud feedbacks in the climate system

Cloud-climate feedback mechanics are revealed in Figure 1.2. Suppose for some reason, solar radiation increases the temperature of the surface of the earth, then evaporation of the water in oceans and evapotranspiration from the land surface increase; Water vapor increases in the atmosphere, therefore, air is saturated. As a result, more clouds are formed. Clouds reflect more incoming solar radiation, causing total incoming solar radiation to the surface to decrease, thus keeping surface temperatures from increasing continuously. This feedback loop is the negative feedback of clouds. On the other hand, more clouds also absorb more outgoing longwave radiation from the earth and re-emit more longwave radiation back to the earth, thus increasing the surface temperature. This fact is obviously positive feedback of clouds. Clouds spontaneously have these positive and negative feedbacks. Without clouds, days on the earth would be too hot for life, whereas nights would be too cold. In order to parameterize the clouds in the climate system, we have to investigate the radiative properties of clouds. That is, we have to know the albedo, absorption ratio, and emissivity of clouds (Shaw, 1996). The radiative properties of clouds are determined by their physical properties.

1.2 Physical Properties of Clouds and Their Relation with Radiative Effects

Macro- and micro-physical properties of clouds govern their radiative properties, which impact the radiative budget in the climate system. Macro-physical properties of clouds include cloud amount, cloud heights, and cloud phase. Cloud amount (cloud cover) mainly affects both albedo and greenhouse effects of clouds (see N in equations 1.4 and 1.5). A large amount of clouds definitely reflects a high percentage of solar radiation

back to outer space, decreasing net incoming shortwave energy. At the same time, a large amount of clouds re-emits more longwave radiation back to the surface of the earth, increasing longwave radiation energy. Cloud height (T_c in equation 1.4) affects the greenhouse effect. Higher clouds, associated with lower cloud top temperatures emit less longwave radiation energy, and keep more long-wave radiation from emitting to outer space than lower clouds with higher cloud-top temperatures. Cloud phase is a key factor in reflecting solar radiation. Water drops have less reflectance than ice crystals. Radiative properties of clouds highly depend on their micro physical properties (Stephens *et al*., 1990). Micro-physical properties include particle size, shape, and size distribution. Particle shape, size, orientation, and size distribution affect the emissivity, absorption ratio, and reflectivity of clouds. For example, for a given ice water content, clouds with small particle size have a greater optical depth, albedo, and emissvity because they exhibit a greater size distribution projected area. The shape of ice crystals also influences their radiative properties. Ice crystals with complicated shapes have greater optical depth, albedo, and emissivity than the simple ones, owning to their greater projected areas (Mitchell and Arnott, 1994).

Cirrus clouds are high level, cold, and optically thin clouds composed principally of non-spherical ice crystals. They are located high in the troposphere and extend to the lower stratosphere in some occasions where temperatures are somewhat below –40^{o}C. The cloud-top height of cirrus clouds varies from 4 to 20 km (Sassen and Campbell, 2001). Cirrus clouds are composed of various non-spherical ice crystals such as hexagonal plates, solid columns, hollow columns, aggregates, and bullet rosettes. Figure

1.3 (Libbrecht, 2011) gives a detailed description of ice crystal habits as a function of the surrounding temperatures and supersaturation ratios.

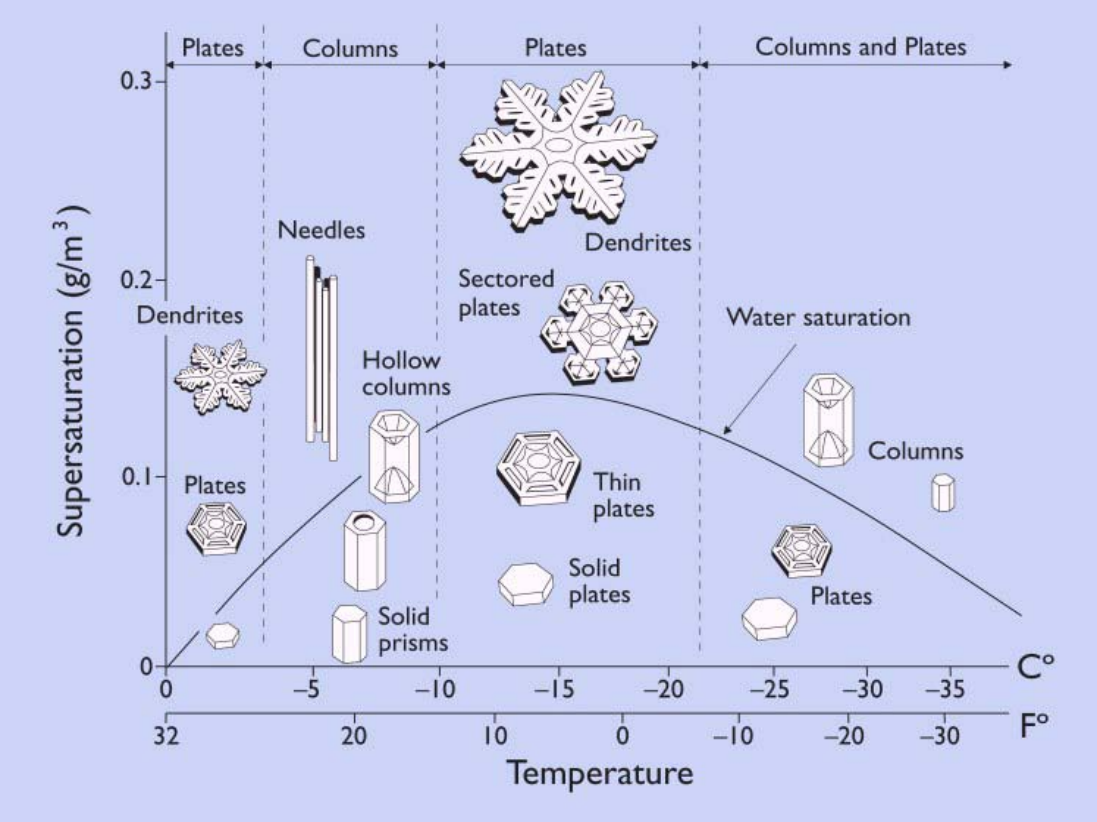

Figure 1.3 Ice crystal habit as a function of temperature and supersaturation

(from Libbrecht, 2011)

Basically, at a given supersaturation, habits of ice crystals change from plates to columns to plates to columns with decreasing temperatures. At a given temperature, habits of ice crystals become more and more complicated with increasing of supersaturatuion. In reality, ice clouds are composed of a mixture of some habits.

Cirrus clouds can be identified by their transparency, which is related to the

visible optical thickness τ (Sassen and Cho, 1992). Clouds with $\tau \leq 3$ are considered to be cirrus clouds, $0.3 \leq \tau \leq 3$ defined as opaque (bluish sky not visible above) cirrus, thin (bluish-colored) cirrus clouds have $0.1 \leq \tau \leq 0.3$, and $\tau \leq 0.1$ are defined as subvisual cirrus clouds. Shapes of ice crystals in cirrus clouds depend on changes in the environmental temperature and suppersaturation with respect to ice. The shape information of cirrus clouds can be evaluated by the linear depolarization ratio measured by Polarization LIDAR (Sassen and Benson, 2001; Noel *et al*., 2004).

1.3 LIDAR Polarization Technique

Because of their sensitivity to particle shape, polarization Lidars are good tools in the research on ice clouds (Sassen, 2000). Polarization Lidars are active remote-sensing devices. They send a laser beam in parallel polarization, and receive both parallel and perpendicular backscattering light from particles. If the particles are perfect spheres, there will be no perpendicular backscattering light in theory, otherwise, perpendicular backscattering light exists. The ratio of perpendicular backscattering light intensity to parallel backscattering light intensity is called linear depolarization ratio (LDR). LDR provides the information of the shape of particles. Spherical particles lead to depolarization ratios equal to zero, whereas irregularly shaped particles can show values as great as 0.6 (Liou and Lahore, 1974), so the linear depolarization ratio can be treated as an indicator of the microphysical shape of ice crystals. Since polarization lidars were demonstrated early on (Schotland *et al*., 1971) to unambiguously discriminate water and ice cloud by their large differences in LDR, they are now widely used in aerosol and ice

cloud research. The Lidar depolarization ratio was used in the classification of the particles effective shape ratio (Noel, *et al*., 2002). Polarization lidars even were used to investigate formation mechanics of ice clouds. Normally, most cirrus cloud measurements (off-zenith) reveal LDR in the 0.4-0.5. Because of their great diversity in particle habits and axis ratio, ice clouds sometimes can be measured to have a wide range of LDR values. Sassen *et al.* (1989) investigated regions associated with Doppler radar-detected updrafts and yielded rather low LDR (~0.2-0.3), which was attributed either to rapidly growing haze particles, as precursors to new ice particles, or to the peculiar shapes of newly formed ice crystals.

1.4 Parameterization of Clouds

Researchers care more about how to parameterize clouds for radiation energy calculation. For this reason, an artificial quantity named effective diameter is introduced to simplify the treatment of microphysical properties of clouds. The use of an effective particle size to represent the size dependence of scattering and absorption processes in radiation transfer in both water and ice clouds has been widely accepted throughout the atmospheric science community (Nasiri *et al.*, 2002; Mitchell *et al*., 2011).

The effective diameter of ice clouds is defined as ice water content divided by the particle projected area and bulk ice density for a given particle size and habit distribution (Mitchell, 2002), i.e.,

$$D_{eff} = \frac{3}{2}\frac{IWC}{\rho_i P}\ , \tag{1.6}$$

where IWC and P are ice water content and total particle projection area of ice crystals with size distribution of N(D), respectively, and ρ_i is the ice bulk density. Effective diameter represents bulk micro-physical property of cloud, not a single ice crystal. Absorption efficiency of clouds then can be obtained by (Van de Hulst, 1981)

$$Q_{abs,ADA} = 1 - \exp(-8\pi n_i D_{eff} / 3\lambda), \tag{1.7}$$

where n_i is the imaginary part of the refractive index and λ is the wavelength, ADA indicates anomalous diffraction approximation, a simplification of Mie theory. Finally the absorption coefficient of clouds is obtained (Mitchell, 2002)

$$\beta_{abs} = Q_{abs,ADA} P_t \ , \tag{1.8}$$

where P_t is the size distribution projected area of clouds. Similarly, the extinction coefficient also can be presented as function of the effective diameter. This means that the effective diameter actually includes both albedo and emissivity information of clouds. Because the atmospheric environment is so different around the earth, there are so many models of cirrus clouds distributed globally. Satellite measurement technology provides us opportunities to study global cirrus cloud characteristics.

1.5 Objective

In this research, Lidar polarization measurement and infrared radiometer measurement from satellite are applied to investigate the cirrus clouds globally with focus on macro-physical properties, shape information, and bulk micro-physical properties. In Chapter 2, instruments and dataset used for this research are introduced. In chapter 3, the

computational method used in this research is introduced. All kinds of algorithms including ice cloud identification, LDR, and effective diameter algorithms are discussed in detail. The error analysis is provided to verify that the analysis methods have an acceptable accuracy. In chapter 4, the cirrus clouds macro-physical properties distributions and changes with respect to the month, season and year are investigated on the global scale. The comparison of cirrus clouds derived by the Cloud-Aerosol Lidar and Infrarred Pathfinder Satellite Observation (CALIPSO) lidar to the International Satellite Cloud Climatology Project (ISCCP) high clouds derivation results is presented. Chapter 5 investigates shape information of cirrus clouds in a global view by using the linear depolarization ratio. Shape modes of cirrus clouds and their change in terms of monthly, seasonal, and annual time ranges are analyzed. In chapter 6, the split-window method and a radiative transfer model are used in the estimation of effective diameters and ice water content. Global distribution of effective diameter and ice water content, as well as their changes, are investigated. The relationship of LDR and effective diameters are discussed. The impact of effective diameters of cirrus clouds on infrared radiative radiance at TOA is discussed. In chapter 7, the main research methods and findings about macro-physical, bulk micro-physical properties, and LDR of cirrus clouds are concluded. The further research areas are also pointed out.

Chapter 2 Instruments, Measurement Theory, and Dataset

2.1 Instruments

This research focuses on investigation of cirrus clouds through analysis of data products from Cloud-Aerosol Lidar and Infrared Pathfinder Satellite Observation. CALIPSO combines an active lidar instrument with passive infrared and visible imagers to probe the vertical structure and properties of thin clouds and aerosols over the globe. CALIPSO is a polar-orbit satellite flying with four other satellites in the "A-Train" formation. Aqua satellite constellation (or A-Train) consists of the Aqua, CloudSat, CALIPSO, PARASOL, and Aura satellite missions. The satellites in the A-Train are maintained in orbit to match the World Reference System 2 (WRS-2) reference grid. The constellation flies in a sun synchronous, near-polar orbit with a nominal orbital altitude of 705 km and inclination of 98 degrees. The orbit inclination of 98 degree provides global coverage between latitude of 82 degree N and 82 degree S. Aqua leads the constellation, with an equatorial crossing time of about 1:30 PM at ascending node. CloudSat and CALIPSO lag Aqua by 1 to 2 minutes and are separated from each other by 10 to 15 seconds. With around 99 minutes flight time per orbit, each satellite completes 14.55 orbits per day, with a separation of 24.7 degrees longitude between each successive orbit at the equator, and produces about 14 daytime and 14 nighttime data files. The solar elevation angle at each location where lidar is probing along the orbit track is recorded. If a location has a solar angle greater than 3 degrees, this location is classified as a daytime

location. The daytime latitude changes with the days in a year. On the CALIPSO payload, there are three instruments: the Cloud-Aerosol Lidar with Orthogonal Polarization (CALIOP), the Imaging Infrared Radiometer (IIR), and the Wide Field Camera (WFC). Tables 2.1, 2.2, and 2.3 from Anselmo *et al.* (2007) list the characteristic parameters of these instruments.

Table 2.1 CALIPSO characteristic parameters

Parameter	**Value**
Laser	Nd:YAG, diode-pumped, Q-switched, frequency doubled
Wavelength	532 nm, 1064 nm
Pulse energy	110 mjoule/channel
Repetition rate	20.25 Hz
Receiver telescope	1.0 m diameter
Polarization	532 nm
Footprint/FOV	100 m/130urad
Vertical resolution	30-60 m
Linear dynamic range	22 bits
Data rate	316 kbps

Table 2.2 IIR characteristic parameters

Parameter	Value
Wavelengths	8.65um, 10.6um, 12.05um
Spectral resolution	0.6um – 1.0 um
IFOV/swath	1 km/64km
NEDT at 210K	0.3 K
Calibration	+/- 1K
Data rate	44 kbps

Table 2.3 WFC characteristic parameters

Parameter	Value
Wavelength	645 nm
Brandwidth	50 nm
FOV/swath	125 m/61 km
Data rate	26 kbps

Figure 2.1 (CALIPSO, 2011) illustrates CALIPSO data orbits and the daytime changes with days. Daytime flights are from south-east to north-west as marked in red lines, and nighttime flights are from north-east to south-west and marked by blue lines. In northern hemisphere summer, daytime flights cover from latitude 66S degree, ascending to 82N degree then descending to 54N degree. In northern hemisphere winter, daytime flights cover from latitude 60S, descending to 82S then ascending to 75N degree.

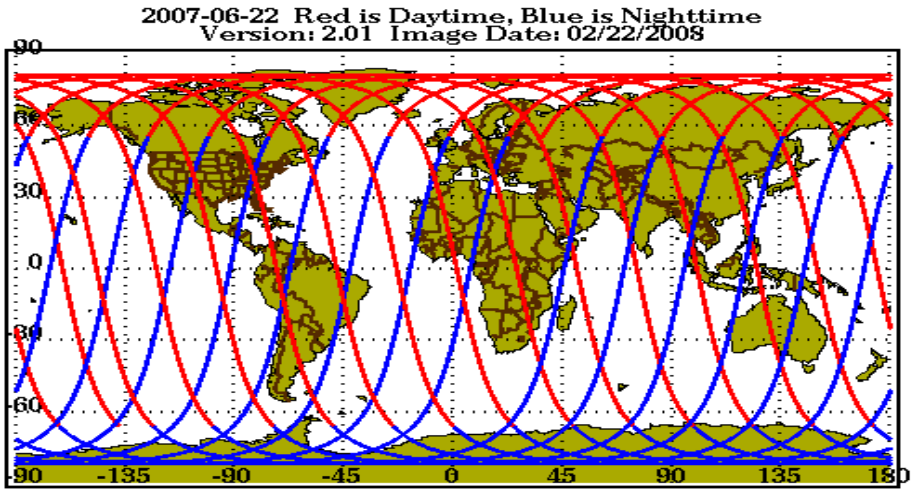

Figure 2.1 CALIPSO orbits in one day

(from CALIPSO, 2011)

2.2 Lidar Measurement Principle

Lidar measures the backscattering signal from molecules, aerosols, and clouds. Scattering from particles can be classified into three regimes according to the size parameter ($\chi = 2\pi * r/\lambda$, where r is the radius of particle and λ is the wavelength of the incident light). If the size parameter is far less than 1, scattering is Rayleigh scattering; around 1, scattering is in the Raleigh-Mie transition zone; far more than 1, scattering is in the Mie and geometrical optics zone. When using 532 nm wavelengths laser light, scattering from air molecules falls into the Rayleigh scattering; scattering from aerosols and just-informed cloud particles is in the Rayleigh-Mie scattering zone, and scattering from clouds falls into the Mie and geometrical optics. The lidar equation for polarization applications describes the backscattering power detected by the lidar system. The power P(R) received by the lidar is related to the strength of the scattering in a volume by (Schotland *et al.*, 1971)

$$P\perp,//(R) = P_0(\frac{ctA_r}{2R^2})\beta_{\perp,//}(R)\exp[-2\int_{R_0}^{R}(\sigma(R))\eta(R)dR], \tag{2.1}$$

where P_0 is the power output (J), c is speed of the light (m s^{-1}), t is the pulse length (m), A_r is the receiver collecting area (m^2), β is the volume backscatter coefficient (m $sr)^{-1}$, σ is the extinction coefficient per volume (m^{-1}), η is the multiple forward-scattering correction factor, and $P_{||}(R)$ and $P_{\perp}$ (R) are backscattering powers from parallel and perpendicular planes with respect to the incident polarization plane, respectively. A common assumption of the relationship between β and σ is expressed as (Klett, 1981)

$$\beta = const \times \sigma^{k} . \tag{2.2}$$

This relation between the scattering and extinction coefficient can be estimated by investigating the scattering from air molecules, because backscattering from air molecules is predicted by Rayleigh theory, and air density can be determined with sufficient accuracy from local balloon-borne radiosonde profiles (Sassen, 1994). After plugging Eq. (2.2) into Eq. (2.1), β can be evaluated by the range square corrected backscattered power. The volume backscattering coefficient β presents the characteristics of particles and is determined by the microphysical properties of particles such as habit, size distribution, and concentration. The linear depolarization ratio δ is defined as the ratio of the perpendicular to the parallel polarized lidar signals as the following (Sassen, 2000)

$$\delta = \frac{P_{\perp}(R)}{P_{\parallel}(R)} \tag{2.3}$$

The depolarization ratio can be used to distinguish the shape and the orientation of a non-spherical ice crystal. Sassen (1976, 1991) presented the depolarization ratio for various types of ice crystals and water droplets derived from laboratory and field studies. Sassen and Benson (2001) have analyzed the LDR in term of cirrus cloud microphysical content using dataset measured by the Facility of Atmospheric Remote Sensing in Utah.

2.3 Radiometer Measurement Principle

Different from active sensing such as lidars and radars, radiometers are passive sensors. They record the specific wavelength range electromagnetic radiation some distance away, where the radiation is characterized by the measured medium, then the scientists interpret and retrieve the characteristics of the medium. Radiometers can be classified in terms of the wavelength which they sense. For atmospheric applications, radiometers are designed in ultraviolet, visible, infrared, and microwave spectrum ranges. The IIR measures the emission of infrared radiation from the earth and the atmosphere. Its three channels are located in an atmospheric window (800-1200cm^{-1}), where absorption due to atmospheric gases shows a minimum, except in the 9.6μm ozone band. The IIR is highly sensitive to the surface, aerosols, and clouds. The equation that governs the transfer of emitted thermal infrared radiance at a given wavenumber, υ, can be described by (Andrews, 2000)

$$I_{\upsilon}(z_{\infty}) = B_{\nu}(T_s)\Gamma_{\nu}(0) + \int_0^{z_{\infty}} B_{\nu}[T(z)]\frac{\partial \Gamma_{\nu}(z)}{\partial z}dz\,, \tag{2.4}$$

where $\Gamma_{\nu}(z)$ is the monochromatic transmittance at height Z, which is defined as (Andrews, 2000)

$$\Gamma_{\nu}(z) = \exp(-\int_z^{z_{\infty}} \sigma(z')dz')\,,$$

$B_{\nu}(T_s)$ is the Planck function at surface temperature, .and $I_{\upsilon}(z_{\infty})$ represents the radiance measured by IIR at the TOA. According to equation (2.4), upwelling radiance is a result

of the product of the Plank function, the spectral transmittance, and the weighting function. The characteristic information of the measured medium is hidden in the spectral transmittance profile. If we know the boundary conditions, e.g. temperature and emissivity of the surface, by some mathematic methods we can solve the inversion problem to get the information on the measured media such as aerosols and clouds. One such mathematic method is the Discrete-Ordinates Method developed by Chandrasekhar (1960). The method involves the discretization of the basic radiative transfer equation and the solution of a set of first-order differential equations. With the advance in numerical techniques for solving differential equations, this method has been found to be efficient and accurate (Stamnes *et al.*, 1988). Solving the inversion problem faces the difficulty of the uniqueness of solution, because the medium under investigation is composed of a number of unknown parameters. For example, the spectral transmittance of clouds is determined by their single-scattering albedo, extinction coefficient, asymmetry parameter, ice water content, effective diameter, etc. Another approach to get the information of the measured medium follows this logic: Field observation and theoretical calculations provide knowledge about the medium. We put this knowledge including different model of clouds into a radiative transfer model and obtain many possible radiances at the TOA, then compare the outputs from the radiative transfer model with measured radiance, and estimate the information of medium. One widely used algorithm to derive cloud properties is called the split-window technique (Inoue 1985). It utilizes the difference of radiances of TOA measured at two wavelengths to retrieve microphysical properties of clouds.

2.4 Data Sets

Three CALIPSO data products are used in this research. They are the lidar level 1 profiles product, the lidar level 2 cloud layer product, and the IIR/lidar track product. The descriptions of the three products are summarized briefly from the CALIPSO Product Document (Anselmo, *et al.*, 2007). The definitions of the three datasets are listed in Appendix B.

2.4.1 Lidar Level 1 Profile Product

The lidar level 1 profile product contains a half orbit (day or night) of calibrated and geo-located lidar profiles. One half-orbit file of the product includes three metadata records and three profile data records. The three metadata records are core metadata, archive metadata, and lidar metadata. The three profile data records are the spacecraft position, attitude, and celestial profile records, the geo-location and view geometry profile records, and the lidar science data profile records, respectively. Table B.1 lists the records in a half-orbit file.

The core metadata record and the archive metadata record structures are omitted. Table B.2 gives the structure of the lidar metadata record. The structures of the three profile records are described in tables B.3, B.4, and B.5, respectively.

In the lidar profile science data record, the profile identification number, the geophysical location, the total attenuated backscatter coefficient, the perpendicular

attenuated backscatter coefficient, temperature, humidity, the quality control flag (QC_Flag), and many other variables are used to identify cirrus cloud layer and calculate the linear depolarization ratio.. The attenuated backscatter coefficient is the product of the volume backscatter coefficient and the two-way optical transmission from the lidar to the sample volume in question (Hostetler, *et al*., 2006).

$$\beta'(z) = \beta(z)T^2 , \tag{2.1}$$

$$T^2(z) = \exp[-2\int_0^z \sigma(z')dz' , \tag{2.3}$$

where β' is attenuated backscatter coefficient, β is volume backscatter, and T^2 is two-way optical transmission.

Figure 2.2 shows two lidar level 1 attenuated backscatter profiles. The profile on the left panel is a profile without any feature layer, and the profile on the right panel includes multiple feature layers. The two layers in this profile are identified as cirrus layers in Chapter 3.

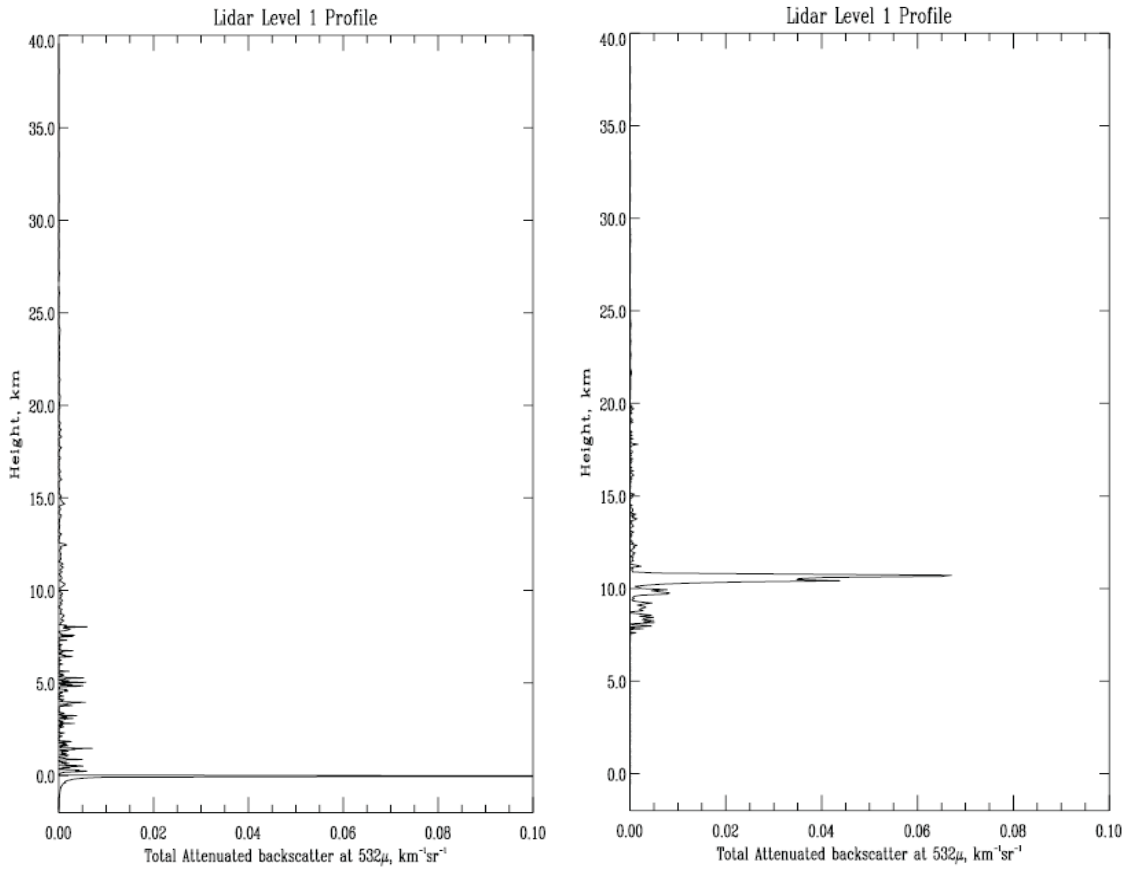

Figure 2.2 Lidar level 1 attenuated backscatter profile

In order to reduce the downlink data volume, an on-board averaging scheme is applied by using different horizontal and vertical resolutions for different altitude regimes, as shown in the Table 2.4.

Table 2.4 Range resolution of different altitude ranges for downlinked data

Altitude Range (km)	Bin Number	Horizontal Resolution (km)	532 nm Vertical Resolution (m)	1064 nm Vertical Resolution (m)
30.1 to 40.0	1-33	5	300	N/A
20.2 to 30.1	34-88	5/3	180	180
8.3 to 20.2	89-288	1	60	60
-0.5 to 8.3	289-578	1/3	30	60
-2.0 to -0.5	579-583	1/3	300	300

2.4.2 Lidar Level 2 Cloud Layer Product

The Lidar Level 2 cloud layer products are produced at three horizontal resolutions: 1/3 km, 1 km, and 5 km. In this research, the 5 km cloud layer products are used. One file of the product contains three metadata records and many column descriptor records. The three metadata records are core metadata, archive metadata, and lidar cloud and aerosol metadata. Table B.6 summarizes records in a 5 km Cloud Layer file. The lidar cloud & aerosol metadata record is described in Table B.7.

The lidar layer products consist of a sequence of column descriptors, each one of which is associated with a variable number of layer descriptors. The column profile data record is described in Table B.8, and the layer information in the column record is listed in Table B.9. One column in the level 2 cloud layer product corresponds to some contiguous profiles in the lidar level1 product. For example, a column in the 5 km cloud layer product represents 15 profiles in the level 1 profile product. The column descriptors

specify the temporal and geophysical location of the column of the atmosphere through which a given lidar pulse travels. Also included in the column descriptors are indicators of surface lighting conditions, information about the surface type, and the number of features (e.g., cloud and/or aerosol layers) identified within the column. The feature layers are identified by 5, 20, and 80 km horizontal range windows. A set of layer descriptors is reported for each of the layers. The layer descriptors provide information about the spatial and optical characteristics of a feature, such as the base and top altitudes, the integrated attenuated backscatter, and the optical depth. The layer descriptors also provide the type of the horizontal range windows used to identify the layer, and a quality control flag of the layer.

2.4.3 IIR/lidar Track Product

The IIR/lidar level 2 track data product contains IIR emissivity and cloud particle data related to pixels that have been co-located to the lidar track. The major categories of the data product are cloud emissivity, cloud properties, and lidar profile data. Image data are registered to a 1 km grid centered on the lidar track. Each grid line occurs every 3 lidar shots, which results in a maximum of 40,095 grid lines per orbit (20,048 grid lines per half orbit). One file of the product contains a core metadata record, an archive metadata record, an IIR track metadata record, and an IIR/lidar track science profile record. Table B.10 describes record summary of one IIR/lidar track product file, the data structure of the metadata record is described in Table B.11, and the IIR/lidar track science record is listed in Table B.12.

In the IIR/lidar track profile record, brightness temperatures at three channels and cloud clear sky radiances at three channels are used for this research. Brightness temperature, clear sky radiance, and cloud top temperature are used to calculate the effective emissivity of clouds. Chapter 3 gives the equation to calculate the effective emissivity of clouds.

Chapter 3 Algorithms

Many physical quantities of cirrus clouds are calculated in this research. The application software that integrates the algorithms to deal with these quantities is developed. These algorithms include identification of cirrus clouds; calculation of macro-physical quantities such as cloud top height, cloud top temperature, and cloud thickness; evaluation of LDR; and estimation of the effective diameter and ice water content. These physical quantities are presented in two formats. One is longitude vs. latitude, and the other is height vs. latitude. During this research, two versions of the application are developed. The main differences in these two versions are the cirrus identification algorithm and the LDR calculation algorithm. A detailed description of the two cirrus identification algorithms is presented this chapter, and a detailed discussion of the two LDR calculation algorithms will be covered in chapter 5. The results produced by the application version 1 were published in the Journal of Geophysical Research (Sassen and Zhu, 2009), and the original published paper is included in Appendix C. The results produced by the application version 2 are included in this dissertation.

3.1 Scheme of the Application Software

The application software developed in this research includes five main steps indicated in the Figure 3.1.

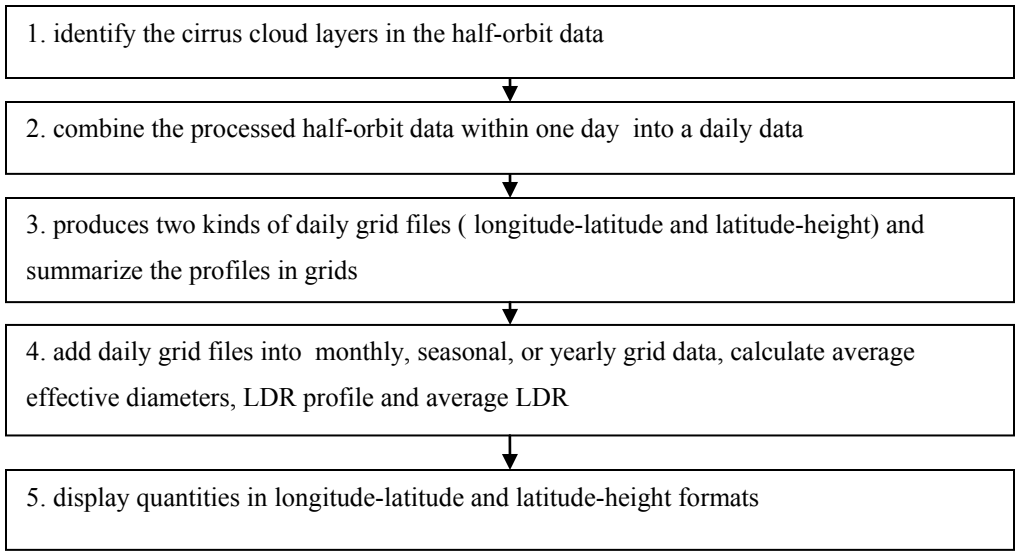

Figure 3.1 Scheme of the application software developed for this study

In step 1, the cirrus cloud identification algorithm is used. For each half-orbit fly of CALIPSO, there are three half-orbit files which are a lidar profile, a lidar 5 km cloud layer, and a IIR/lidar track data files. Step 2 combines the processed results from step 1 into one-day data file. Step 3 produces two kinds of grid files from the one-day file. One is longitude vs. latitude, the other is latitude vs. height. Step 4 adds the one-day grid files into month, season, and year files and calculates LDR profile, mean effective diameter, and average LDR for each grid. Step 5 displays the grid data of physical quantities such as cloud frequency of occurrence, height, thickness, temperature, LDR, and effective diameter. Table B.13 lists the names and function descriptions of the process programs, and names of the processed data files.

3.2 Identification of Cirrus Clouds Algorithm

Before introducing the algorithm, it is worth mentioning that the identification of the cirrus cloud algorithm does not distinguish polar stratospheric clouds (PSC) from cirrus clouds, which means the results shown later include both PSC and cirrus clouds. The family of cirrus clouds has traditionally been defined on the basis of visual observations from the surface by trained observers (Lynch, 2002). Later lidar studies (Sassen and Cho, 1992) indicated that estimated visible optical depths of $\tau < 0.03$ were typical for subvisual cirrus, $0.03 < \tau < 0.3$ for thin (i.e., bluish colored) cirrus, and $0.3 < \tau < 3.0$ (white or grayish) for opaque cirrus. Based on previous studies, a group of criteria developed for identifying cirrus clouds (Sassen *et al*., 2008) is used to identify if clouds along the lidar track are cirrus clouds. These criteria are: clouds must be transparent to lidar probing; and cloud top temperatures must be colder than -40ºC. Cirrus clouds normally have visible optical depth not exceeding $\tau \approx 3.0$ if they can be visually identifie d (Sassen and Cho, 1992; Sassen and Benson, 2001), and CALIOP lidar probing is restricted to visible optical depth $\tau <\sim 3.0 – 4.0$, so cirrus clouds are "seen" by lidar as be transparent. The second criteria is based on a maximum allowable cirrus cloud top temperature of -40ºC, the homogeneous freezing point of pure water, which distinguishes all pure ice clouds from the possibility of mixed phase clouds containing supercooled liquid (Prauppacher and Klett, 1997). The correctness of these cirrus identification criteria are verified by the results of a climatology of midlatitude cirrus clouds using extended lidar measurement (Sassen and Campbell, 2001; Sassen, 2002).

The level 2 IIR/lidar track product includes many columns along the half-orbit track. A column represents a 5 km horizontal resolution bin. The column includes the number of layers, layer types, and the layer heights. These layers are identified within three kinds of horizontal range windows along the half-orbit track, and the window information is included in the column. The 5, 20, and 80 km horizontal range window corresponds to 15, 60, and 240 level 1 lidar profiles, respectively. If the return signal from a cloud layer is strong, the cloud layer can be identified in 5 km window, but if the return signal from a cloud layer is weak, the cloud layer can only be identified in the 20 km or even in the 80 km windows.

The background noises in the return lidar signals are much greater at daytime than at nighttime. Figure 3.2 illustrates two lidar level 1 profiles, one is a daytime profile, and another is a nighttime profile. It shows that the background noises at daytime are much greater than at nighttime. Let us study the day versus night difference of the background noise for the partial profiles from 30 km to 40 km. Table 3.1 lists the statistic values of the day and night partial profiles.

Table 3.1 Statistic values of day and night partial profiles

The unit of the numbers is 1.0E-05 $km^{-1}sr^{-1}$.

	Min	Mean	Max	STDDEV	Max-min	
Day	-48.97	-4.64	30.58	18.75	79.56	
Night	-0.26	1.84	9.98	2.40	10.24	

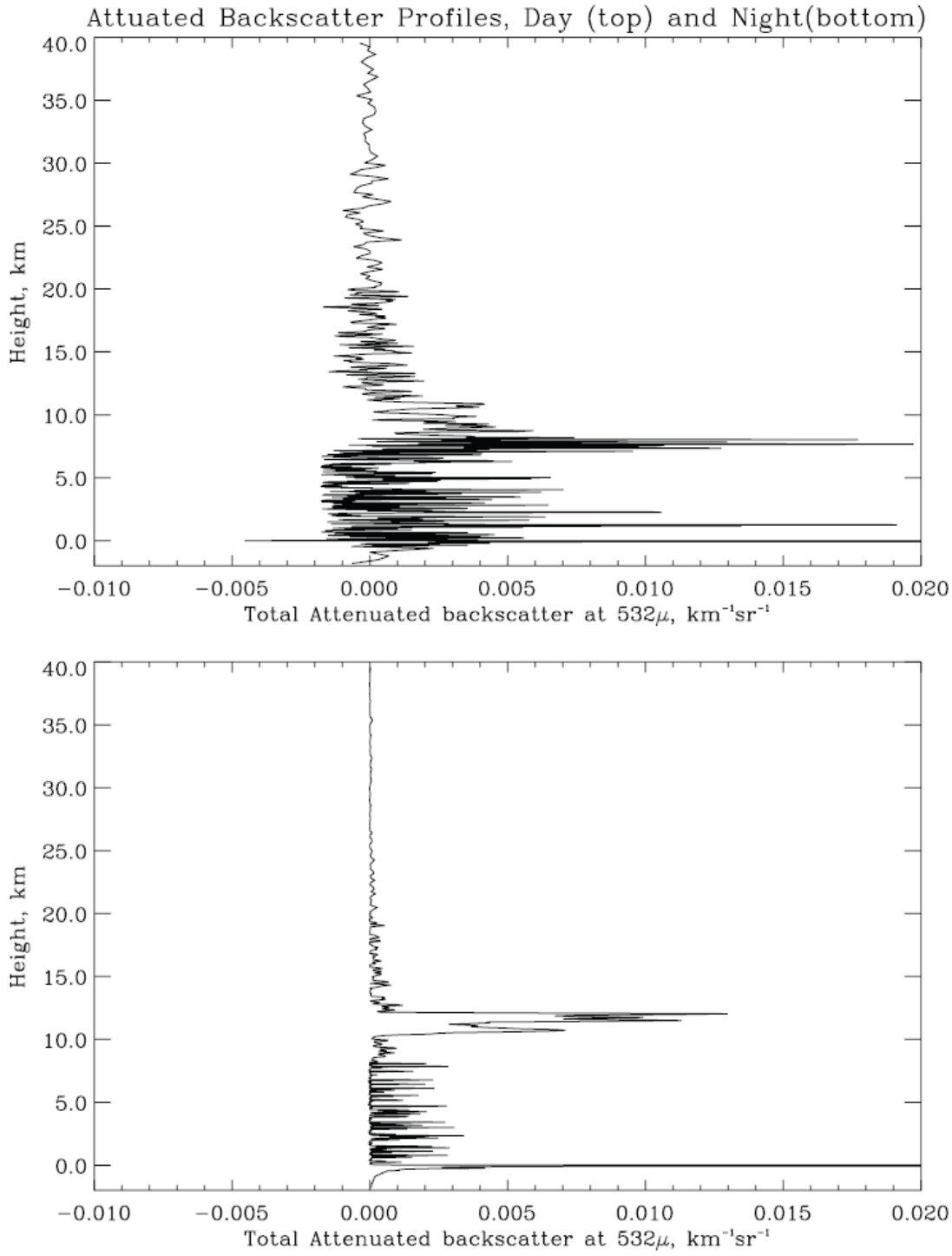

Figure 3.2 Comparison of day and night total attenuated backscatter profiles

As shown in Table 3.1, the daytime variation range of total attenuated backscatter is around 8 times greater than the nighttime variation, and the daytime value standard deviation is also around 8 times greater than the nighttime value standard deviation.

A thin cloud layer may not be measured in daytime, because the return signal of the cloud layer has been immersed in the strong background noise at daytime; but a similar thin cloud layer may be measured at nighttime, because the background noise at nighttime is weak, and the return signal from the thin cloud layer are still good enough to be identified. In the application version 1, the cirrus cloud identification algorithm considers all layers identified by the 5, 20, or 80 km windows as candidates to identify the cirrus cloud layers; while in the application version 2, only layers identified by 5 km window are chosen to identify the cirrus cloud layers.

In this thesis, lidar attenuated backscatters are used to determine if the clouds are transparent. If the maximum of lidar attenuated backscatters occur below the suitable cloud layer level, or at the earth's level, this layer is identified as transparent to lidar probing. By using these criteria, dense ice, water, and mixed phase clouds are distinguished from cirrus clouds. Figure 3.3 is the flowchart of the algorithm developed for this thesis. The logic of the algorithm is as follows:

A. Read in level 1 lidar profile data, level 2 5km cloud layer data, and level 2 IIR/lidar track data.

B. Loops go through each column in level 2. For each column, check the QC flag to make sure it is a good quality column.

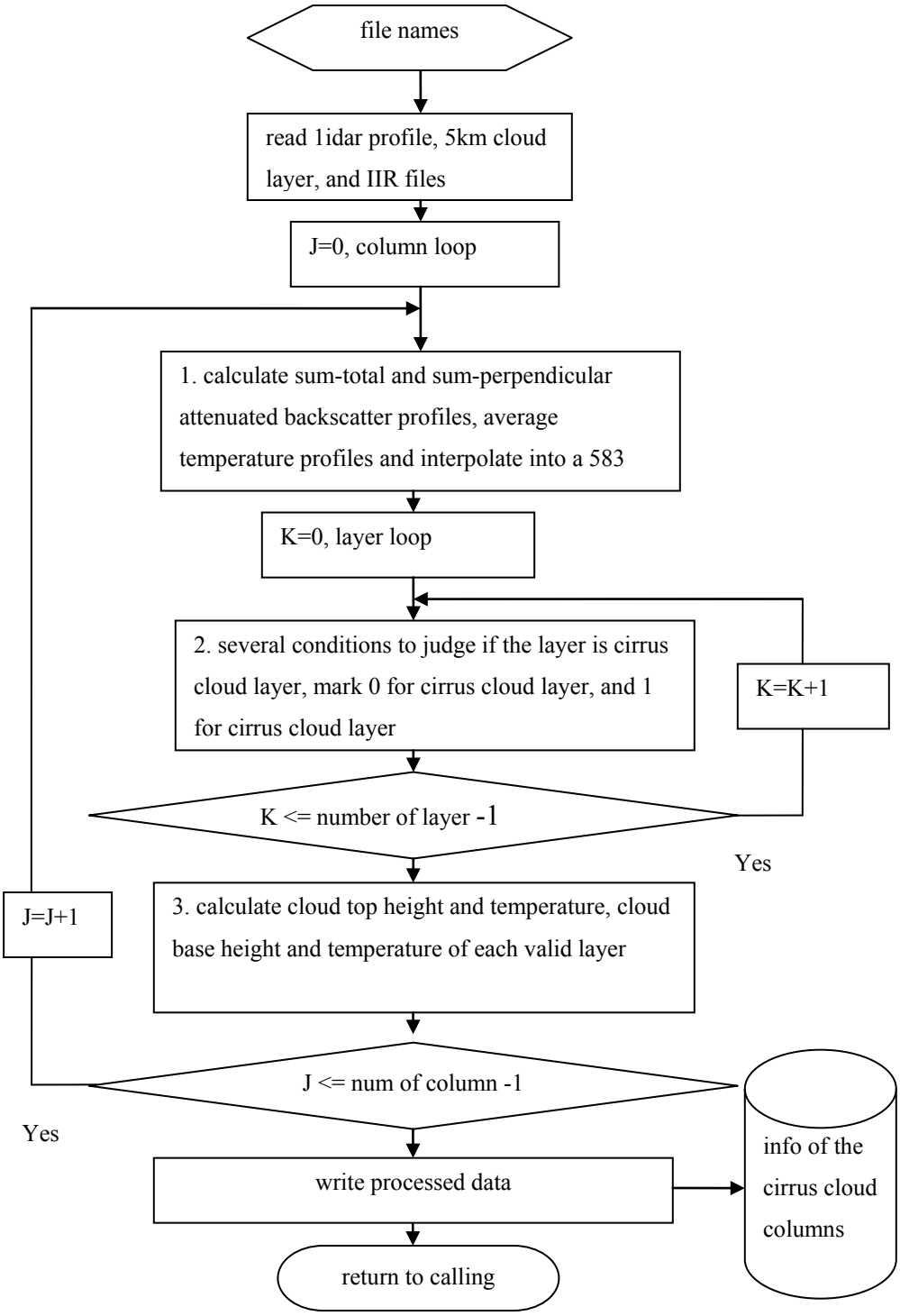

Figure 3.3 One file data process algorithm

If the column is of bad quality, do not process the column, go directly to next column; if the column is of good quality, then locate the related 15 profiles in level 1 lidar profiles, and sum these profiles to get the total attenuated backscattered coefficient profile TOT(z) and attenuated backscatter coefficient profile PER(z), again, only good quality profiles marked by the QC flag in the profile data are summed up; average the temperature profiles of 15 profiles and interpolate into 583-point temperature profile T(z). After determining the above profiles, the algorithm goes through layer loops of the column to identify if the layers are cirrus clouds. A cirrus cloud layer must meet two conditions: the layer top temperature must be less than -40ºC, and the layer must be transparent. If the layer is cirrus cloud, it is marked as 1, otherwise, it is marked as 0, and the layer information is recorded. After going through the layer loop, the program calculates the cirrus cloud base and top temperature.

C. After finishing the column loop, all the profiles and layer information are stored in the data zone in the memory if the column includes a cirrus cloud layer.

In the level 1 and level 2 data, there are quality flags to indicate the quality of the data. These QC flags are used in the algorithm to assure the quality of processed results.

Figure 3.4 gives an example of a column in 5 km cloud data (top panel), 15 lidar level 1 profiles which correspond to the column (middle panel), and the average profile of these 15 profiles (bottom panel).

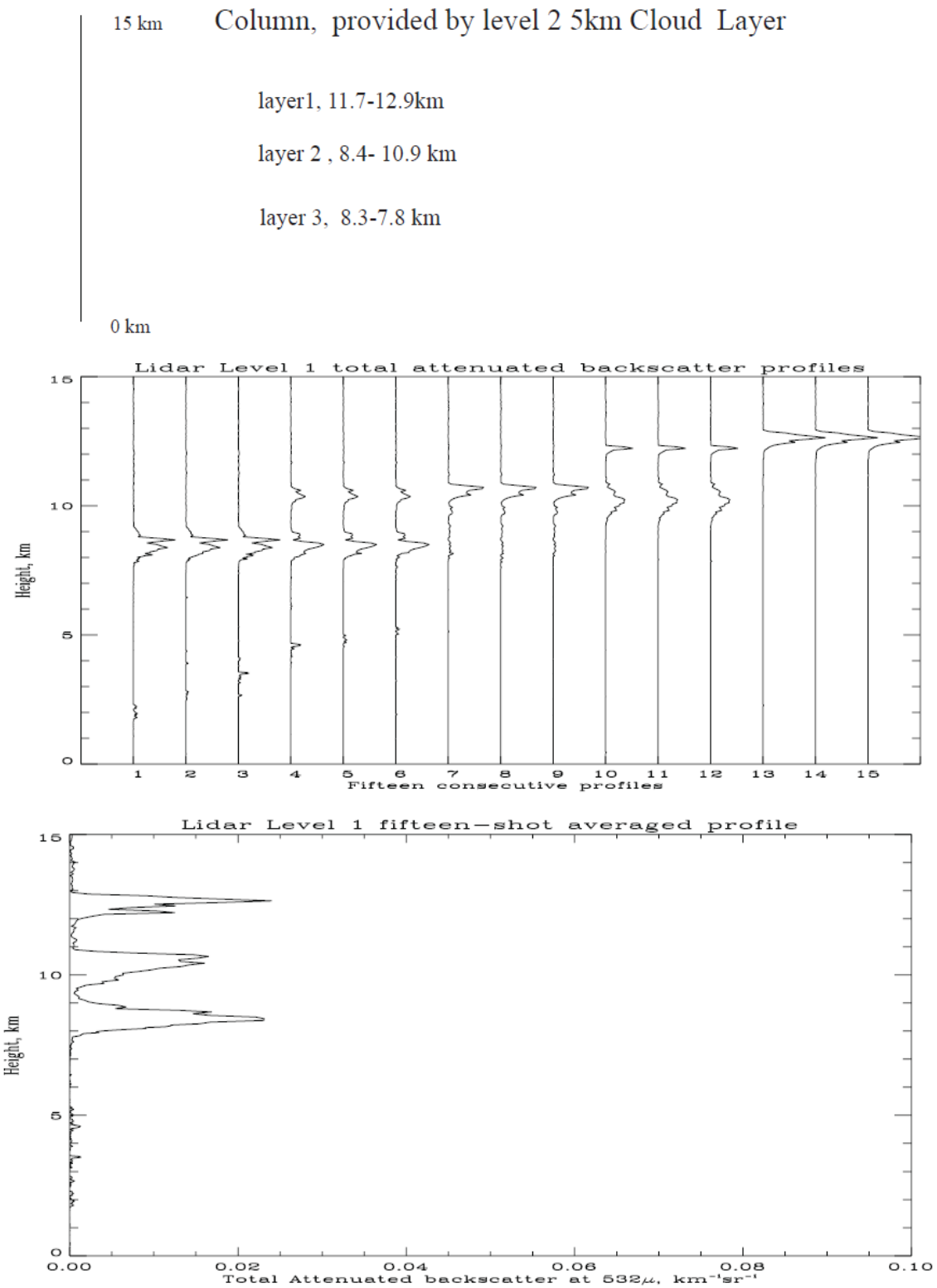

Figure 3.4 Example of a column, related lidar profiles, and averaged profile

There are three feature layers in the column. Two of them are identified as cirrus cloud layers in the average profile by the cirrus cloud identification algorithm.

Figure 3.5 describes how to arrive at the sums of the total and perpendicular attenuated backscattering coefficient profiles and calculate the average temperature profile.

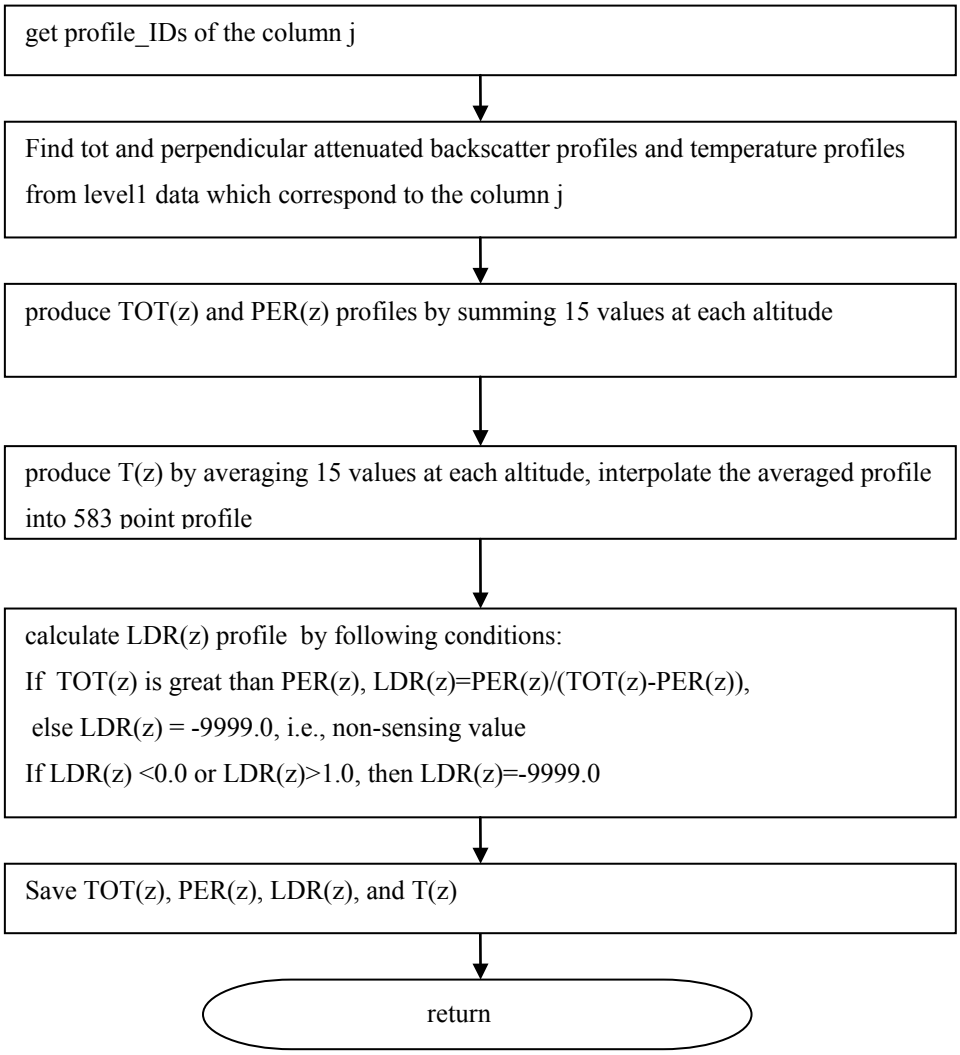

Figure 3.5 Flowchart to calculate the profiles

First, locate those profiles in the level 1 profile file, according to the start and end profile IDs of column K, then sum the total and perpendicular attenuated backscattering coefficients, respectively, to form the total attenuated backscattering coefficient profile (TOT(z)) and perpendicular backscattering coefficient profile (PER(z)). Second, locate those temperature profiles in level 1, and average those temperature values, except for those nonsense values, at each altitude to form an average temperature profile. A temperature profile is 33 point profile, whereas a TOT (z) and a PER (z) are 583 point profiles, so a temperature profile needs be interpolated into a 583-point profile. In this study, the value of -9999.0 indicates missing value due to control of QA/QC or missing data.

The cirrus cloud layer identification algorithm is presented in Figure 3.6. In each column, there are several cloud layers. The identification logic must go through each layer. In this research, only layers which are detected by using 5 km horizontal distance profiles are considered. The program first checks the layer's top temperature. If the temperature is above -40ºC, the layer is not a cirrus cloud layer, and the program returns to the calling program. Otherwise, the program goes further to check the transparency of the layer. If the layer is not the lowest layer, then the layer is cirrus cloud layer. If the layer is the lowest layer, and its maximum total attenuated backscattering coefficient is great than three times of the total attenuated backscattering coefficient from surface, the layer is considered non-transparent, and the layer is not considered a cirrus cloud layer. Otherwise, the layer is cirrus cloud layer.

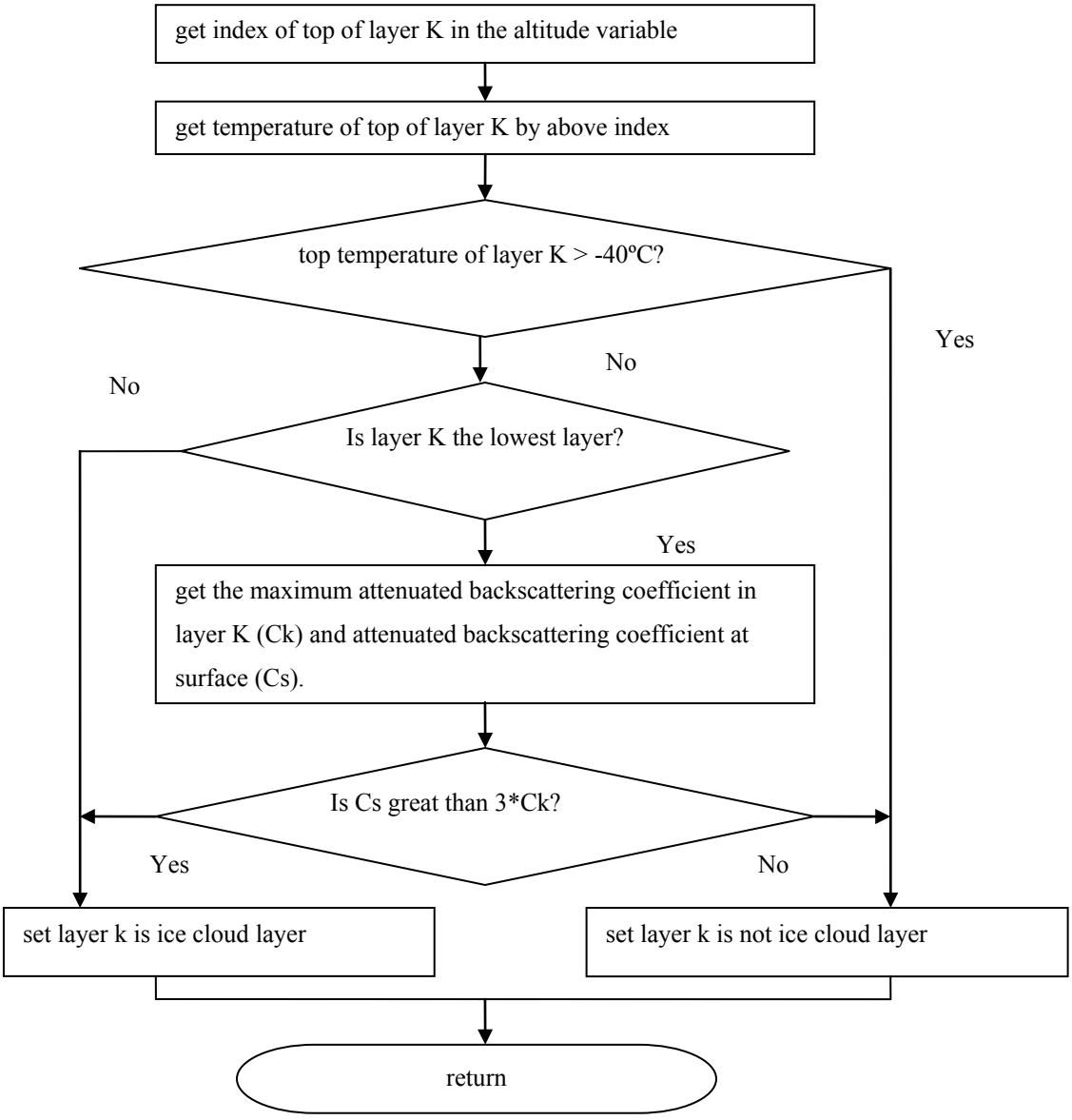

Figure 3.6 Cirrus cloud layer identification flowchart

As pointed out before, the CALIPSO produces around 14 daytime files and 14 nighttime files per day. Daytime and nighttime files are processed separately. 14 daytime or nighttime files are combined by the program to produce daytime or nighttime one-day

data files with file names of yyyy-mm-dd_ZD[N].dat. The data fields in the processed data files are listed in Table B.14. Figure 3.7 describes the flowchart to produce the grid data.

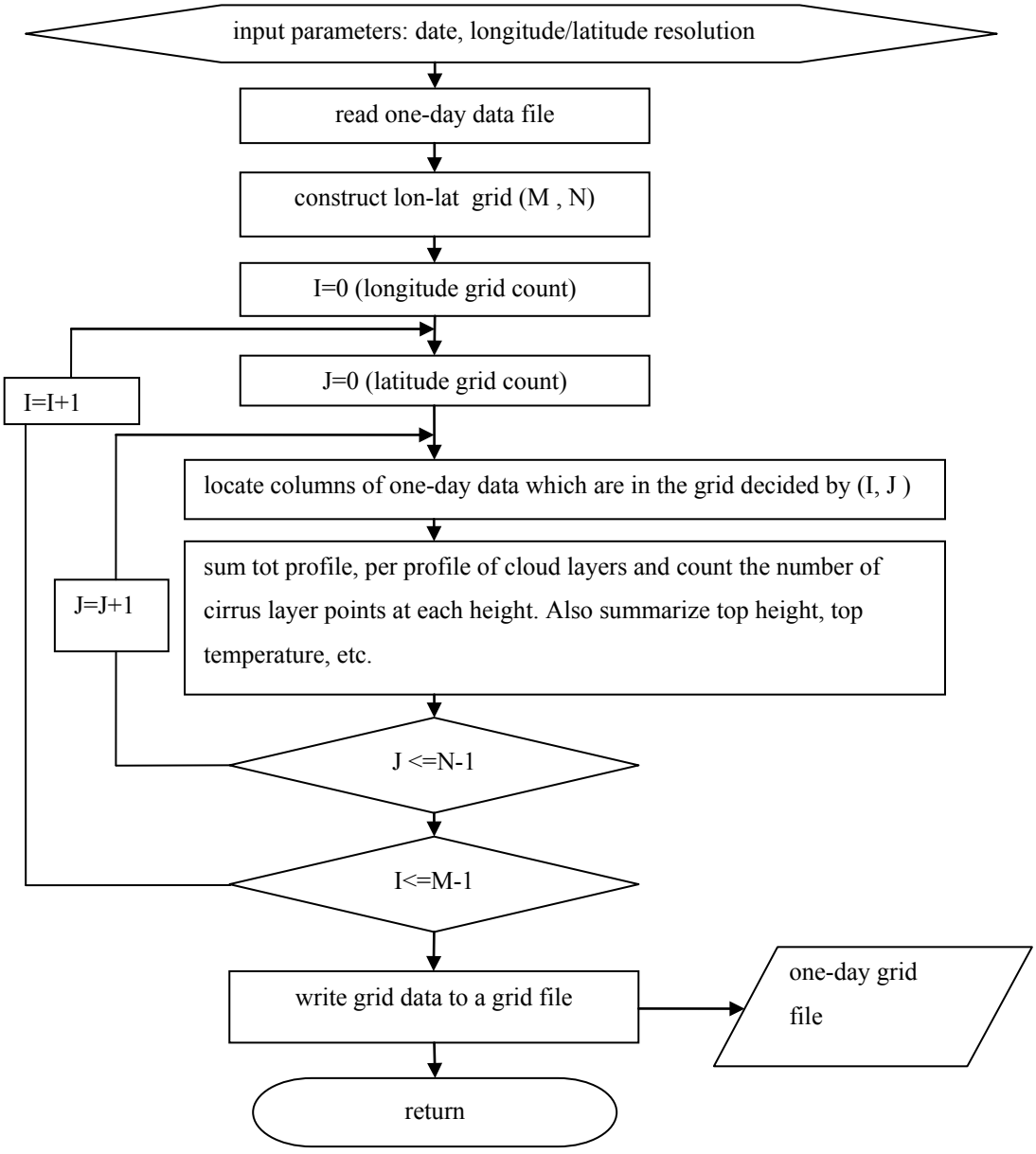

Figure 3.7 Flowchart to calculate daily longitude vs. latitude grid data

The daily data are grouped into the 5 degree longitude by 5 degree latitude boxes which are called grids. As described in Figure 3.7, the program calls the subroutine described in Figure 3.8 to calculate the sums of the total attenuated backscatter, perpendicular attenuated backscatter, temperature, and count profiles. The count profile counts how many cirrus cloud layers are summed at each height.

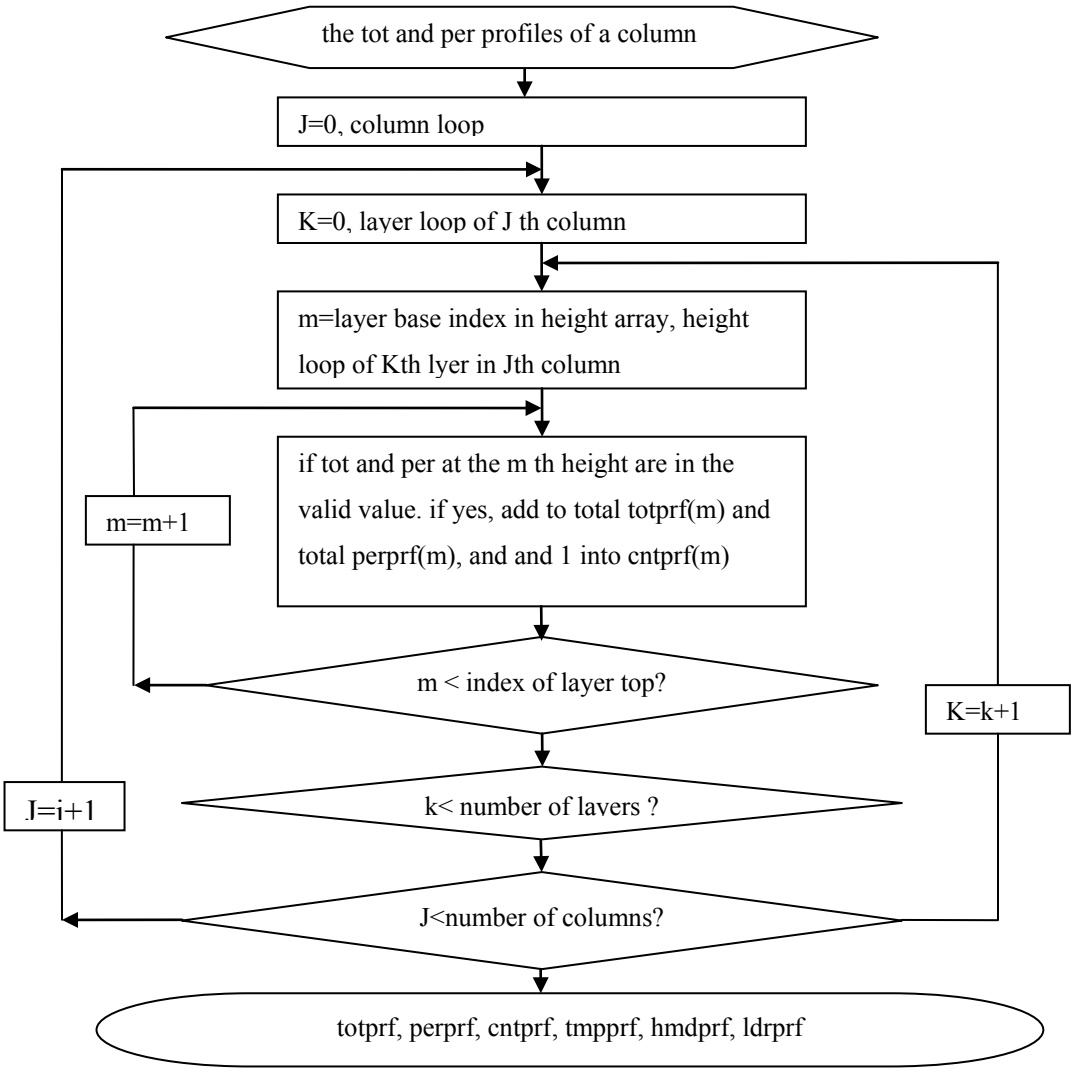

Figure 3.8 Flowchart to calculate profiles in a grid

Figure 3.8 is the flowchart to calculate the profiles in a grid. This program calculates the sums of the total and the perpendicular attenuated backscatter of cloud layers, the LDR profile, the temperature profile, and the average LDR of the grid. The data fields of the daily longitude-latitude grid data are described in Table B.15.

Monthly, seasonal, and yearly grid data are obtained by adding the daily grid data. Figure 3.9 is the flowchart to add the daily longitude versus latitude grid data.

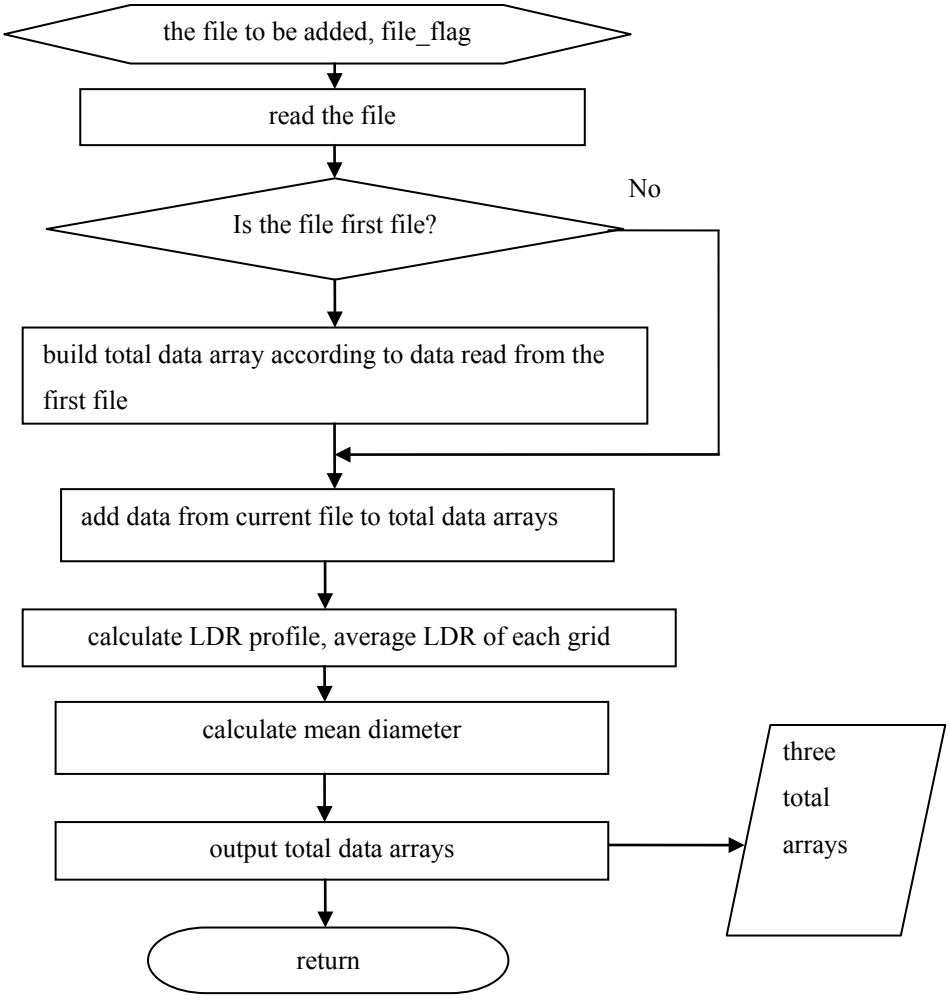

Figure 3.9 Flowchart to add the longitude-latitude grid data

This program accepts two input parameters: names of files whose data will be added in the total data arrays and a flag which indicates that total data arrays are empty. It reads the grid data files. By using adding grid data subroutine, any time length grid data can be easily added together for analysis.

3.3 Linear Depolarization Ratio Algorithm

The calculation methods of LDR profiles of the grids in monthly, seasonal, or yearly grid files are different in the two version applications. In the application version 1, the LDR profiles are calculated for the columns in a half-orbit file, then the LDR profile for a grid is calculated by averaging the LDR profiles in the grid, and the average LDR of the grid is calculated by averaging the LDR profile. The LDR calculated in this method shows a great day versus night variation. In chapter 5, we discuss in detail the version 1 LDR algorithm and compare the results produced by the two version LDR algorithms.

In the application version 2, the LDR profile of a grid is calculated by the sum of the perpendicular attenuated backscatters and the sum of the total attenuated backscatters. The calculation method for the LDR profile in a grid in the application version 2 can be described by Equation (3.1).

$$LDR(z) = \sum_{j=1}^{m} PER(z) \Big/ \sum_{j=1}^{m} [TOT(z) - PER(z)] , \tag{3.1}$$

where $TOT(z)$ is the summed total attenuated backscatter profiles, $PER(z)$ is the summed perpendicular attenuated backscatter profiles, m is the number at height z. The

summed total attenuated backscatters profiles of cirrus clouds are calculated in this way: because each total attenuated backscatter profile includes 583 points, and each point associates a height which is indicated in the height profile (583). If the points are within the cirrus cloud layers, they are valid points, and their values are kept, if the points are not within the cirrus cloud layers, the values of these points are set to -9999.0. The total attenuated backscatter profiles in the grid are added at each height. Only valid points are added and recorded in a sum profile, and numbers of valid points are recorded in a count profile. In the same way, the summed perpendicular attenuated backscatter can be calculated. The LDR profile then can be evaluated by calculating the ratio of the summed perpendicular attenuated backscatter to the summed total attenuated backscatter minus the summed perpendicular attenuated backscatter.

As for calculation of the average LDR, we have to consider the factor that lidar profiles have different vertical resolutions. The summed perpendicular and total attenuated backscatter profiles are weight-added, respectively, and the average LDR is obtained by the weight-added results. This method is illustrated by Equation 3.2.

$$LDR = \sum_{k=1}^{n}\{\sum_{bk}^{tk}[a_z sumper(z)]\} \Big/ \sum_{k=1}^{n}\{\sum_{bk}^{tk}[a_z(sumtot(z) - sumper(z)]\} \quad , \tag{3.2}$$

where n represent the number of cirrus cloud layer, a_z is the weight factor, tk and bk represent the top and base height of the k layer, and $sumper(z)$ and $sumtot(z)$ is the sum of the perpendicular and the sum of total backscatter profiles calculated in Equation (3.1), respectively. If weight 1 is used for the points in 30 meter resolution, then weight 2 is

used for the points in 60 meters resolution. In the same way, points at 180 and 300 meters resolutions are weighted 6 and 10, respectively. Points in the perpendicular attenuated backscatter profile (i.e., $sumper(z)$) are added by weight-addition method to get the sum of the perpendicular attenuated backscatters. In the same way, the sum of the total attenuated backscatters is obtained by weight-adding the points of the total attenuated backscatters profile (i.e., $sumtot(z)$). The average LDR can be evaluated by divide the sum of the perpendicular attenuated backscatters by the difference of the sum of the attenuated backscatters and the sum of the perpendicular attenuated backscatters. There is another way to calculate the sums of perpendicular and total backscatters, respectively. It is called the interpolation method. The vertical resolutions of the profiles are 30, 60, 180, 300 meters. One point is inserted with the value which is the same as the lower height point between points within 60 meter distance. In similar way, 5 points are inserted between points within 180 m, and 9 points between points within 300 meters.

The calculation method in the application version 1 is not reasonable when one considers the definition of the LDR of a grid. In this research, we are concerned with at least monthly average values of physical properties of cirrus clouds. A grid with a month of data includes about 8000 level 1 profile. With this large number of profiles, the two LDR calculation methods produce less difference when they are used to calculate the LDR profile and average LDR of a grid. A detailed discuss about the difference is covered in Chapter 5.

Figure 3.10 gives the flowchart to calculate the LDR profile and the average LDR in a grid. Monthly longitude-latitude grid data are calculated by summing the daily

longitude-latitude grid data. The data fields of the monthly longitude-latitude grid data are the same as the daily longitude-latitude data files. The monthly longitude-latitude grid data are converted into monthly latitude-height grid data. The data fields of the latitude-height grid data are described in Table B.16.

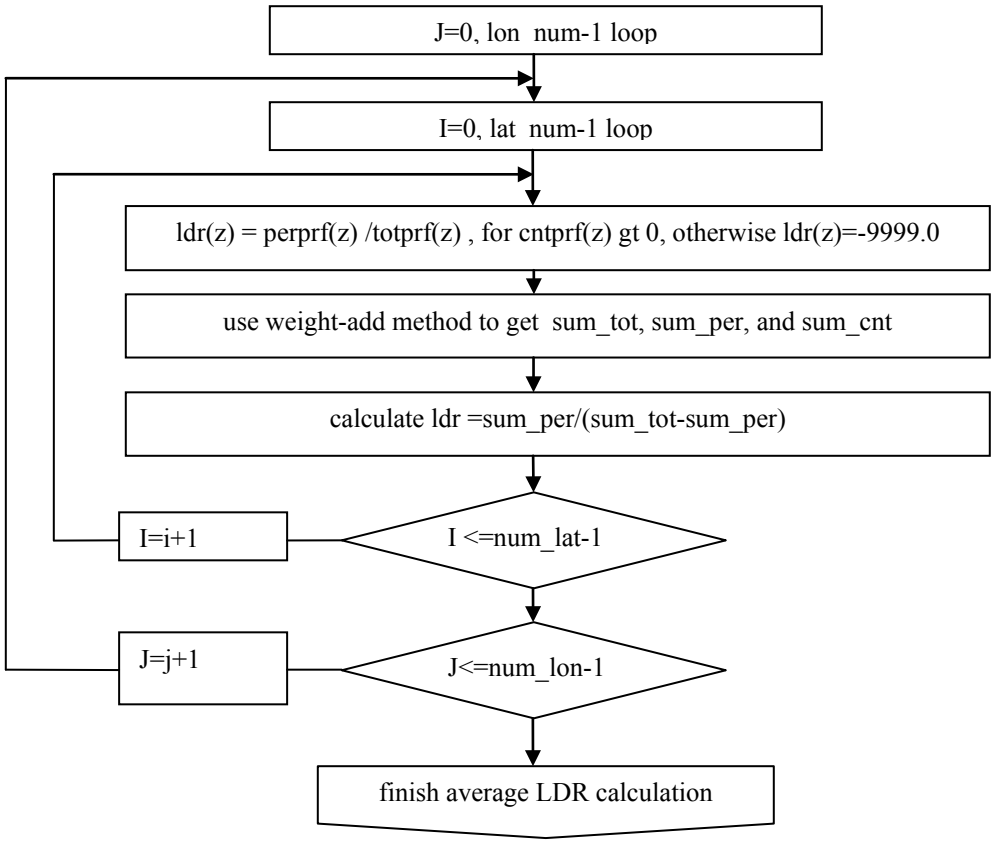

Figure 3.10 Calculation of the LDR profile and average LDR of a grid

3.4 Effective Diameter Algorithm

The split-window method is a popular approach to estimate the effective size of ice crystals and the ice water content of ice clouds. The effective emissivity of clouds can be evaluated by (Chomette *et al.*, 2003)

$$\varepsilon_{eff,k} = [R_k - R_{k,BG}]/[B_k(T, Z_c) - R_{k,BG}], \tag{3.3}$$

where R_k is the calibrated radiance measured in channel k, and $R_{k,BG}$ is the outgoing top of the atmosphere background radiance which would be observed in the absence of the studied cloud (this reference background radiance corresponds to clear sky radiance in case of single layer system), and $B_k(T, Z_c)$ is the radiance of cloud located at the reference altitude Z_c, corresponding to a temperature T. The effective emissivity of cirrus clouds is sensitive to the mean effective diameters of ice crystals of ice clouds. CALIPSO level 2 IIR/track data set provides radiances at three wavelengths (i.e., 8.65μm, 10.6μm, and 12.5μm) at the top of atmosphere. If we present the difference of effective emissivities at two wavelengths as a function of emissivity at one wavelength, we find this function depends on the mean effective diameter of ice crystals. This interactive relationship is shown in Figure 3.11. As shown in the figure, the mean effective diameters determine the curvature and the position of curves, which indicate the relationships between the difference of emissivities at two wavelengths and the emissivity at one wavelength. One can construct a look-up table by simulation of the emissivities of clouds in terms of effective diameters and other macro-physical properties.

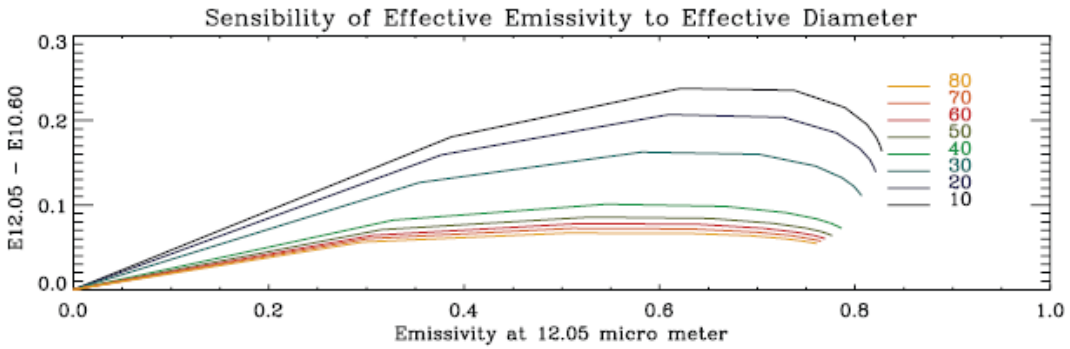

Figure 3.11 Difference of effective emissivities as a function of emissivity

E12.05 represents the effective emissivity of clouds at 12.05 μm, and E12.05-E10.60 represents the difference between the effective emissivity of cloud at 12.05μm and the effective emissivity of cloud at 10.60 μm. The numbers corresponding to curves are effective diameters in unit of μm.

By comparing measured effective emissivities with those in the look-up table, one can estimate the mean effective diameters and the ice water content. Figure 3.12 presents the scheme of the split-window method for estimation of the microphysical properties of ice clouds. There are two main steps in the method. In step 1, one constructs a look-up table which includes the simulation results of running a radiative transfer (RT) model to simulate emissivities at three wavelengths (8.65μm, 10.60μm, and 12.05μm) as a function of cloud physical quantities. The radiative transfer model used in the simulation is named *streamer*, which was developed by Key and Schweiger (1998). The inputs to the radiative transfer model include cloud-top height, cloud thickness, and effective diameter. The outputs of the radiative transfer model are radiances at the TOA at three wavelengths. The radiances are converted into effective emissivities of clouds by Eq. (3.3).

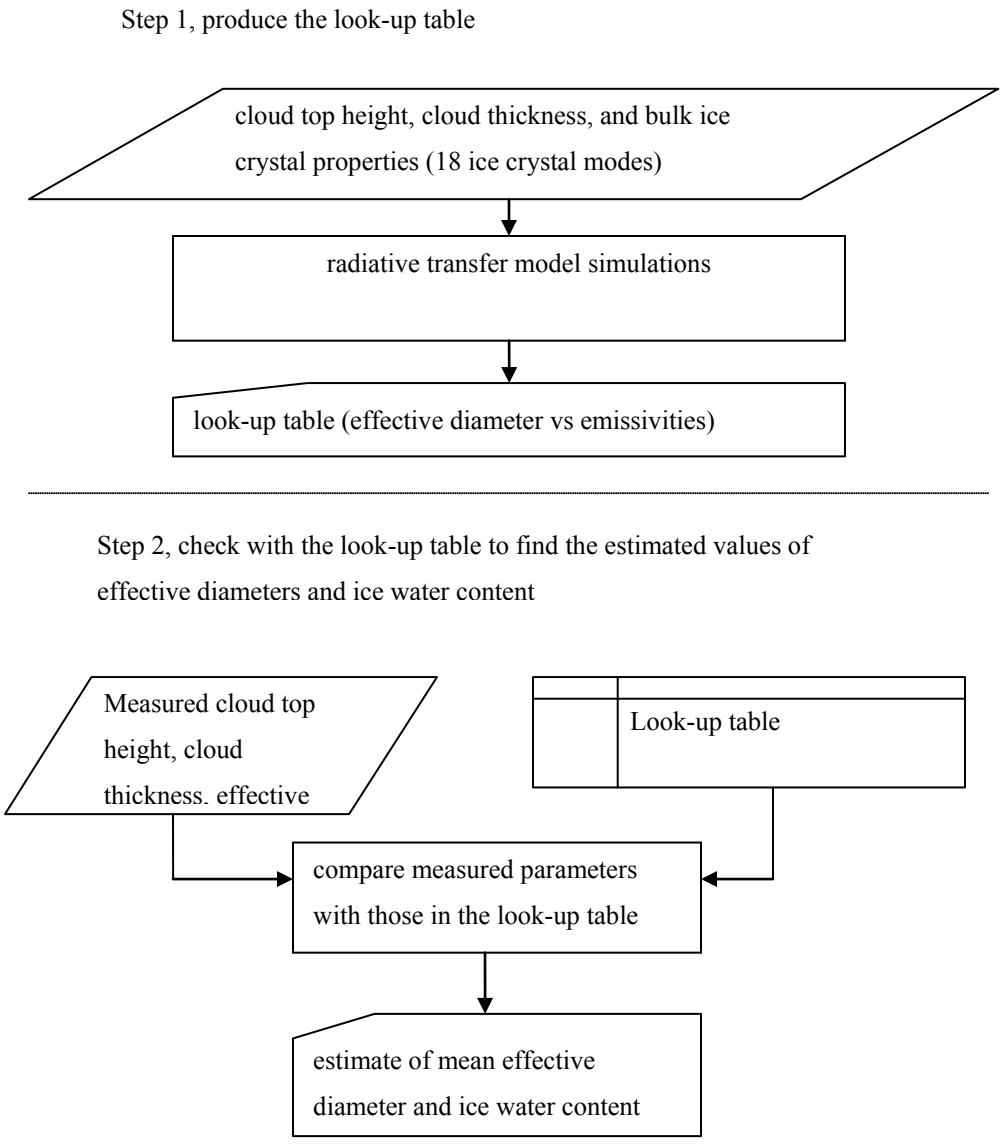

Figure 3.12 Scheme of split-window for calculation of effective diameter

In these simulations, the height of cloud top changes from 7 km to 14 km with 1km resolution, thickness of clouds is in the range of 0 km to 4 km with 0.5 km resolution, and 18 ice crystal bulk scattering models from the mid-wave to far IR spectral

region (e.g. 3.08 μm to 100 μm) are used. The ice crystal bulk scattering models were developed by Baum and co-workers (Baum *et al.*, 2011).

In step 2, one compares measured emissivities with simulation results to get the effective diameters. This thesis uses the squared distance method to determine the effective diameter. Within a 2-D coordinate system, where the y-coordinate is the difference of emissivities at two wavelengths and the x-coordinate is the emissivity at a wavelength, the squared distance between the measured values ($e_{j,m}$, $\Delta_{j,k,m}$) and the simulated values ($e_{j,s}$, $\Delta_{j,k,s}$) for simulation cases are calculated by

$$\Delta = (\Delta_{j,k,m} - \Delta_{j,k,s})^2 + (e_{j,m} - e_{j,s})^2 . \quad (3.2)$$

The case with the minimum of squared distance is used to estimate the effective diameter.

The radiative transfer model *streamer* is a band model. It can be used to calculate either radiances or irradiances. The major features (Key, 2002):

• Fluxes (irradiances) may be computed using two or more streams, either broadband or narrow band. The method for calculation of two streams comes from Toon *et al*. (1989), and the method for calculation of more than two streams comes from Stamnes *et al*. (1988).

• Radiances (intensities) may be computed for any polar and azimuthal angles, using 4 or more streams. TOA albedos or brightness temperatures are calculated along with the radiances.

• Upwelling and downwelling shortwave and longwave, as well as net fluxes, cloud radiative effect ("cloud forcing"), and heating rates can be computed.

• There are 24 shortwave and 105 longwave bands.

• Gas absorption is parameterized with overlapping gases. Gaseous absorption may be turned on or off.

• Liquid and ice cloud optical properties, five aerosol optical models, and four aerosol vertical profiles are part of the model database. Clouds may be specified as some combination of particle size, water content, optical and geometrical thicknesses, or the optical properties and phase function can be input. A variety of different ice particle shapes (column, aggregate, etc.) are available. Mix-phase clouds (liquid and ice or ice and ice) can also be specified.

• There are seven standard atmospheric profiles. They are tropical, mid-latitude summer, mid-latitude winter, subarctic summer, subarctic winter, arctic summer, and arctic winter. Either standard or user-defined profiles can be used, or total column amounts of water vapor, ozone, and/or aerosols can be specified

• Each computation is done for a "scene," where the scene can be a mixture of up to 10 cloud types occurring individually, up to 10 overlapping cloud sets of up to 10 clouds each, and clear sky, and all are above some combination of up to three surface types.

• Various built-in surface types may occur within the scene: open ocean (sea water), melt-ponds, bare ice, snow, vegetation (grass, dry grass, deciduous forest, and coniferous forest), and dry sand. Spectral albedo and bidirectional reflectance models (BRDF) are included, or BRDF data can be used as input.

In order to simulate effects of ice clouds with an RT model, precise knowledge of the bulk single-scattering properties of non-spherical ice crystals in ice clouds is required.

An exact scattering theory for the solution covering all size parameters does not exist. There are many approximations and numerical approaches depending on the size parameter. Baum *et al.* (2005), for instance, developed a set of ice crystal bulk single-scattering property models in the infrared spectral region by adopting theories and in-site measurements. They used in-situ data in midlatitude and tropical ice clouds from airborne sampling probes and balloon-borne replicators as the basis for the development of the model. Their research indicates that no single habit accurately replicates the derived ice water content and mean median mass diameters, but a mixture of habits can significantly improves the comparison of theoretical calculation with in situ measurement. The percentage of each habit used in the integration of a given property over a particle size distribution is based on the particle's maximum dimension. D < 60 microns: 100% droxtals; 60 microns < D < 1000 microns: 15% 3D bullet rosettes, 50% solid columns, and 35% plates; 1000 microns < D < 2500 microns: 45% hollow columns, 45% solid columns, and 10% aggregates; 2500 microns < D < 9500 microns: 97% 3D bullet rosettes, and 3% aggregates. The models provided bulk microphysical and optical properties, such as ice water content (IWC), median mass diameter, extinction efficiency, asymmetry factor, and single scattering albedo, at 1 cm^{-1} spectral resolution and spectral range from 100 cm^{-1} to 3250 cm^{-1}. The detailed information about the models is described by Baum *et al.* (2011). The main features of the model are:

• Size distributions are based on 45 size bins (particle size ranges from 2 to 9500 microns).

• Ice particle habit distributions vary as a function of the maximum dimension of a ice crystal.

• New ice crystal scattering property libraries have been calculated for a variety of habits, including droxtals, plates, hollow and solid columns, 3-D bullet rosettes, and aggregates.

• Each model contains the mean and standard deviation of each microphysical and optical property, including the ice water content, mean mass diameter, single scatter albedo, asymmetry factor, extinction efficiency, and the scattering phase function in selected wavenumber regions.

A set of 18 ice crystal bulk single scattering models was proposed according to effective diameter (D_e) from 10 to 180 microns in increments of 10 microns. The habit mixture as described above is used for all calculations of microphysical and optical properties using the idealized ice particles for which they have theoretical scattering calculations. Table 3.2 gives an example of the models (models not complete).

Table 3.2 Example of ice crystal bulk single scattering models

Effective diameter(um): 10			
Average of iwc(gm-3): 0.0059			
Acerage of media mass diameter(um): 13.39			
Average of total area(um^2): 75.52			
Average of total volume(um^3): 647.7			
Wavenumber (cm-1)	Single-scattering albedo	Asymmetry factor	Extinction coefficient
100	0.3786	0.5504	0.2146
101	0.3765	0.5467	0.2190
102	0.3745	0.5431	0.2233
Continue to 3250			

The look-up table describes the effective diameters as function of cloud top height, cloud thickness, and emissivities at three wavelengths (8.65 μm, 10.60 μm, and 12.05 μm). As mentioned before, cloud-top height from 7 km to 14 km with 1 km resolution, cloud thickness from 0 km to 4 km with 0.5 km resolution, and 18 bulk ice crystal models are used as inputs of the radiative transfer model to produce the look-up table in this study. The format of the look-up table is shown in Table 3.3.

Table 3.3 Look-up table of simulations of effective diameter

E8.65 represents effective emissivity at 8.65μm, E8.65-E12.05 represents the difference of effective emissivity at 8.65μm minus the effective emissivity at 12.05μm. D represents effective diameter in μm, Hgt represents cloud-top height in km, Tck represents thicknes in km.

D	Hgt	Tck	E8.65	E10.6	E12.5	E8.65-E10.6	E8.65-E12.05	E10.6-E12.05
10	7.0	1.0	0.365	0.384	0.622	-0.019	-0.257	-0.238
30	8.0	3.0	0.778	0744	0.839	0.034	-0.06	-0.095
not complete table								

CALIPSO provides infrared radiation measurements in three wavelengths, so one needs to decide which wavelength pair is the best for the estimation of effective diameter. For the purpose of comparing the sensibility of three emissivity difference pairs to the effective diameter, the radiative transfer model simulation results with a fixed 7 km cloud-top height and 2 km cloud thickness, and various effective diameters from 10 to 80 micro meters are plotted in Figure 3.13.

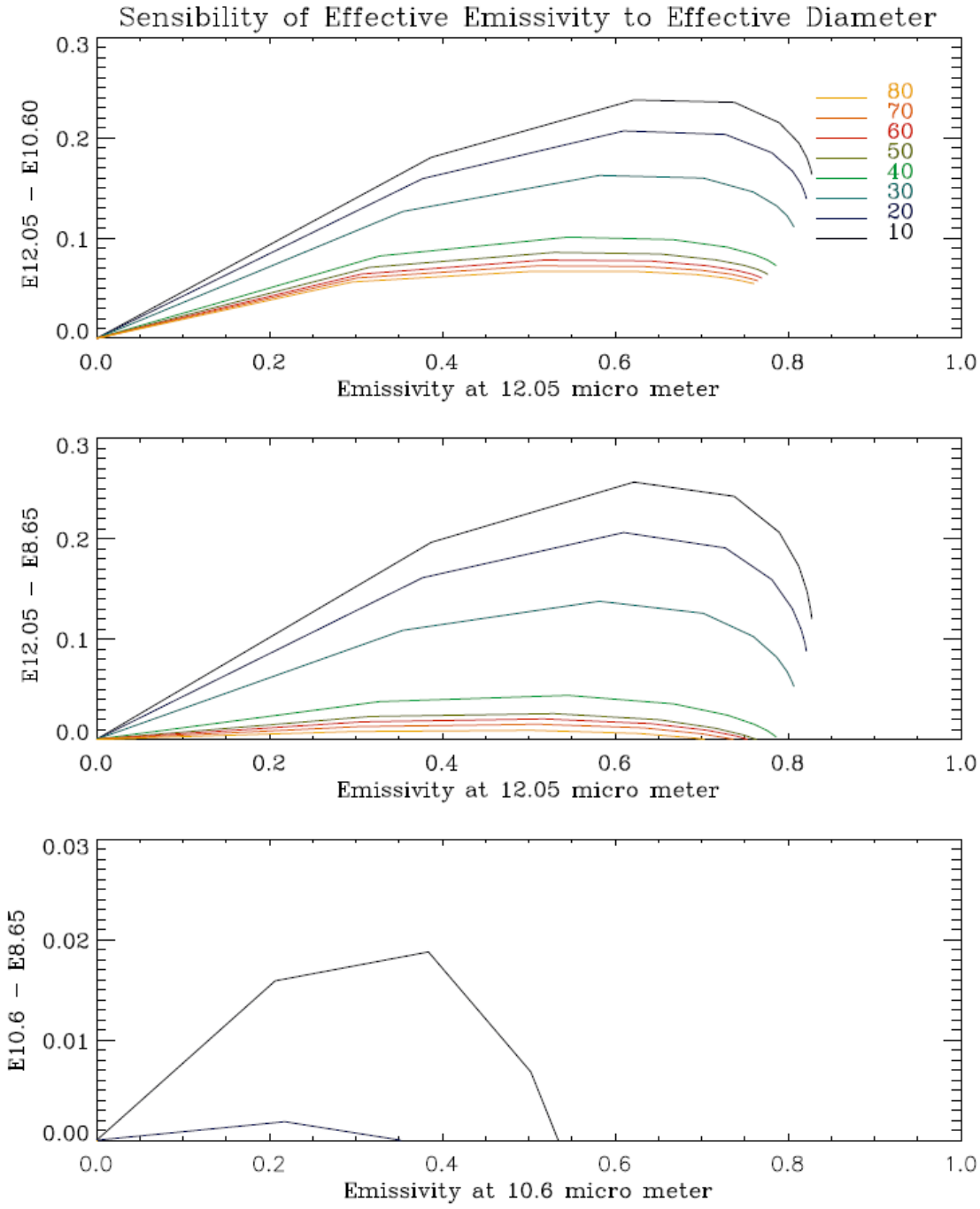

Figure 3.13 Comparison of sensitivity of emissivity to effective diameter

In Figure 3.13, E10.6 represents emissivity at 10.6 μm wavelength, E10.6-E8.65 represents the difference of emissivities at 10.6μm and 8.65μm. Figure 3.13 shows that E10.6-E8.65 has the lowest sensitivity to large effective diameter; E12.05-E8.65 has a slightly higher sensitivity to small effective diameter than E12.05-E10.6, but its sensitivity to large effective diameter is not as high as E12.05-E10.6. In overview, E12.05-E10.6 has the highest sensitivity to effective diameter, therefore, is picked to estimate the effective diameter in this research. Instruments have spectral response functions. The band-weight files provided by the IIR science team are the input to the RT model for radiative calculation.

3.5 Error Analysis for Estimation of Quantities

Before one can use the estimated physical quantities to describe the properties of clouds, one has to know how accurate these quantities are. The errors for quantities can be estimated by using classical statistic theory. As an example, the error by using the sample frequency to estimate the frequency of occurrence of ice clouds is analyzed. One month of data from 2006/07 is randomly picked to illustrate the error analysis procedure. Figure 3.14 shows the sample size to estimate the physical quantities. The white background in the display means there is no available data.

There are a lot of columns in a grid. As mentioned before, each column corresponds to 15 lidar profiles, so the total lidar profiles in the grid is the number of columns multiplied by 15. The numbers of columns in the grids with latitude between 60S and 60N degree do not spread out widely.

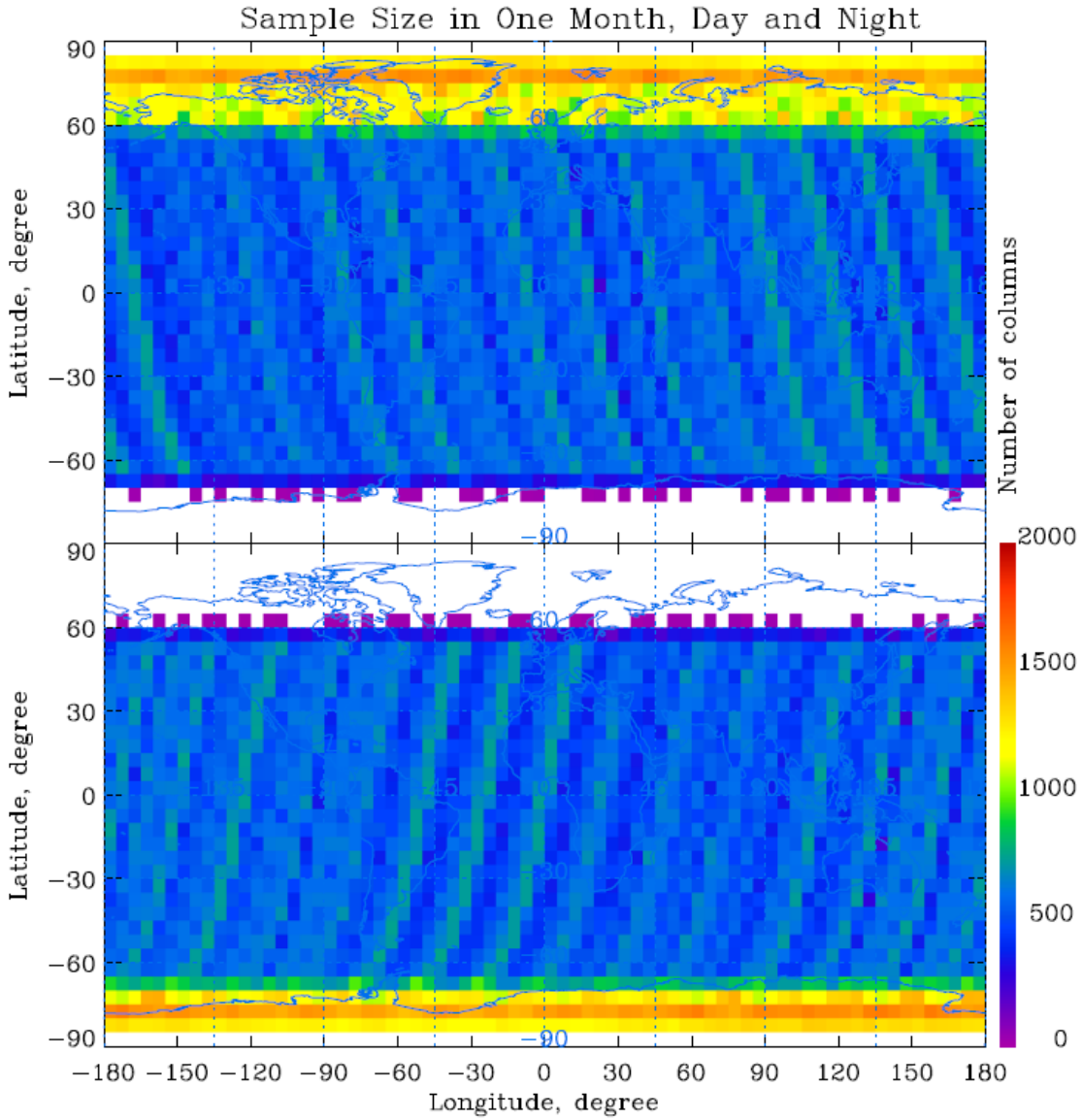

Figure 3.14 Sample size to estimate the physical quantities of cirrus clouds

They have a mean value of 551 and a standard deviation of 94. Because of many overridden flights at both the northern and southern regions, the numbers of columns in the grids with greater than 60N latitude in the northern hemisphere or less than 60S latitude in the southern hemisphere are much larger, so estimation error for grids in these regions are smaller than for those between 60S and 60N latitude.

The following analysis shows that the physical quantities estimated for the grids in the range of latitude of 60S to 60N are consistently accurate. According to basic statistic theory, the frequency of occurrence of cirrus clouds (p) is the population frequency. In order to estimate this frequency, N samples are measured. The sample frequency is $\overline{p}$. As long as N is large, $\overline{p}$ is approximately normally distributed. The mean of $\overline{p}$ equals the population proportion: $\mu_{\overline{p}} = p$ and the standard deviation of $\overline{p}$ is defined as (Weiss, 2008)

$$\sigma_s = \sqrt{\frac{\overline{p}(1-\overline{p})}{N}} . \tag{3.3}$$

The margin of error by using $\overline{p}$ to estimate p with confidence level of 1-α is (Weiss, 2008)

$$E = Z_{\alpha/2}\sigma_s . \tag{3.4}$$

The frequency of occurrence of ice clouds in one month is illustrated in Figure 3.15. The errors of estimation with 95% confidence level are calculated by the equation (3.4), and the result is shown in Figure 3.16.

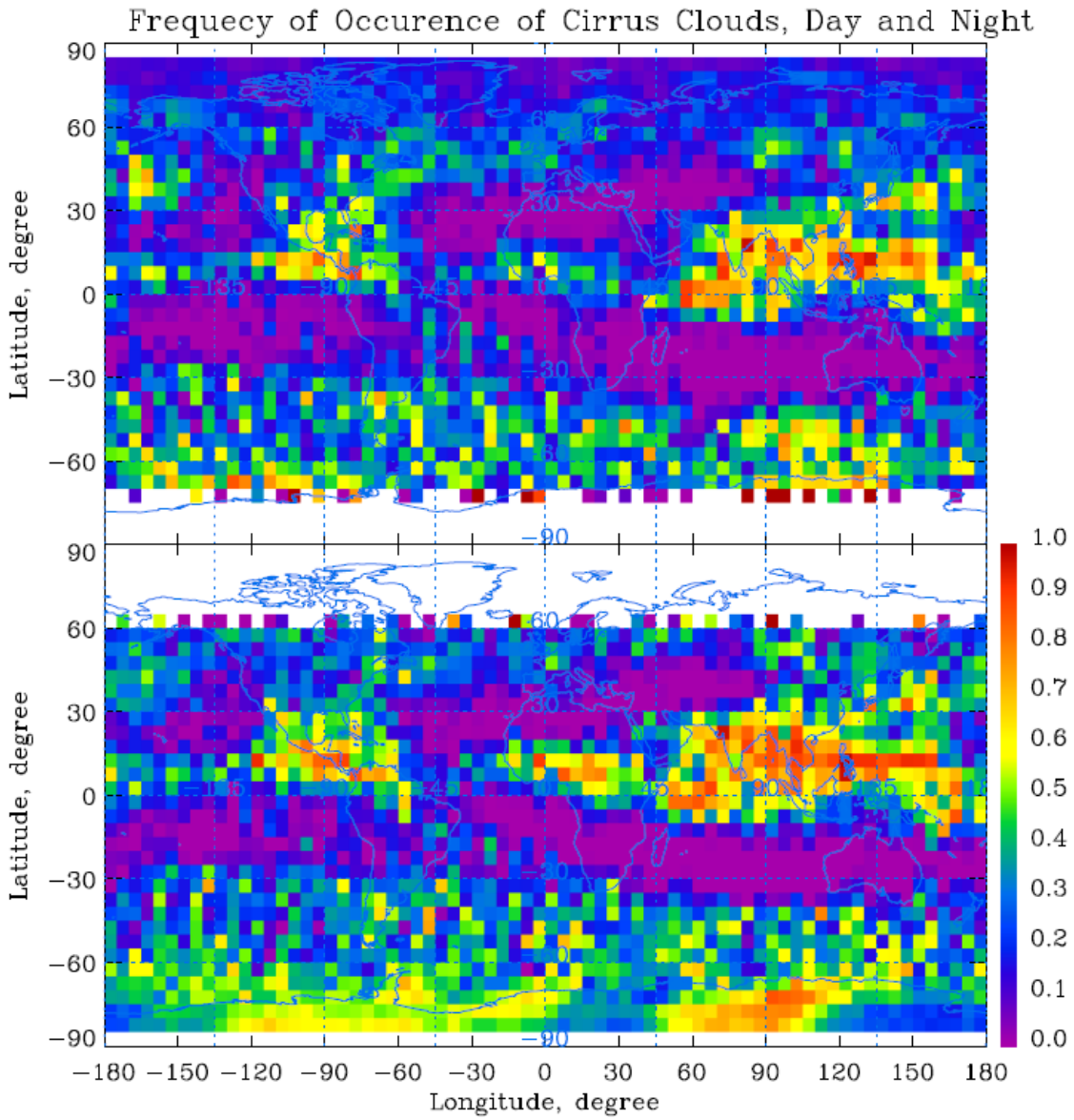

Figure 3.15 Frequency of occurrence of cirrus clouds

Zero frequency of occurrence at a grid (5 longitudes by 5 latitudes) indicates that either there is no ice cloud if the grid is in the measurement range, or there is no observation data if the grid is out of measurement range. The estimation errors for frequency of occurrence of ice clouds are presented in Figure 3.16. As shown in this

figure, the majority of the estimation errors are very small. Only very few grids with large errors exist either less than 65S latitude daytime or more than 60N latitude nighttime. The mean margin of error is 0.028 and 0.031 at daytime and nighttime, respectively.

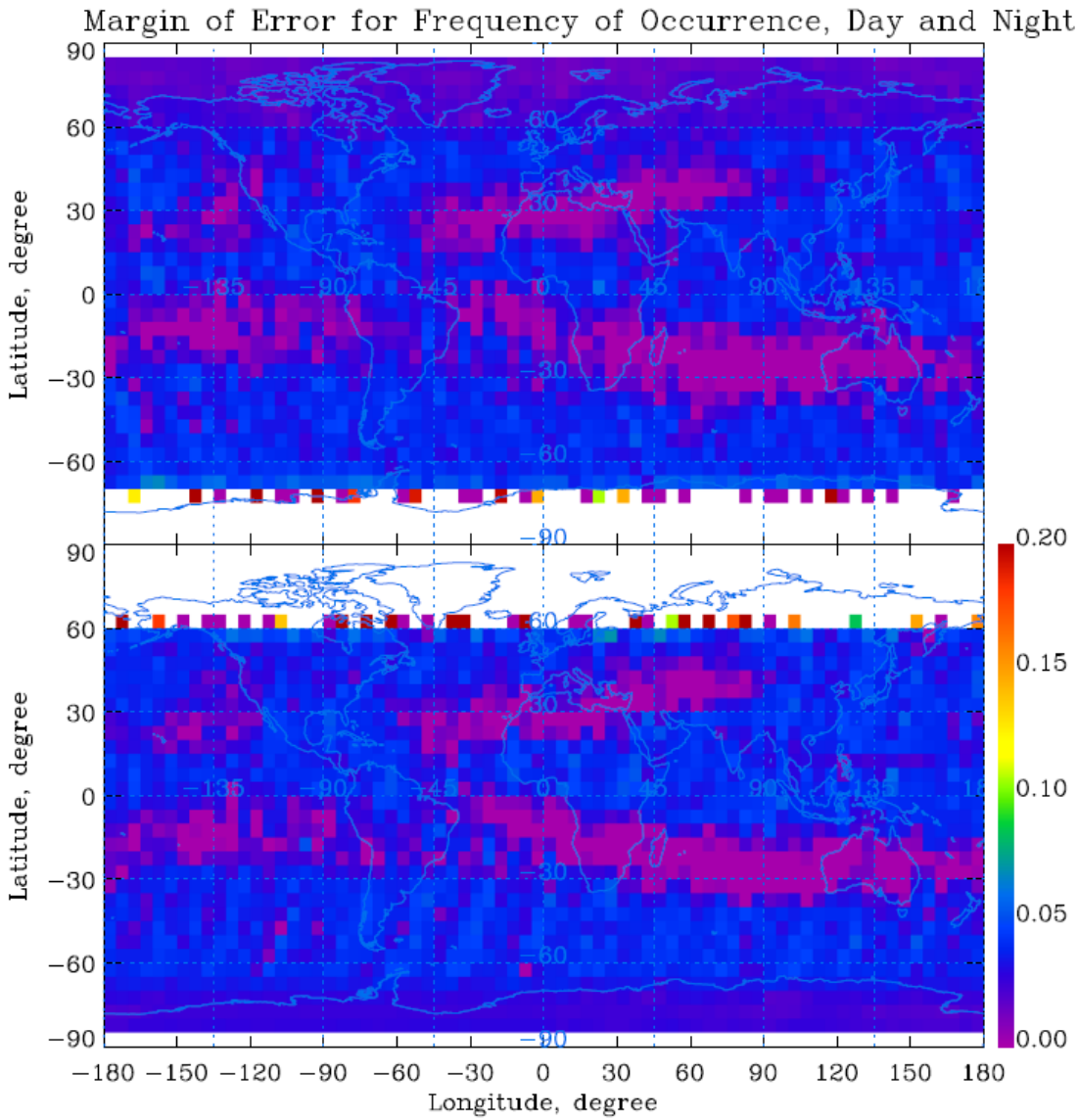

Figure 3.16 Margin of error for estimation of frequency of occurrence

By calculation, one obtains the maximum, mean, and standard deviation values at daytime are 0.24, 0.03, and 0.02, respectively, and the maximum, mean, and standard deviation values at nighttime are 0.38, 0.03, and 0.02, respectively. This means that one has 95% confidence to say that the frequency of occurrence of cirrus clouds at daytime is in the range between 0.21 and 0.27, and the frequency of occurrence of cirrus clouds at nighttime is in the range between 0.35 and 0.41. The estimation errors for other physical quantities such as cloud-top height, thickness, and cloud-top temperature are analyzed in the same way.

Chapter 4 Macro-physical Properties of Cirrus Clouds

As pointed out before, the macro-physical properties of cirrus clouds presented in the thesis include the cloud amount, cloud-top height, cloud-top temperature, and cloud thickness, and strongly impact the radiative effects of clouds. Global characteristics of cirrus cloud macro-physical properties are investigated in this chapter.

4.1 Overview of Cirrus Cloud Formation

For better understanding and explanation of the global distribution of cirrus clouds, the formation mechanics of cirrus clouds are viewed. Compared to water clouds, which contain relatively high concentrations of small cloud droplets, cirrus clouds typically contain low concentrations of large ice crystals with various non-spherical shapes. Thus the impacts of cirrus clouds on the climate system differ from those of water clouds. There are five types of formation mechanics of cirrus clouds. Table 4.1 summarizes the generating mechanisms responsible for cirrus cloud formation (Sassen, 2002).

Table 4.1 Type of cirrus clouds in terms of generating mechanism

Category	Mechanism
Synoptic (jet stream, frontal, etc.)	Top-down generation
Injection cirrus	Thunderstorm anvil-derived
Mountain-wave updraft	Orographic, terrain-induced
Cold trap	Tropopause-topped thin layer
Contrail-cirrus	Rapid cooling of aircraft exhausts

These mechanisms demonstrate the connections between cirrus cloud generation and weather processes. Synoptic cirrus clouds often appear at midlatitudes over land and ocean. They form in connection with jet streams, and frontal and low-pressure systems. These types of clouds tend to form from cloud top ice nucleating zones, where temperature is very low, and the ice supersaturation ratio is relatively high, therefore, homogeneous nucleation of haze particles can happen. As long as ice nuclei forms, the environment is favorable to the growth of ice crystals. Moist air brought by synoptic weather makes ice crystals grow to form cirrus clouds.

Injection cirrus clouds are formed by strong updrafts in deep convective clouds. Cumulonimbus clouds occur over both land and ocean in summer, and are especially concentrated in the Inter-Tropical Convergence Zone (ITCZ) and other tropical regions. Deep convective activity transfer large amounts of water high into the atmosphere. As some water clouds reach these low temperature levels, some cloud drops freeze. As long as there are some ice crystals, favorable condition for ice crystal growth leads to injection cirrus clouds form.

Mountain wave cirrus cloud formation follows in the way that mountains force air mass up drafting, thereby bringing relatively warm water vapor rich air to the upper troposphere, where the air is cooled and ice crystals form. Mountain wave cirrus clouds can persist over long distances downwind of the responsible terrain features.

Cold trap cirrus clouds occur in the tropics at very high altitudes and very cold temperatures. The moisture supply comes from thunderstorm activity.

Contrail cirrus clouds are caused by the exhausts from jet air traffic in the upper troposphere. Water vapor from the jet plane exhausts can easily freeze homogeneously in the upper troposphere and function as the ice nuclei to initialize the ice crystal growing process.

4.2 Result and Analysis

The macro-physical properties of cirrus clouds are investigated in terms of their global distributions and variations with time.

4.2.1 Yearly Average Macro-physical Properties of Cirrus Clouds

Figure 4.1 illustrates the annual average global distribution of identified cirrus clouds and the surface level pressure in 2007 in terms of longitude versus latitude display presented on 5.0 degree longitude by 5.0 degree latitude resolution. 2007 annual average surface level pressure data are from the HadSLP2 data (Allan and Ansell, 2006), provided by the Earth System Research Laboratory (2011). As shown in Figure 4.1, the global distribution of cirrus clouds has close relationship with the global distribution of the surface level pressure. Cirrus clouds are abundant in regions where low pressure dominates, and are absent in regions where high pressure dominates. The global distribution of cirrus clouds has a zonal band pattern. Cirrus clouds also change by locations in each band. The maximum cirrus coverage band occurs in the ITCZ. Low

surface level pressure dominates in the ITCZ, and deep convection pushes up abundant warm moist air, as a result, a lot of injection cirrus clouds form in this narrow band.

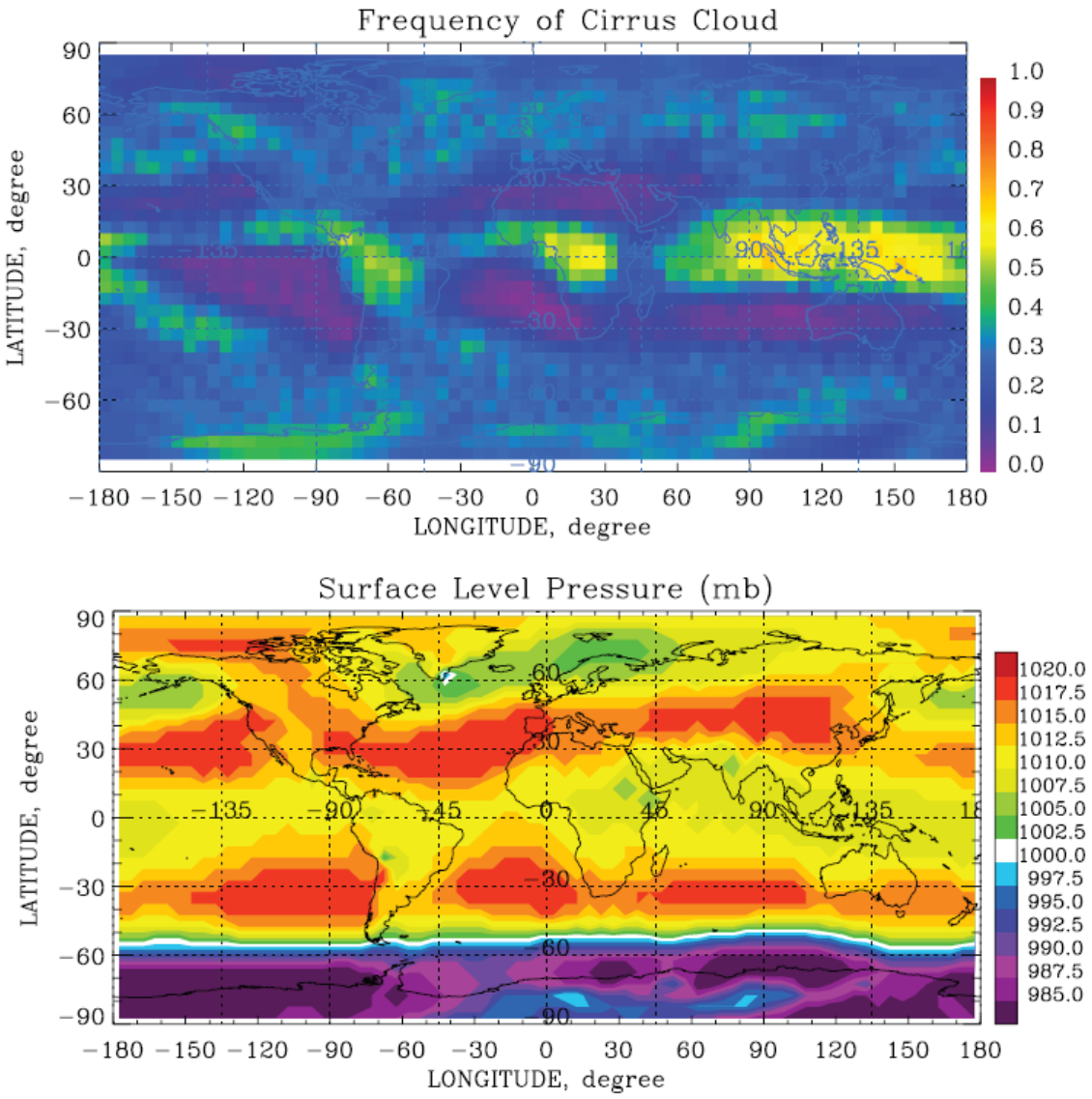

Figure 4.1 2007 frequency of occurrence and surface level pressure

Seasonal monsoonal circulation contributes to the change of cirrus cloud coverage by location. Cirrus cloud coverage of up to ~60% appears at central southern America, western Africa, Indonesia, and the west-central Pacific Ocean warm pool. Less cirrus coverage bands occur in the northern and southern midlatitude storm tracks zones. Abundant synoptic weather systems produce synoptic cirrus clouds. At the Aleutian and Icelandic lows regions, synoptic cirrus clouds occur more frequently than in other regions. In between the ITCZ and midlatitudes (around northern 30 and southern 30 degree latitude zones), few cirrus clouds occur because these bands are located right in the high pressure zones of the Hadley cell circulation, where large-scale descending air motion depresses generation of clouds. In particular, Northern Africa, Central Australia, and the south-western United States are in the subtropical high-pressure zones where subsidence and divergent flow dominate, leading to the absence of cirrus clouds. In the northern and southern polar regions, few cirrus clouds exist because of the polar highs.

Figure 4.2 shows the frequency of occurrence of cirrus clouds varies with height.

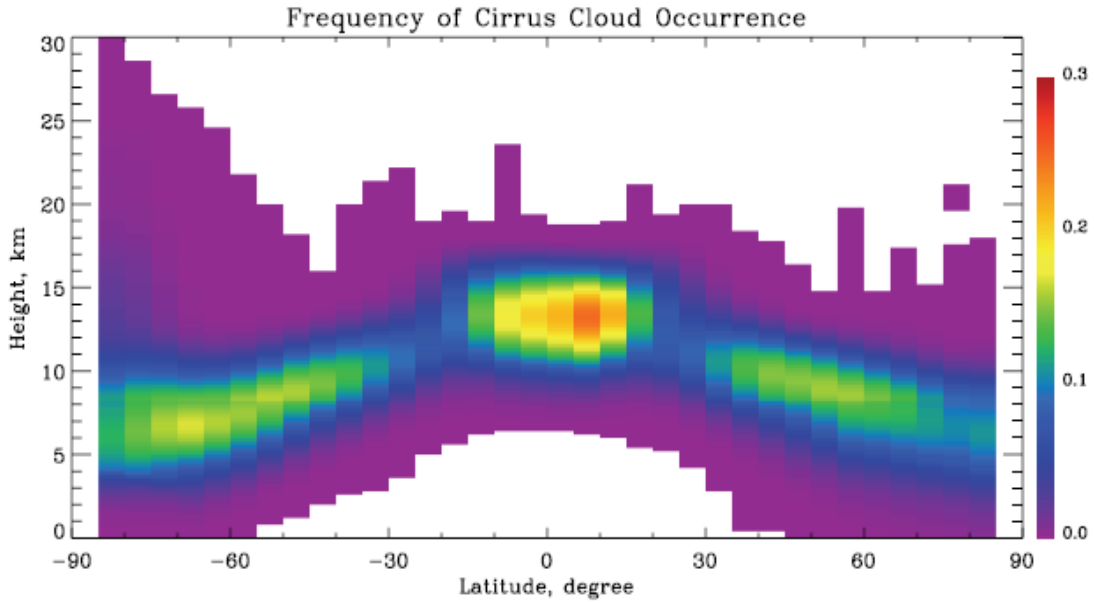

Figure 4.2 Frequency of occurrence of cirrus clouds varies with height

As shown in Figure 4.2, although cirrus clouds occurred in large height ranges during a year, the majority of cirrus clouds occur in the narrow height band. The highest values of frequency of cirrus cloud occurrence are located around the ITCZ, and the least values occur at around 30 degree south and north midlatitudes. The height, where cirrus clouds most frequently occur, decreases with the increase of latitude.

The distributions of cloud-top height, cloud-top temperature, and thickness of cirrus clouds are shown in Figure 4.3, named as distribution of annual average macro-physical properties of cirrus clouds. The distribution of cloud-top height of cirrus clouds has an apparent three zonal-band pattern. The cloud-top height of cirrus clouds is the highest in the tropical regions, low in the midlatitude regions, and lowest in the polar regions. Cirrus clouds at the ITCZ have the highest cloud tops (about 14 km). Cloud top

height decreases gradually as the poles are approached in both hemispheres. The lowest cloud-top height in the northern polar region (85N degree latitude) is 8 km.

The cloud-top temperature of cirrus clouds has the similar pattern as the cloud-top height of cirrus clouds. The cloud-top temperature is the lowest in the equatorial belt, relatively low in polar regions, and highest in midlatitude regions. Because different latitude zones of the earth accept different magnitudes of radiation from the sun, for example, the tropical regions accept the most radiative energy from the sun, and the polar regions obtain the least radiative energy, the distribution of the surface temperature of the earth has a zonal band pattern. The surface temperature is high, middle, low in the tropical, the midlatidute, and the polar regions, respectively.

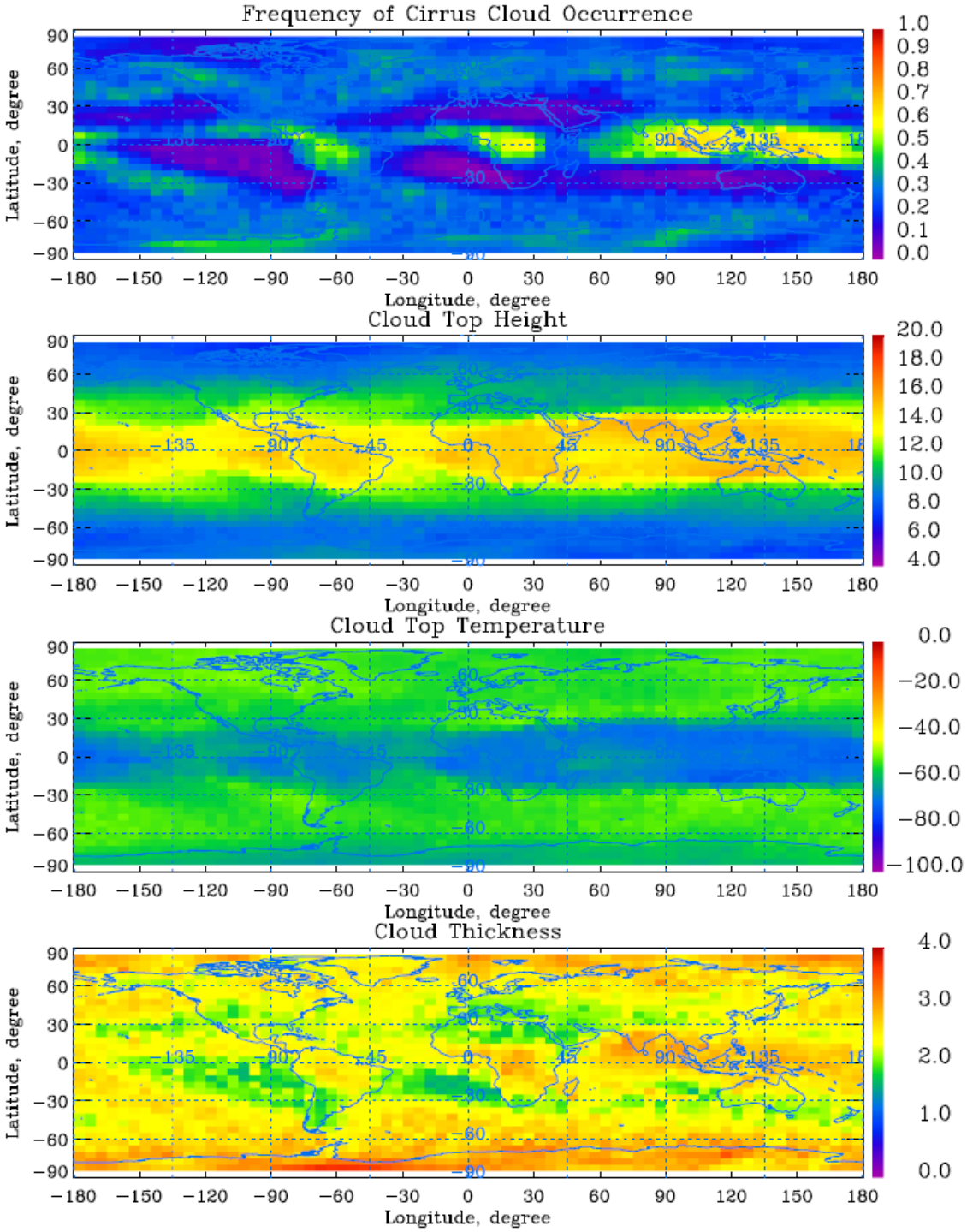

Figure 4.3 2007 annual average macro-physical properties of cirrus clouds

The atmosphere temperature profiles are primarily impacted by the surface temperature. As a result, the high levels, where air is saturated and clouds possibly form, vary with latitude.

The yearly average macro-physical properties are summed in Table 4.2. One can obtain the conclusion that 2007 and 2008 annual average macro-physical properties are very similar.

Table 4.2 2007 annual average macro-physical properties of cirrus clouds

	Frequency of occurrence	cloud-top height (km)	cloud-top temperature(ºC)	cloud thickness (km)
Polar region	0.28	8.4	-53	2.5
Midlatidute regions	0.26	10.3	-52	2.3
Tropical regions	0.27	13.7	-63	2.1
Globe	0.27	10.9	-56	2.3

Figure 4.4 illustrates the annual average macro-physical properties variation with latitude. It shows the band patterns of the cloud-top height, cloud-top temperature. The variation pattern of cirrus cloud thickness is not similar to the patterns of cloud-top height and cloud-top temperature.

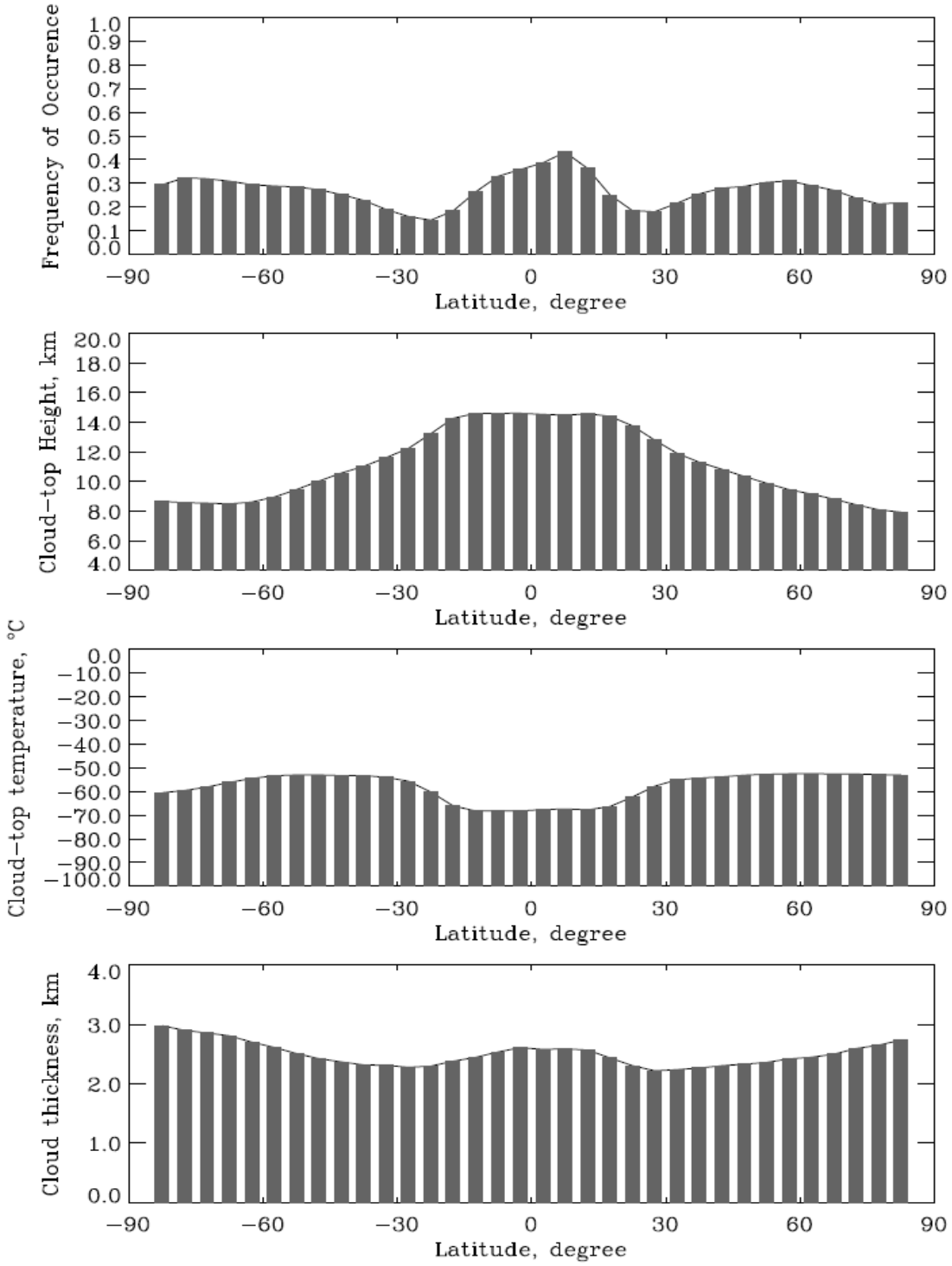

Figure 4.4 Yearly average macro-physical properties variation with latitude

As derived from the algorithm developed for this thesis

In general, cirrus clouds in the polar regions are thicker than those in the midlatitude region. Cirrus clouds are thin in the regions where cirrus clouds are few. The relation between the frequency of occurrence and cloud thickness of cirrus clouds is obvious. For the regions where clouds do not easily form, the thickness of the clouds is small, and for the region where cirrus clouds are abundant, the thickness of the cirrus clouds are relatively thick.

4.2.2 Diurnal Variation of Cirrus Clouds

The diurnal variation of the macro-physical properties of cirrus clouds is measured by CALIPSO data and shown in Figure 4.5, Figure 4.6 shows the difference between the macro-physical properties of cirrus clouds at nighttime and the macro-physical properties of cirrus clouds at daytime, and Figure 4.7 illustrates day versus night variation with latitude. The frequency of occurrence of cirrus clouds over the globe is slightly greater at nighttime than at daytime. In the polar regions and in South America and central Africa, the day versus night variation of the frequency of occurrence of cirrus clouds is greater than in other regions. The annual average frequency of occurrence of cirrus clouds is 24% and 30% at day and night time, respectively. The cloud-top height of cirrus clouds is slightly higher at night (average 11.28 km) than at daytime (average 10.95 km). The cloud-top temperature of cirrus clouds at nighttime (-65.4ºC) is about 5ºC lower than the cloud-top temperature at daytime (-59.2ºC). The cloud thickness of cirrus clouds has a great diurnal variation with much greater cloud thickness at nighttime than at daytime. The cloud thickness is 1.95 km and 2.98 km at day and night, respectively.

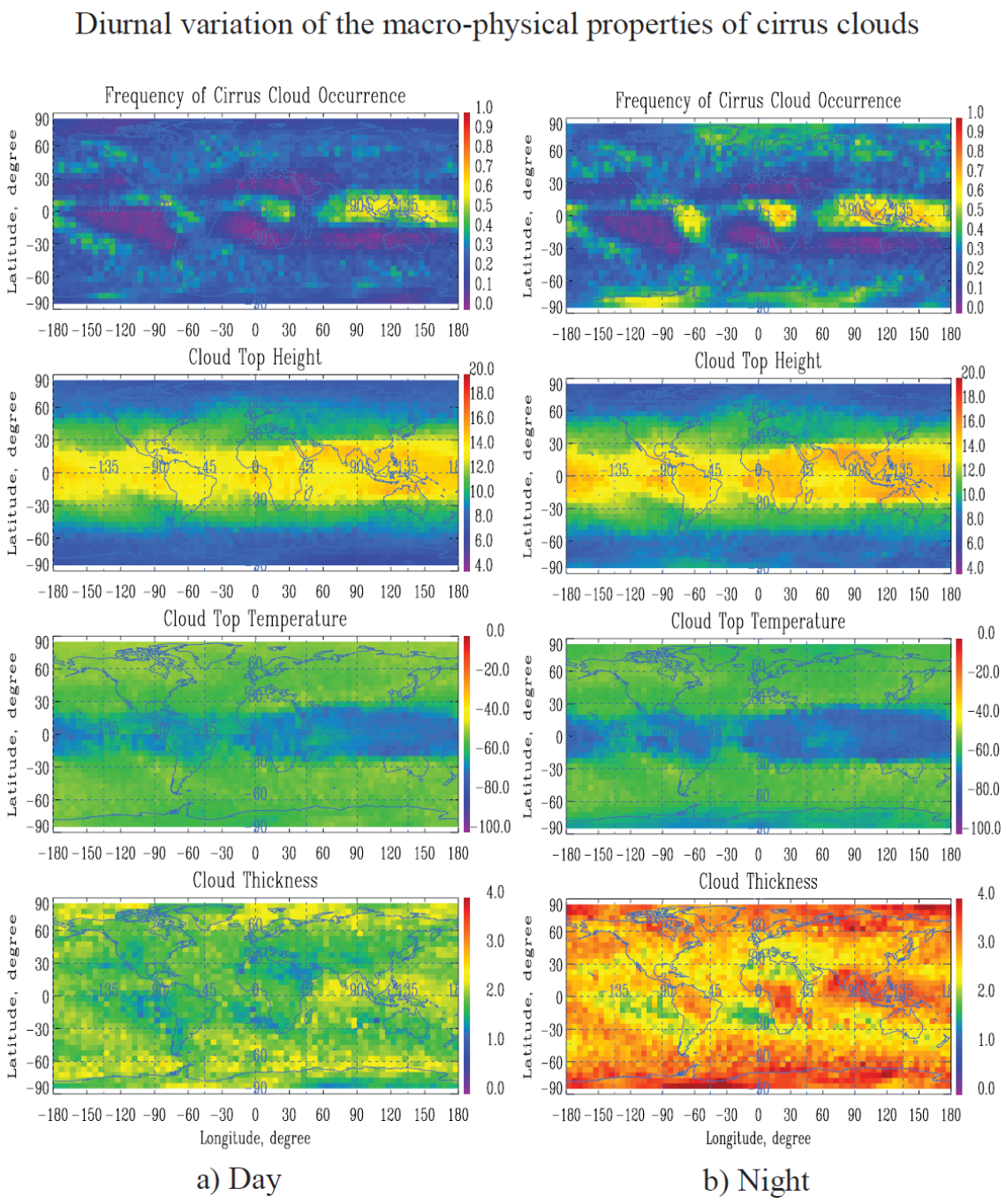

Figure 4.5 Day versus night variation of macro-physical properties

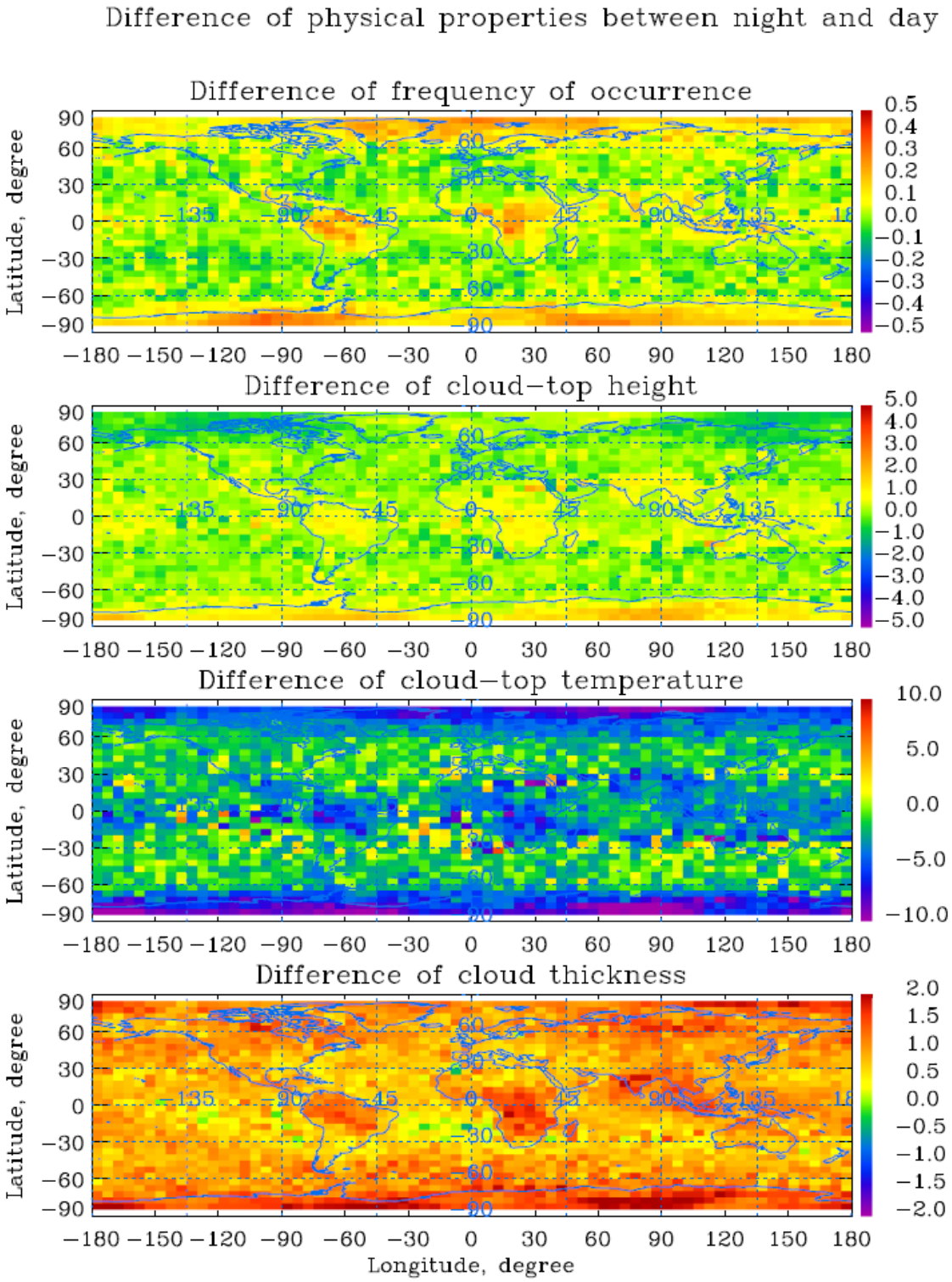

Figure 4.6 Difference of macro-physical properties between night and day

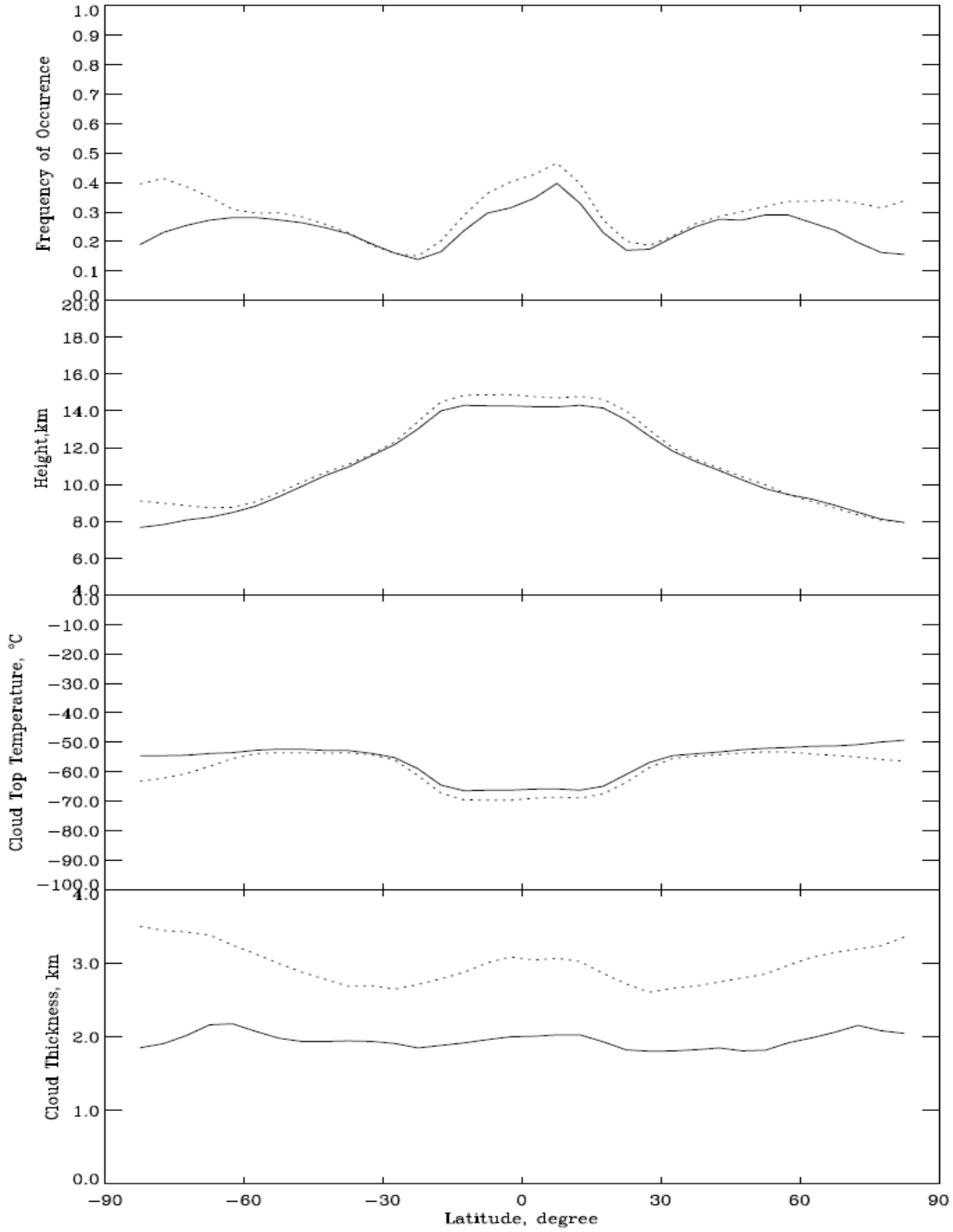

Figure 4.7 Diurnal variation of macro-physical properties

The solid lines represent the properties at daytime and dot lines represent the properties at nighttime.

The cause for the measured diurnal variations of cloud-top height, cloud-top temperature, and cloud thickness of cirrus clouds is measurement error. The solar light causes strong background noise in the perpendicular and parallel return signals during daytime, but the background noise is weak at nighttime. As a result, a very thin cirrus cloud layer which is not identified by the lidar at daytime can be measured at nighttime; for a thick cirrus cloud layer, the lidar measures a lower cloud-top height and a higher cloud-base height at daytime than at nighttime. The day versus night variation of background noise in the return signals also causes measured diurnal variance of the frequency of occurrence of cirrus clouds. Another reason for the measured diurnal variation of the frequency of occurrence of cirrus clouds relates to the CALIPSO measurement timing. Remember that CALIPSO always flies over the equator at around 1:30 pm local time in a day and 2:15 am local time at night, therefore, the frequency of occurrence of cirrus clouds during daytime in the tropical region actually reflects the cloud amount at around 1:30 pm local time in a day, and the frequency of occurrence of cirrus clouds during nighttime in the tropical region actually reflects the cloud amount at around 2:15 am local time at night. In the tropical region, cirrus clouds are produced mainly by deep convection. Thunderstorms over land normally form in the later afternoon (Sassen *et al.*, 2009). As a result, more cirrus clouds are measured at night than at day in the South America and the Central Africa regions. In conclusion, measured diurnal variation of macro-physical properties of cirrus clouds results from strong day versus night difference of background noise.

4.2.3 Seasonal Variation of Cirrus Clouds

Seasonally averaged frequency of cirrus cloud occurrence, cloud-top height, cloud thickness, and cloud-top temperature are illustrated in Figures 4.8 to 4.11, respectively. As shown in Figure 4.8, the ITCZ has a north-south migration pattern. In northern hemispheric summer (JJA), the ITCZ is north of the equator; while in the northern hemispheric winter (DJF), it migrates to south of the equator. Cirrus clouds in the northern midlatitude zone change a lot by season. In DJF, the polar jet stream locates at low latitude, and cirrus clouds occur to the high side of the polar jet stream. In JJA, the polar jet stream migrates back to high latitude (around 60 degree latitude), and the cirrus cloud amount in the midlatitude zone decreases. The Indian Ocean monsoons strongly influence the cirrus clouds in the region. During JJA, the high surface temperature over the Tibetan plain generates a thermal low. This low pressure and convergence dominate the circulation over southern Asia. Warm, moist air from the adjacent ocean flows onto the landmass and rises to form aloft a lot of cirrus clouds. In the winter season, high-pressure and subsiding dry air dominate the Tibetan plain, and winter monsoons flow off the Asia continent. As a result, there are few cirrus clouds over the region.

Polar Stratospheric Clouds show a strong seasonal variation. In the southern hemisphere winter (JJA), a lot of polar stratospheric clouds form in the South Pole. Over all, the frequency of occurrence of cirrus clouds is 26.8%, 27.4%, 26.8%, and 27.0% in DJF, MAM, JJA, and SON season, respectively.

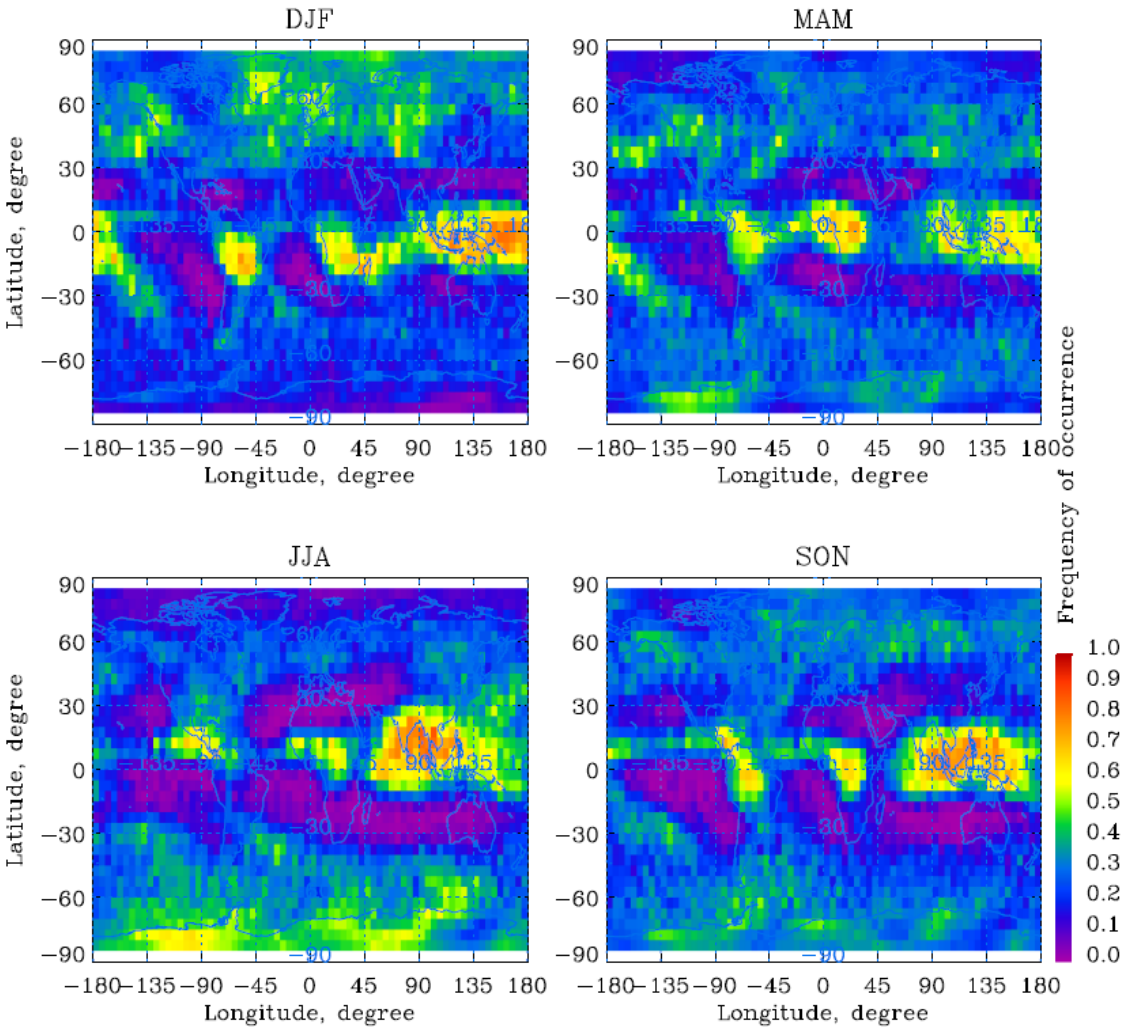

Figure 4.8 Seasonal average frequency of occurrence of cirrus clouds

Cloud-top height also shows some seasonal variation. Cirrus clouds in the ITCZ occur at higher level in DJF than in JJA, while the variation of the midlatitude cirrus cloud-top height is the opposite, i.e., the cloud-top height of the midlatitude cirrus clouds is lower in DJF than in JJA season. The seasonal global average of cloud-top height is 10.73 km, 10.81 km, 11.30 km, and 10.82 km in DJF, MAM, JJA, and SON, respectively.

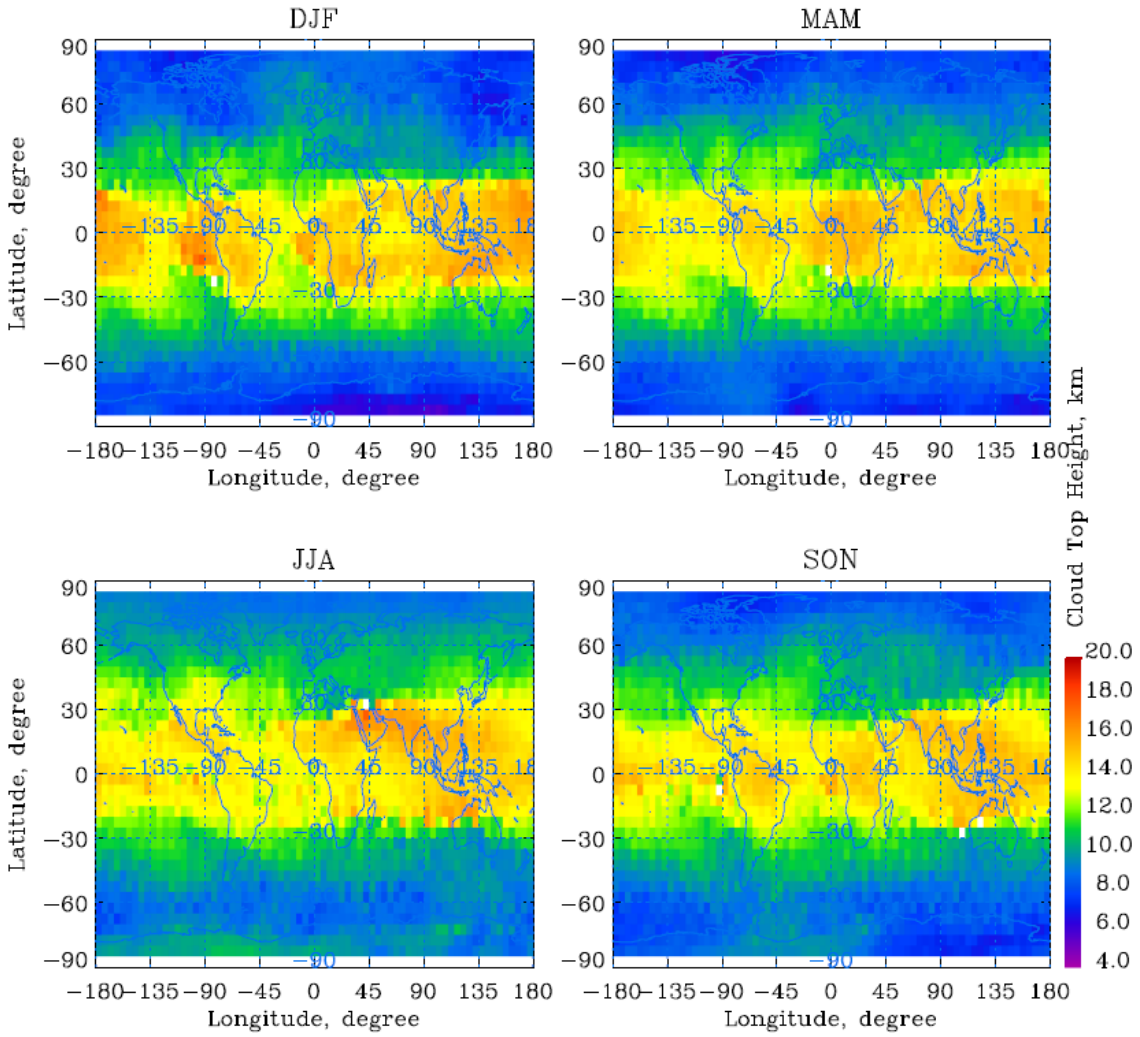

Figure 4.9 Seasonal average cloud-top height of cirrus clouds

Cloud thickness does not show apparent seasonal variation except in the polar regions. In DJF, northern polar region is cold, some PSCs occur there. In JJA, southern polar region is extremely cold, a lot of PSCs occur during that season. PSCs are responsible for great thickness variation in the polar regions. The seasonal average cloud thickness of cirrus clouds is 2.29 km, 2.31km, 2.31 km, and 2.26 km in DJF, MAM, JJA, and SON season, respectively.

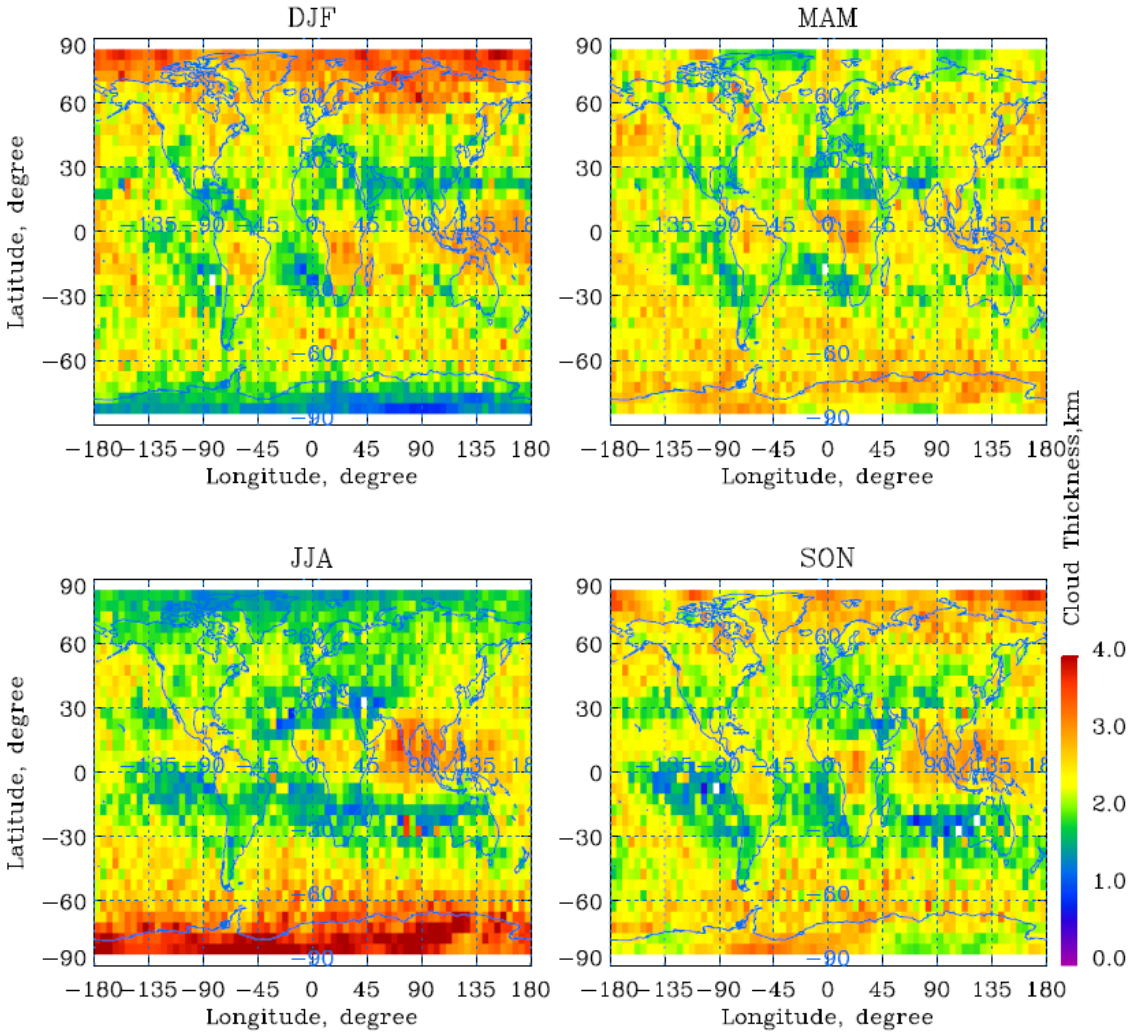

Figure 4.10 Seasonal average thickness of cirrus clouds

The cloud-top temperature seasonal variation is very small. Because PSCs in the polar regions, cloud-top temperature is low in DJF in the northern polar region and in JJA in the southern polar region. The seasonal average cloud-top temperature is -56ºC through all seasons.

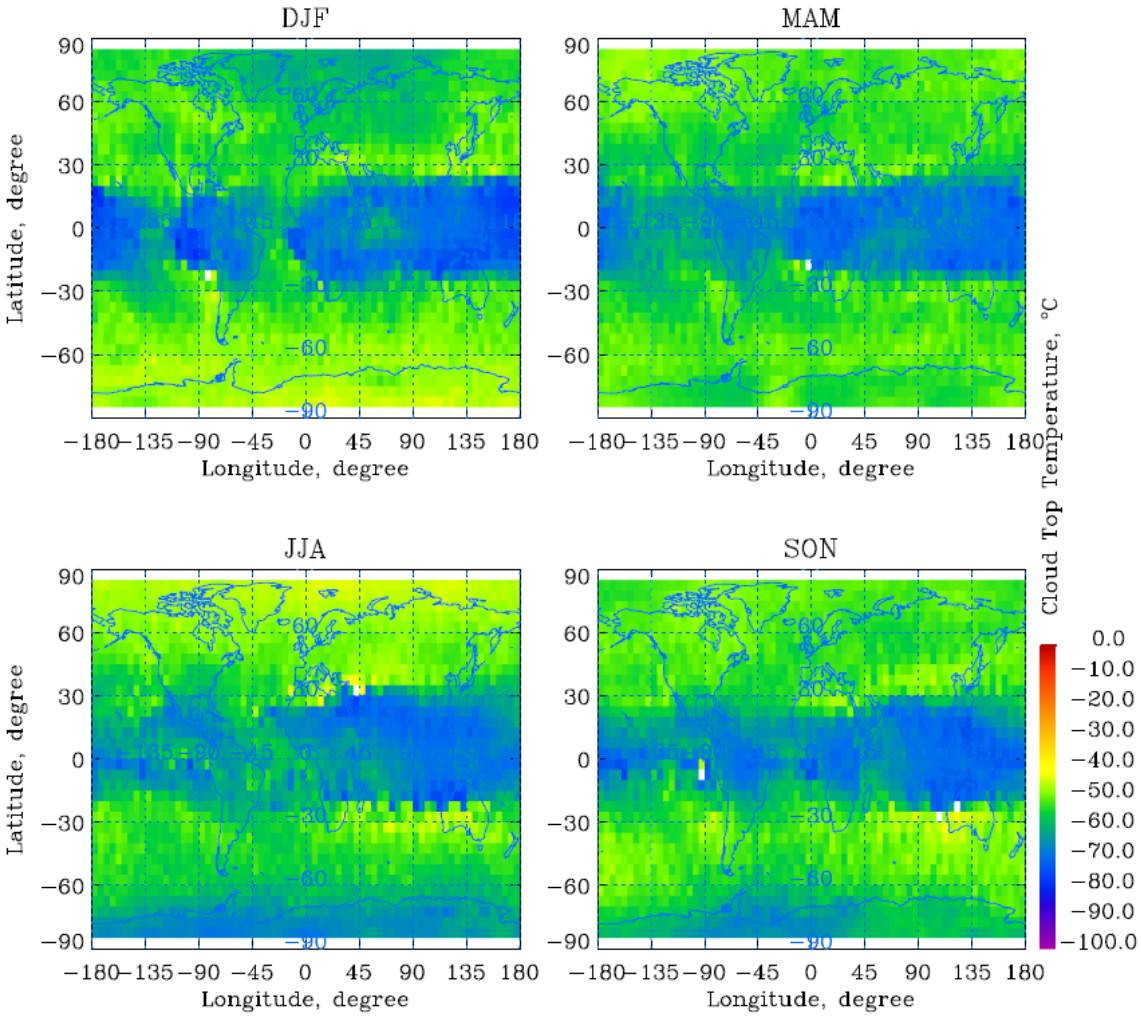

Figure 4.11 Seasonal average temperature of cirrus clouds

4.2.4 Monthly Variation of Cirrus Clouds

The monthly variation of macro-physical properties of cirrus clouds in 2007 is shown in Figure 4.12. The monthly variation of macro-physical properties of cirrus clouds clearly reveals the migration of ITCZ. As shown in the top panel in Figure 4.12, from January to March, ITCZ is in the south of the equator; ITCZ usually begins its shift

to north in April; in May to October, ITCZ stays in north of the equator; and it beings to migrate back to south of the equator in November and December.

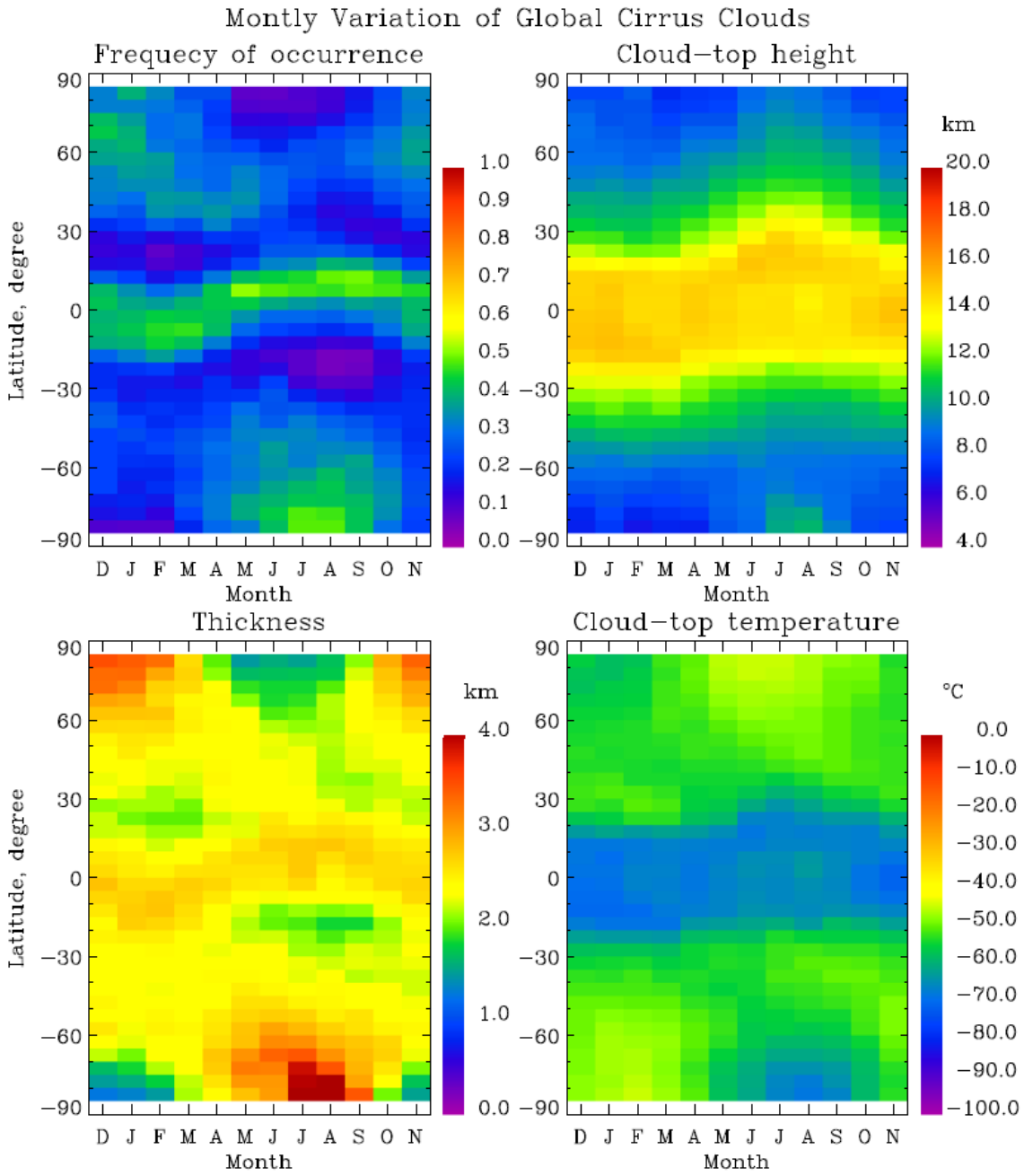

Figure 4.12 Monthly variation of macro-physical properties of cirrus clouds

The cloud loud-top height, cloud-top temperature, and cloud thickness do not show apparent variations in the tropical and midlatitude regions, but show great variation in the polar regions. Again, PSCs in the polar regions are main factor in influencing these variations.

The monthly variation of macro-physical properties of cirrus clouds with latitude is shown in Figure 4.13. The monthly variation of macro-physical properties of cirrus clouds depends on the latitude. The monthly variation of cirrus clouds is great in the polar regions, middle in the midlatitude regions, and small in the tropical regions. The monthly variation of the solar radiation on these three latitude regions is responsible for the monthly variation of the cirrus clouds with latitude. In the tropical regions, solar radiation has small monthly variation, the atmospheric environment variation over these regions is small, as a result, the monthly variation of cirrus clouds is small. The polar regions experience the great monthly variation of incoming solar radiation, the PSCs occur in these regions because of very cold weather in local winter time. Cirrus clouds over these regions have the greatest monthly variation.

4.2.5 Year to Year Comparison

Studying the year-to-year variation of cirrus clouds has a climatological meaning. Figure 4.14 shows the global distribution of annual average macro-physical quantities in 2008, and Figure 4.15 shows the difference that the macro-physical properties of cirrus clouds in 2008 minus the macro-physical properties of cirrus clouds in 2007.

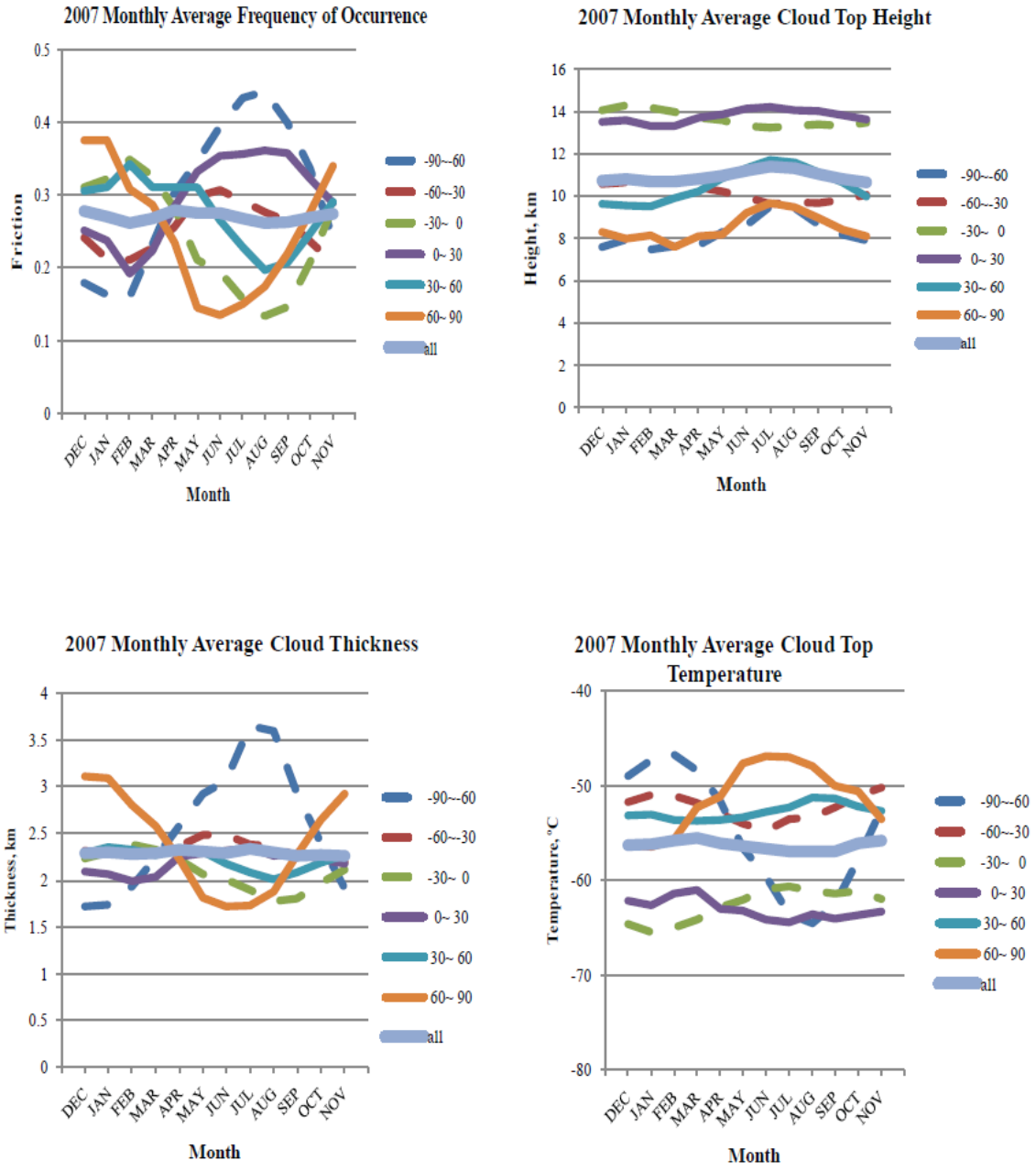

Figure 4.13 Monthly variation of macro-physical properties with latitude

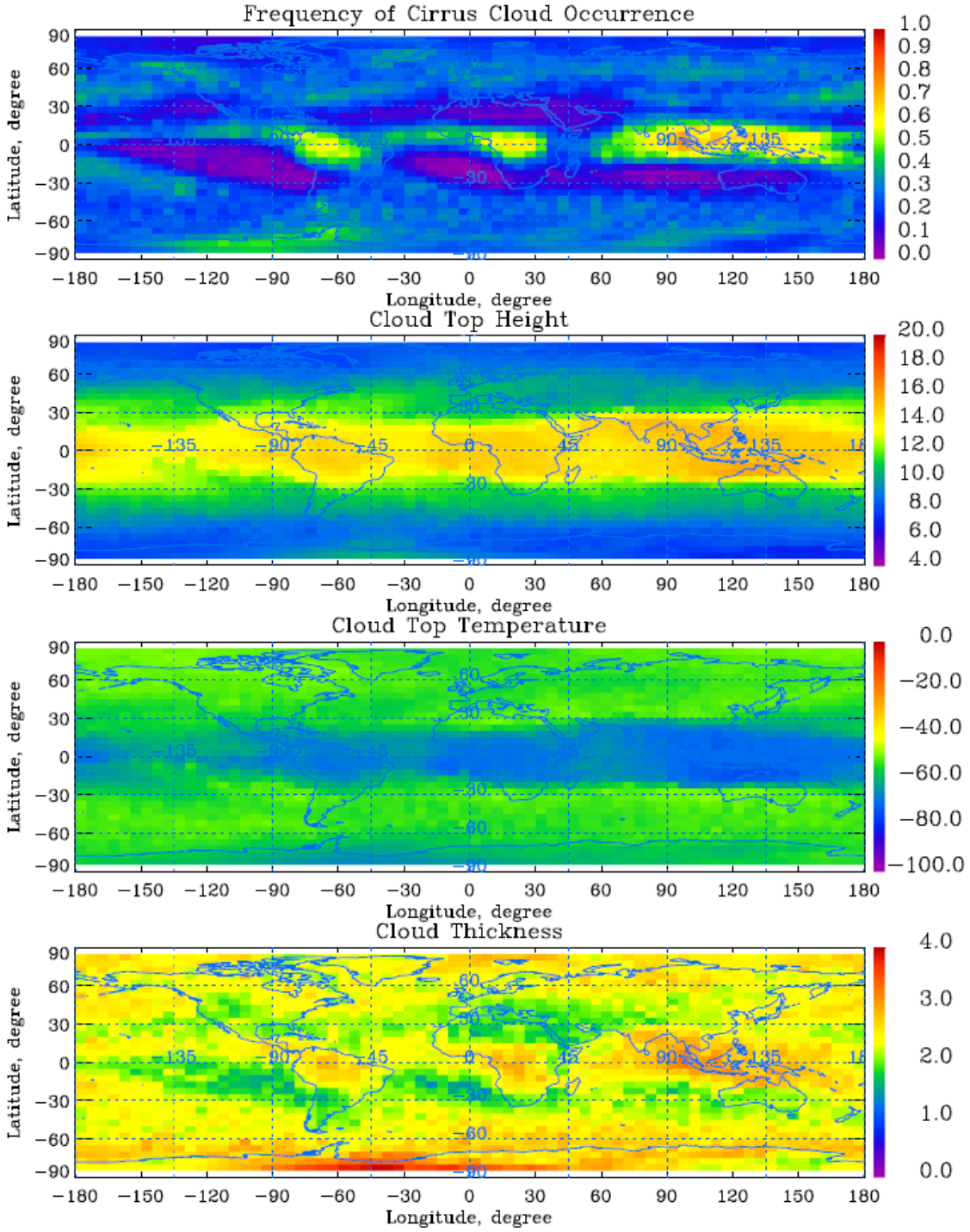

Figure 4.14 2008 yearly average cirrus cloud macro-physical properties

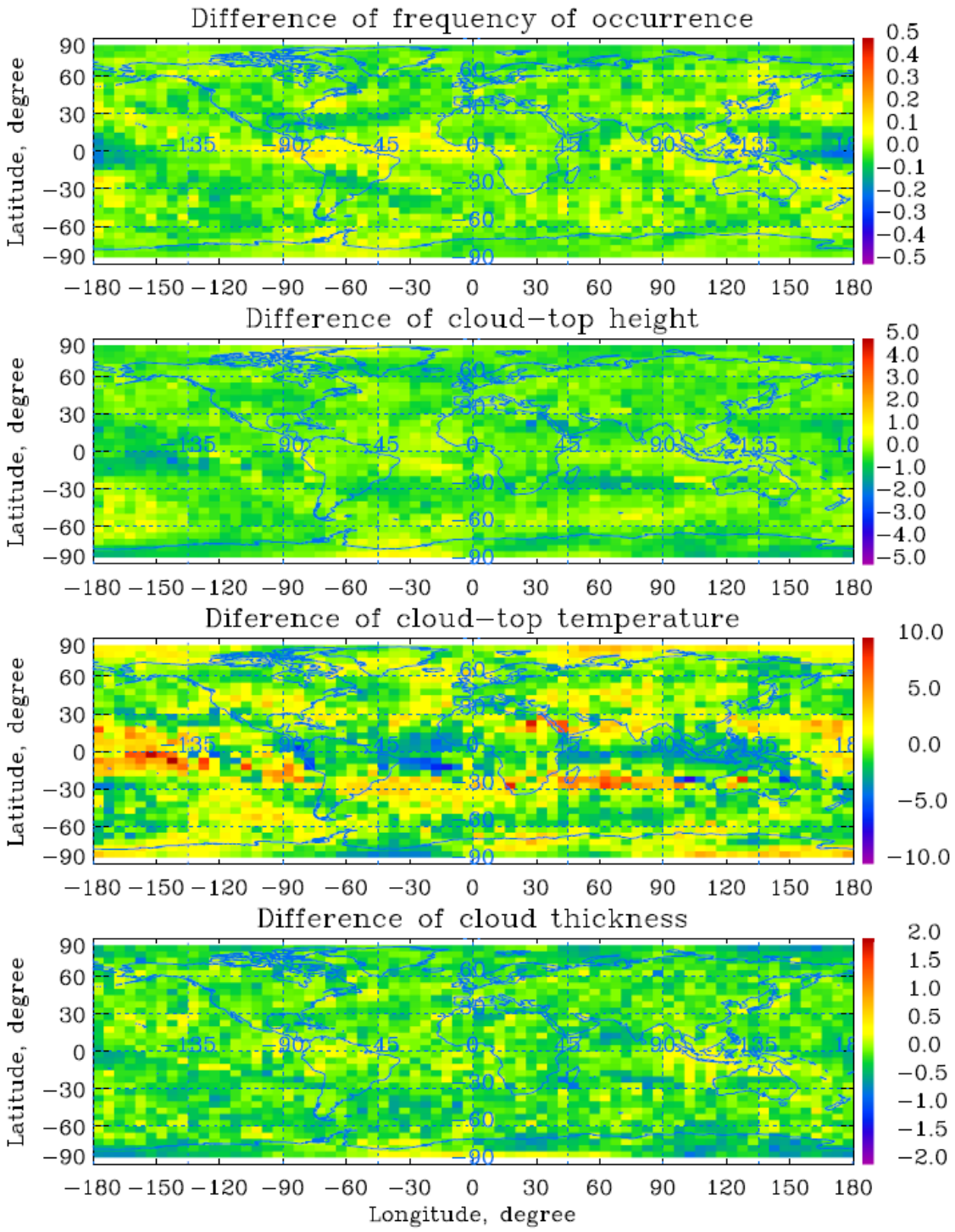

Figure 4.15 Differences between 2008 and 2007 macro-physical properties

In general, the two figures show similar characteristics. Zones with high and low frequencies of cirrus cloud occurrence are located at similar locations in 2007 and 2008. Annual average cloud-top height, cloud thickness and cloud-top temperature in 2007 and 2008 are also very similar. Table 4.3 compares the annual mean values of macro-physical properties of cirrus clouds in 2007 and 2008. This implies that the year-to-year variation of annual average macro-physical quantities of cirrus clouds is very small.

Table 4.3 2007 and 2008 micro-physical properties of cirrus clouds

	2007		2008	
	Mean	Std. Dev.	Mean	Std. Dev.
Freq. of cloud Occurrence	0.27	0.11	0.27	0.12
Cloud Top Height	11.05	2.38	10.91	2.38
Cloud Top Temperature	-57.50	6.13	-57.10	6.20
Cloud Thickness	2.45	0.32	2.35	0.31

4.3 Climatological Comparisons

CALIPSO findings describing the characteristics of cirrus clouds on a global scale are compared with the International Satellite Cloud Climatology Project (ISCCP) high cloud data and a surface observation data set. The ISCCP was established in 1982 as a part of the World Climate Research Programme (WCRP). It coordinates world satellite radiance measurements to infer the global distribution of clouds, their properties, as well as their diurnal, seasonal, and interannual variations. The ISCCP IR cirrus clouds and

cirrus plus cirrostratus data of 2007 are used for the comparison. The surface observation dataset used in the comparison comes from Hahn and Warren (1999). Figure 4.16 shows yearly mean frequency of cirrus cloud occurrence derived from CALIPSO and ISCCP.

In general, both data sets disclose a similar global pattern; the peak value occurs at the same latitude. At northern and southern 30 latitudes, both measurements show rather low frequencies. The only exception is the relatively great frequencies in polar regions which are shown in the data obtained by the CALIPSO method, because the polar stratosphere clouds are included in CALIPSO method, but apparently not in the ISCCP. Cirrus clouds in ISCCP findings are less than in the CALIPSO findings, especially at tropical regions where thin to sub-visible cold trap cirrus clouds are expected. Because both methods use a similar upper optical depth to identify cirrus clouds (optical depth <3), this difference may be due to the fact that passive satellite data have difficulties in detecting optically thin ice clouds, Because the passive measurement actually measures the radiances in visible channels, converts the radiances into reflectance to retrieve cloud information, and the radiative radiance is very weak for optically thin ice clouds, the passive measurement is not sensitive to this kind of cirrus cloud. When comparing ISCCP cirrus clouds (Ci) plus cirrus stratus clouds (CiSt) with CALIPSO measurement, a better agreement is achieved.

2007 zonal-average frequencies of occurrence of cirrus cloud measured by CALIPSO are compared with ISCCP and surface observation in Figure 4.17.

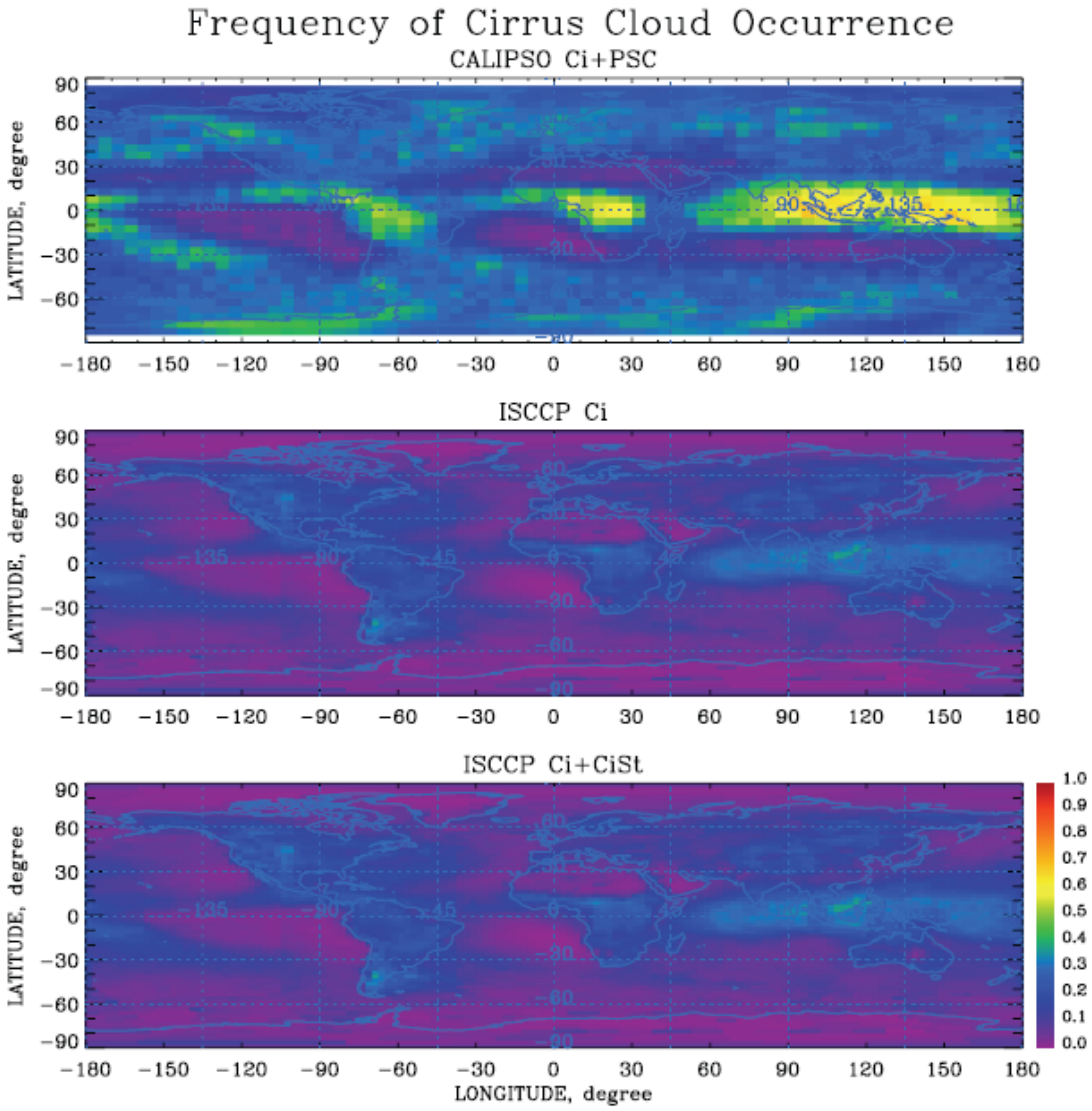

Figure 4.16 Yearly average of frequency of cirrus cloud occurrence

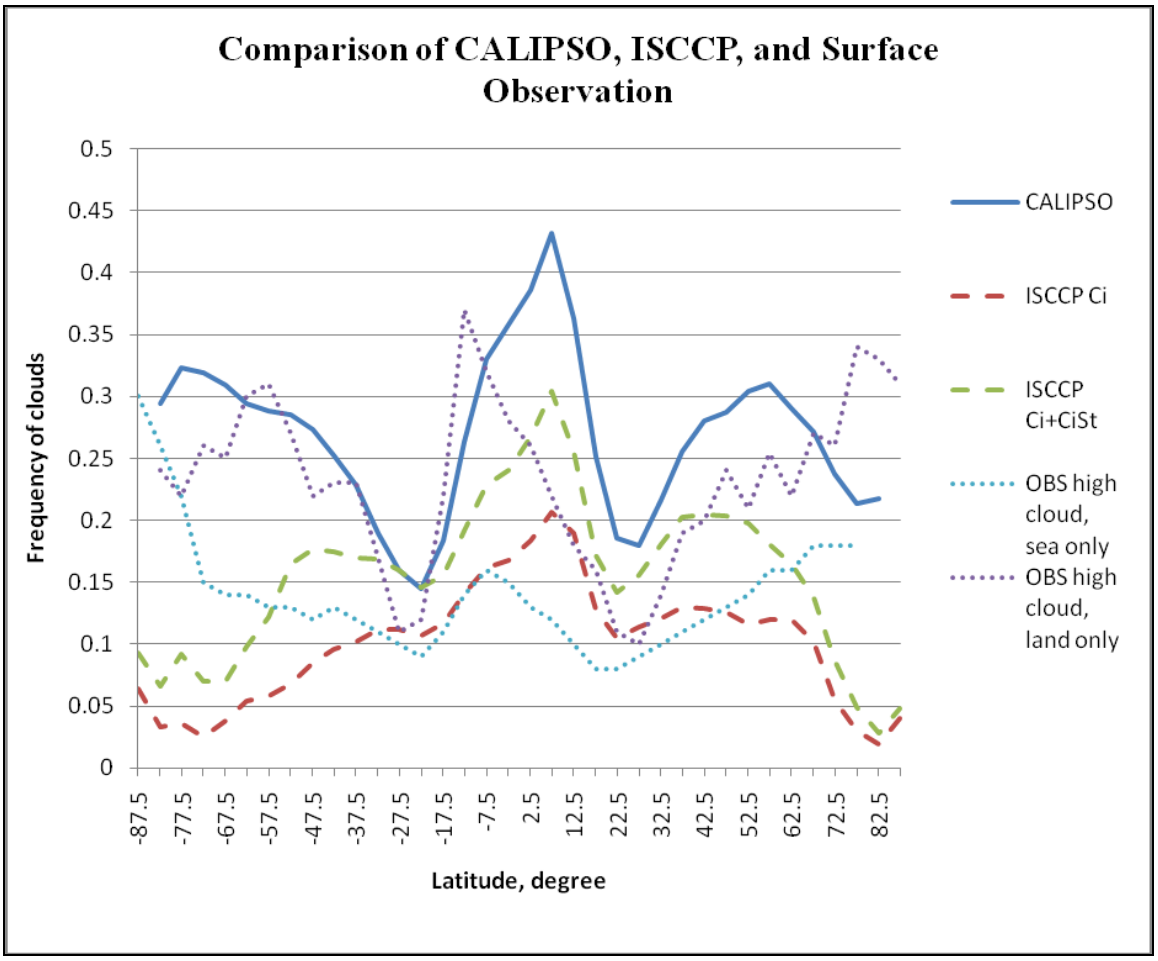

Figure 4.17 Zonal-average frequency of occurrence of cirrus clouds.
The maximum frequency of occurrence of cirrus clouds is 1.

It should be kept in mind that the surface observation data used to be compared here are 1971 to 1996 average cloud amounts of high level clouds. The effects of interannual weather variations may lead to unrepresentative findings in comparison. Figure 4.17 shows the asymmetric distribution characteristics of the frequency of occurrence of cirrus clouds in all three data sets. Both CALIPSO and ISCCP data show that cirrus clouds occur most frequently in regions around 5N degree. Cirrus clouds occur

more frequently in the northern midlatitude region than in the southern midlatitude region. Land coverage is greater in the northern hemisphere than in the southern hemisphere, terrain-induced cirrus clouds occur more frequently in the northern hemisphere. The frequency of occurrence of cirrus clouds derived from CALIPSO is higher in the southern polar region than in the northern polar region, but this phenomena does not occur in the frequency of occurrence of cirrus clouds derived from ISCCP. As a result, the difference of the frequencies of occurrence derived from CALIPSO and ISCCP has an asymmetric behavior. The primary reason is that CALIPSO data sets include the PSCs but ISCCP data sets do not, and the PSCs occur more frequently in the southern polar region than in the northern polar region.

The statistical results of the 2007 zonal-average frequencies of cirrus cloud occurrence versus latitude are shown in Table 4.4. The frequencies of cirrus cloud occurrence determined by CALIPSO are greater than those determined by ISCCP Ci plusing CiSt data set in the tropical (26.9%), the midlatitude (32.6%) and the polar regions (67.9%). The greatest difference between CALIPSO and ISCCP measurements occur at polar regions (74.0% in the south polar region, and 61.8% in the northern polar region). This difference is significant. Apart from the primary reason that the polar stratospheric clouds are included in the CALIPSO measurement, another possible reason is that the cirrus cloud identification methods used in ISCCP and CALIPSO are different. This also implies that lidar measurement from space is better than passive measurement.

Table 4.4 Zonal-average cirrus cloud frequency versus latitude

Percentages of differences of ISCCP Cirrus only and ISCCP Cirrus plus Cirrostratus correspond to CALIPSO are to the right of frequencies in corresponding columns.

Latitude (degree)	CALIPSO (%)	ISCCP-Ci (%)	ISCCP-Ci+CiSt (%)	SOB, land	SOB, sea
~-85 to -60	30.8	3.7(88.0)	8.0(74.0)	25.4	20.2
-60 to -30	25.3	8.7(65.6)	16.2(36.0)	23.8	12.3
-30 to -15	16.3	11.2(31.3)	15.4(5.5)	15.0	10.0
-15 to +15	35.5	17.6(50.4)	24.8(30.1)	27.2	13.3
+15 to +30	20.6	11.6(43.7)	15.7(23.8)	12.3	8.0
+30 to +60	27.6	12.6(54.3)	19.5(29.3)	20.6	12.7
+60 to ~+85	24.6	6.5(73.6)	9.4(61.8)	28.8	17.5
All	27.0	10.0	15.5	22.8	12.4

Surface observation has its inherent limit. When mid or low-level clouds occur, cirrus clouds above these clouds cannot be observed. But if many years of observation data are used for comparison, the impact of the limit of the surface observation decreases. Surface observation reveals a similar cirrus cloud zonal distribution pattern that is determined by CALIPSO. In polar regions, surface observation shows relatively large amounts of cirrus clouds. This overestimation may be due to poor sampling in polar regions or misidentification of low- or mid-level ice clouds as cirrus clouds. If the interannual variations of the surface observation data are excluded, one may conclude that the surface observation results are closer to the CALIPSO measurement results than to the passive measurement results. The total global average frequency of occurrence of cirrus clouds in 2007 derived from CALIPSO, ISCCP Ci and ISCCP Ci+CiSt are 27.0%,

10.0% and 15.5%, respectively. The 1971-1996 high level cloud amounts by surface observation are 22.8% over land and 12.4% over sea.

The Lidar in CALIPSO satellite has a high resolution and is highly sensitive to tiny ice crystals in the cirrus clouds. The passive measurement that ISCCP provided is not sensitive to optically thin cirrus clouds. Surface observation cannot accurately derive the frequency of occurrence of cirrus clouds because of its inherent limit. Therefore, lidar on a satellite is an ideal tool for measuring cirrus clouds. The comparison results presented in Table 4.3 indicate that cloud measurement is a challenge, and one should use as many measurement methods as possible to retrieve the cloud properties.

Chapter 5 Global Linear Depolarization Ratio

The microphysical properties of clouds include shape, size, and size distribution of the particles which compose clouds. Because ice clouds are composed of various shapes and sizes of ice crystals, their micro-physical and radiative properties are difficult to completely understand. In order to obtain knowledge of cloud global distribution and cloud properties, people use satellite measurements. Linear Depolarization Ratio is an indicator to reflect the habits of ice crystals in ice clouds. In this chapter, global distribution of cirrus cloud LDRs and their changes in terms of time are studied.

As mentioned before, there are two differences between the application version 1 and the application version 2. One is the cirrus identification algorithm, and the other is the LDR calculation algorithm. The LDR results produced by the application version 1 are shown in Appendix C, and the LDR results produced by the application version 2 are present in this chapter. It is necessary to investigate these two version applications and their results before analyzing the LDR results.

5.1 Discussion of the Difference of Two Version Applications

Two versions of cirrus cloud identification algorithms have already been discussed in detail in Chapter 3. The cirrus cloud identification algorithm version 1 checks all layers to determine if they are cirrus cloud layers, while the cirrus cloud identification algorithm version 2 checks the layers identified only by the 5 km window

to determine if they are cirrus cloud layers. Figure 5.1 shows the October 2006 monthly average LDR by using the cirrus cloud identification algorithm version 1 and the LDR calculation algorithm version 2, and Figure 5.2 shows the same monthly average LDR derived by using the cirrus cloud identification algorithm version 2 and the LDR calculation algorithm version 2.

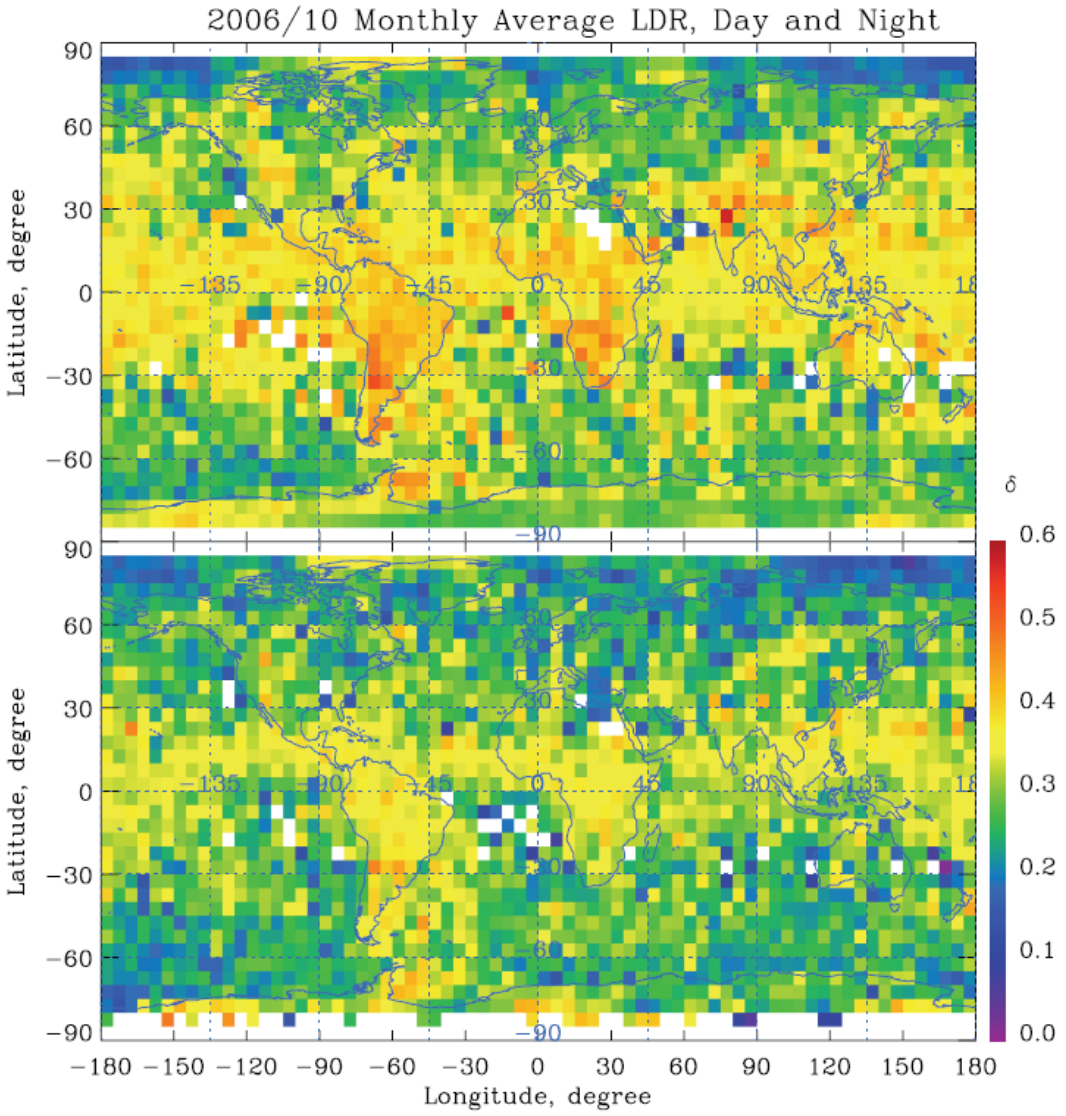

Figure 5.1 Monthly average LDR by cirrus cloud identification algorithm v.1

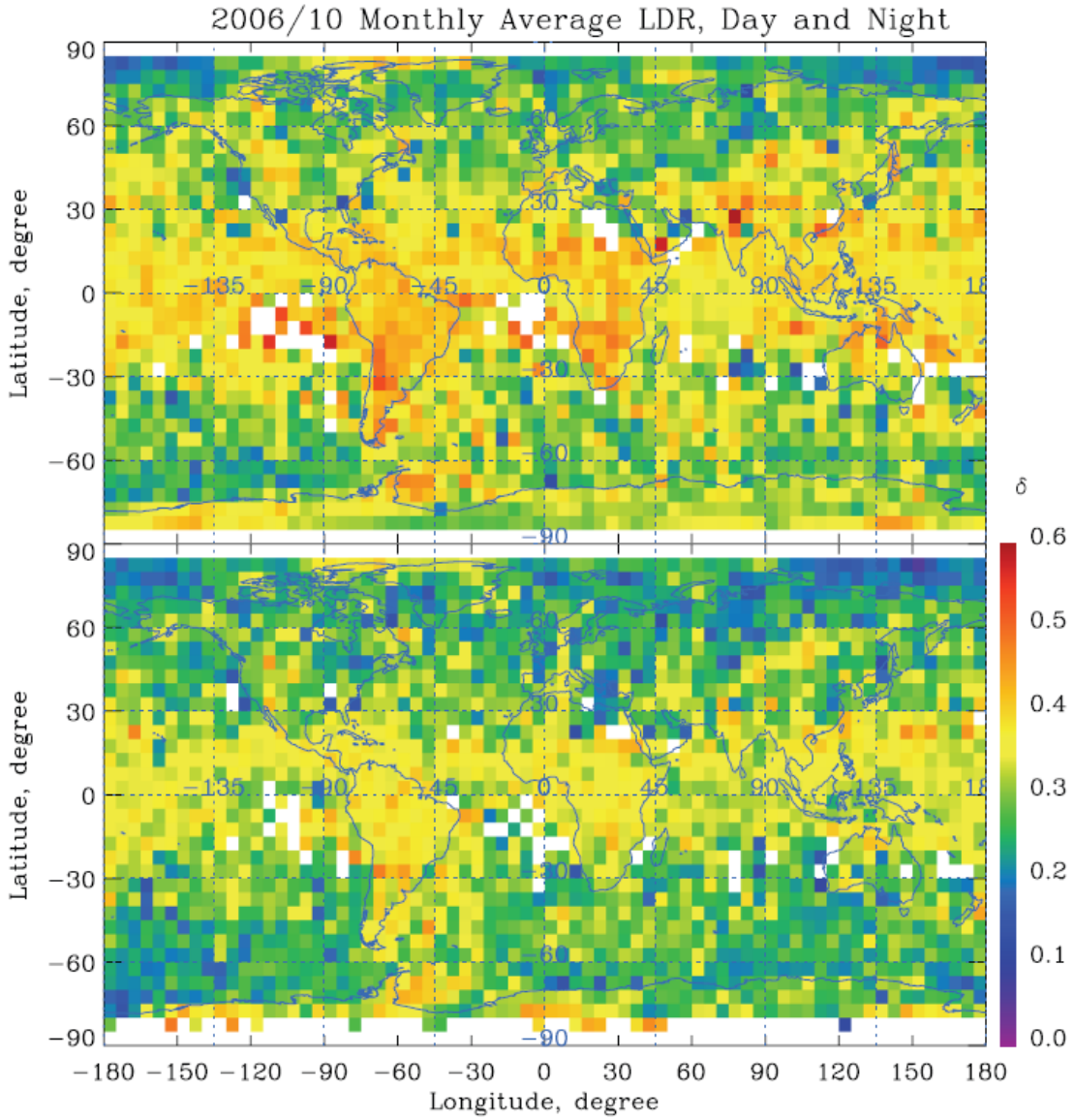

Figure 5.2 Monthly average LDR by cirrus cloud identification algorithm v.2

As shown in Figures 5.1 and 5.2, the LDR values determined by the cirrus cloud identification algorithm version 2 are slightly greater than those determined by the cirrus cloud identification algorithm version 1. Because the cirrus cloud layers identified by the cirrus cloud identification algorithm version 1 includes more thin cirrus layers than those

identified by the cirrus cloud identification algorithm version 2 and thin cirrus cloud layers usually have small LDR values, the LDR values of the cirrus clouds determined by the cirrus cloud identification algorithm version 1 are smaller than the LDR values of those determined by the cirrus cloud identification algorithm version 2. Table 5.1 lists the average LDR values determined with different algorithms. As shown in this table, the variation of the average LDR values determined by two cirrus cloud identification algorithms is not significant (daytime and night differences by two versions are 0.04).

Table 5.1 Monthly average LDR determined by different algorithms

CI_v1 and CI_v2 represent the cirrus cloud identification algorithm version1 and version2, respectively, and ldr_v1 and ldr_v2 represent the LDR calculation algorithm version 1 and version 2, respectively.

AVERAG LDR	Daytime	Nighttime	Daytime-Nighttime
CI_v1, ldr_v1	0.35	0.23	0.12
CI_v1, ldr_v2	0.30	0.26	0.04
CI_v2, ldr_v2	0.31	0.27	0.04

There are two versions of the LDR calculation algorithms. The version 2 LDR calculation has already been discussed in detail in Chapter 3.The detailed steps in the version 1 LDR calculation algorithm include:

Step 1, calculate LDR values of the columns in a half-orbit file.

A. calculate the LDR profile

B. calculate the LDR values of the cirrus cloud layers in the column

C. average the LDR values of the layers to obtain the LDR of this column

Step 2, calculate the LDR profile and LDR value of a grid

D. LDR profile of a grid is calculated by averaging the LDR profiles in the grid

E. LDR of a grid is calculate by summing the LDR values of the columns in the grid

The version 1 LDR calculation algorithm calculates the LDR of columns, then averages the LDR values of columns to obtain the LDR values of a grid, while the version 2 LDR calculation algorithm calculates the sums of the total and perpendicular attenuated backscatters in a grid, respectively, then calculates the LDR of the grid by these two sum values. Another key difference is that the impact of the variation of the vertical resolution in lidar profiles is not considered in the version 1 LDR calculation algorithm, while in the version 2 LDR calculation algorithm, the weight-addition method is used to calculate the sums of the total and perpendicular attenuated backscatter profiles, respectively. Figure 5.3 shows a monthly average LDR determined by the cirrus cloud identification algorithm version 1 and the LDR calculation algorithm version 1. By comparing Figures 5.3 and 5.1, we found that the LDR values determined by the two versions of LDR calculation algorithms are much different. The LDR values at daytime determined by the version 1 LDR calculation algorithm are greater than those determined by the version 2 LDR calculation algorithm, but the LDR values at nighttime determined by the version 1 LDR calculation algorithm is smaller than those determined by the version 2 LDR calculation algorithm. Table 3.1 shows that the LDR difference between daytime and nighttime determined by the version 1 LDR calculation algorithm (0.13) is greater than that determined by the version 2 LDR calculation algorithm (0.04).

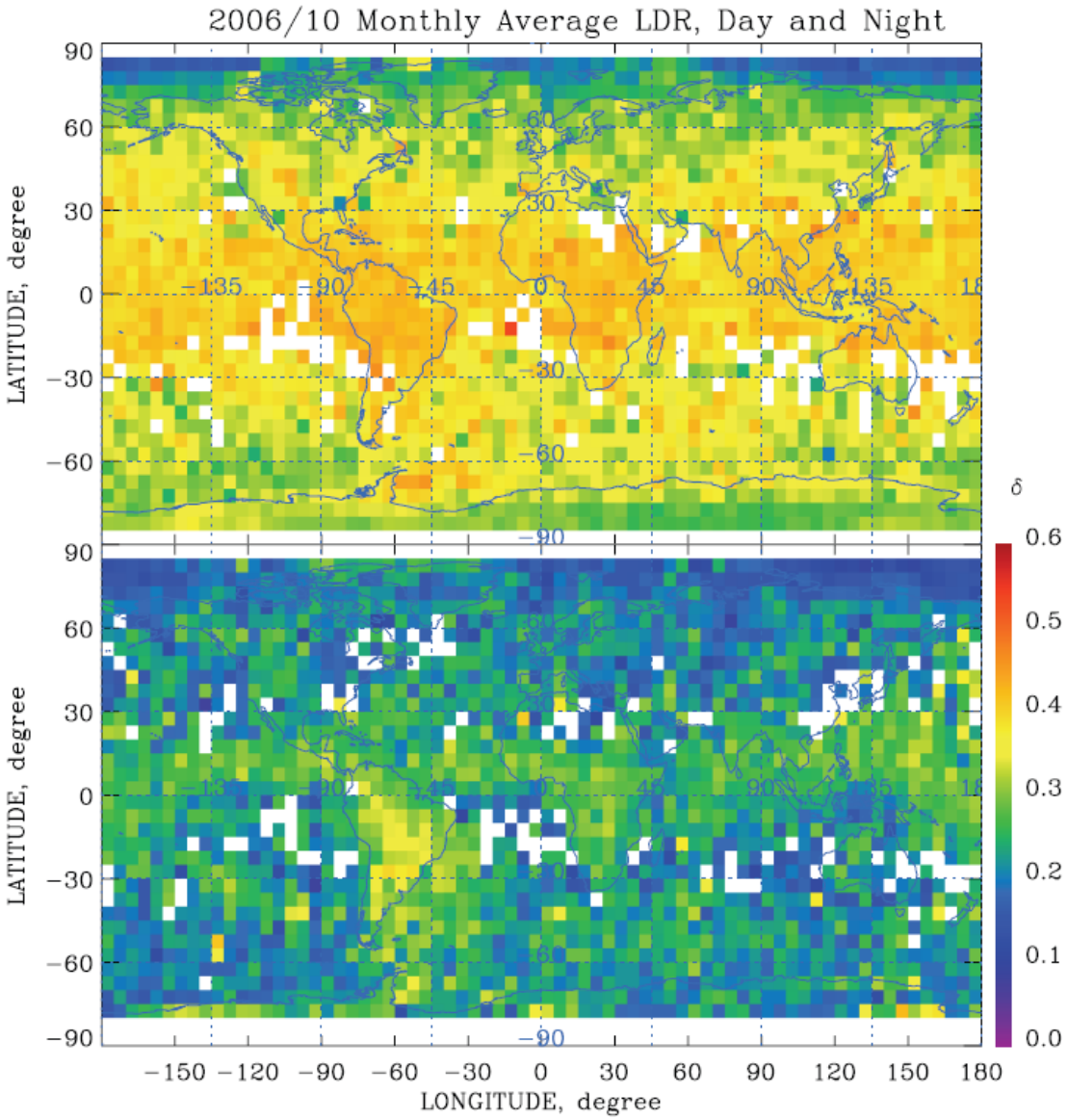

Figure 5.3 Monthly average LDR calculated by LDR calculation algorithm v.1

As discussed in Chapter 3, because the background noise at daytime is much stronger than that at nighttime, measured thin cirrus cloud layers at nighttime occur much more often than daytime. In the version 2 LDR calculation algorithm, we first sum attenuated backscatter, then calculate LDR. Because the thin cirrus cloud layers have

small attenuated backscatters, the small attenuated backscatters have less contribution to the summary values. Therefore, thin cirrus cloud layers have less impact on calculation of average LDR than the thick cirrus cloud layers. In the version1 LDR calculation algorithm, we calculate the LDR of the layers, average the LDR of layers to obtain the LDR of the column, and then average the LDR of columns in a grid to obtain the LDR of the grid. In this way, the LDR values from the thin cirrus cloud layers are equally weighted as the LDR values from the thick cirrus cloud layers. As a result, the nighttime LDR values determined by the LDR calculation algorithm version 1 are much smaller than those determined by the LDR calculation algorithm version 2.

In conclusion, the results produced by the application version 1 and 2 are slightly different. Among these differences, the LDR day versus night difference is the greatest. The LDR calculation algorithm is the primary cause to these differences.

5.2 Global Distribution of LDR

LDR distributions in terms of longitude versus latitude and latitude versus height are presented in Figure 5.4, and the zonal average LDR values are listed in Table 5.2. In general, the average LDR values are different in three zonal zones. Cirrus clouds that occur in the tropical, midlatidue, and polar regions have average LDR of 0.36, 0.31, and 0.29, respectively. Because of the existence of polar stratospheric clouds, the averaged LDR values present strong variability in space of both poles.

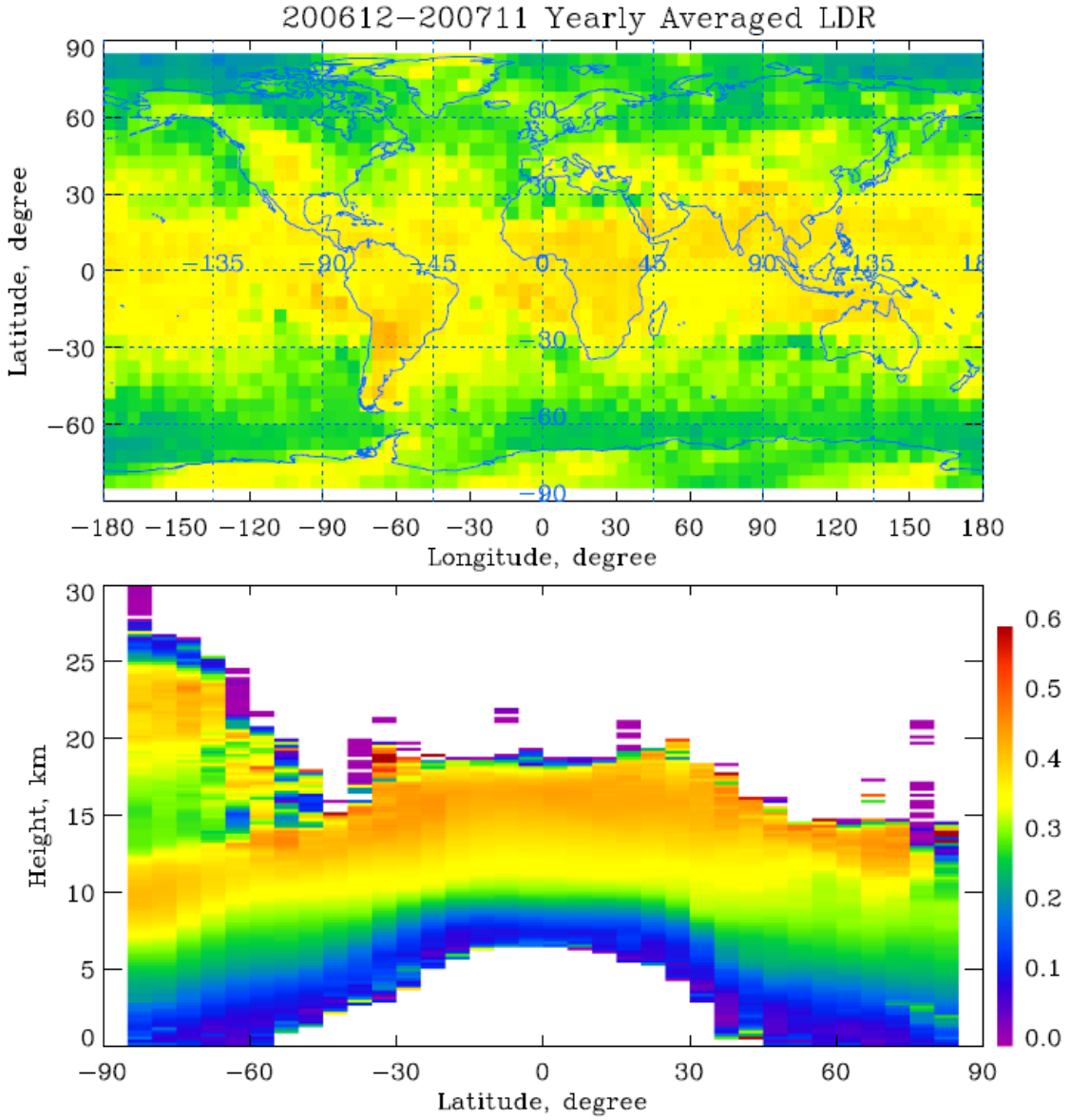

Figure 5.4 2007 annual average LDR of cirrus clouds

Table 5.2 Comparison of zonal average LDR at day and night

Latitude	LDR	LDR-day	LDR-night	(day-night)/day %
-85 to -60	0.295	0.294	0.295	0
-60 to -30	0.306	0.314	0.298	5
-30 to -15	0.359	0.373	0.344	8
-15 to +15	0.372	0.386	0.359	7
+15 to +30	0.358	0.376	0.341	9
+30 to +60	0.316	0.333	0.295	11
+60 to +85	0.275	0.280	0.269	4

Cirrus clouds with greatest LDR values (>0.35) occur in places where the frequency of cirrus cloud is also greatest (>43%), such as central southern America, western Africa, Indonesia, and the west-central Pacific Ocean warm pool.LDR values of cirrus clouds increase with the increase of height. The average LDR at cloud base is 0.1, with average 2.5 km cloud- thickness, the average LDR at the cloud top is 0.44. In the southern polar region, there are lots of PSCs, which extend to 27 km in height. The average LDR of the PSCs experiences variation with increasing height. The average LDR of the PSCs at cloud base is about 0.2, with increasing height, the average LDR increases to about 0.4, then it decreases with increase of height, at cloud top, the average LDR of the PSCs is about 0.1. Over Antarctica, the PSCs with about 0.1 LDR are generally present in the lower stratosphere, and higher PSCs have greater LDR values. This fact indicates that PSCs have various particle shape, size, or orientation along height. PSCs with greater LDR values (0.45-0.50) are associated with low-stratospheric nacreous clouds in both hemispheres. Nacreous clouds are induced by mountain-waves, and they

occur in mountainous regions such as Antarctic Peninsula and Victoria Land, and Greenland.

As pointed out before, ice crystal shapes are determined by temperature and supersaturation density. Because the average cloud thickness of cirrus clouds is about 2 km, the supersaturation density does not vary much within the cirrus clouds, so temperature becomes a key factor in determining the ice crystal shape in cirrus clouds. With an increase of height, i.e., decrease of the temperature, ice crystal shapes are more complicated. So the LDR increases with height.

As discussed in Chapter 4, tropical cirrus clouds are associated with deep convection, and synoptic systems produce midlatitude cirrus clouds. A large amount of moist air is brought by deep convection to higher level in the troposphere, where cold temperature and high humidity allow for more complicated ice crystal shapes. Deep convection also supports a long time of growth for ice crystals. Therefore, cirrus clouds in tropical regions are usually thicker and last longer than those in other regions. In addition, compared to those in other regions, ice crystals in the tropical region are more complicated. Synoptic cirrus clouds usually have extended horizontal structure. The ice crystals in these clouds have a relatively narrow size distribution, and their shapes are relatively simple. As a result, the average linear depolarization ratios of synoptic cirrus clouds (0.31) are smaller than the average LDR of the tropical cirrus clouds (0.36). In polar regions, where the humidity of air is low, ice crystals do not grow fast or form complicated shapes; therefore, cirrus clouds in polar regions usually have small LDR values. Worldwide PSCs in the southern polar region have various LDRs with height and

space, so the average LDR of cirrus clouds over the southern polar region (0.29) is greater than that over the northern polar region (0.28), and varies with locations. PSCs form at very low temperature, below -78ºC. These temperatures can occur in the lower stratosphere in winter time. In the Antarctic, the temperature in the lower stratosphere is below -88°C, so PSCs occur frequently in the southern polar region. Generally speaking, in the northern polar region, the temperature in the lower stratosphere is higher than that in southern polar region. As a result, PSCs occur less frequently in the northern polar region than in the southern polar region, and cloud thickness of PSCs in the northern polar region is smaller than that in the southern polar region. In the Northern hemisphere, the generation of lee waves by mountains may locally cool the lower stratosphere and lead to the formation of PSCs.

5.3 Diurnal Difference of LDR

The difference of LDR values between daytime and nighttime in 2007 is presented in Figure 5.5. Generally speaking, daytime LDR values are higher than nighttime LDR values. The day versus night difference is greater in the tropical and northern midlatitude regions than in other regions, and the difference is apparent in those locations where LDR values are great. The diurnal variation of the LDR values of cirrus clouds is easy to reveal in the difference between daytime LDR and nighttime LDR. Figure 5.6 shows the LDR day versus night differences in 2007 and 2008. The LDR difference is defined as the daytime LDR minuses the nighttime LDR.

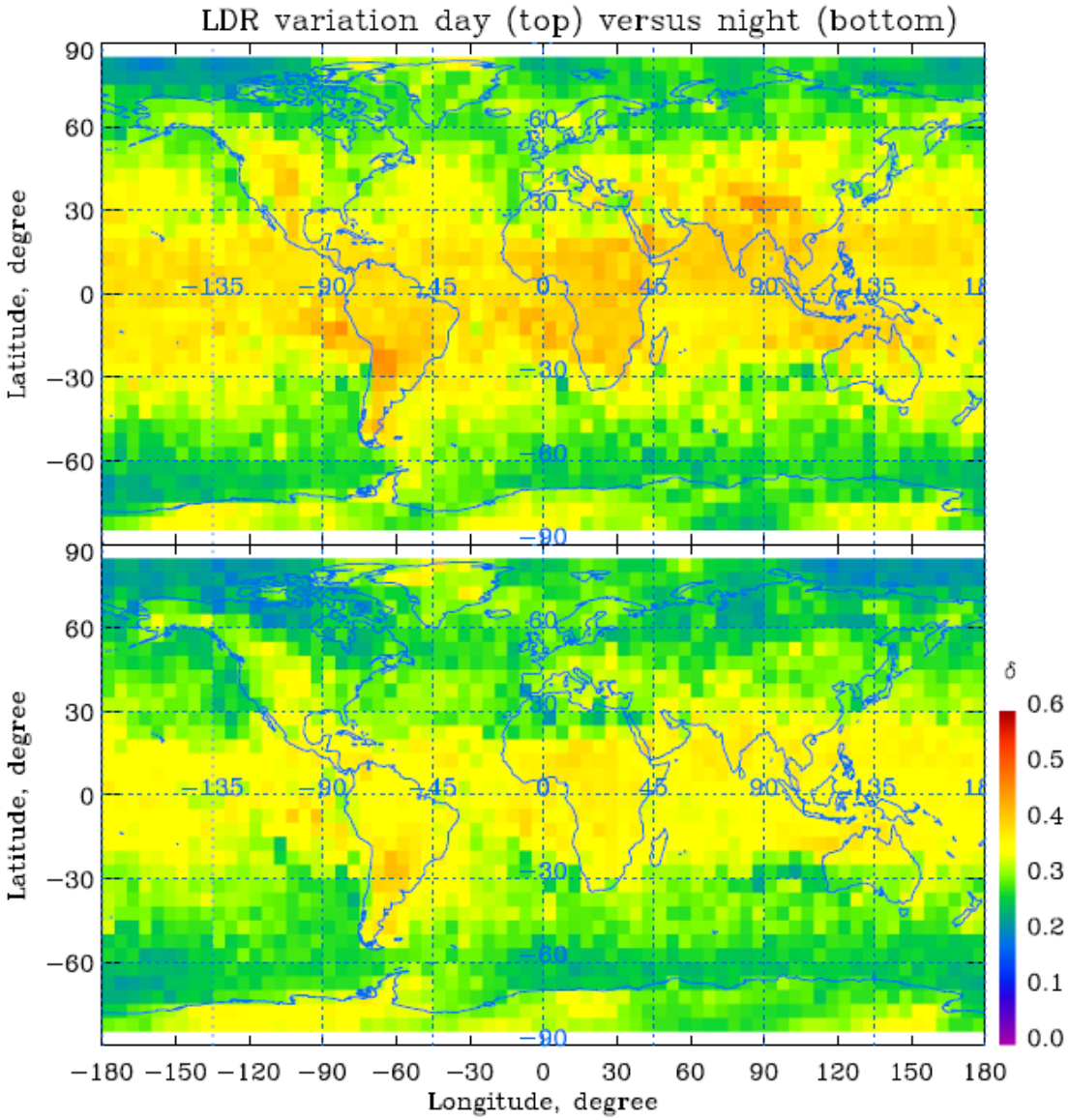

Figure 5.5 LDR variations between daytime and nighttime

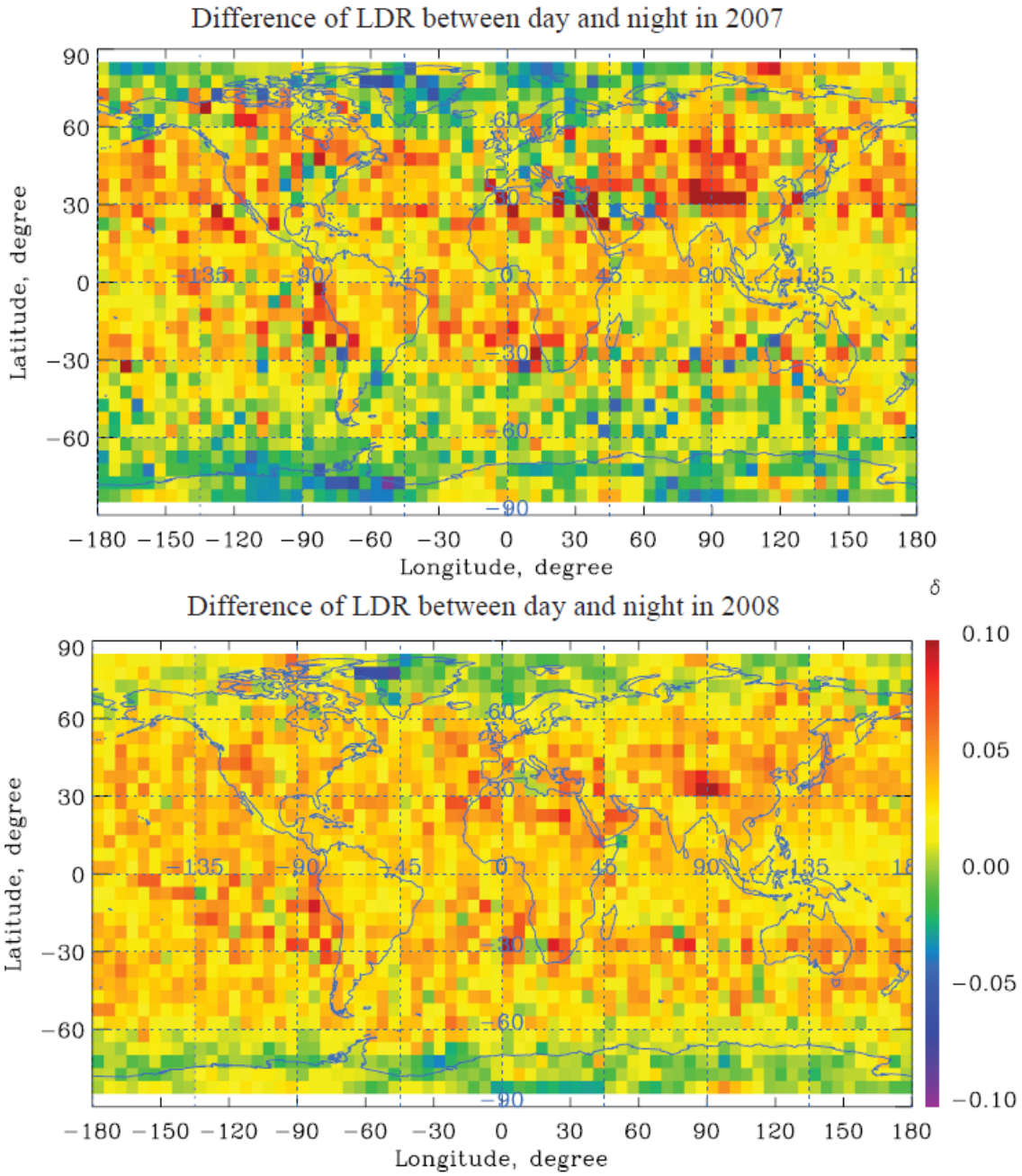

Figure 5.6 LDR difference between daytime and nighttime

As shown in Figure 5.6, the diurnal variation of the LDR values of cirrus clouds in 2007 and 2008 shows that daytime LDR values are greater than nighttime LDR values over the major part of the globe.

For a quantitative comparison, we analyze the variation of zonal average LDR values between daytime and nighttime in 2007. As shown in Figure 5.7, the greatest day-night zonal average LDR difference (0.04) occurs in northern midlatitude (30N to 60N) regions, a lesser zonal average LDR difference (0.03) occurs in tropical and subtropical zones (30S to 30N), and in the southern polar region, there is no zonal average LDR difference between daytime and nighttime.

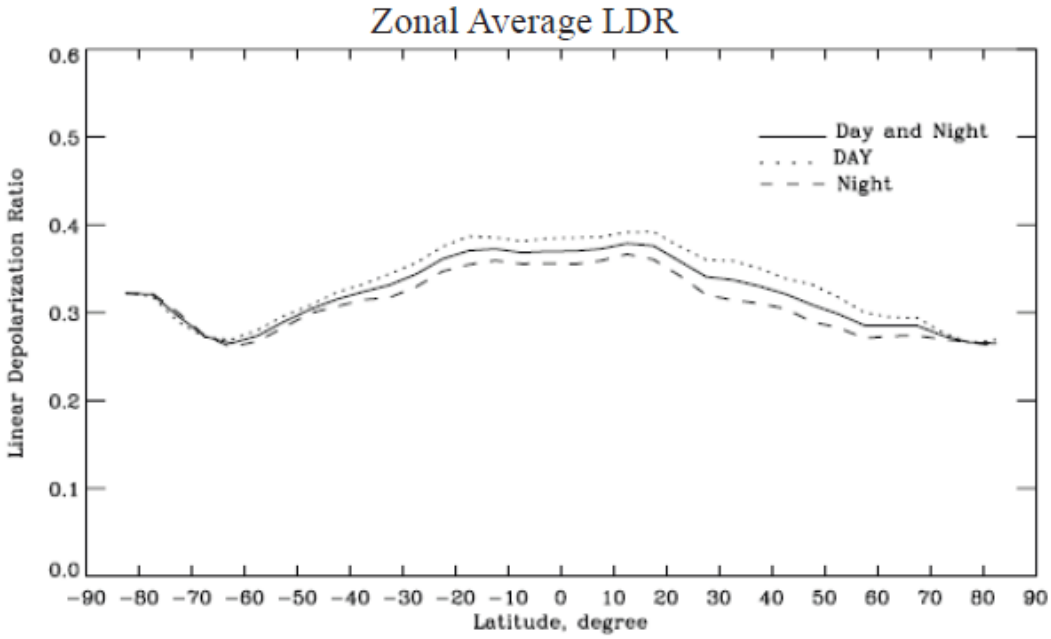

Figure 5.7 Zonal average LDR variation between daytime and nighttime

The yearly zonal average LDRs of cirrus clouds for daytime, nighttime, and day plus night time were listed in Table 5.2. The statistic results verify that the greatest difference of LDR between day and night is located in 30N to 60N latitude, and the least difference occurs in the southern polar region (85S to 60S latitude). The yearly total annual averaged LDR values of daytime, nighttime, and day plus night time in 2007 are 0.33 0.31, and 0.32, respectively. The yearly average LDR difference between daytime and nighttime in 2007 is not significant (0.02).

The measured diurnal variation of LDR results from the measurement error which is caused by the strong diurnal variation of the background noise. As discussed in chapter 4.2.2, the variation of the background noise between day and night impacts the measurement of macro-physical properties of cirrus clouds. The measured cloud bases are higher at daytime than those at nighttime, and the LDR values of cloud bases are smaller than the LDR values of cloud tops. As a result, the average LDR values are greater at daytime than those at nighttime.

5.4 Seasonal Variations of LDR

Figure 5.8 displays the seasonal average LDR of cirrus clouds in 2007. The seasonal change of LDR values of cirrus clouds is not apparent, except in the southern polar region. Because in JJA, abundant polar stratospheric clouds occur in the southern polar region, and the LDR values of these polar stratospheric clouds are greater than those of cirrus clouds, the average LDR values in JJA are greater than those in DJF. Figure 5.9 presents the 2007 seasonal average LDR values in latitude versus height. It

shows that abundant polar stratospheric clouds occur in the southern polar region in SON and JJA, only a few polar stratospheric clouds occur in the northern polar region in DJF. This result verifies that PSCs occur in local winter time. The global average LDRs are 0.29, 0.29, 0.30, and 0.30 in DJF, MAM, JJA, and SON, respectively.

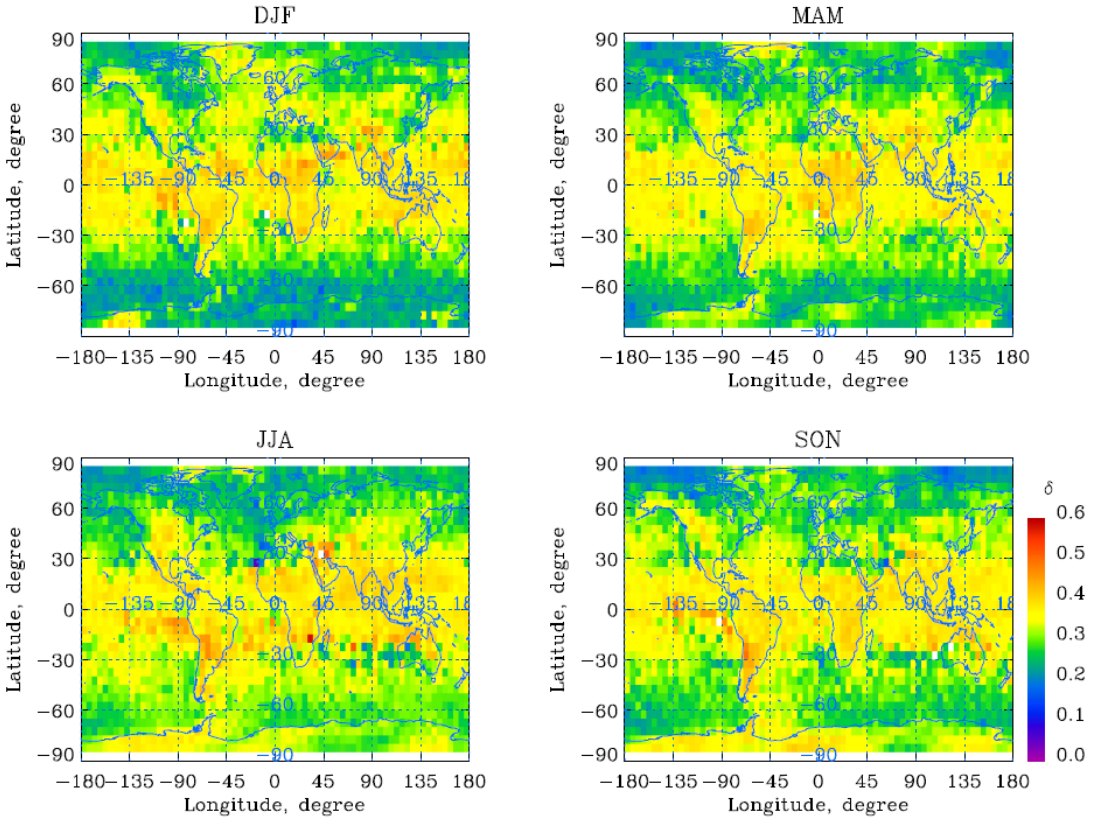

Figure 5.8 Seasonal average LDR of cirrus clouds in longitude vs. latitude

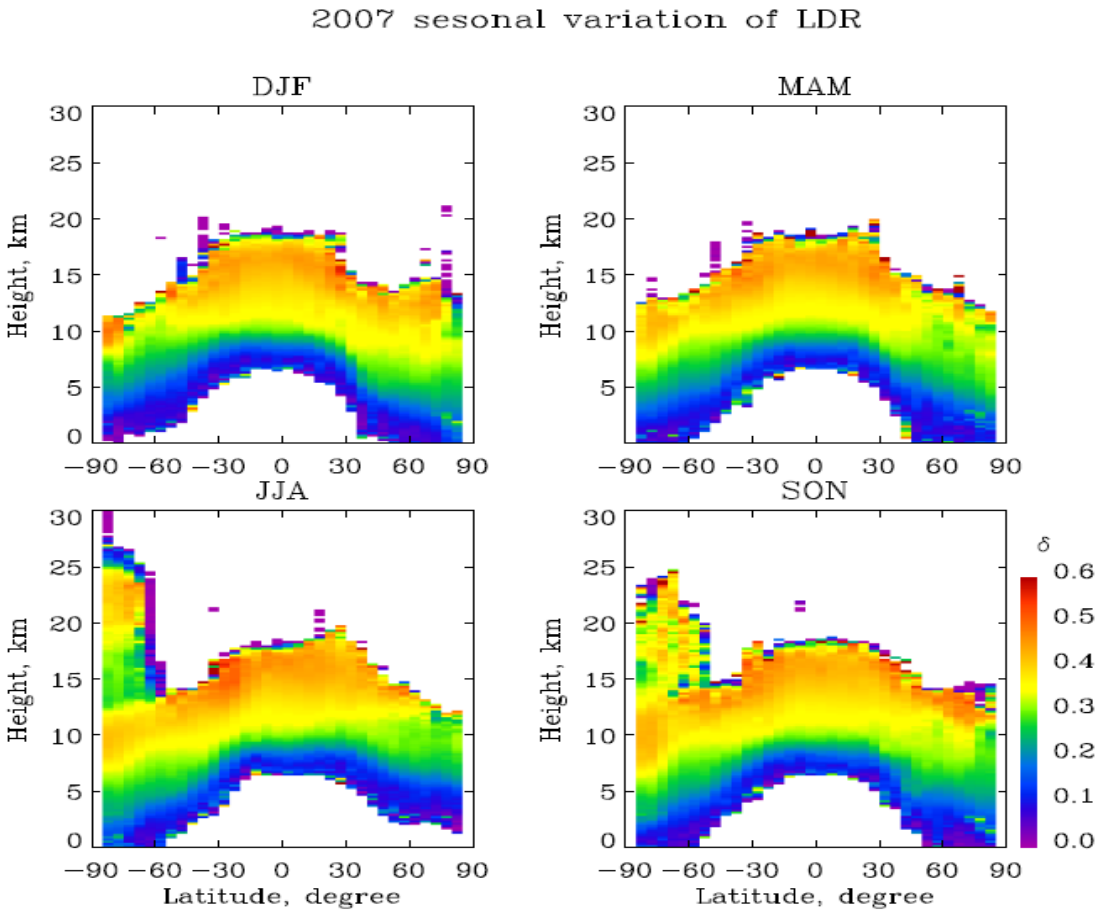

Figure 5.9 Seasonal average LDR of cirrus clouds in latitude vs. height

5.5 Monthly Variations of LDR

The 2007 monthly variation of the LDR values confirms that the shape characteristics of ice crystals varies with location, but do not vary with time. Figure 5.10 shows the LDR values of cirrus clouds vary monthly, and Figure 5.11 is the plot of variation of LDRs with month and latitude.

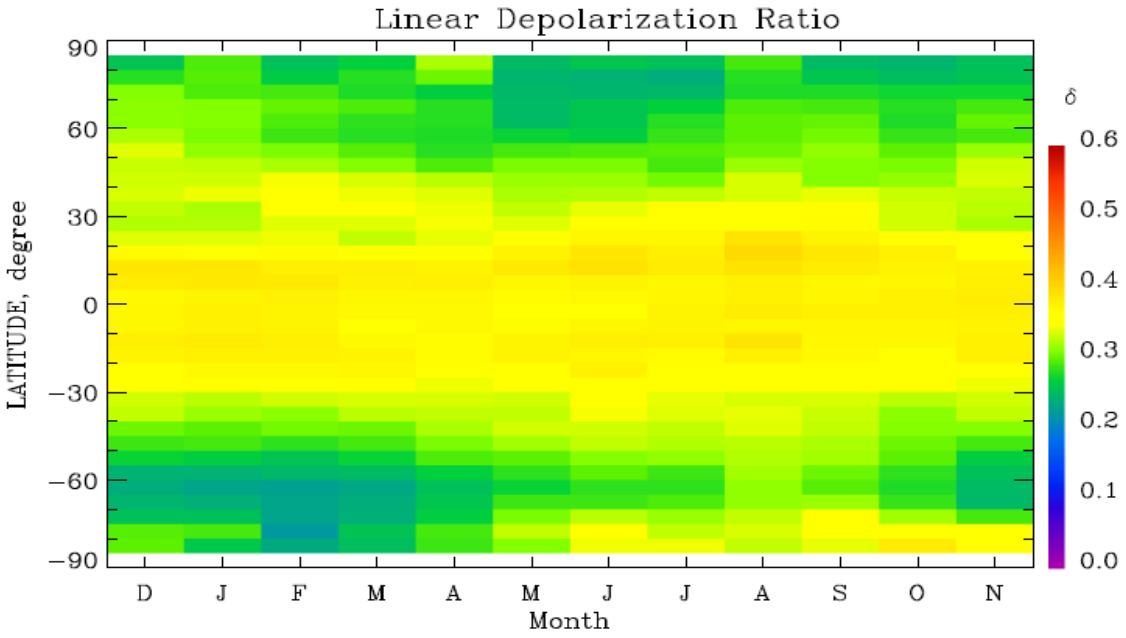

Figure 5.10 Monthly variation of LDR with latitude

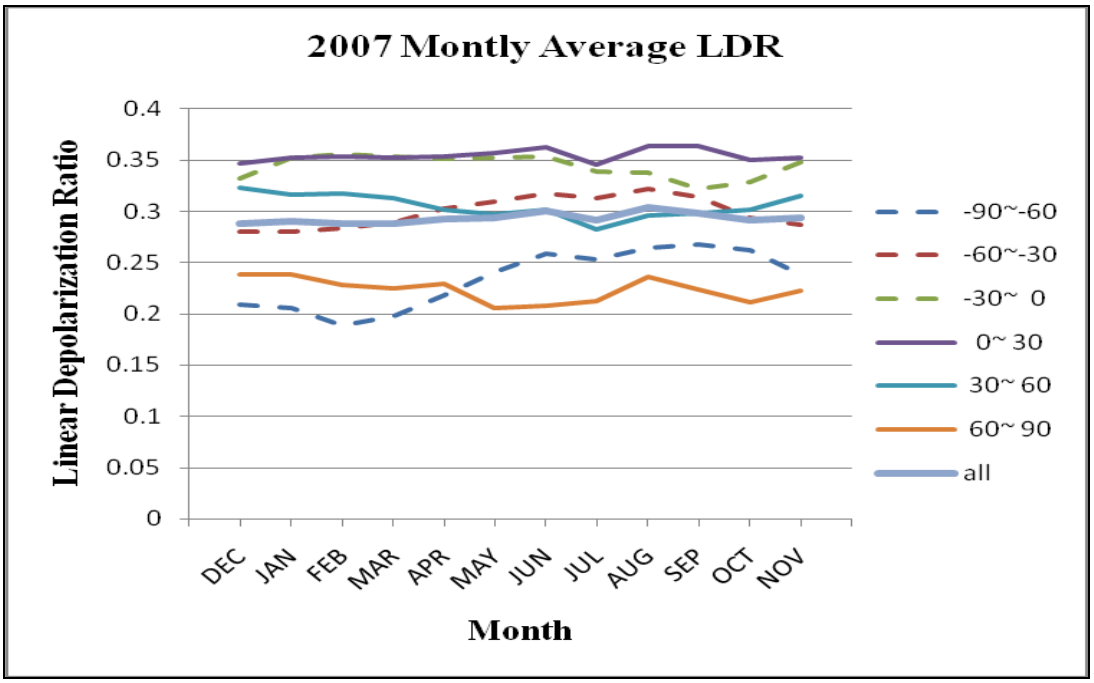

Figure 5.11 Monthly variation of LDR

Figures 5.10 and 5.11 illustrate that the monthly variation of global LDRs is very small. The global average LDR in 2007 is within the range of 0.288 to 0.303; the monthly variations of LDRs are different with latitude. The monthly variation of LDRs in the southern polar region (range from 0.188 to 0.268) is the greatest among all latitude regions. As pointed out before, the appearance of polar stratospheric clouds in the southern polar region results in the variation of LDR values from month to month. If PSCs could be excluded from our analysis, the LDR values of cirrus clouds in the southern polar region would present much less change with time of the year.

5.6 Nadir versus Off-Nadir Measurement Results

In satellite-based lidar measurement, the nadir measurement means the sensor points from directly above at a 90º angle vertical to the horizontal level of the surface of the earth, and off-nadir measurement means the sensor tilts a small angle to the vertical direction. Before November 28, 2007, CALIPSO satellite operated at a 0.3 degree viewing angle which was very close to nadir direction (except for a brief period of off-nadir data collected after August 27, 2007). After that time, it has operated in a 3 degree off-nadir direction. Both nadir and off-nadir data allow us to investigate the horizontally orientated planar ice crystals. When the laser hits ice clouds composed of a significant fraction of horizontally orientated planar ice crystals in nadir direction, the LDR values could be considerably low. Figure 5.12 shows the global distribution of the 2008 yearly average LDRs of cirrus clouds, and Figure 5.13 shows the difference of the LDRs between 2008 and 2007.

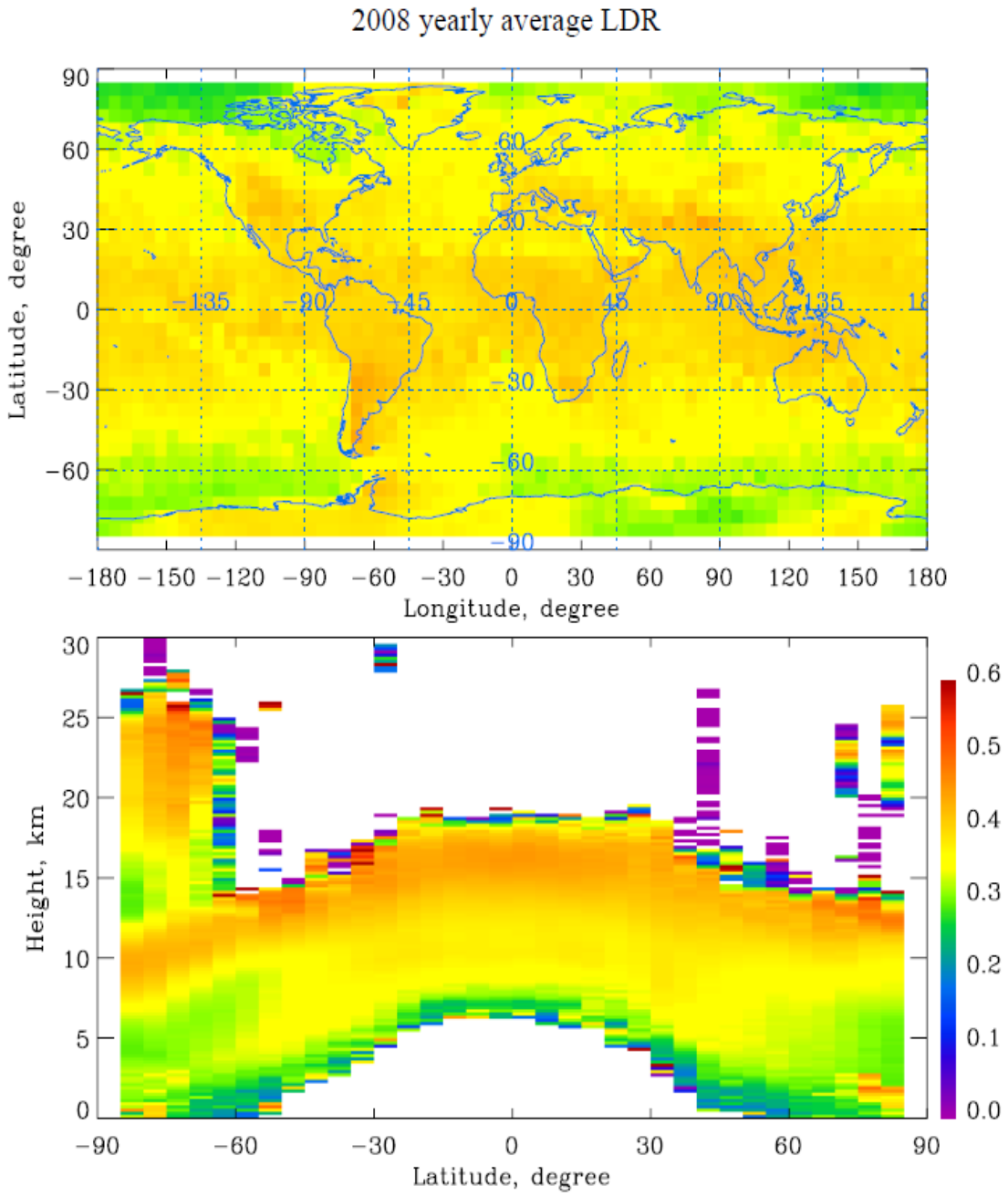

Figure 5.12 2008 yearly average LDR of cirrus clouds

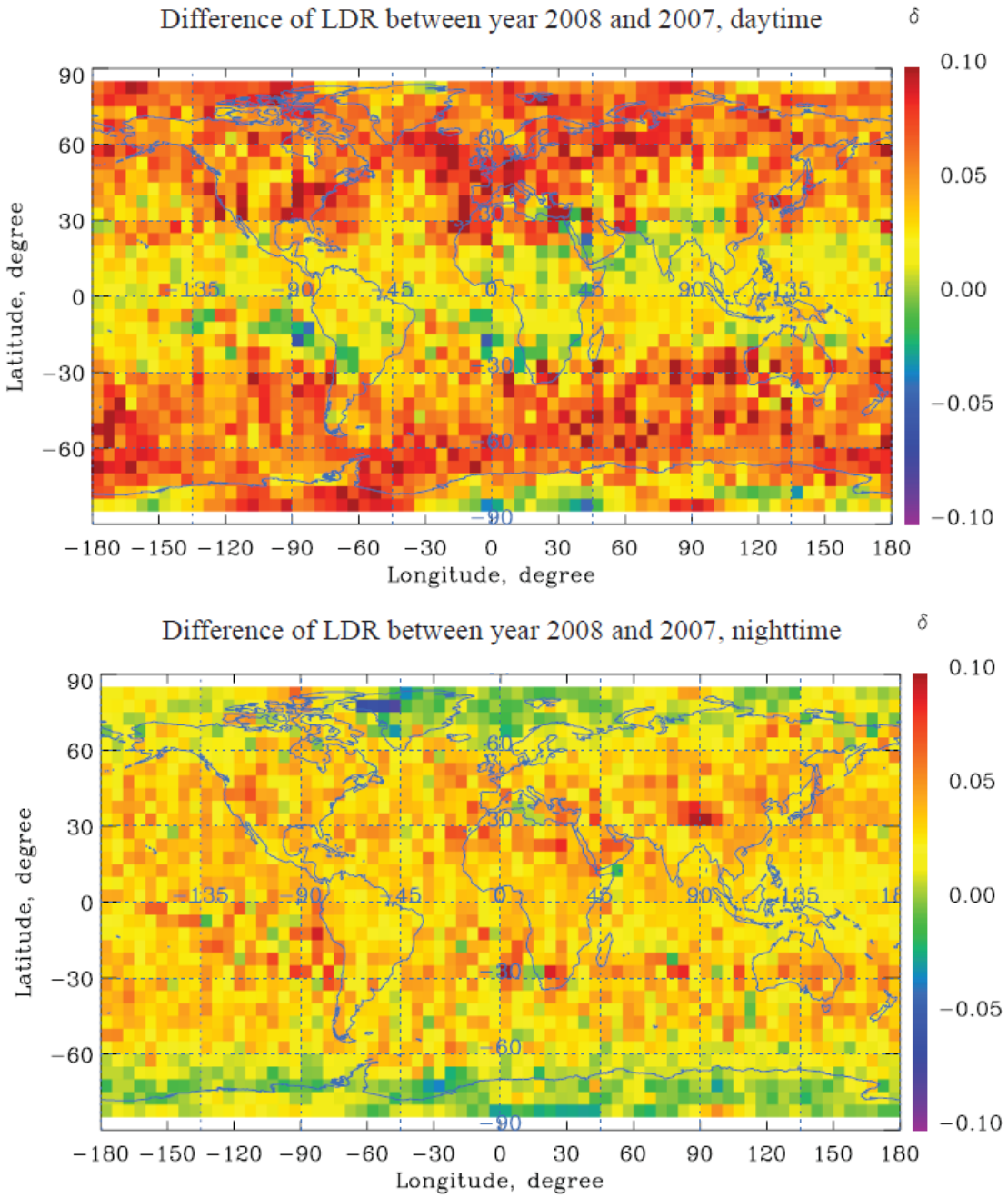

Figure 5.13 LDR difference between 2008 and 2007

By the comparison of Figure 5.12 with Figure 5.4, we know, in general, that LDR values measured by the off-nadir measurement are greater than those by the nadir

measurement. It means there are some horizontal-orientated ice crystals in cirrus clouds. Figure 5.13 indicates that the LDR variation between the off-nadir and nadir measurements is greater at daytime than at nighttime. When solar light hits horizontal-orientated ice crystals, these crystals reflect the light. If the solar zenith angle is equal to the lidar view zenith angle, then strong noise is introduced in both parallel and perpendicular return power of the lidar, so the LDR is very low. Every half-orbit lidar measurement is around 45 minutes, and the CALIPSO passes the equator at about 1:30 pm local time. The solar zenith angle is close to the lidar view zenith angle. The horizontal-orientated ice crystals introduce very strong background noise at daytime to make the nadir measured LDR very low at daytime.

Figure 5.13 also shows that the variation of LDR between off-nadir and nadir at daytime depends on latitude. The difference of LDRs between the off-nadir and the nadir measurements is greater in the midlatitude and polar regions than in the tropical regions. A possible reason is that midlatitude and polar cirrus clouds include more horizontal-orientated ice crystals than tropical cirrus clouds. Tropical cirrus clouds result from deep convection; ice crystals in these clouds move up and down fast. They do not easily form as horizontal-orientated ice crystals. Ice crystals in the midlatitude and polar cirrus clouds are calmer than those in the tropical cirrus clouds, so they easily fall steady to form horizontal-orientated ice crystals.

Table 5.3 gives the statistic values of LDRs in 2007 and 2008. The annual average LDR of 2007 is 0.32, and the annual average LDR of 2008 is 0.37. That means horizontal-orientated ice crystals cause a 14.9% increase of annual average LDR. This is

consistent with general knowledge. In fact, many ice crystals exist with plate structures, and they are usually laying on their long axis horizontally in air. With the laser beam in nadir, the parallel backscatter light is very strong, whereas the perpendicular backscatter light is almost zero. As a result, LDR is almost zero. When the laser beam transmits in off-nadir, the LDR increases very much.

Table 5.3 Yearly global average LDR in 2007 and 2008

2007(Nadir)			2008(off_Nadir)		
Day	Night	all	Day	Night	All
0.3286	0.3085	0.3181	0.3807	0.3520	0.3654

5.7 Relationship between LDR and Temperature

Ice crystals in cirrus clouds have various shapes, and the shapes are determined by the cloud's temperature and humidity (see Figure 1.3). Figures 5.14 and 5.15 exhibit the relationship between the average LDR values and the temperatures of cirrus clouds. As shown in Figures 5.14 and 5.15, the average LDR values of cirrus clouds increase with a decrease of temperature of the cirrus clouds. At a given temperature, LDRs of cirrus clouds vary with latitude. Cirrus clouds have greater LDR in tropical regions than those in polar regions. These relations agree with the discussion in Chapter 1 that ice crystals shape is a function of temperature and the suppersaturation density of the clouds.

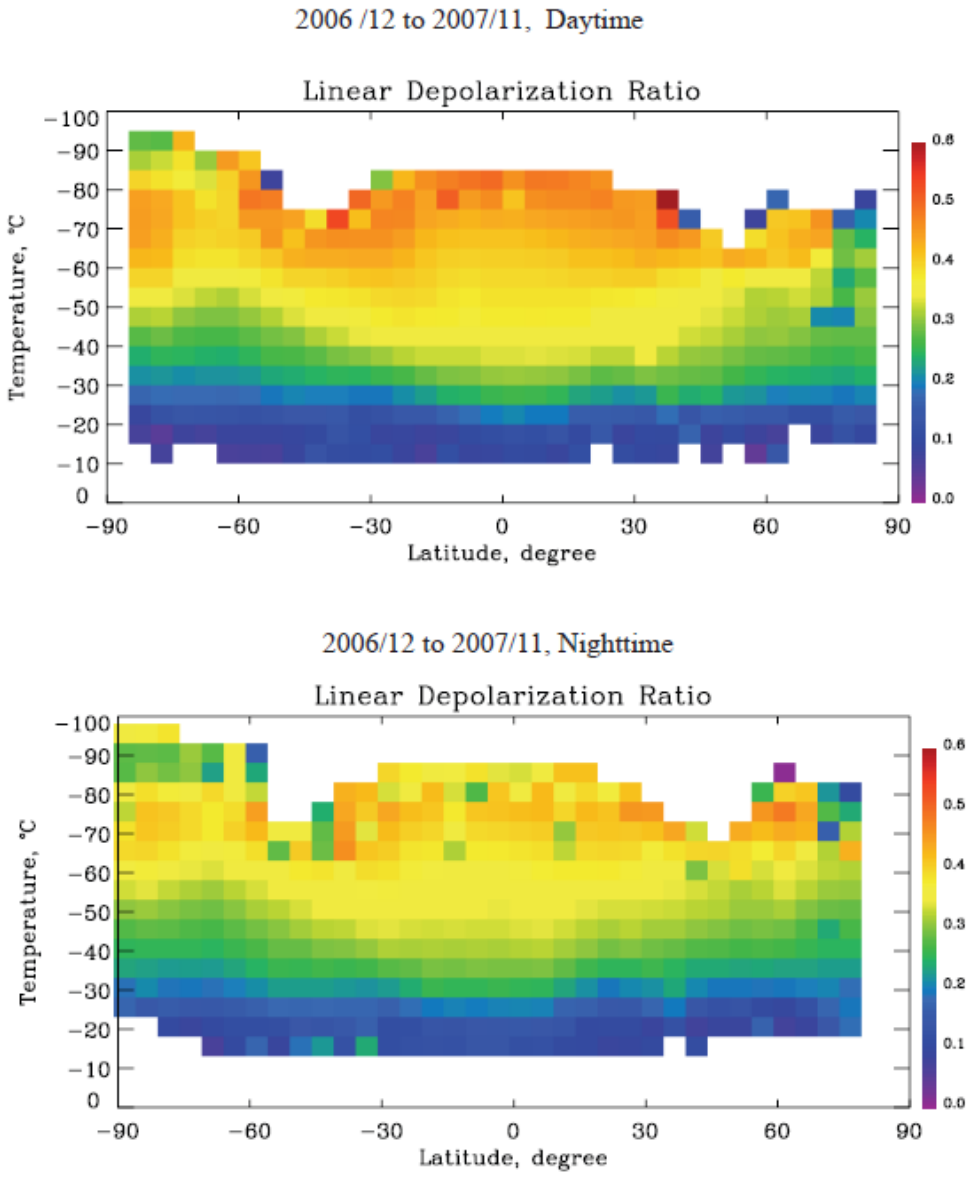

Figure 5.14 2007 annual average LDR variation with cloud- top temperature

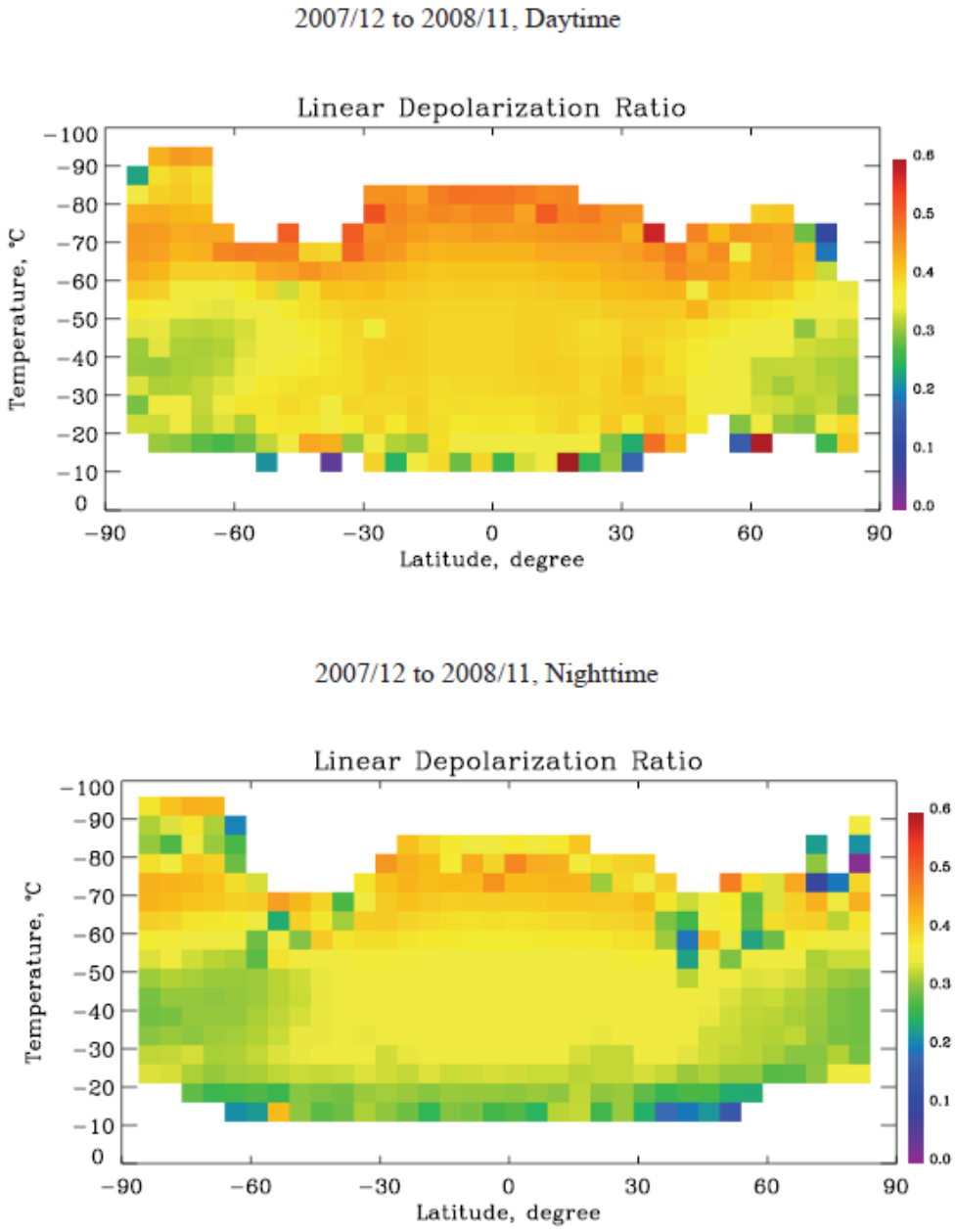

Figure 5.15 2008 annual average LDR variation with cloud-top temperature

Ice crystal shapes become more complicated with decreasing temperature of clouds, and more complicated shapes of ice crystals produce greater LDR values. Tropical cirrus clouds have greater supersaturation densities than the polar cirrus clouds.

The shapes of ice crystals of tropical cirrus clouds are more complicated than those of polar cirrus clouds, so the LDR variation with latitude is observed. As shown in Figures 5.14 and 5.15, LDR values of cirrus clouds vary with temperature, and the magnitude of the variation depends on latitude. For example, the range of variation of LDRs is greater in tropical regions than in midlatitude or polar regions. In tropical regions, greater humidity is favorable to form more complicated shapes of ice crystals. So, cirrus clouds in the tropical regions have greater LDR values. This finding verifies that ice crystal shapes are impacted by the humidity of clouds. If you pay attention to the LDR change of PSCs in the southern polar region, you will find that the LDR value change exhibits a cycle: small to great, then great back to small. As we know, theoretical research results conclude that the ice crystal shape experiences the cycle change with the temperature, and this conclusion was supported by earlier experiment results. This research findings derived from the LDR behavior obtained from CALIPSO data indicate that the ice crystal growth theory is correct.

Chapter 6 Investigation of Effective Diameter of Cirrus Clouds

One of the ultimate goals in cloud research is parameterization of clouds for climate and weather models (Fu and Liou, 1992; Khairoutdinov and Randall, 2001). As an integrated part of a climate/weather model, a radiative transfer model is applied to calculate the radiative energy. Clouds exert a profound influence on the climate radiation budget. An accurate parameterization of radiative effects of clouds is necessary. Because ice clouds are composed of various shapes and sizes of ice crystals, they are even harder to parameterize. We introduce some quantities to effectively represent the radiative effect of ice clouds. In current atmospheric models, the science community uses the effective diameter and ice water content (IWC) to represent the bulk-microphysical properties of ice clouds. Ice water content with size distribution is defined as

$$IWC = \int \rho_i V(D) N(D) dD \,, \tag{6.1}$$

where $V(D)$ is the volume of an ice crystal with maximum size of D, and $N(D)$ is the size distribution of ice crystals in the ice cloud, ρ_i is the bulk density of ice crystals. The definition of an effective diameter of cirrus clouds has been given in chapter 1 (Eq. (1.6)). Ice water content and effective diameter assemble information of shape, size, and size distribution of ice crystals of cirrus clouds. They completely represent the bulk-microphysical properties of cirrus clouds for radiation energy calculation purposes. From the point of view of climate, cloud radiative properties depend on cloud macro-physical properties and cloud optical properties. By using the IWC and effective diameter, optical

properties of clouds can be calculated. Slingo and Schrecker (1982) presented a set of equations to calculate optical depth, single scatter albedo, and asymmetry parameter for water clouds. Because ice crystals have various shapes, the optical properties of ice clouds are much more difficult to retrieve. Baum, *et al*. (2005) studied large amounts of in-situ data collected from cirrus clouds and derived both particle size distribution and particle habit distribution of cirrus clouds; and developed 18 ice cloud bulk scattering modes, which are presented in term of ice water content and effective diameter of ice clouds. Once ice cloud bulk optical properties and macro-physical properties are available, the radiative effect of ice clouds can be estimated by a radiative transfer model.

6.1 Radiative Influence of Effective Diameter and Ice Water Content

Radiative effects of clouds are determined by both macro and bulk-microphysical properties of clouds. Ice water content and effective diameter are bulk microphysical properties of clouds. One effective method to investigate how the radiative effects of clouds are determined by the cloud physical properties is by analyzing the radiative transfer simulation results obtained by running a radiative transfer model with different inputs. In this study, the radiative transfer model developed by Key and Schweiger (1998) is used to study the dependence of cloud radiative forcing on cloud ice water content and effective diameter. the radiances at the TOA over Fairbanks are calculated by the radiative transfer model to analyze the radiative effects of clouds. Cloud radiative forcing, cloud solar radiative forcing, and cloud terrestrial radiative forcing is defined by the equations 1.3, 1.4, and 1.5, respectively. The inputs for the radiative transfer model

calculation include: U.S. standard atmosphere conditions; a single-layer ice cloud located at Fairbanks in summer time at noon with cloud top height of 9 km, and cloud thickness of 2.0 km. Three typical ice water contents and 14 effective radii ranging from 5 to 130 micro-meters are used in the simulation study. Cloud radiative effects in solar and terrestrial wavelength bands are studied separately.

Figure 6.1 shows the cloud solar radiative forcing at TOA. In general, cloud solar radiative forcing is influenced by both ice water content and effective radius. It increases with the increase of ice water content and/or with decrease of effective radius. When ice water content of clouds increases, albedo of clouds increases. Therefore, solar radiative forcing of clouds increases. On the other hand, at a given ice water content, when the effective radius of clouds decreases, total areas of size distribution of clouds increase. Increase of the total areas of size distribution of clouds increase albedo of clouds (see Eq. (1.6), Chapter 1). As a result, cloud solar radiative forcing increases. In order to explain the degree of the influence of effective radius on radiative forcing, the sensitivity of radiative forcing to the effective radius is defined as the ratio of radiative forcing to the effective radius. The sensitivity of solar radiative forcing is great at smaller effective radius from 0 to 40 μm. Ice water content also influences the sensitivity of solar radiative forcing. As shown in Figure 6.1, the sensitivity of solar radiative forcing increases with the increase of ice water content.

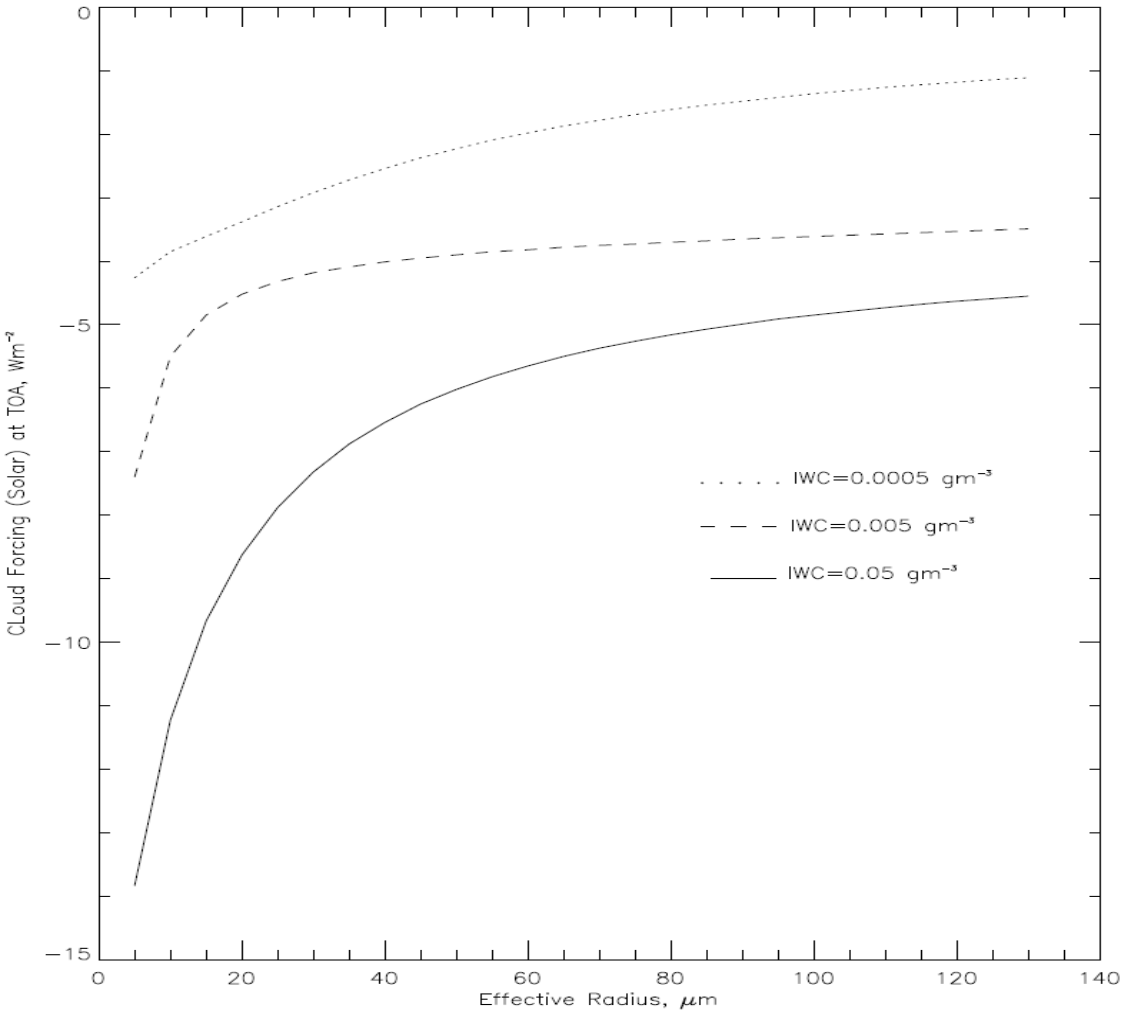

Figure 6.1 Cloud shortwave radiative forcing variation with effective radius as obtained with the radiative transfer model, for initial conditions and assumptions selected.

Figure 6.2 shows how the ice water content and effective radius of clouds influence the cloud longwave radiative forcing. As shown in this figure, longwave radiative forcing increases non-linearly with increase of ice water content. At a given ice water content, longwave radiative forcing increases non-linearly with decrease of the effective radius. Longwave radiative forcing is more sensitive to small effective radius

from 0 to 40 μm. The sensitivity of longwave radiation is impacted by the ice water content of cloud. When clouds are very thin, and ice water content of clouds is very small, the sensitivity of longwave radiative forcing to the effective radius is small.

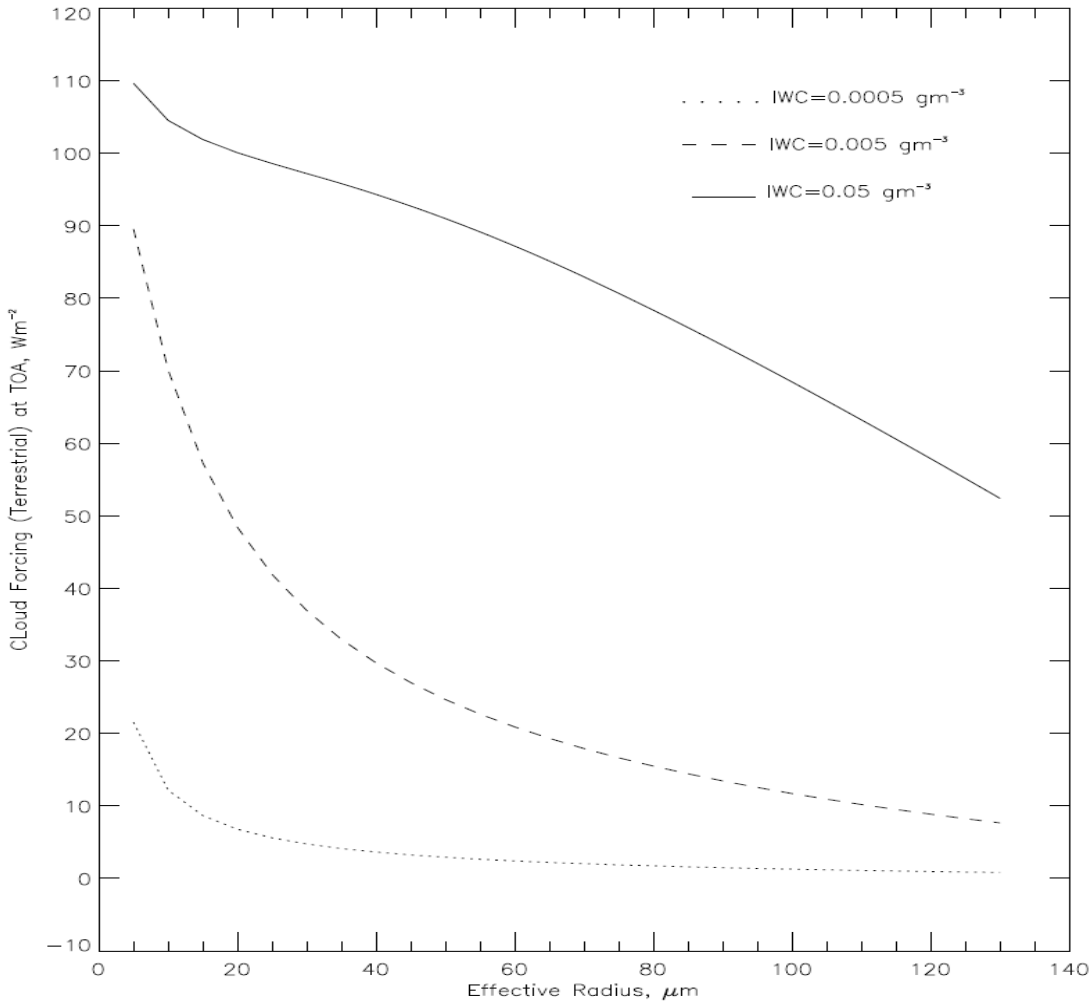

Figure 6.2 Cloud longwave radiative forcing variation with effective radius as obtained from the simulation with the radiative transfer model, for initial conditions and assumptions selected.

Cloud radiative forcing is the combination of shortwave and longwave radiative forcing. Figure 6.3 illustrates the variations of cloud radiative forcing with effective

radius and ice water content. In this specific high cloud simulation case (9 km cloud-top height and 2 km cloud thickness), longwave radiation dominates the cloud radiative forcing; as a result, the cloud warms the TOA. Cloud radiative forcing increases with the increasing of ice water content, and decreases with increasing effective radius. Cloud radiative forcing is sensitive to large ice water content and small effective radius.

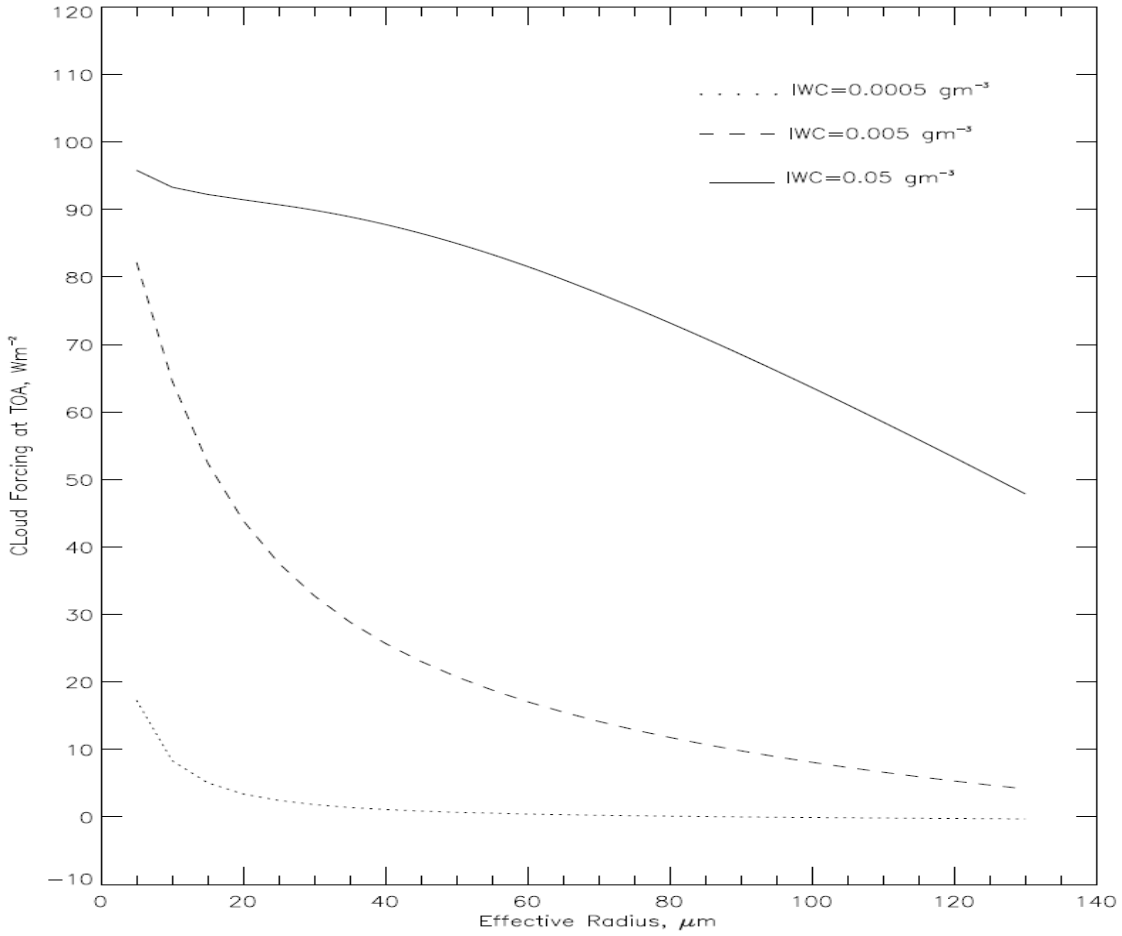

Figure 6.3 Cloud radiative forcing variation with effective radius.

Cloud radiative forcing is the sum of cloud shortwave radiative forcing and cloud longwave radiative forcing.

Cloud radiative forcing at the surface of the earth is displayed in Figure 6.4. Cloud radiative forcing, at the surface as a function of ice water content and effective radius, is similar to cloud radiative forcing at the TOA, except that clouds enforce more radiative effects at TOA than at the surface of the earth.

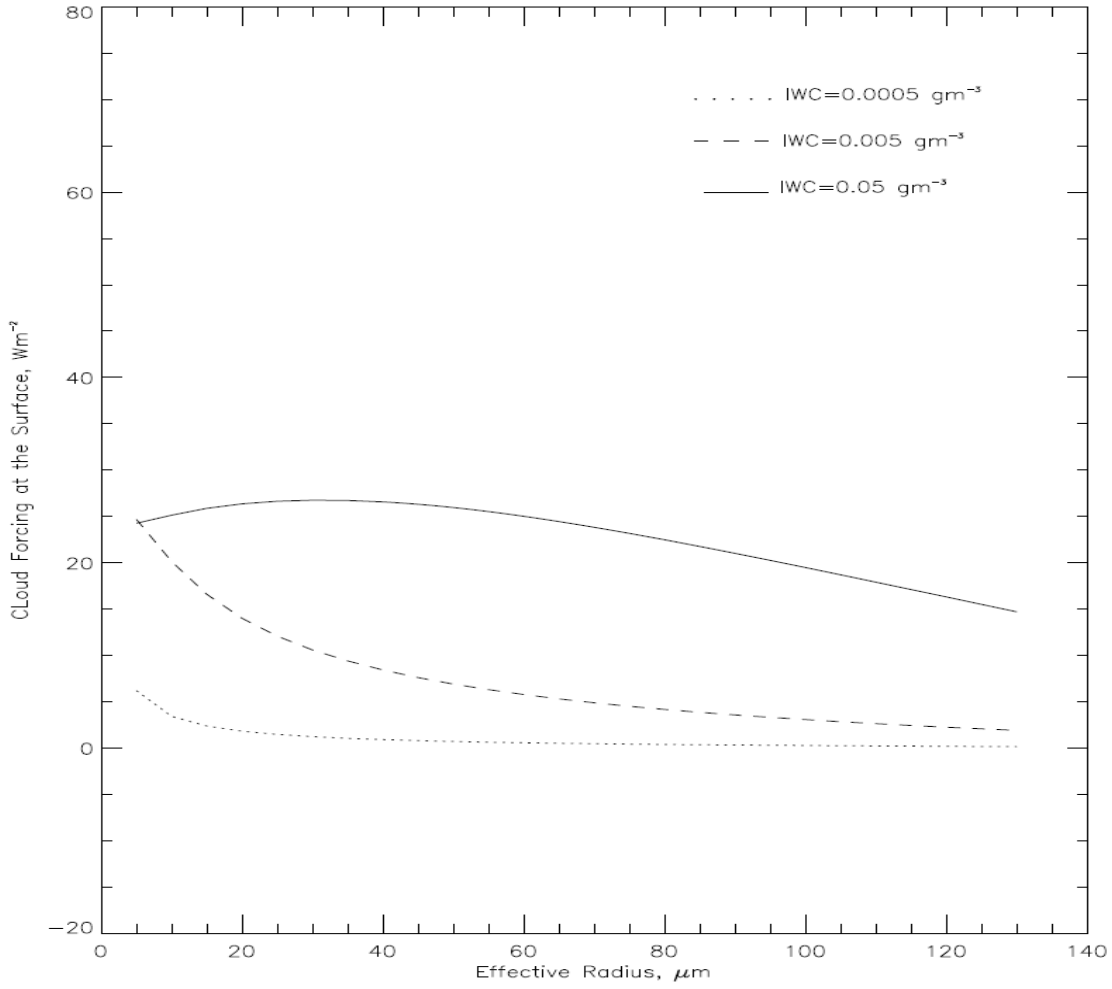

Figure 6.4 Cloud radiative forcing at the surface

as obtained with the same radiative transfer model, initial conditions and assumptions selected as those used to produced results in Figure 6.3 but for cloud radiative forcing at the surface of the earth.

6.2 Results and Analysis for Effective Diameter of Cirrus Clouds Globally

The global distribution of yearly averaged effective diameters of cirrus clouds and yearly zonal averaged effective diameters are illustrated in Figures 6.5 and 6.6, respectively. The effective diameters are large in the tropical and the subtropical regions (140 ~150 μm), and gradually decrease in the midlatitude regions. The small values of effective diameters occur in the southern polar region (about 30 μm). In both northern and southern 30 degree latitude regions, effective diameters are largest (150 μm). This finding infers that similar weather conditions yield similar microphysical properties of ice clouds. Effective diameters are smaller in the southern polar region (~60 μm) than in the northern polar region (~90μm). The reason is that polar stratospheric clouds have very small effective diameters, and more PSCs exist in the southern than in the northern hemisphere. As shown in Table 5.2, annual zonal average LDR values of cirrus clouds are greater in the southern polar region (0.30) than those in the northern polar region (0.28). Clouds with greater LDRs are composed of more non-spherical ice crystals. More non-spherical ice crystals increase the total area of size distribution. Recalling that the effective diameter is proportional to the ice water content and inversely proportional to total area of size distribution, one can conclude: when clouds have greater LDR values, the effective diameters of the clouds are smaller.

Cirrus clouds in the tropical and subtropical regions normally are composed of large and more complicated shapes of ice crystals, and the ice water content of these clouds is high. For a single ice crystal, the relation between the shape and the area of the ice crystal is simple: an ice crystal with complicated shape has a great projection area.

For many ice crystals in clouds, the relation between the shapes distribution and the total projection area is more complicated than that for a single ice crystal. At a given IWC, if clouds are composed of large individual ice crystals, the total area of size distribution of clouds is small. Therefore, the great effective diameters in the tropical region are due to high ice water content and large ice crystals. On the other hand, cirrus clouds in the polar regions have small ice water content, and ice crystals in these polar cirrus clouds are small and their shapes are simple. At a given IWC, if clouds are composed of small ice crystals, the number of ice crystals is high. As a result, the total area of size distribution of clouds is great. Because polar cirrus clouds have small IWC and great total area, their effective diameters are small. In midlatutude regions, various effective diameters are results of various total areas of ice crystal size distribution in cirrus clouds.

Maritime cirrus clouds usually have greater effective diameters than continental cirrus clouds. For example, continental cirrus clouds over South America, southern Africa, and Australia have relatively smaller effective diameters than nearby maritime cirrus clouds. Compared to cirrus clouds over Arctic Ocean, Arctic continental cirrus clouds over Greenland have rather smaller effective diameters. The only exception occurs in northern Africa, the cirrus clouds over this region seem to have similar effective diameters as the nearby ocean. Usually maritime cirrus clouds and continental cirrus clouds have comparable ice water contents, but the ice crystals in maritime cirrus clouds are greater than those in continental cirrus clouds. As a result, maritime cirrus clouds usually have greater effective diameters than nearby continental cirrus clouds. Northern Africa is dominated by high pressure, the continental cirrus clouds over this region occur

very infrequently, and the total number of ice crystals in the cirrus clouds is small. Therefore, both ice water content and total projection area of these continental cirrus clouds are small. The effective diameter is proportional to the ice water content and inversely proportional to the total projection area of cirrus clouds. Because the degree of the decrease of the total projection area is greater than that of the ice water content of these cirrus clouds, the effective diameter of these cirrus clouds is comparable to that of nearby maritime cirrus clouds.

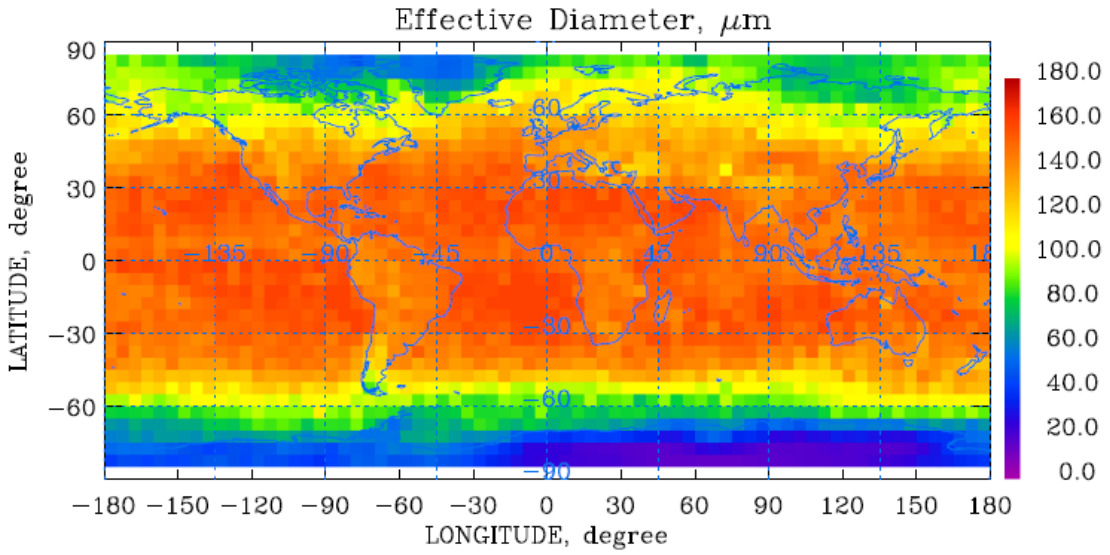

Figure 6.5 2007 annual average effective diameters of cirrus clouds

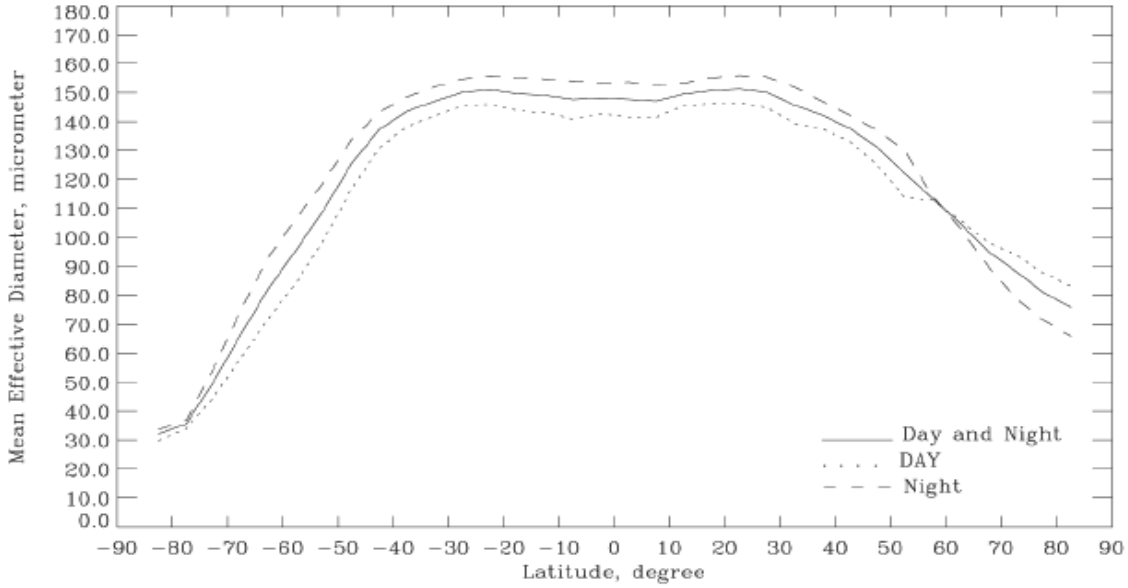

Figure 6.6 Annual zonal average effective diameters

Table 6.1 gives statistical results of effective diameter changes with latitude. Cirrus clouds have the greatest average effective diameters in the tropical regions (~150 μm), middle average effective diameters in midlatitude regions (~130 μm), and smallest average effective diameters in the polar regions (~70 μm). Effective diameters of cirrus clouds have day versus night variation. Table 6.1 shows that cirrus clouds have greater effective diameters at nighttime than at daytime in almost all latitude regions, except in the northern polar region.

Table 6.1 Zonal average effective diameter

Eff. D represents the effective diameter, and the unit of the effective diameter is μm.

Latitude, degree	Eff. D (day and night)	Eff. D (day)	Eff. D (night)
85S to 60S	53.49	47.87	58.85
60S to 30S	126.60	118.75	134.03
30s to 15S	150.27	145.08	155.20
15S to 15N	148.22	142.52	153.62
15N to 30N	150.72	145.80	155.50
30N to 60N	132.06	126.96	137.08
60N to 85N	89.09	93.87	81.95

Seasonal variation of the effective diameter of cirrus clouds is presented in Figure 6.7, and annual zonal average effective diameter variation with season is illustrated in Figure 6.8. The effective diameter of cirrus clouds in the tropical and the subtropical regions do not have apparent seasonal change. In the northern polar region, effective diameters of continent cirrus clouds do have apparent seasonal change. The majority of continent cirrus clouds have small effective diameters (~20 to 40 μm) in DJF, with total zonal average effective diameter of ~65 μm; in summer JJA, the effective diameters of cirrus clouds in the same region are relative large (~110 to130 μm), with total zonal averaged effective diameter of ~120 μm. In summer, the higher surface temperature in the northern polar region yields an increased deposition of water vapor in the upper troposphere to support the growth of polar cirrus cloud, thus, the northern polar cirrus clouds have larger effective diameter values.

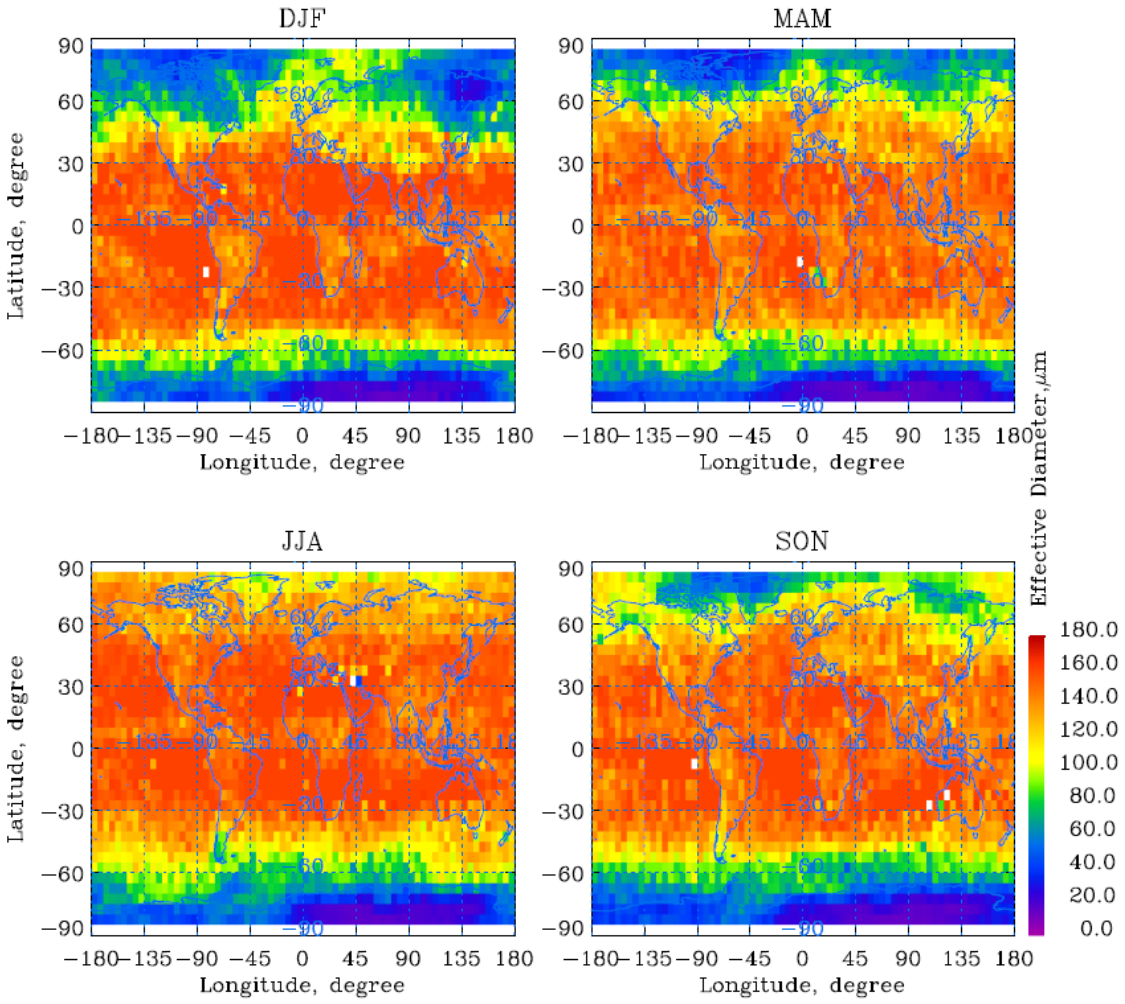

Figure 6.7 Seasonal variation of effective diameter global distribution

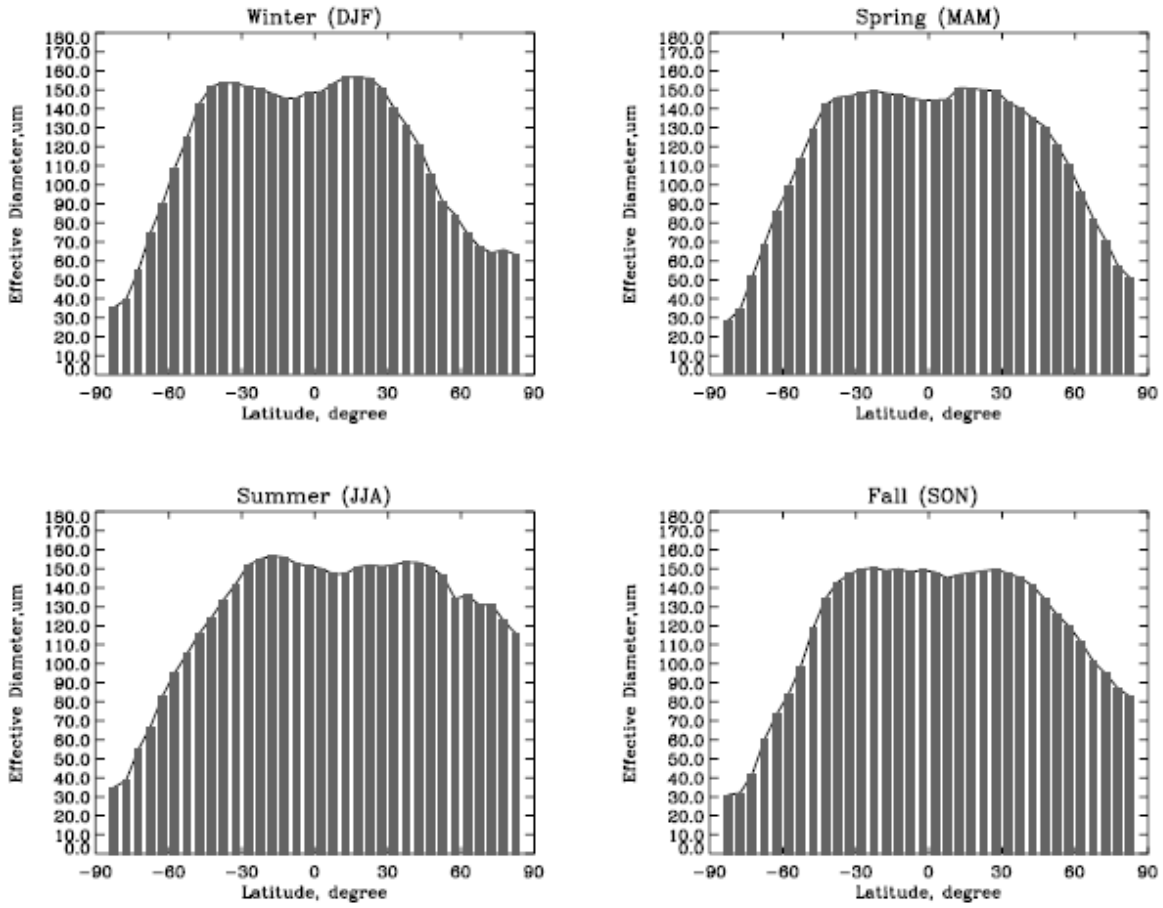

Figure 6.8 Seasonal variation of zonal average effective diameter

As shown in Figures 6.9 and 6.10, the monthly variation of the effective diameter of cirrus clouds is great (from ~60 μm in DJF to ~ 130 μm in JJA) in the northern polar region but small in the southern polar region. The Arctic Ocean experiences freezing in winter and melting in summer. Air over this region is very dry in DFJ, but not in JJA. The ice water content of cirrus clouds over this region has a great seasonal variation.

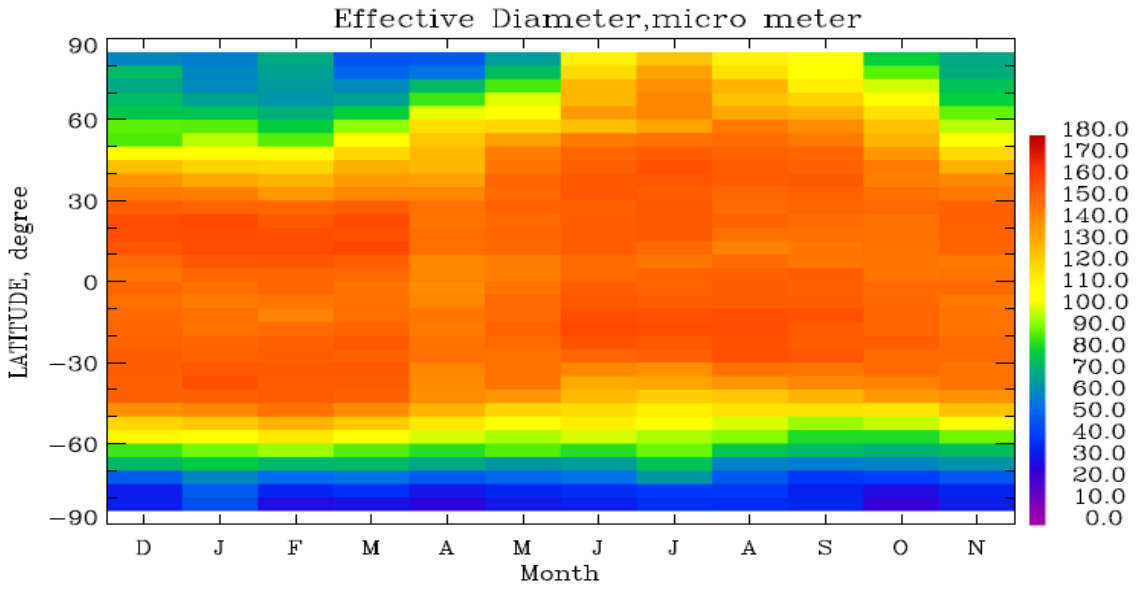

Figure 6.9 2007 monthly variation of average effective diameter

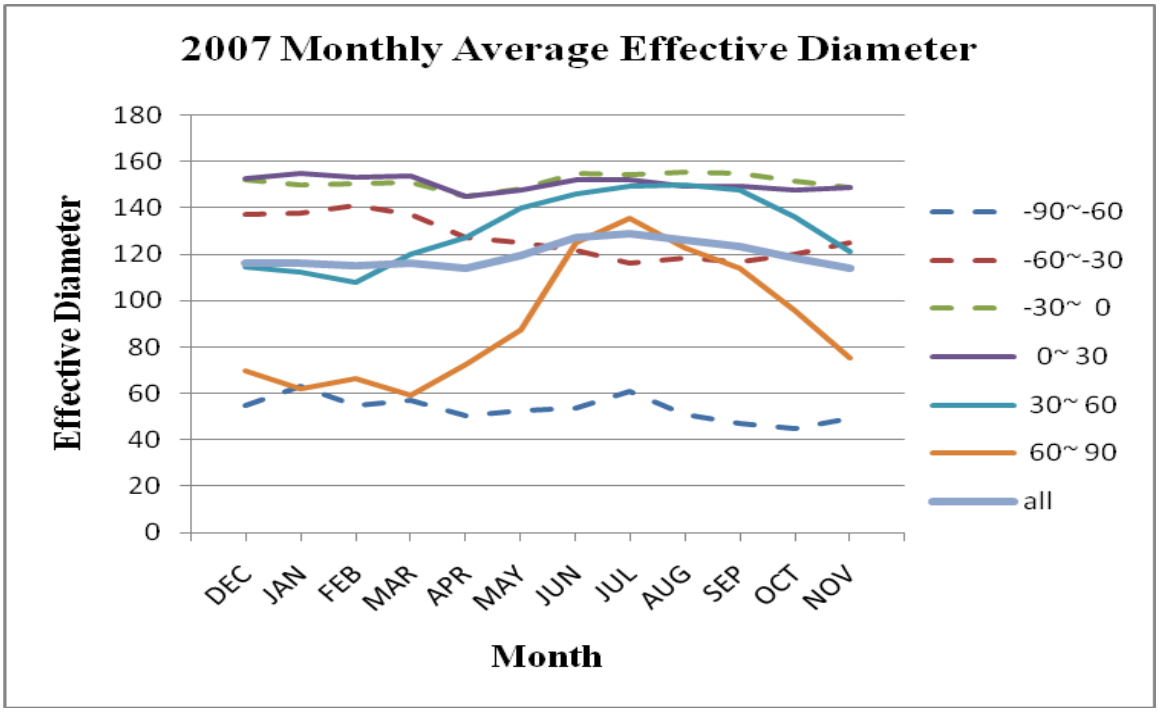

Figure 6.10 2007 monthly variation of zonal average effective diameter

Ice crystal shape of cirrus clouds over this region do not have great variation, so the great seasonal variation of ice water content of cirrus clouds over this region results in great seasonal variation of effective diameters of cirrus clouds. The Antarctic is covered by snow year-round, and the atmospheric environment does not have great variation, so the ice water content of cirrus clouds over this region does not have great monthly variation, and ice crystal shape of cirrus clouds over this region varies some. Therefore, the effective diameter of cirrus clouds over the southern polar region shows little monthly variation.

The effective diameter of cirrus clouds in both midlatitude regions experiences monthly variation (from ~110 μm to ~ 150 μm in the northern midlatutude region and from ~120 μm to ~140 μm in the southern midlatitude region). The effective diameters in tropical regions are greatest (~ 150μm), and do not have variation over the year. Because there are more land covers in the northern midlatitude region, atmospheric circulation is much more complicated, so, cirrus clouds in this region have more abundant types. As a result, the effective diameter of cirrus clouds in the region varies within a year.

Strong convergence in the ITCZ pushes moist air up into the high troposphere, the ice crystals in cirrus clouds over the ITCZ have greater size than those over other tropical regions, while the ice water content of cirrus clouds over all tropical regions does not have great variation, as a result, the effective diameters of cirrus clouds over the ITCZ are slightly smaller than those over other tropical regions. In Figure 6.9, one can observe the smaller effective diameters of cirrus clouds over the ITCZ and the migration pattern of the ITCZ.

6.3 Effective Diameter and Average LDR of Cirrus Clouds

As we know, the LDR of cirrus clouds reflects the information of ice crystal shapes in these clouds; the effective diameter is affected by the shape information of ice crystals. Thus, LDR and effective diameter of cirrus clouds are related. Figures 4.12, 5.10, and 6.9 exhibit the monthly variation of the macro-physical properties, linear depolarization ratio, and effective diameter of cirrus clouds, respectively. Cirrus clouds in the tropical and subtropical regions are consistent within a single year: cloud heights, LDRs, and effective diameters keep almost the same values; while mid-latitude cirrus clouds experience some variation, the most variation occurs in the polar regions.

The statistical results for cloud amount, cloud thickness, linear depolarization ratio, and effective diameter of cirrus clouds in the polar regions are listed in Table 6.2. In the northern polar region, cirrus cloud amount, cloud thickness, and LDR are greater in winter than in summer. However, the effective diameter is smaller in winter than in summer, because the ice water content of cirrus clouds over the northern polar region is smaller in winter than in summer. Cirrus clouds in the southern polar region have a similar variation pattern as the northern polar cirrus clouds with the exception that effective diameters do not have significant variation over a year. The reasons for this exception is that the ice water content of cirrus clouds over the southern polar region does not vary significantly over a year, and the ice crystal shape of cirrus clouds does not vary greatly, so the variation of the effective diameter is small over a year.

Table 6.2 Seasonal variation of cirrus cloud in the polar regions

loc., season / property	Northern Polar Cirrus Clouds		Southern Polar Cirrus Clouds	
	Winter(DJF)	Summer(JJA)	Summer(DJF)	Winter(JJA)
Amount (%)	35	14	15	42
Thickness (km)	3.5	1.8	1.6	3.9
LDR	0.33	0.28	0.26	0.35
Eff. Diameter(um)	65.0	110.0	40.0	40.0

6.4 Effective Diameter and Emissivity

As pointed out in section 6.1, the effective diameter influences the radiative effects of clouds, because clouds with different effective diameters have different albedo values and emissivity values. The effective emissivity of clouds is defined by Equation 3.3. Emissivity of clouds represents the ability of emitting longwave radiation by clouds. Figure 6.11 shows the global distribution of effective emissivity of cirrus clouds at 12.05 micro-meter wavelength. The distribution of cloud emissivity has band pattern. Cirrus clouds with great emissivity values (> 0.5) occur over midlatutude regions. Figure 6.11 also shows the emissivity of cirrus clouds varies with location. Cirrus clouds have small emisivities in the west coast of central-south America, west coast of South Africa, Arabia, and the west coast of Australia. By studying the bottom panel in Figure 4.3, one can find that the global distribution of cloud thickness has similar pattern with the global

distribution of cloud emissivity. For example, over previous mentioned regions where cloud emissivity is small, cloud thickness is also small.

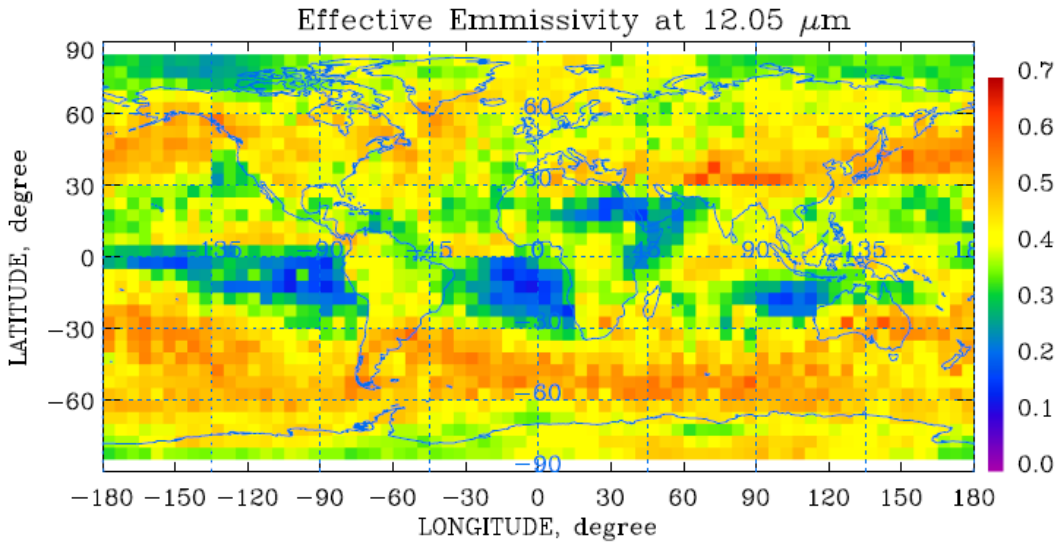

Figure 6.11 2007 annual average effective emissivity of cirrus clouds

By comparing Figure 6.10 with Figure 6.5, one can conclude that the effective diameter of cirrus clouds do not have strong impact on the effective emissivity of cirrus clouds. This finding tells us that effective diameter and emissivity of cirrus clouds have a certain relationship, but cloud thickness has a primary impact on effective emissivity of cirrus clouds. Actually, the emissivity of clouds is derived by the ice water path and the effective diameter of cirrus clouds (Garrett *et al.*, 2002). Ice water path is defined as the integration of ice water content through cloud thickness. This means that emissivity of clouds is basically a function of cloud thickness. In other words, macro-physical properties of clouds play a major role in deciding radiative properties of clouds.

Chapter 7 Conclusions

This research investigates cirrus clouds globally. The frequency of occurrence, cloud-top height, cloud-top temperature, cloud thickness, LDR, and effective diameter of cirrus clouds are analyzed.

The datasets used in this research are from the CALIPSO satellite. They are: lidar level 1 profile dataset, lidar level 2 cloud layer dataset, and IIR/lidar track dataset. In each dataset, half-orbit data are organized in separated files. First, the cirrus cloud identification algorithm is used to check these half-orbit data files. Second, one month of data is combined and grouped into 5 degree longitude by 5 degree latitude grids. The statistic theory is applied for error analysis. The error analysis indicates that error resulting from using the grid data to estimate the physical quantities is very small. For example, the error for estimating the frequency of occurrence of cirrus clouds in grids is 0.05 with 95% confidence. The frequency of occurrence, cloud-top height, cloud-top temperature, and cloud thickness in a grid is calculated by averaging the corresponding quantity of columns within the grid, respectively. The summed perpendicular and total attenuated backscatter profiles are obtained by summing up the perpendicular and total attenuated backscatter profiles in a grid, respectively. The average LDR profile of the grid is obtained by dividing the summed perpendicular attenuated backscatter coefficient profile by the summed parallel attenuated backscatter coefficient profile in the grid. The parallel attenuated backscatter coefficient is equal to the total attenuated backscatter coefficient minus the perpendicular backscatter coefficient. The lidar profiles have

various vertical resolutions. The average LDR of the grid is obtained by dividing the total perpendicular attenuated backscatters by the total parallel attenuated backscatters. The total perpendicular and parallel attenuated backscatter coefficient is calculated by weight-adding the summed perpendicular and parallel attenuated backscatter coefficient profiles, respectively. The effective diameter in the grid is estimated by the split-window method. The lookup table is produced by the radiative transfer model (Key and Schweiger, 1998). By analyzing the radiative transfer model simulation results, the relationship between the cloud radiative forcing and ice water content and effective diameter of clouds is investigated. Three other relations are analyzed. These relations are: LDR and the temperature of cirrus clouds, the LDR and effective diameter of cirrus clouds, and the effective diameter and effective emissivity of cirrus clouds.

The frequency of occurrence of cirrus clouds varies with latitude and location. Cirrus clouds occur mostly in the Inter-tropical Convergence Zone (ITCZ). Cirrus cloud coverage of up to ~60% appears at central southern America, western Africa, Indonesia, and the west-central Pacific Ocean warm pool. Between mid-latitude and subtropical regions, cirrus clouds occur very infrequently. The frequency of occurrence of cirrus cloud experiences seasonal variation. The most apparent seasonal variation occurs in ITCZ. Cirrus clouds occur in the southern hemisphere side in winter, and they shift back to the northern hemisphere side in summer. Annual average frequency of occurrence of cirrus cloud globally is about 27%. The cloud-top height of cirrus clouds decreases with the increase of latitude. The annual average cloud-top height of cirrus clouds is about 14, 10, and 8 km, in tropical, mid-latitude, and polar regions, respectively. The cloud-top

temperature of cirrus clouds increases with the increase of latitude within tropical and midlatitude regions. Large amounts of PSCs with cold cloud-top temperature occur in the southern polar region. The annual average cloud-top temperature is -63, -52, and -53ºC in tropical, mid-latitude, and polar regions, respectively. The cloud thickness does not show apparent variation with latitude. The annual average cloud thickness is 2.1, 2.3, and 2.5 km in tropical, mid-latitude, and polar regions, respectively. The monthly variations of cloud-top height, cloud-top temperature, and cloud thickness are small. The measured diurnal variations of frequency of occurrence (24% day and 30% night), cloud-top height (11.0 km day and 11.3 km night), and cloud-top temperature (-59ºC day and -65 ºC night), are small, but measured diurnal variation of cloud thickness (2 km day and 3 km night) is great. The annual average frequency of occurrence of cirrus clouds derived by the CALIPSO (27%) is greater than that from the ISCCP measurement (16%). The CALIPSO-derived frequency of occurrence of cirrus clouds is close to that from the land surface observations (23%).

The average LDR values vary with latitude and height. Cirrus clouds have the greatest average LDR value (0.36) in tropical regions, the middle average LDR values (0.31) in midlatitude regions, and the small average LDR value (0.28) in polar regions. LDR values of cirrus clouds increase with the increase of cloud height (about 0.1 at cloud base and 0.44 at cloud top). In the southern polar region, the average LDR value of PSCs varies in a small-large-small cycle (about 0.26 in the height range from 12 to 17 km, 0.4 in the height range from 17 to 25 km, and 0.1 above the height of 25 km). The average LDR values of cirrus clouds are measured with day versus night variation (0.33 at

daytime and 0.31 at nighttime). The average LDR is 0.29, 0.29, 0.30, and 0.30 in DJF, MOM, JJA, and SON, respectively. Both diurnal and seasonal variations are not significant. LDRs derived by nadir measurement (0.32) are smaller than those derived by off-nadir measurements (0.37). The effective diameter of cirrus clouds decreases with the increase of latitude. The average effective diameter is about 150, 130, and 70 μm in tropical, midlatitude, and polar regions. The effective diameter of cirrus clouds in the northern polar region varies significantly over a year. The average effective diameter of cirrus clouds in the northern polar region is 65 and 130 μm in DJF and JJA, respectively. Maritime cirrus clouds usually have greater effective diameters than nearby continental cirrus clouds. The effective diameter of clouds impacts the effective emissivity of these clouds. Compared to the impact of macro-physical properties of clouds on the effective emissivity of clouds, the impact from the effective diameter is small.

The macro-physical properties of cirrus clouds are determined by atmospheric circulation. The strong convergence of air in the ITCZ produces large amount of cirrus clouds. The surface pressure pattern is closely related to the frequency of occurrence of cirrus clouds. Low pressure dominates where the cirrus clouds occur the most frequently. Cirrus clouds occur rarely in the subtropical regions where the high pressure of Hadley circulation depresses air. The migration of the ITCZ results in the great seasonal variation of cirrus clouds over this region. The northern hemisphere has more land cover than the southern hemisphere, the seasonal variation of land-ocean temperature difference is greater in the northern hemisphere than in the southern hemisphere, therefore, the seasonal variation of macro-physical properties of cirrus clouds in the northern

hemisphere is greater than in the southern hemisphere. The measured diurnal variation of macro-physical properties of cirrus clouds is caused by a measurement error. Because strong background noise is introduced in both parallel and perpendicular return signals, daytime measurements miss some very thin cirrus clouds, and miss some cloud-top and cloud-base of cirrus clouds. The CAIPSO measurement and land surface observation include the PSCs, while the ISCCP measurement does not. As a result, the derived frequency of cirrus clouds at high latitude regions is much greater from the CALIPSO measurement and land surface observation than from the ISCCP measurement. For deriving the cloud-top height and cloud thickness, an active lidar remote sensing is far more accurate than a passive remote sensing because lidar directly measures the return power from clouds, while a passive measurement needs to retrieve the cloud-top and cloud thickness based on the measured radiance.

Cirrus clouds form based on different formation mechanics in tropical and midlatitude regions. Tropical cirrus clouds form based on convection and convergence. Both convection and convergence push the moist air up into the higher troposphere, where cirrus clouds form and grow with abundant water vapor, so ice crystals in these cirrus clouds have great and complicated shapes. Because midlatitude cirrus clouds form based on synoptic weather phenomena, the ice crystals of cirrus clouds in midlatitude regions have smaller and simpler shape than in tropical regions. As a result, the LDRs of tropical cirrus clouds are greater than those of midlatitude cirrus clouds. LDR reflects the shape information of ice crystals in cirrus clouds. Ice crystal shape of cirrus clouds is a function of cloud temperature and super-saturation density. The ice crystals vary from

simple shapes to complicated shapes to simple shapes with temperature. At a given temperature, the shapes of ice crystals increase in complexity with the increase of super-saturation density. This research indicates the correctness of the theory that the ice crystal shape is a function of temperature and supper-saturation density. There are always some horizontal-orientated ice crystals in cirrus clouds. When a polarized lidar light hits these ice crystals, the perpendicular backscatter signal is almost zero, thus, the LDR is almost zero. In the nadir measurement, lidar vertically points to the horizontal plane of the surface of earth, i.e., lidar light vertically hits the horizontal-orientated ice crystal surface, so the LDR derived by nadir measurement is smaller than that derived by off-nadir measurement.

The cloud radiative forcing is impacted by the ice water content and effective diameter of clouds. When the effective diameter is small (< 40 μm), the cloud radiative forcing is very sensitive to the variation of the effective diameter. When the effective diameter is large (> 40 μm), the ice water content has greater impact on the cloud radiative forcing than the effective diameter. The effective diameter of clouds is proportional to the ice water content and reverse proportional to the total projection area of size distribution of clouds. Cirrus clouds in tropical regions have comparable ice water content with midlatitude cirrus clouds, but ice crystals in the tropical cirrus clouds are greater than those in the midlatitude cirrus clouds. As a result, the effective diameter of cirrus clouds is greater over the tropical regions than over midlatitude regions. The ice water content of polar cirrus clouds is much smaller than that of tropical and midlatitude cirrus clouds. Therefore, the effective diameter of cirrus clouds is smaller in polar regions

than in tropical and midlatitude regions. The Arctic Ocean experiences large variation within a year. In summer, the higher surface temperature in the northern polar region yield to increased deposition of water vapor in the upper troposphere to support the growth of polar cirrus cloud, thus, the northern polar cirrus clouds have larger effective diameter values. Maritime cirrus clouds are composed of larger ice crystals than nearby continental cirrus clouds, while the ice water contents of these two clouds are comparable. As a result, the effective diameter of maritime cirrus clouds is greater than that of nearby continental cirrus clouds. The effective emissivity of clouds is derived by ice water path and effective diameter of these clouds. Ice water path is the integration of the ice water content with cloud thickness. Cloud thickness has a far stronger impact than the effective diameter on the effective emissivity of clouds.

This research uses active Lidar measurement on a satellite platform. It has profound benefits in revealing the vertical structure and providing a global view of clouds. Passive global measurements and research have accumulated large amounts of data and achievements. Combining active remote sensing with passive remote sensing is an important method in cloud research.

References

Allan, R. J. and T. J. Ansell, 2006: A new globally complete monthly historical mean sea level pressure data set (HadSLP2): 1850-2004. *Journal of Climate*, **19**, 5816-5842.

Andrews, D. G., 2000: *An Introduction to Atmospheric Physics.* Cambridge University Press, 229 pp.

Anselmo, T., R. Clifton, W. Hunt, K. P. Lee, T. Murray, K. Powell, S. D. Rodier, M. Vaughan, O. Chomette, M. Viollier, O. Hagolle, A. Lifermann, A. Garnier, J. Pelon, J. C. Currey, M. Pitts, and D. Winker, 2007: Cloud -Aerosol LIDAR Infrared Pathfinder Satellite Observations Data Management System Data Products Catalog. Release 2.4, Document No: PC-SCI-503, 100 pp.

Baum, B. A., A. J. Heymsfield, P. Yang, S. T. Bedka, 2005: Bulk Scattering Properties for the remote Sensing of Ice Clouds, Part I: Microphysical Data and Models, *J. Appl. Meteor*., **44**, 1885-1895.

Baum, B. A., P. Yang, A. J. Heymsfield, and C. Schmitt, cited 2011: The development of ice cloud scattering models for use in remote sensing applications. [available online at http://www.ssec.wisc.edu/~baum/Cirrus/IceCloudModels.html]

CALIPSO, NASA, cited 2011: Lidar Browse Images for Production Release [v3-01]. [http://www-calipso.larc.nasa.gov/]

Chandrasekhar, S., 1960: *Radiative Transfer*, 14th ed., Dover Publications, 393 pp.

Charlock, T. P., and V. Ramanathan, 1985: The albedo field and cloud radiative forcing produced by a general circulation model with internally generated cloud optics. *J. Atmos. Sci.*, **42**, 1408-1429, 1985.

Chomette, O., A. Garnier, A. Lifermann, and J. Pelon, 2003: Retrieval of cloud emissivity and particle size in the frame of the CALIPSO mission. *Proc. IGARSS '03,*Toulouse, France, IEEE International, 1520–1522.

Earth System Research Laboratory, NOAA, cited 2011: HadSLP2 (andHadSLp2r) [*http://www.esrl.noaa.gov/psd/gcos_wgsp/Gridded/data.hadslp2.html*]

Ellis, J. S., and T. H. VonderHaar, 1976: Zonal average radiation budget measurements from satellites for climate studies. Atmospheric Science Paper 240, Dept. of Atmospheric Sciences, Colorado State University, 57 pp.

Fu, Q., and K. N. Liou, 1992: Parameterization of the radiative properties of cirrus clouds. *Journal of the atmospheric sciences*, **50**, 2008-2025.

Garrett, T. J., F. R., Lawrence, and P. V. Hobbs, 2002: Aerosol Effects on Cloud Emissivity and Surface Longwave Heating in the Arctic. *J. Atmos. Sci.*, **59**, 769–778.

Hahn, C. J., and S. G. Warren, 1999: Extended Edited Cloud Reports from Ships and Land Stations over the Globe, 1952-1996. Numerical Data Package NDP-026C, Carbon Dioxide Information Analysis Center (CDIAC), Department of Energy, Oak Ridge, Tennessee ,79 pp. [http://cdiac.ornl.gov/epubs/ndp/ndp026c/ndp026c.html]

Hostetler, C. A., Z. Liu, J. Reagan, M. Vaughan, D. Winker, M. Osborn, W. H. Hunt, K. A. Powell, and C. Trepte, 2006: CALIOP Algorithm Theoretical Basis Document Calibration and Level 1 Data Products, PC-SCI-201, Release 1.0, 66 pp.

Inoue, T., 1985: On the temperature and effective emissivity determination of semi-transparent cirrus clouds by bispectral measurements in the 10 microns windows region. *J. Meteor. Soc. Japan*, **64**, 88-99.

Key, J. R., 2002: Streamer version 3.0 User's Guide. 60 pp.

Key, J., and A. Schweiger, 1998: Tools for atmospheric radiative transfer: Streamer and FluxNet. *Comput. Geosci*., **24**, 443-451.

Khairoutdinov, M. F., and D. A. Randall, 2001: A cloud resolving model as a cloud parameterization in the NCAR community climate system model: preliminary results. *Geophys. Res. Lett.*, **28**, 3617-3620.

Kiehl, J, T., and K. E. Trenberth, 1997: Earth's Annual Global Mean Energy Budget. *Bull. Amer. Meteor. Soc.*, **78**, 197-208.

Klett, J. D., 1981: Stable analytical inversion solution for processing lidar returns. *Appl. Opt.,* **20,** 211-220.

Libbrecht, K. G., cited 2011: A snowflake Primer. [http://www.its.caltech.edu/~atomic/snowcrystals/primer/primer.htm]

Liou, K. N., and H. Lahore, 1974: Laser sensing of cloud composition: A backscattered depolarization technique. *J. Appl. Meteor.*, **13**, 257-263.

Lynch, D., 2002: Cirrus: History and definitions, *Cirrus*, D. K. Lynch, K. Sassen, D. O'C. Starr and G. Stephens, Eds., Oxford Univ. Press, New York, 3-10.

Mitchell, D. L., 2002: Effective Diameter in Radiation Transfer: General Definition, Applications, and Limitations, *J. Atmos. Sci.*, **59**, 2330-2346.

Mitchell, D. L., and W. P. Arnott, 1994: A model predicting the evolution of ice particle size spectra and radiative properties of cirrus clouds. Part II: Dependence of absorption and extinction on ice crystal morphology, *J. Atmos. Sci*., **51**:817-832.

Mitchell, D. L., R. P. Lawson, and B. Baker, 2011: Understanding effective diameter and its application to terrestrial radiation in ice clouds. *Atmospheric Chemistry and Physics*, **11**, 3417-3429.

Nasiri, S. L., B. A. Baum, A. J. Heymsfield, P. Yang, M. R. Poellot, D. P. Kratz, and Y. Hu, 2002: The Development of Midlatitude Cirrus Models for MODIS Using FIRE-I, FIRE-II, and ARM In Situ Data. *J. Appl. Meteor.*, **41**, 197–217.

Noel, V., D. M. Winker, M. McGill, and P. Lawson, 2004: Classification of particle shapes from lidar depolarization ratio in convective ice clouds compared to in situ observations during CRYSTAL-FACE. *J. Geophys. Res.*, **109**, D24213.

Noel, V., H. Chepfer, G. Ledanois, A. Delaval, and P. H. Flamant, 2002: Classification of particle effective shape rations in cirrus clouds based on the lidar depolarization ratio, *Applied Optics*,.**41**, 4245-4257.

Prauppacher, H. R., and J. D. Klett, 1997: *Microphysics of Clouds and Precipitation*. Kluwer, Dordrecht, Netherlands, 954 pp.

Sassen, K., 1976: Polarization diversity lidar returns from virga and precipitation: Anomalies and the bright band analogy. *J. Appl. Meteor.*, **15**, 292-300.

Sassen, K., 1991: The polarization lidar technique for cloud research: A review and current assessment. *Bull. Amer. Meteor. Soc.*, **72**, 1848-1866.

Sassen, K., 1994: Advances in polarization diversity lidar for cloud remote sensing. *Proc. IEEE*, **82,** 1907-1914.

Sassen, K., 2000: Lidar backscatter depolarization technique for cloud and aerosol Research. *Light Scattering by Nonspherical Particles: Theory, Measurements, and Geophysical Applications*, M. L. Mishchenko, J. W. Hovenier, and L. D. Travis, Eds., Academic Press, 393-416.

Sassen, K., 2002: Cirrus Clouds: A modern perspective. *Cirrus*, D. K. Lynch, K. Sassen, D. O'C. Starr and G. Stephens, Eds., Oxford Univ. Press, New York, 11-40.

Sassen, K., and B. S. Cho, 1992: Subvisual-thin cirrus lidar dataset for satellite verification and climatological research. *J. Appl. Meteor.*, **31,** 1275-1285.

Sassen, K., and J. R. Campbell, 2001: A midlatitude cirrus cloud climatology from the Facility for Atmospheric Remote Sensing. Part I: Macrophysical and synoptic properties. *J. Atmos. Sci.*, **58,** 481-496.

Sassen, K., and J. Zhu, 2009: A global survey of CALIPSO linear depolarization ratios in ice clouds: Initial findings. *J. Geophys. Res*., **114**, D00H07.

Sassen, K., and S. Benson, 2001: A midlatitude cirrus cloud climatology from the Facility for Atmospheric Remote Sensing. Part II: Microphysical properties derived from lidar Depolarization. *J. Atmos. Sci.*, **58,** 2103-2112.

Sassen, K., D. O'C. Starr, and T. Uttal, 1989: Mesoscale and microscale structure of cirrus clouds: Three cases studies*, J. Atmos. Sci*., **46**,371-396.

Sassen, K., Z. Wang, and D. Liu, 2008: Global distribution of cirrus clouds from CloudSat/Cloud-Aerosol Lidar and Infrared Pathfinder Satellite Observations (CALIPSO) measurements, *J. Geophys. Res.*, **113**, D00A12.

Sassen, K., Z. Wang, and D. Liu, 2009: Cirrus clouds and deep convection in the tropics: Insights from CALIPSO and CloudSat. *J. Geophys. Res.*, **114**, D00H06.

Schotland, R. M., K. Sassen, and R. J. Stone, 1971: Observations by lidar of linear depolarization ratios by hydrometeors. *J. Appl. Meteorol*. **10**, 1011-1017.

Shaw, G. E., 1996: *Clouds and Climate Change*, University Science Books, 21 pp.

Slingo, A., and H. M. Schrecker, 1982: On the shortwave radiative properties of straiform water clouds. *Quart. J. Roy. Meteor. Soc*., **108**, 407-426.

Stamnes, K., S. C. Tsay, W. Wiscombe, and K. Jayaweera, 1988: Numerically stable algorithm for discrete-ordinate-methodradiative transfer in multiple scattering and emitting layered media. *Applied Optics*, **27**, 2502-2509.

Stephens, G., S. C. Tsay, P. Stackhouse Jr., and P. Flatau, 1990: The relevance of the microphysical and radiative properties of cirrus clouds to climate and climate feedback, *J. Atmos. Sci*., **47**, 1742-1753.

Toon, O. B., C. P. McKay, and T. P. Ackerman, 1989: Rapid calculation of radiative heating rates and photodissociation rates in inhomogeneous multiple scattering atmospheres. *Journal of Geophysical Research*, **94**, D13, 16287–16301.

Van de Hulst, H. C., 1981: *Light Scattering by Small Particles*. Dover, 470 pp.

Weiss, N. A., 2008: *Introductory Statistics*. Person Custom Publishing, 846 pp.

Appendix A

This appendix includes many figures which supplement the research findings. The figures cover the monthly average frequency of occurrence, cloud-top height, cloud-top temperature, cloud thickness, LDR, and effective diameter of cirrus clouds, in terms of day and night in two years. They reveal the global variation patterns of the physical quantities within one year, as well as the variation patterns of the physical quantities at specific regions. Each figure includes 12-month monthly average of a physical property at daytime or at nighttime. The monthly average physical property from December to November of the next year is shown in the panels from top to bottom, and from left to right.

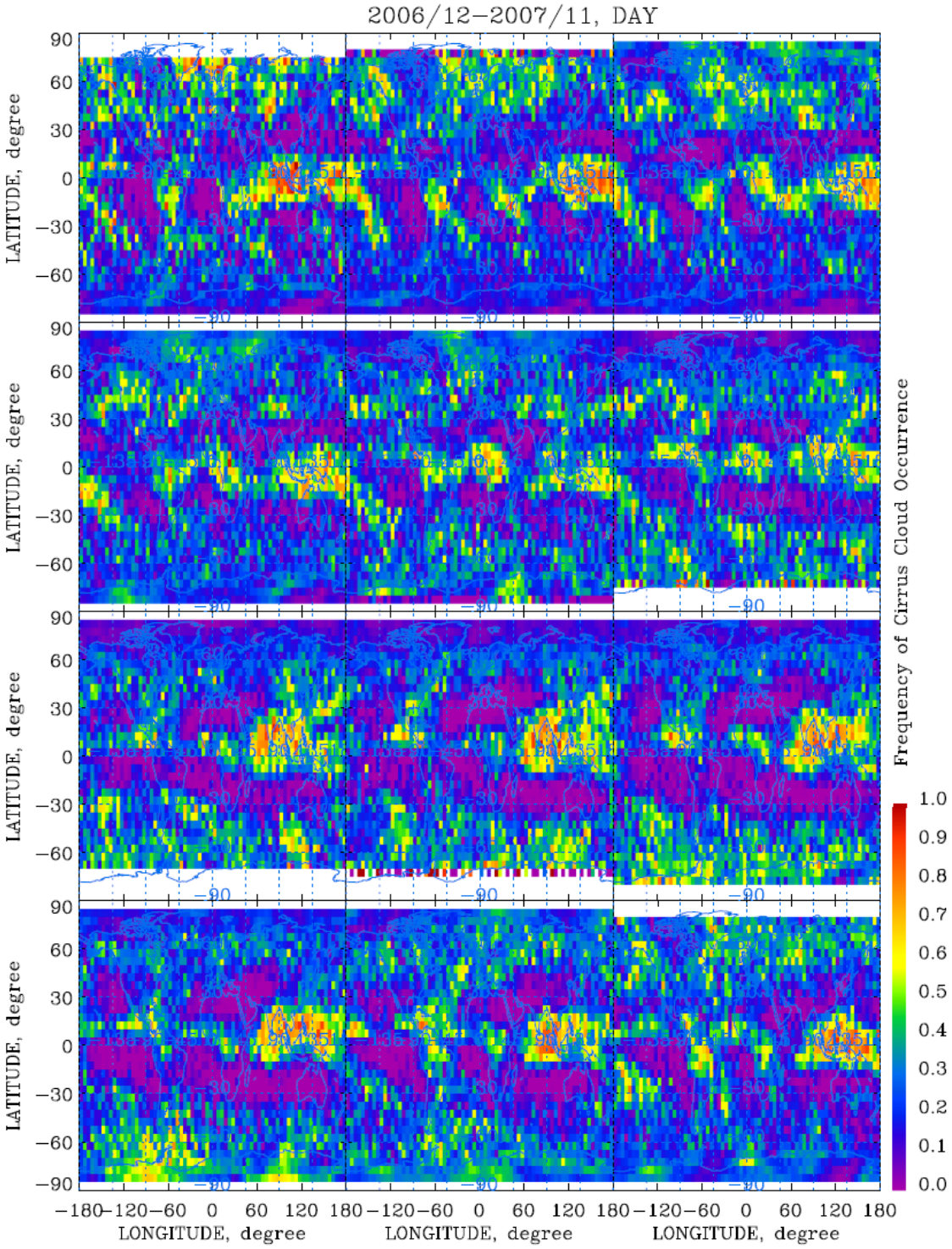

Figure A.1 2007 daytime monthly average frequency of occurrence

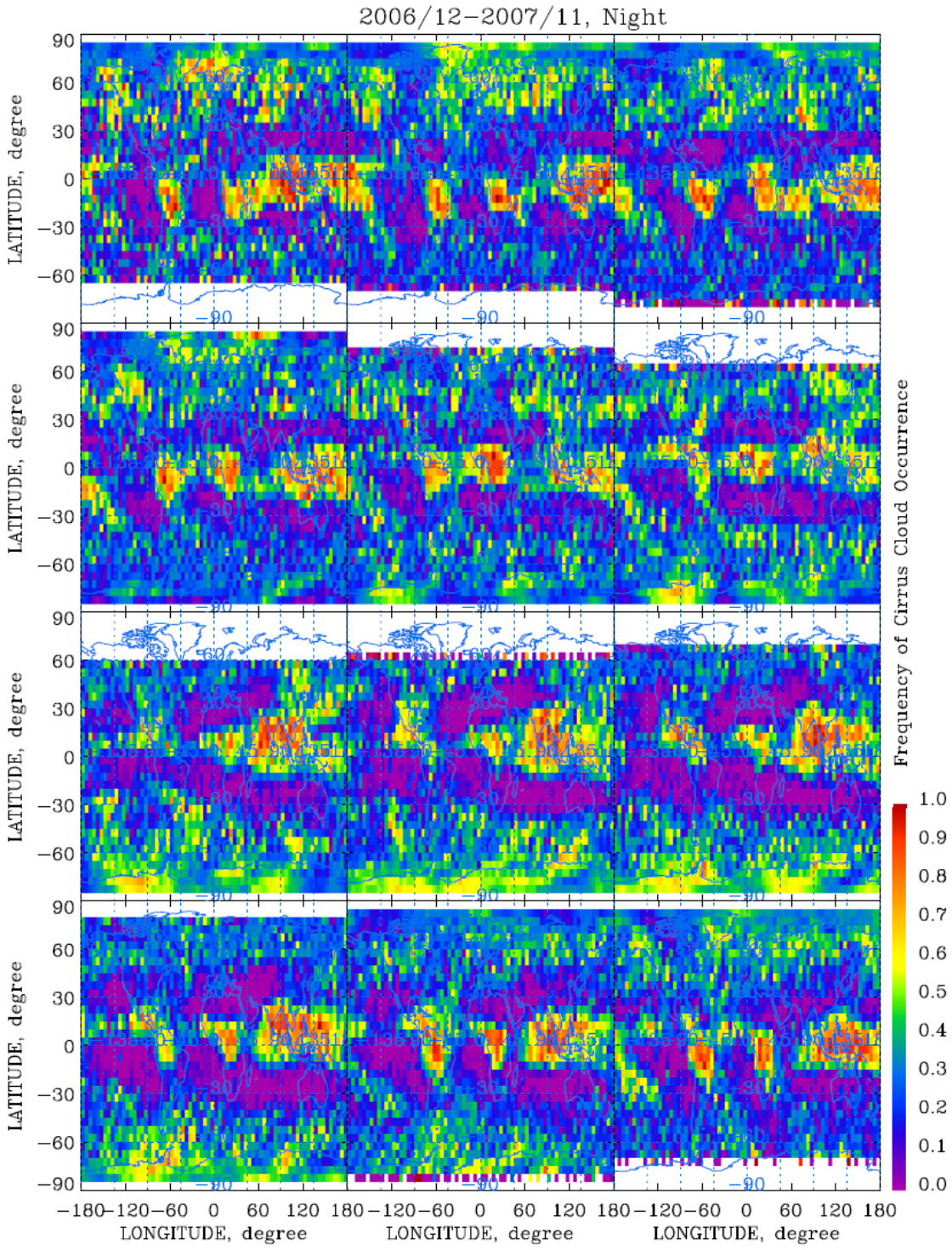

Figure A.2 2007 nighttime monthly average frequency of occurrence

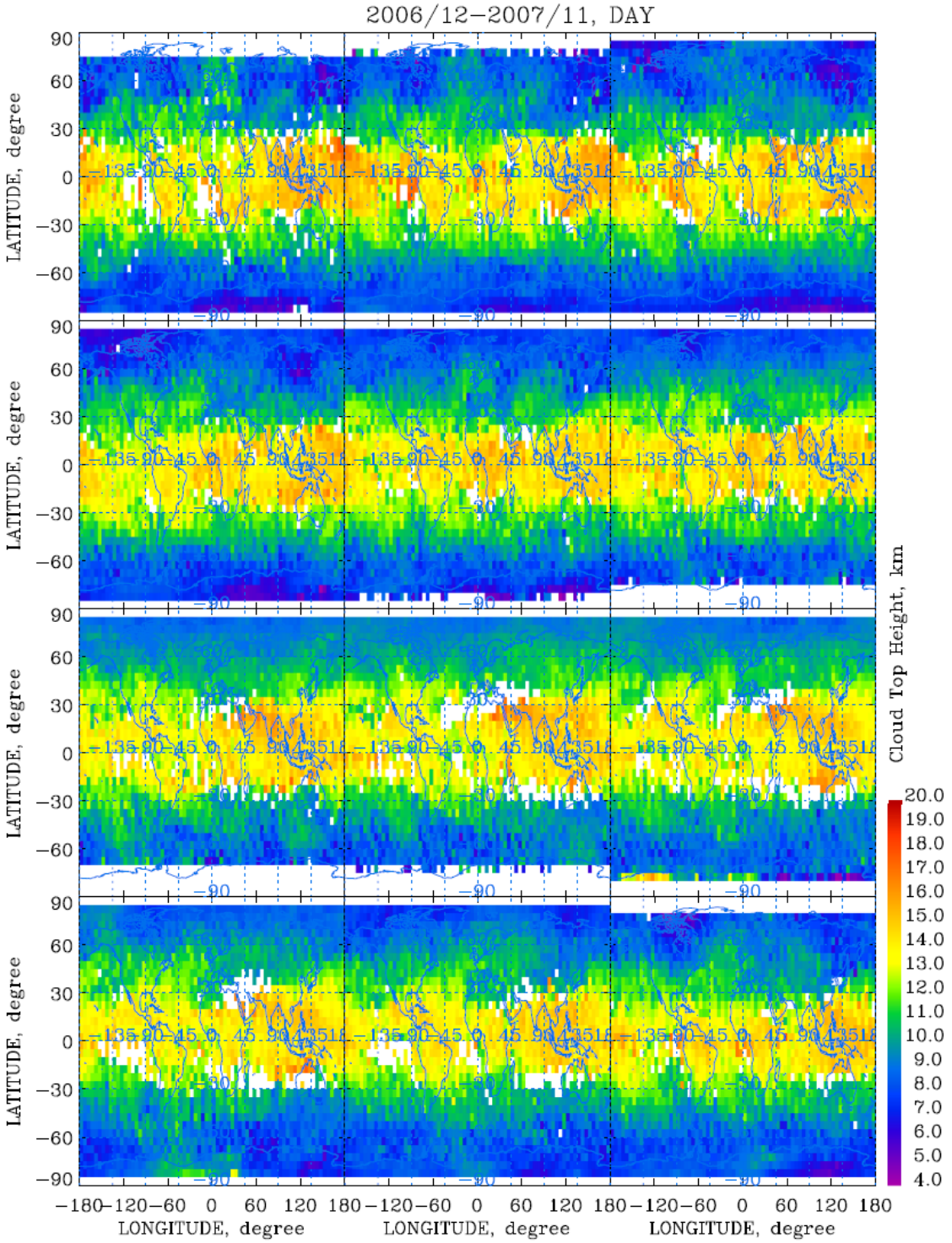

Figure A.3 2007 daytime monthly average cloud-top height

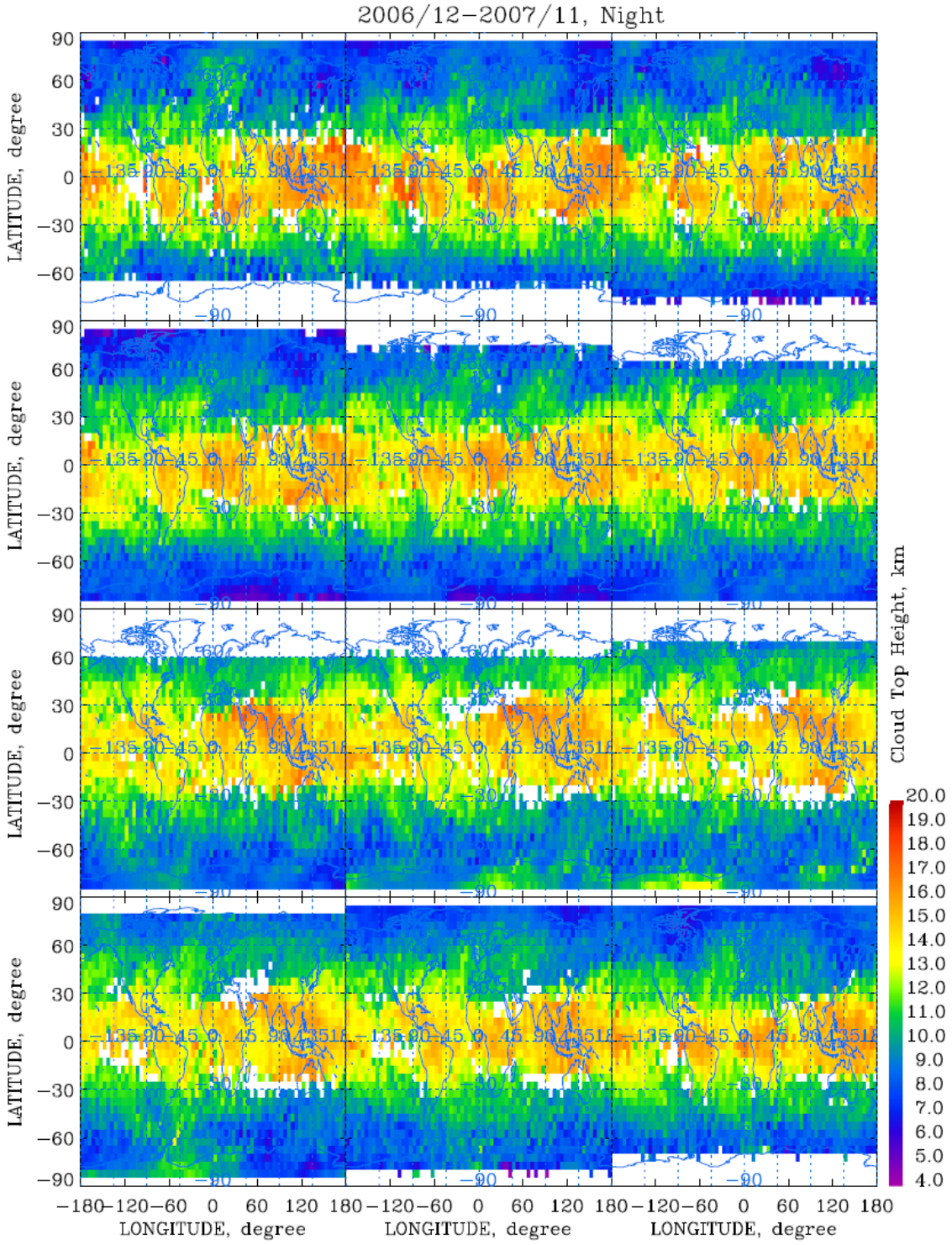

Figure A.4 2007 nighttime average cloud-top height

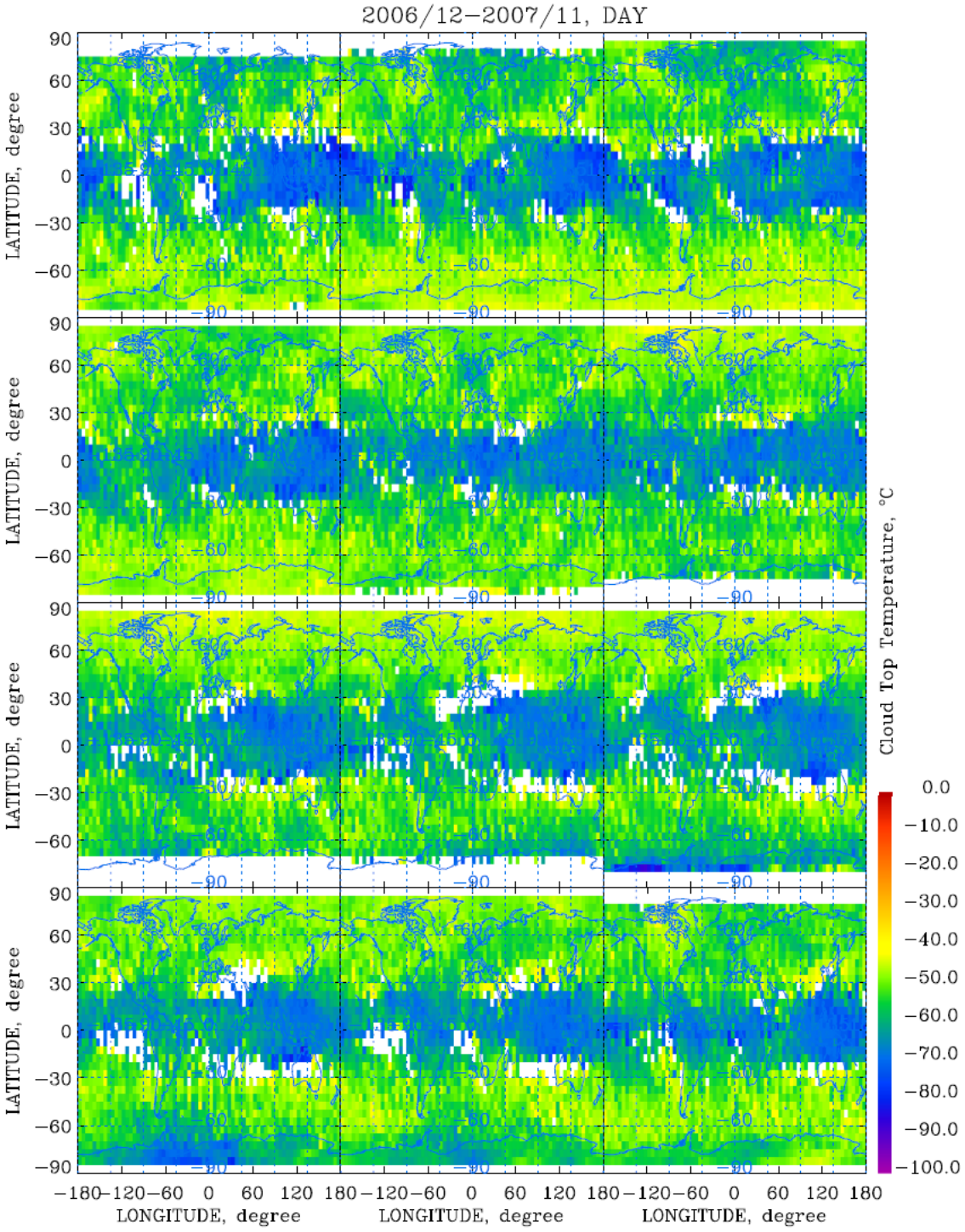

Figure A.5 2007 daytime monthly average cloud-top temperature

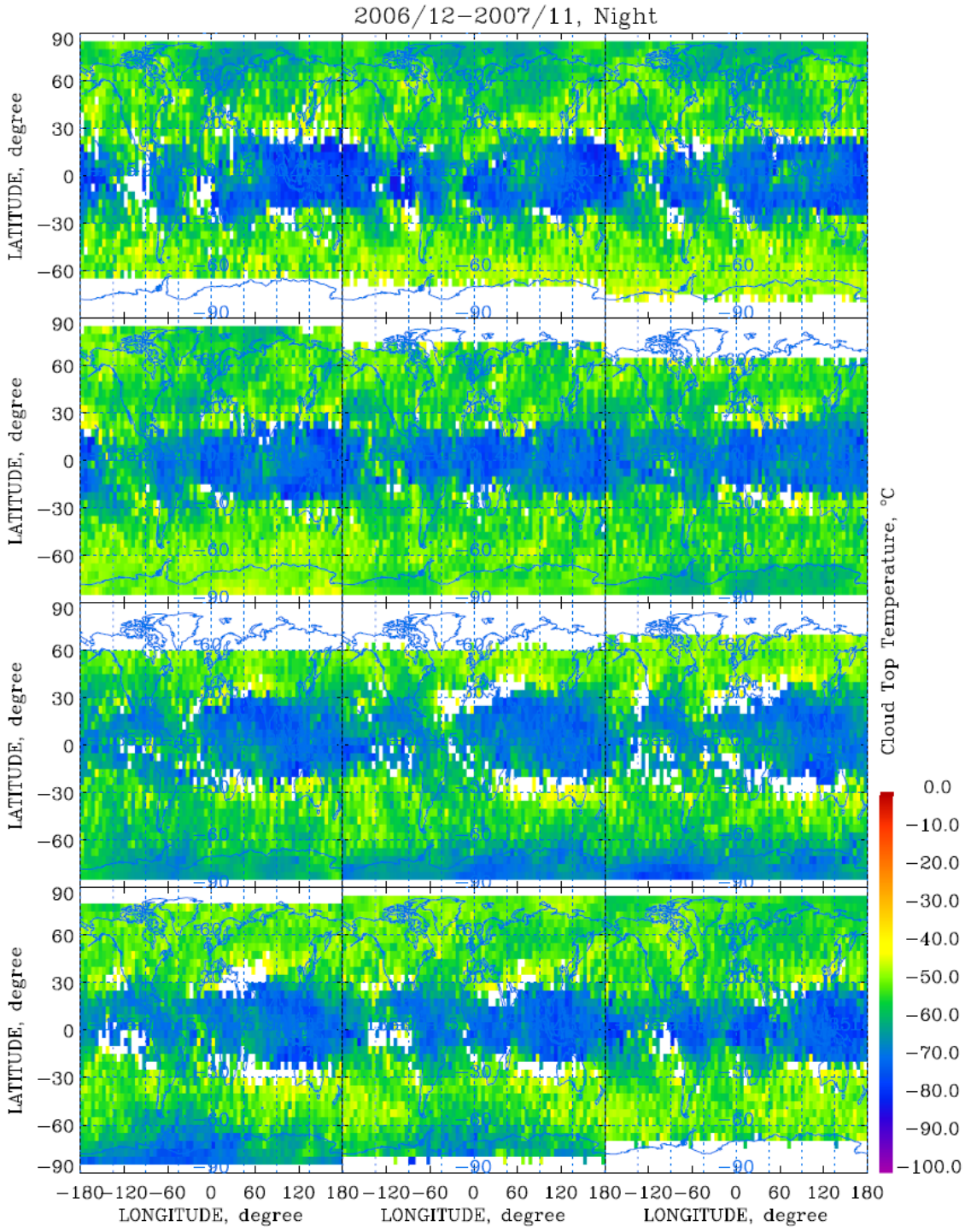

Figure A.6 2007 nighttime monthly average cloud-top temperature

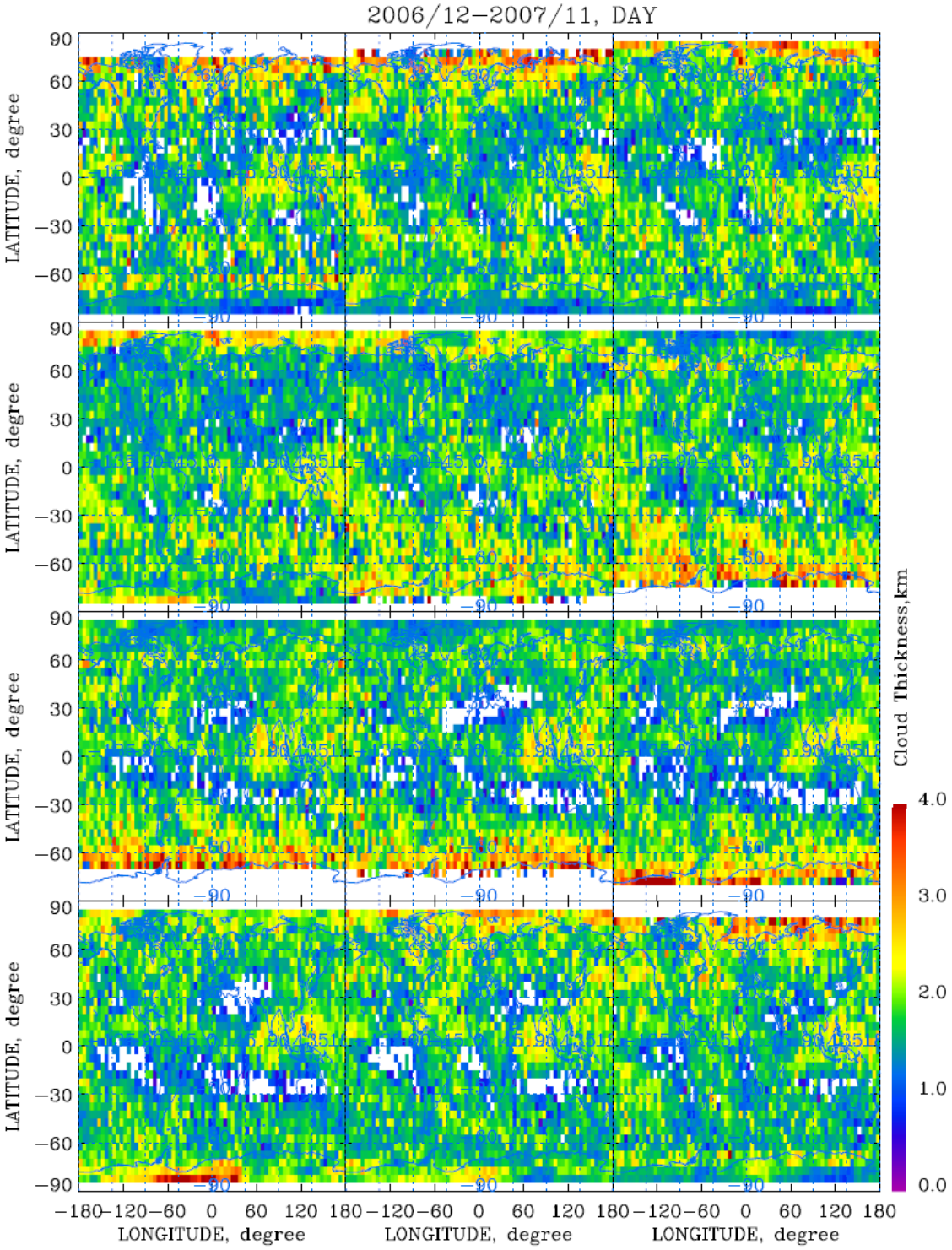

Figure A.7 2007 daytime monthly average cloud thickness

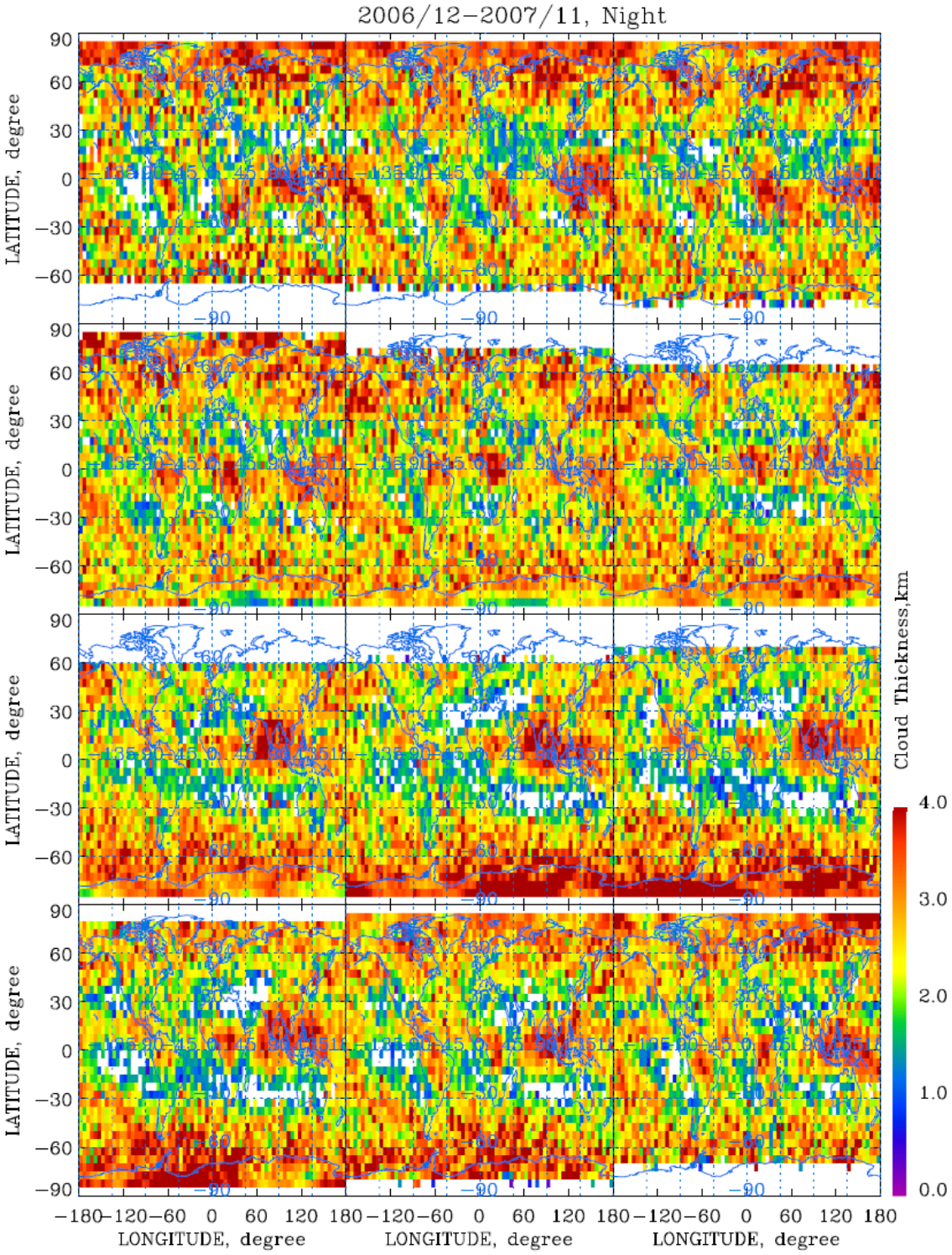

Figure A.8 2007 nighttime monthly average cloud thickness

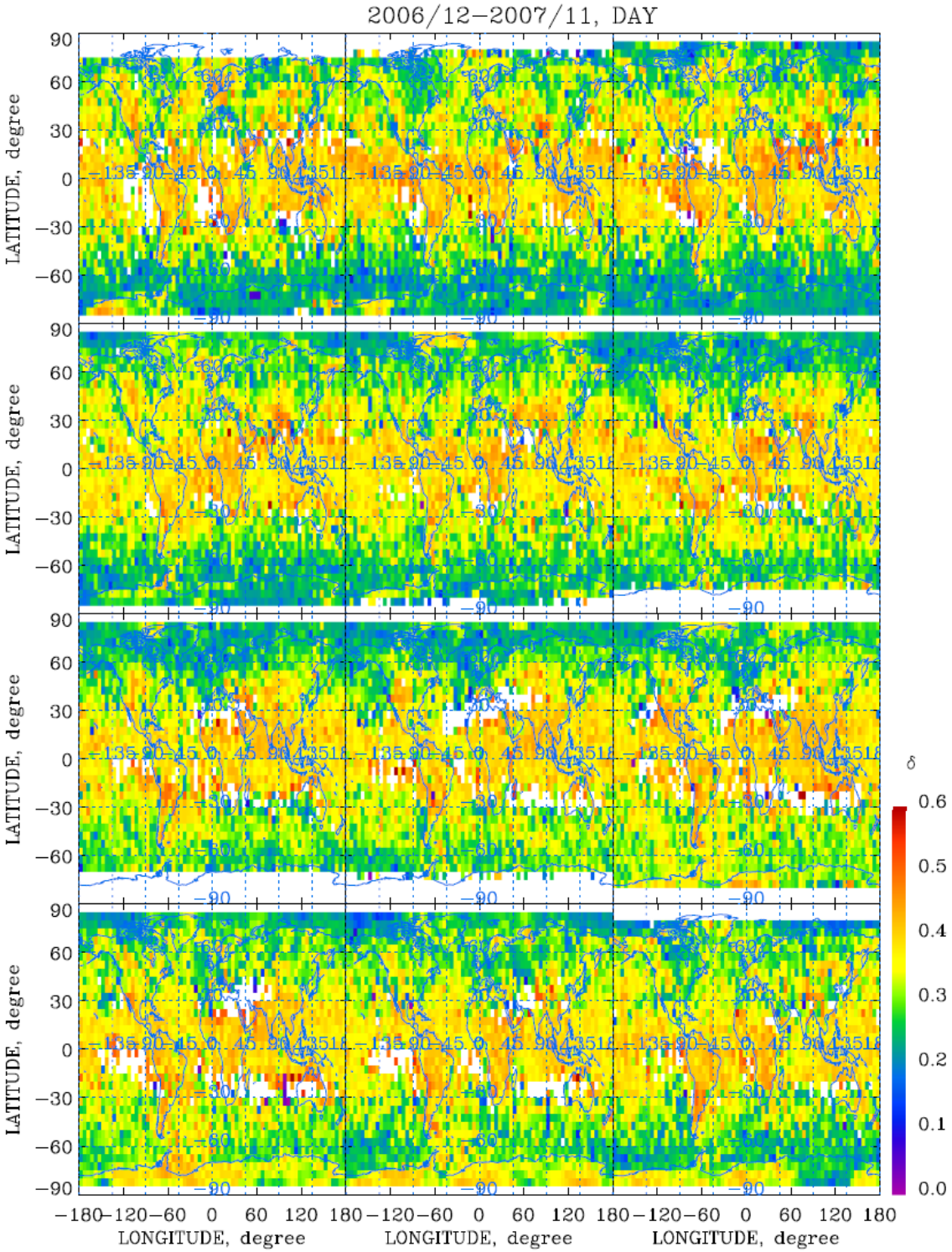

Figure A.9 2007 daytime monthly average LDR

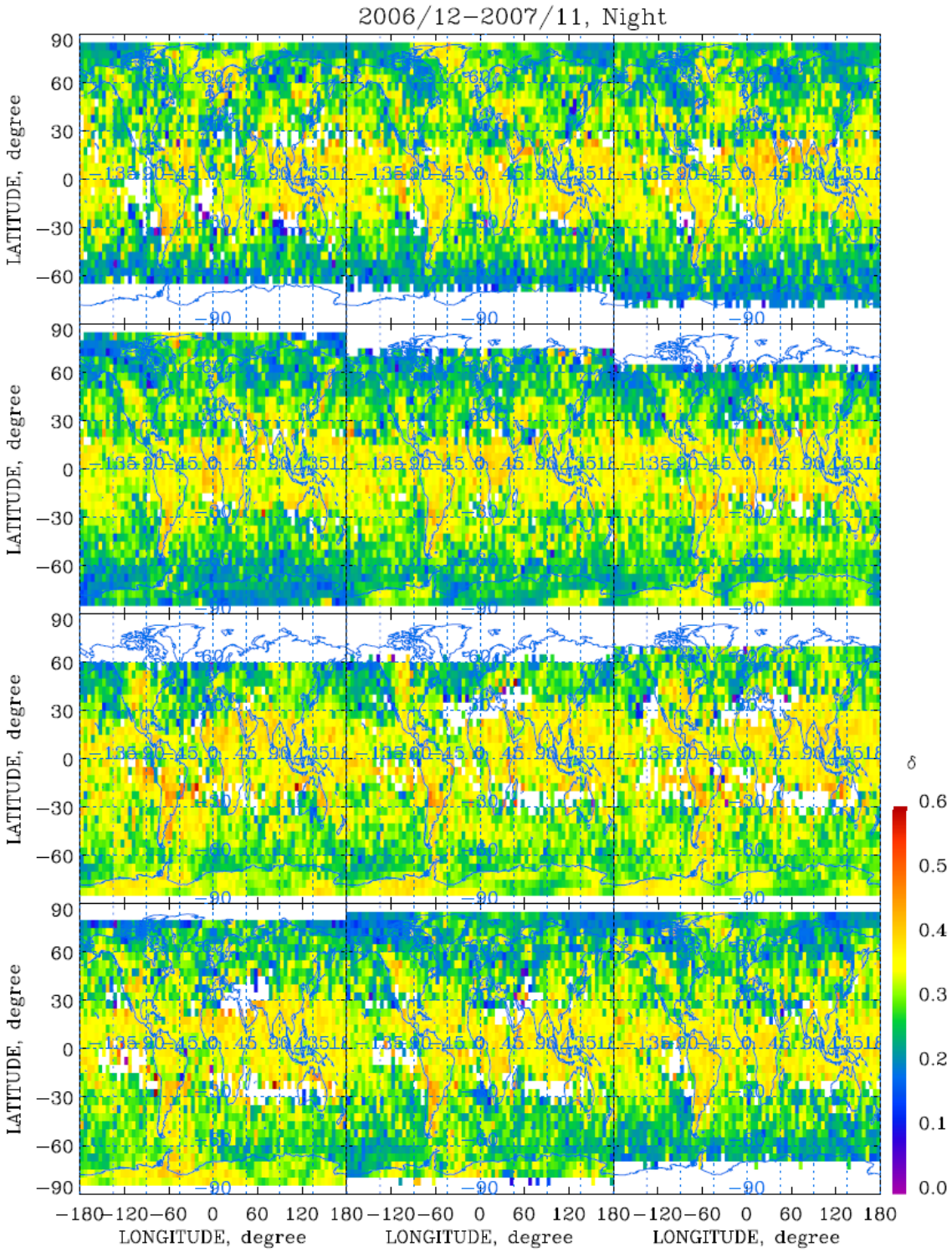

Figure A.10 2007 nighttime monthly average LDR

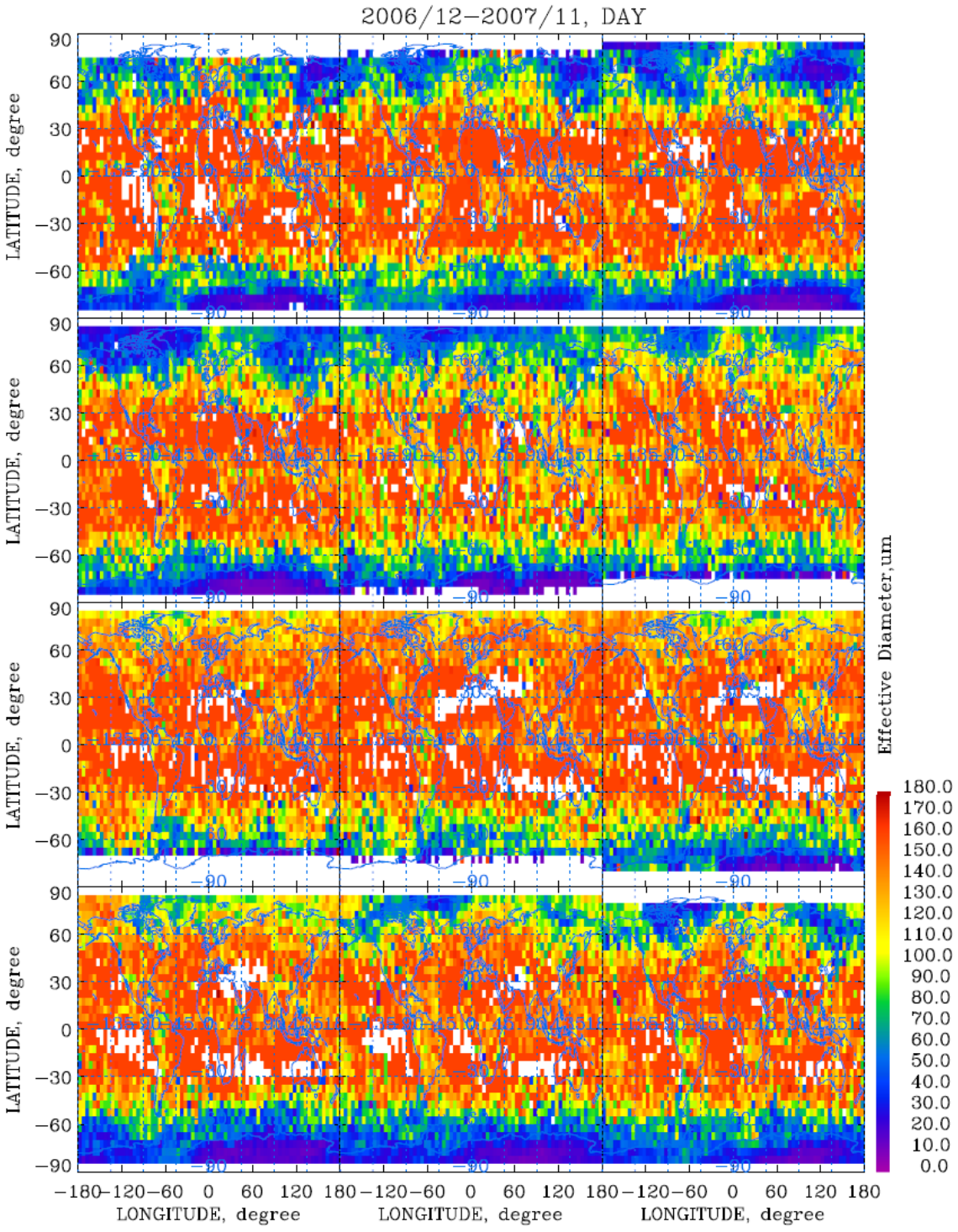

Figure A.11 2007 daytime average effective diameter

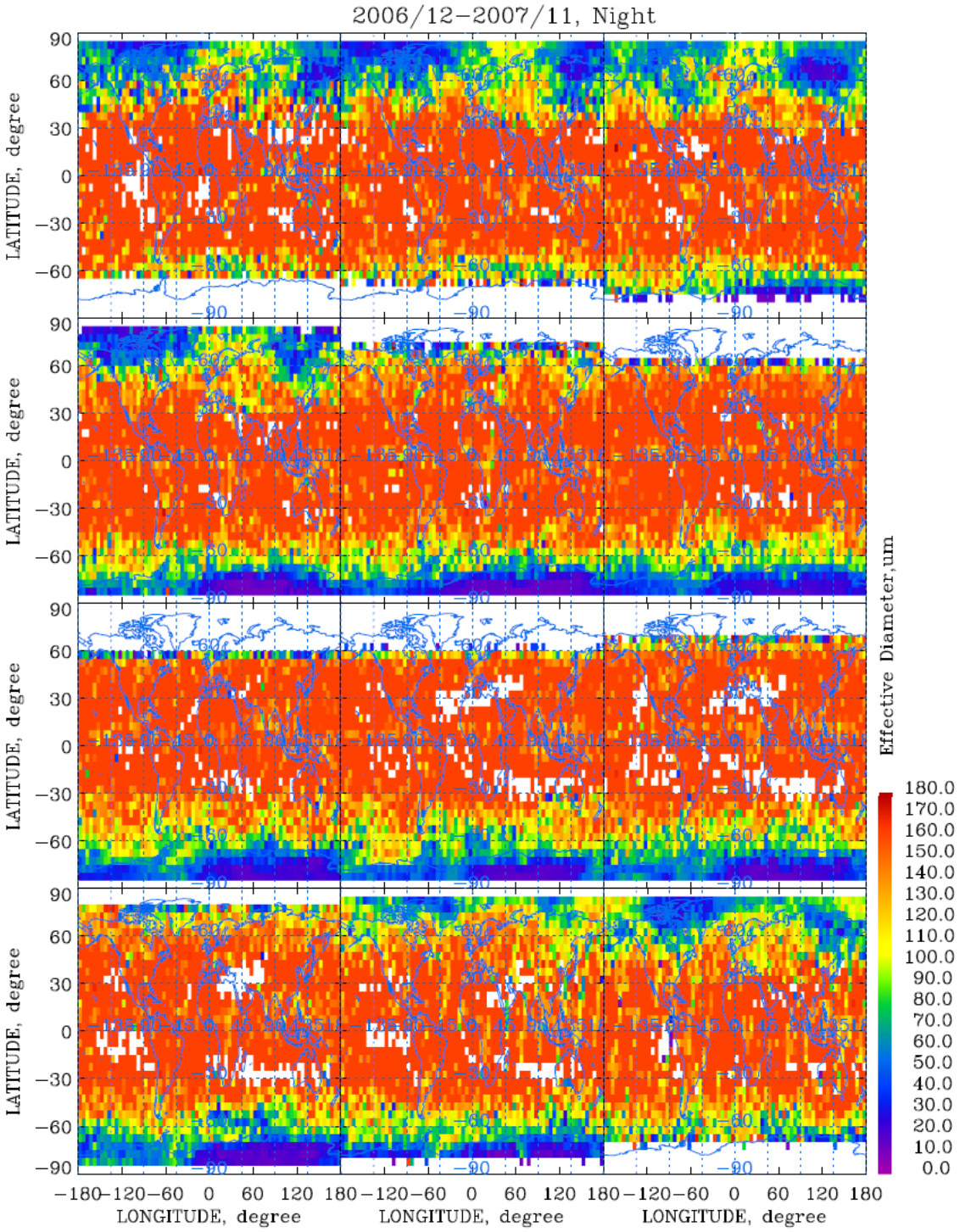

Figure A.12 2007 nighttime monthly average effective diameter

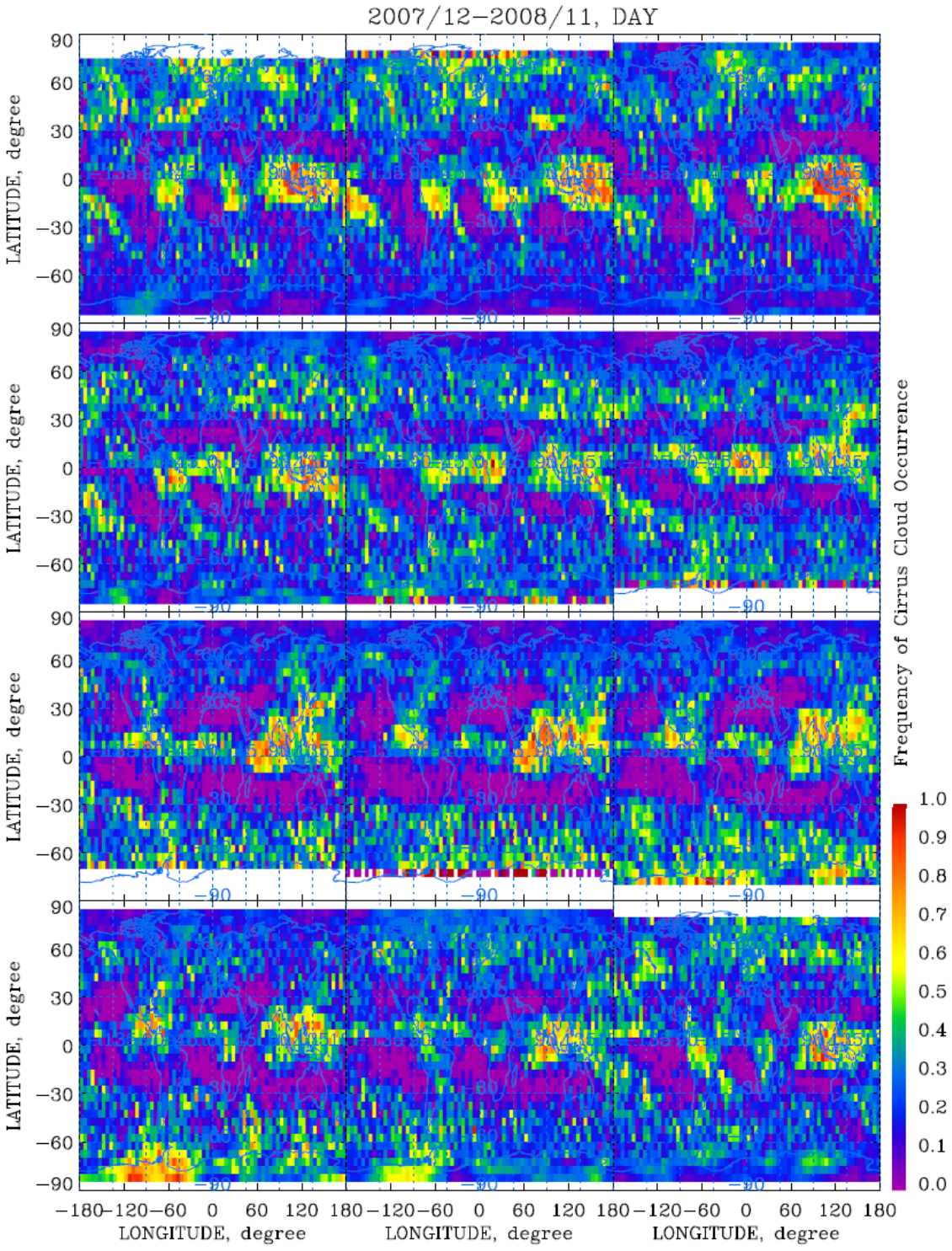

Figure A.13 2008 daytime monthly average frequency of occurrence

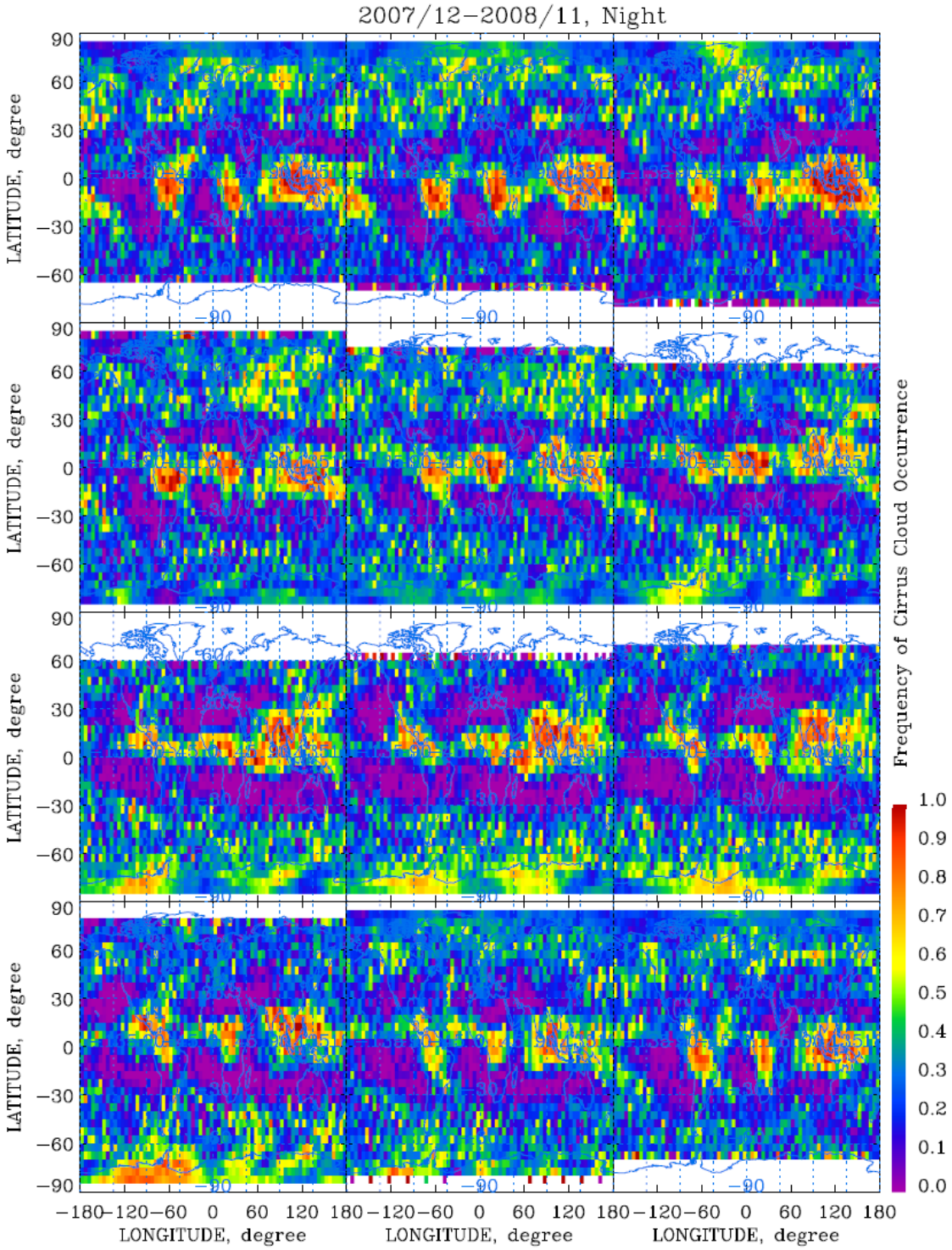

Figure A.14 2008 nighttime monthly average frequency of occurrence

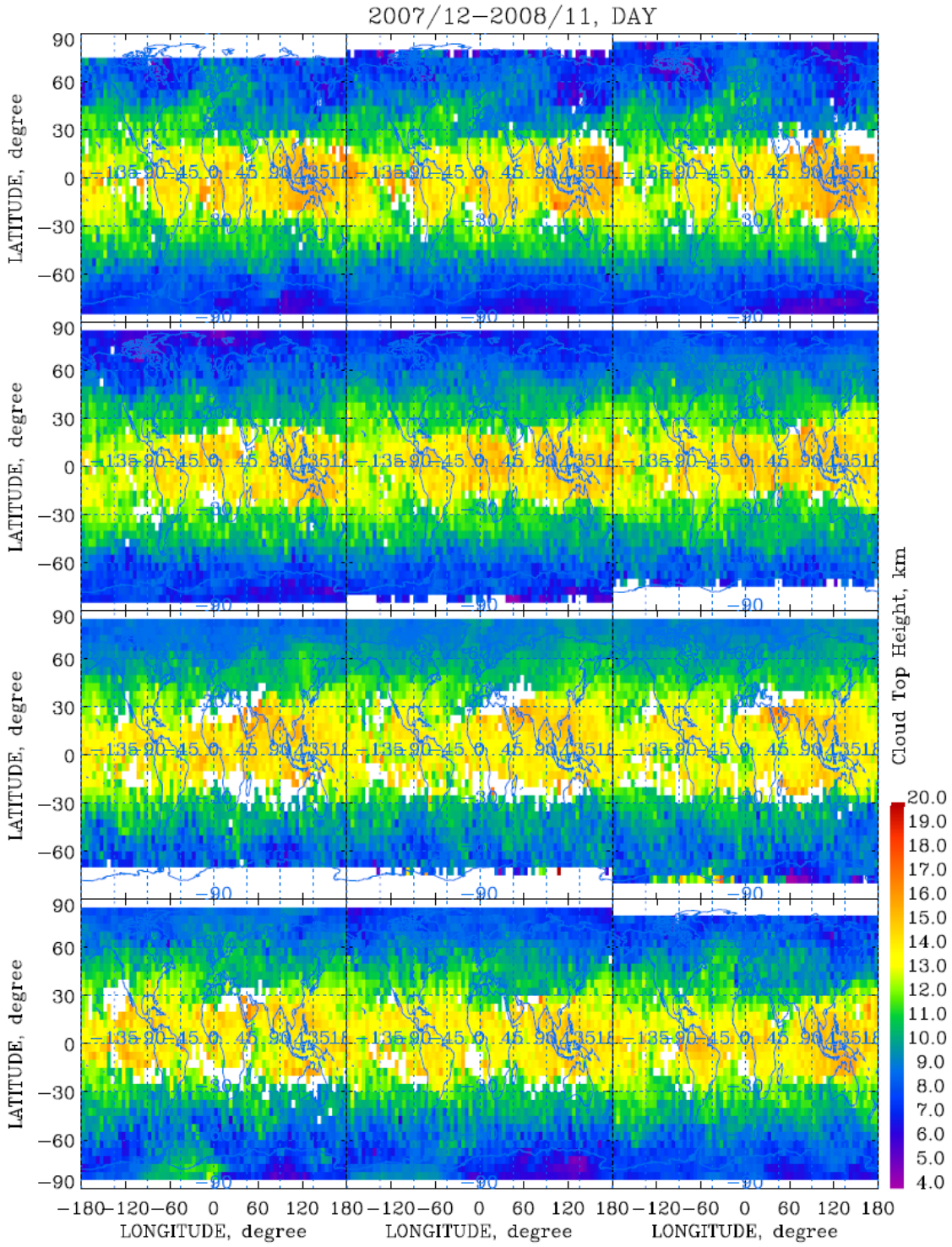

Figure A.15 2008 daytime monthly average cloud-top height

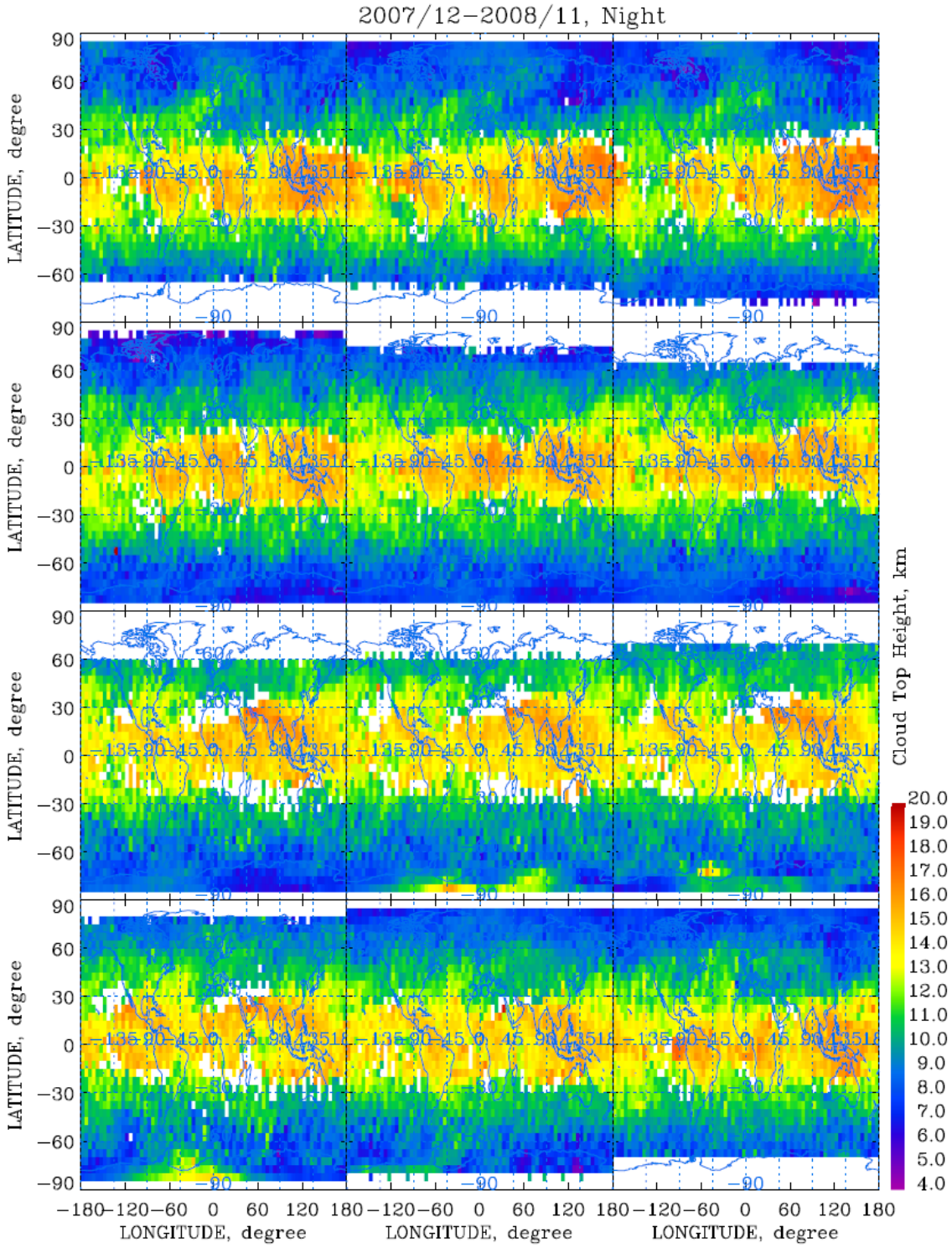

Figure A.16 2008 nighttime monthly average cloud-top height

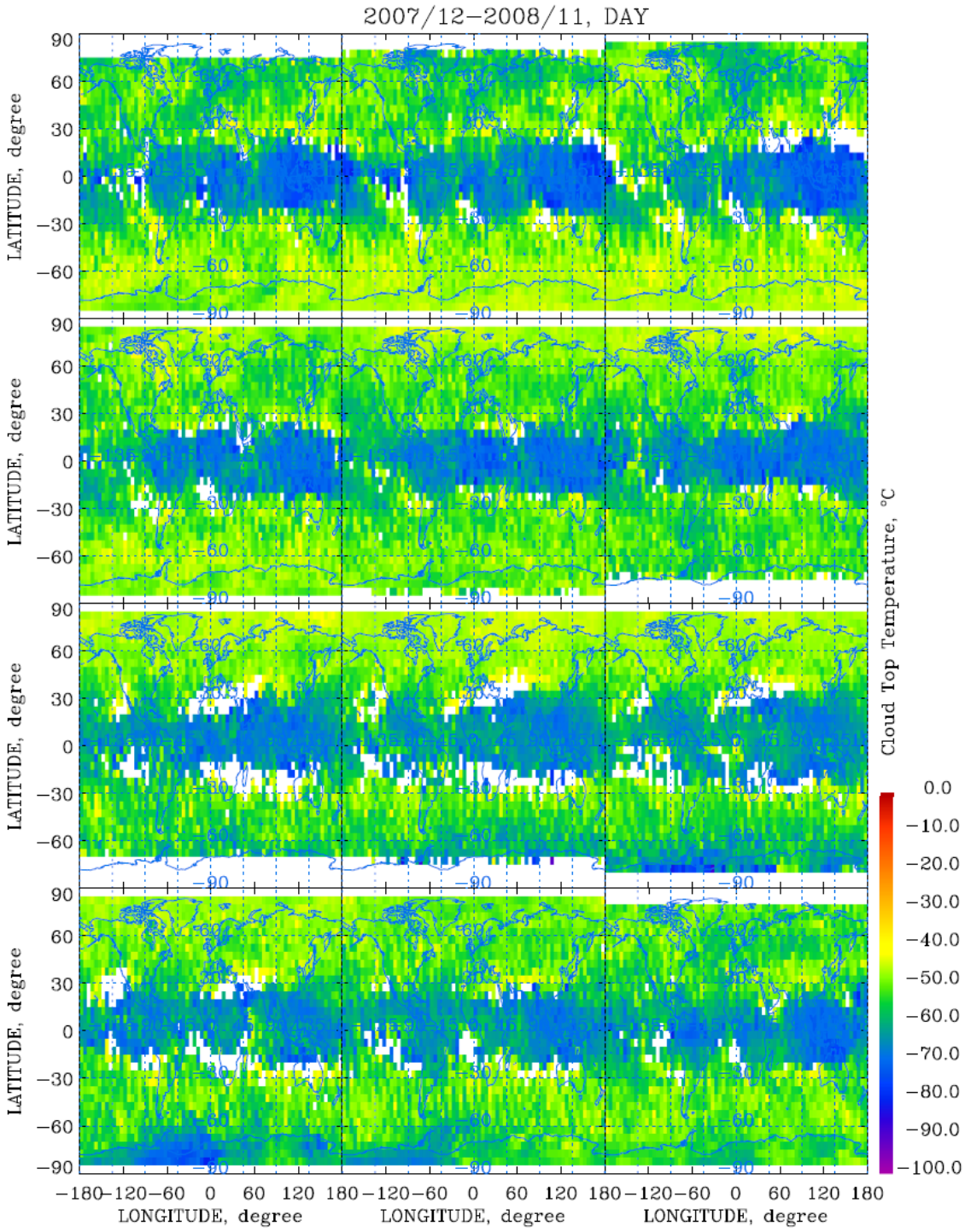

Figure A.17 2008 daytime monthly average cloud-top temperature

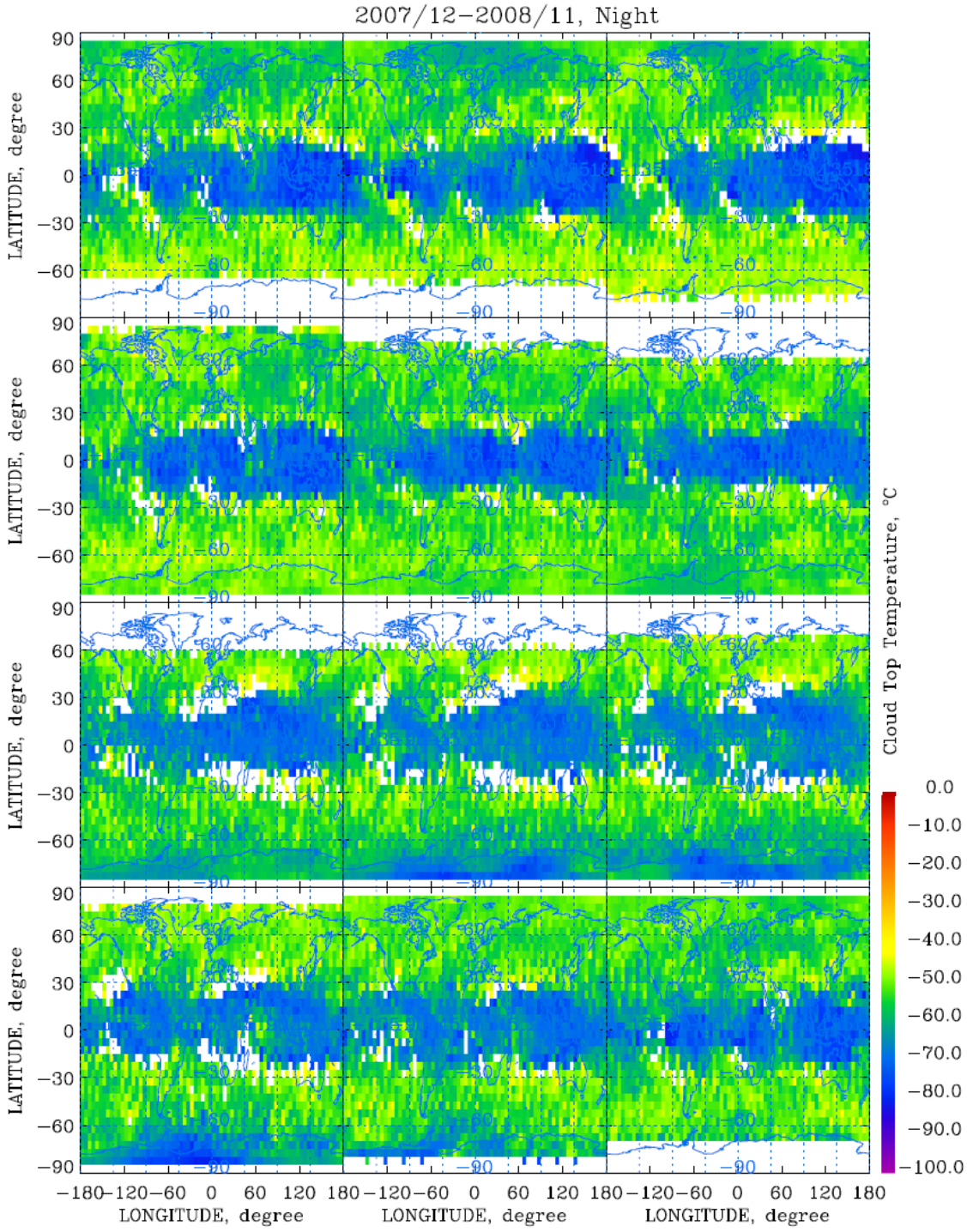

Figure A.18 2008 nighttime monthly average cloud-top temperature

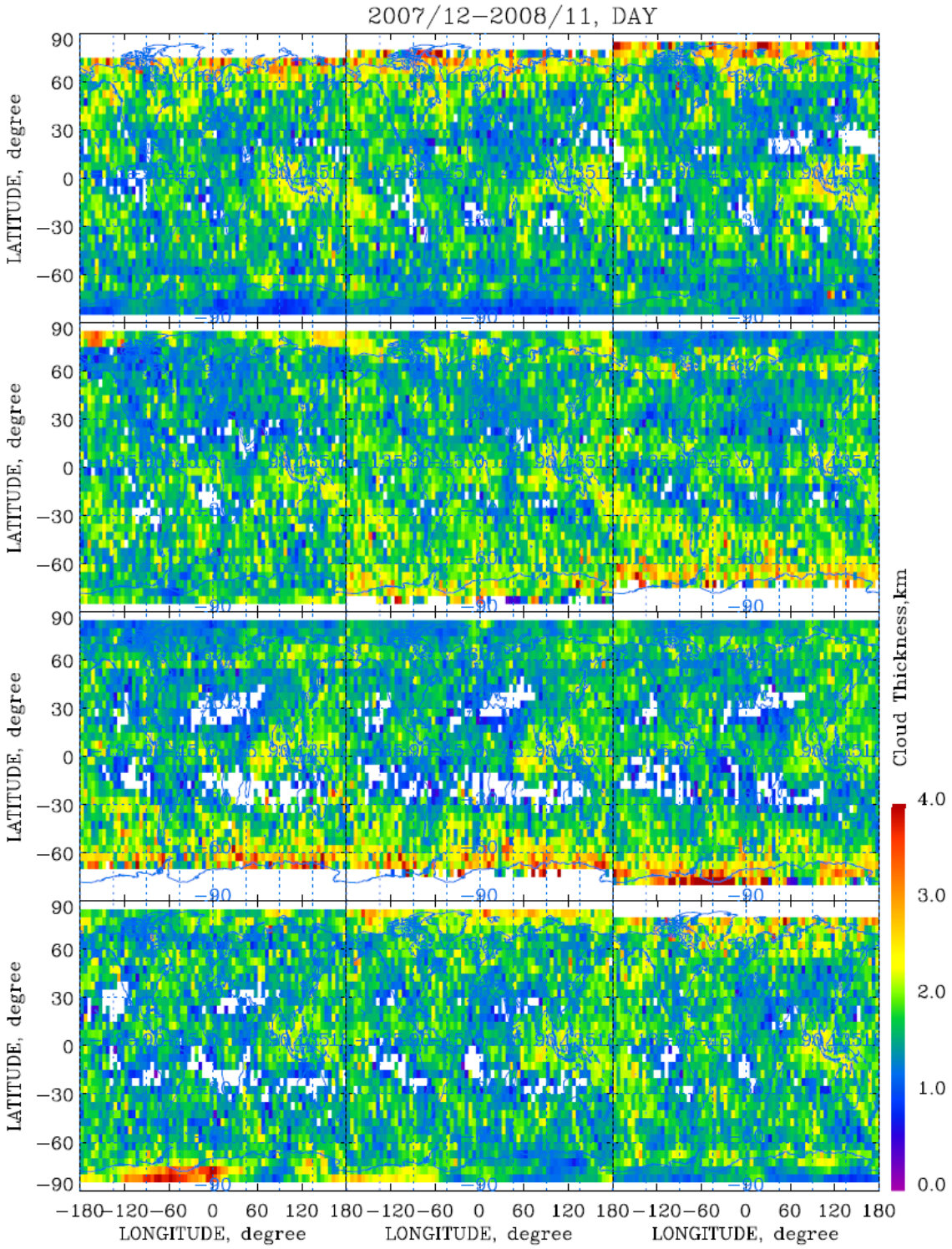

Figure A.19 2008 daytime monthly average cloud thickness

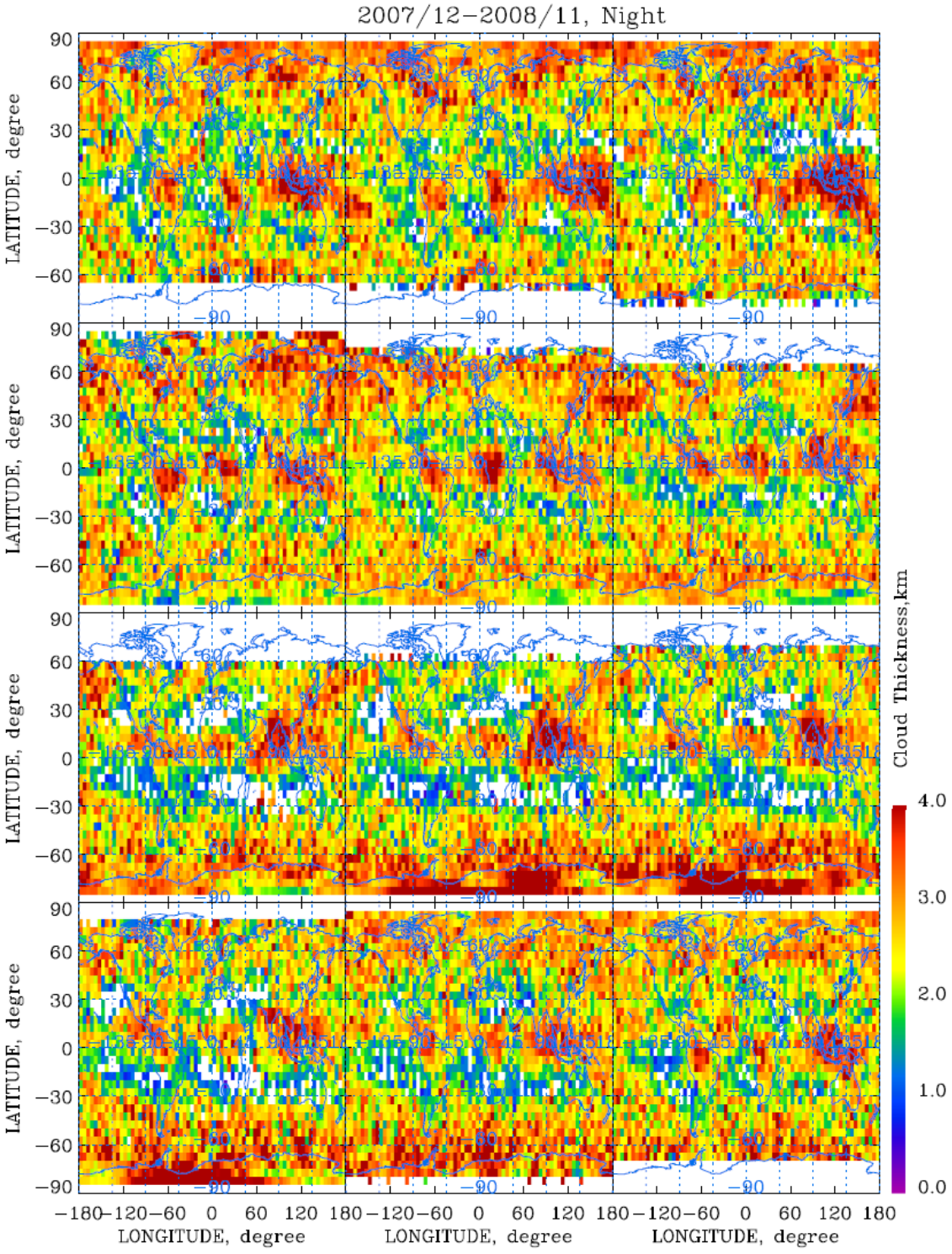

Figure A.20 2008 nighttime monthly average cloud thickness

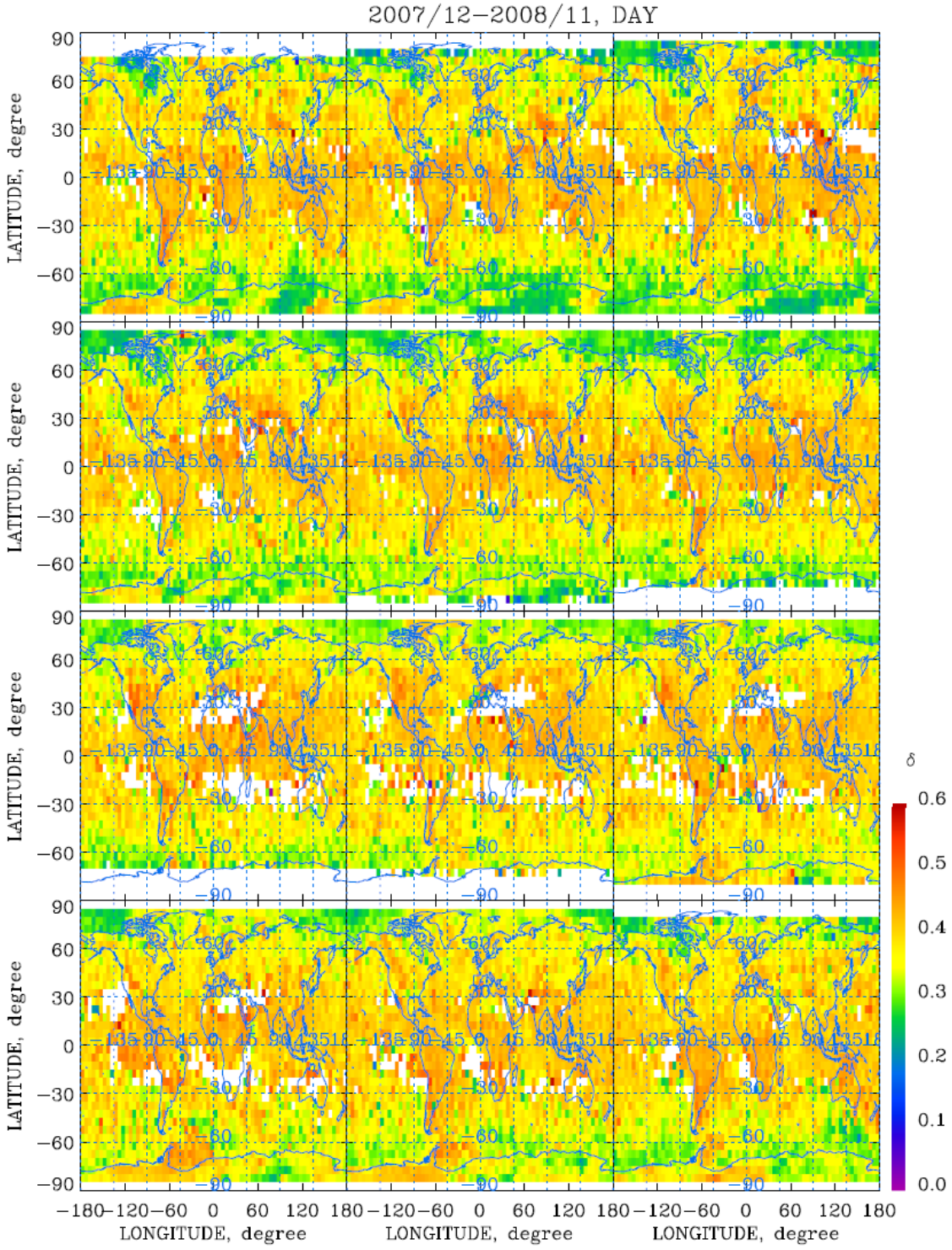

Figure A.21 2008 daytime monthly average LDR

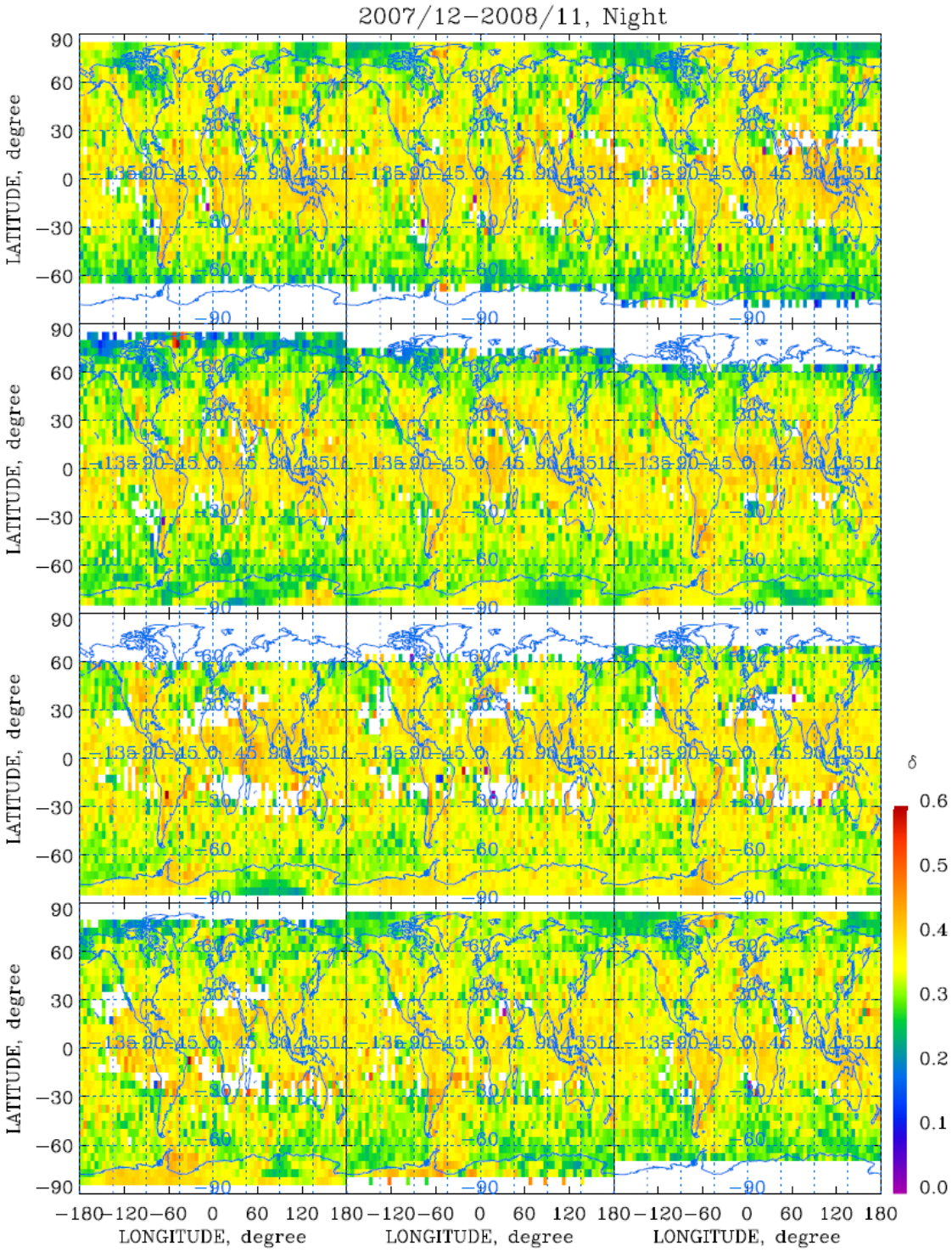

Figure A.22 2008 nighttime monthly average LDR

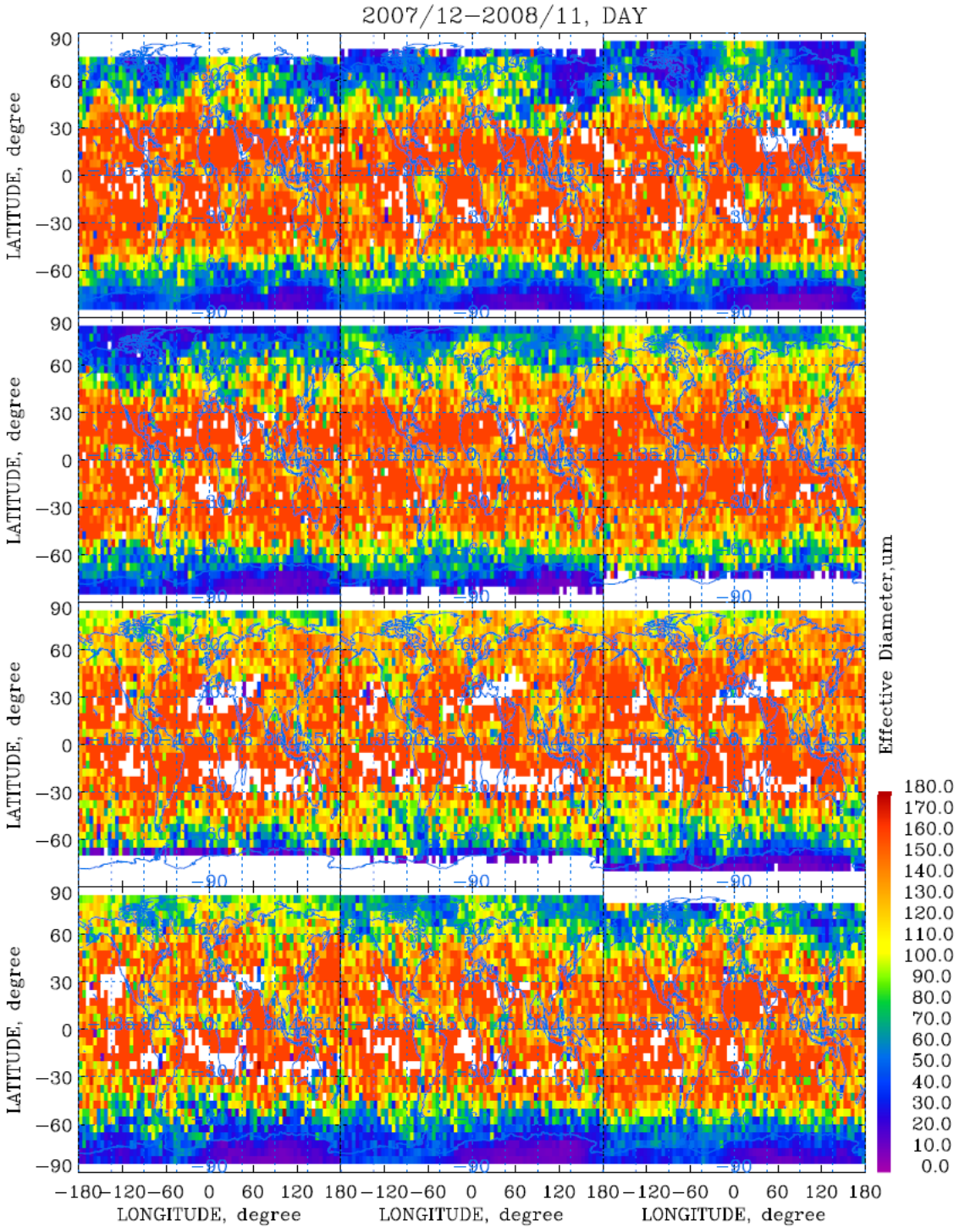

Figure A.23 2008 daytime monthly average effective diameter

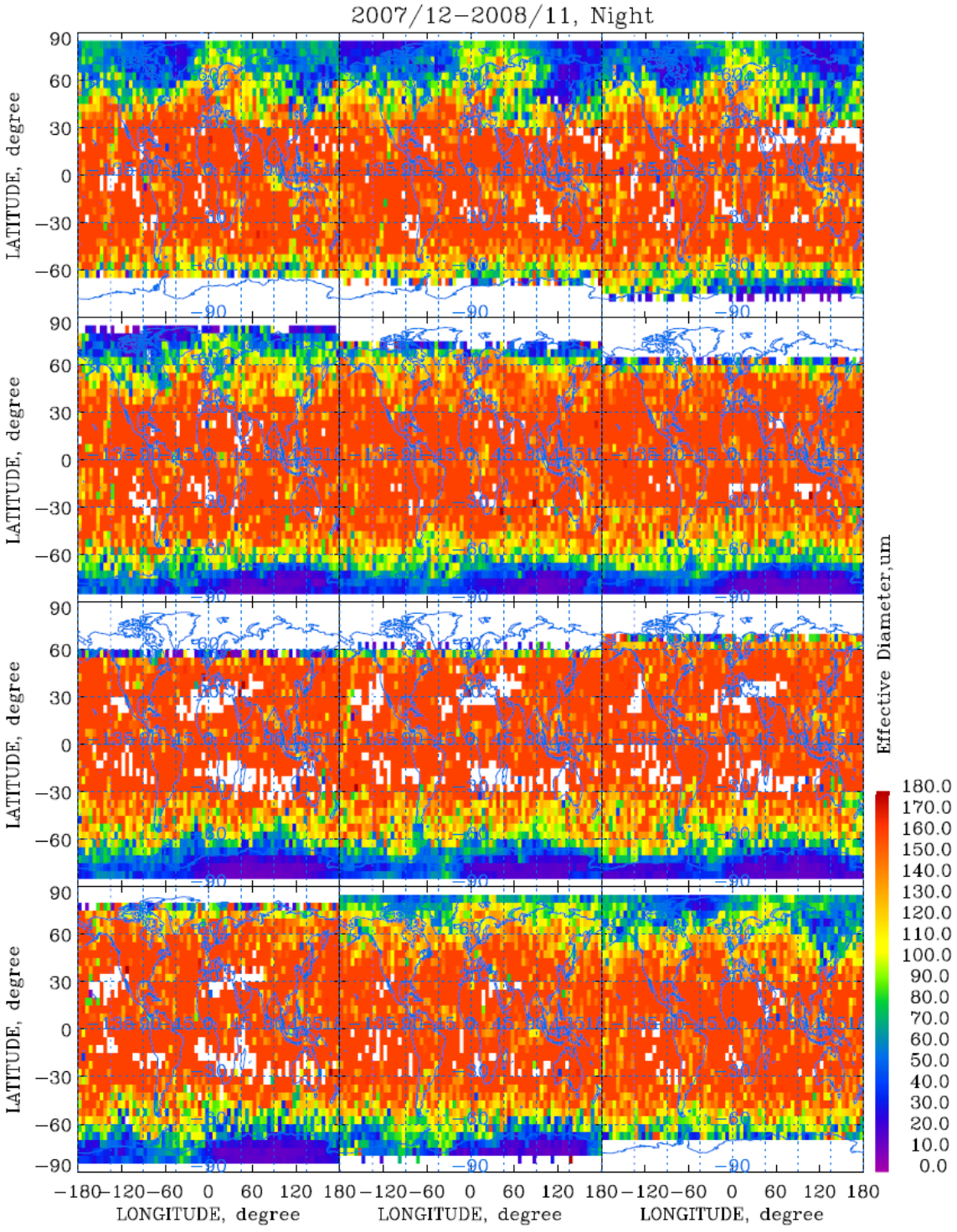

Figure A.24 2008 nighttime monthly effective diameter

Appendix B

This appendix includes many tables. These tables define the data structures of three product data sets. The definitions of the data structures of the processed data are also included in the appendix. Tables B.1 to B.12 are citied from Anselmo *et al*. (2007).

Table B.1 Lidar instrument record summary

Record Name	**Reference**	**Record Size**	**Records/ File**	**File Size (bytes)**
Core Metadata Record	Omitted	870	1	870
Archive Metadata Record	Omitted	4	1	4
Lidar Metadata Record	Table 2.5	3,075	1	3,075
Spacecraft Position, Attitude, and Celestial Record	Table 2.6	124	63,500	7,874,000
Profile Geolocation and Viewing Geometry	Table 2.7	40	63,500	2,540,000
Lidar Profile Science Record	Table 2.8	7,806	63,500	485,267,000
Total Size Bytes				**495,684,949**
Total Size Mbytes				**472.722**

Table B.2 Lidar metadata record

Parameter	Data Type	Units	Range	Elem/ Rec	Bytes
Product_ID	Char	NoUnits	N/A	80	80
Date_Time_at_Granule_Start1	Char	NoUnits	1/1958…6/2137	27	27
Date_Time_at_Granule_End1	Char	NoUnits	1/1958…6/2137	27	27
Date_Time_of_Production1	Char	NoUnits	1/1958…6/2137	27	27
Number_of_Good_Profiles	Int_32	NoUnits	0…63,630	1	4
Number_of_Bad_Profiles	Int_32	NoUnits	0…63,630	1	4
Initial_Subsatellite_Latitude	Float_32	deg	-90.0…90.0	1	4
Initial_Subsatellite_Longitude	Float_32	deg	-180.0…180.0	1	4
Final_Subsatellite_Latitude	Float_32	deg	-90.0…90.0	1	4
Final_Subsatellite_Longitude	Float_32	deg	-180.0…180.0	1	4
Ephemeris_Files_Used	Char	NoUnits	2 file names max.	160	160
Attitude_Files_Used	Char	NoUnits	2 file names max.	160	160
GEOS_Version	Char	NoUnits	N/A	64	64
Percent_532-parallel_Bad	Float_32	%	0.0…100.0	1	4
Percent_532-perpendicular_Bad	Float_32	%	0.0…100.0	1	4
Percent_1064_Bad	Float_32	%	0.0…100.0	1	4
Percent_532-parallel_Missing	Float_32	%	0.0…100.0	1	4
Percent_532-perpendicular_Missing	Float_32	%	0.0…100.0	1	4
Percent_1064_Missing	Float_32	%	0.0…100.0	1	4
Cal_Region_Top_Altitude_532	Float_32	km	0.0...40.0	1	4
Cal_Region_Base_Altitude_532	Float_32	km	0.0...40.0	1	4
Lidar_Data_Altitudes	Float_32	km	-1.845…39.855	583	2,332
Met_Data_Altitudes	Float_32	km	-1.845…39.855	33	132
Record Size (bytes)					**3,075**

1) UTC CCSDS ASCII Time Code Format A 2) Julian date format

Table B.3 Lidar spacecraft position, attitude, and celestial record

Parameter	Data Type	Units	Range	Elem/Rec	Bytes
Spacecraft_Altitude	Float_32	km	700.0…720.0	1	4
Spacecraft_Position2	Float_64	km	-8000.0…8000.0	3	24
Spacecraft_Velocity2	Float_64	km · sec -1	-10.0…10.0	3	24
Spacecraft_Attitude	Float_64	deg	-180.0…180.0	3	24
Spacecraft_Attitude_Rate	Float_64	deg · sec -1	-10.0…10.0	3	24
Subsatellite_Latitude	Float_32	deg	-90.0…90.0	1	4
Subsatellite_Longitude	Float_32	deg	-180.0…180.0	1	4
Earth-Sun_Distance	Float_64	ua	0.98…1.02	1	8
Subsolar_Latitude	Float_32	deg	-90.0…90.0	1	4
Subsolar_Longitude	Float_32	deg	-180.0…180.0	1	4
Record Size (bytes)					**124**

Table B.4 Lidar profile geolocation and view geometry

Parameter	Data Type	Units	Range	Elem/Rec	Bytes
Latitude	Float_32	deg	-90.0…90.0	1	4
Longitude	Float_32	deg	-180.0…180.0	1	4
Off_Nadir_Angle	Float_32	deg	0.0…20.0	1	4
Viewing_Zenith_Angle	Float_32	deg	0.0…90.0	1	4
Viewing_Azimuth_Angle	Float_32	deg	-180.0…180.0	1	4
Solar_Zenith_Angle	Float_32	deg	0.0…180.0	1	4
Solar_Azimuth_Angle	Float_32	deg	-180.0…180.0	1	4
Scattering_Angle	Float_32	deg	0.0…180.0	1	4
Surface_Altitude_Shift	Float_32	km	TBD	1	4
Number_Bins_Shift	Int_32	NoUnits	TBD	1	4
Record Size (bytes)					**40**

Table B.5 Lidar profile science record

Parameter	Data Type	Units	Range	Elem/ Rec	Bytes
Profile_Time3	Float_64	sec	4.204E8…7.389E8	1	8
Profile_UTC_Time4	Float_64	NoUnits	60,426…160,601	1	8
Profile_ID	Int_32	NoUnits	N/A	1	4
Land_Water_Mask	Int_8	NoUnits	N/A	1	1
IGBP_Surface_Type	Int_8	NoUnits	N/A	1	1
NSIDC_Surface_Type	UInt_8	NoUnits	N/A	1	1
Day_Night_Flag	Int_8	NoUnits	N/A	1	1
Frame_Number	Int_16	NoUnits	N/A	1	2
Lidar_Mode	Int_16	NoUnits	N/A	1	2
Lidar_Submode	Int_16	NoUnits	N/A	1	2
Surface_Elevation	Float_32	km	-1.0…9.0	1	4
Laser_Energy_532	Float_32	J	-0.04…0.12	1	4
Perpendicular_Amplifier_ Gain_532	Float_32	V/V	28.2…178.0	1	4
Par_Amplifier_Gain_532	Float_32	V/V	28.2…178.0	1	4
Perpendicular_Backgroun d_Monitor_532	Float_32	counts	800.0…4000.0	1	4
Parallel_Background_Mon itor_532	Float_32	counts	-100.0…4000.0	1	4
Depolarization_Gain_Rati o_532	Float_32	No Units	0.0…2.5	1	4
Depolarization_Gain_Rati o_Uncertainty_532	Float_32	No Units	0.0…TBD	1	4
Calibration_Constant_532	Float_32	km3·sr· counts	TBD	1	4
Calibration_Constant_Unc ertainty_532	Float_32	km3·sr· counts	0.0…TBD	1	4
Total_Attenuated_Backsca tter_532	Float_32	km-1 sr -1	0.0…0.4	583	2,332
Perpendicular_Attenuated _Backscatter_532	Float_32	km-1 sr -1	0.0…0.2	583	2,332

Table B.5 continued

Perpendicular_RMS_Baseline_532	Float_32	counts	20.0…25000.0	1	4
Parallel_RMS_Baseline_532	Float_32	counts	20.0…25000.0	1	4
Laser_Energy_1064	Float_32	J	0.0…0.12	1	4
Amplifier_Gain_1064	Float_32	V/V	102.0…195.0	1	4
Calibration_Constant_1064	Float_32	km3·sr· counts	TBD	1	4
Calibration_Constant_Uncertainty_1064	Float_32	km3·sr· counts	0.0…TBD	1	4
Attenuated_Backscatter_1064	Float_32	km-1 sr -1	0.0…0.4	583	2,332
RMS_Baseline_1064	Float_32	counts	220.0…1800.0	1	4
Molecular_Num_Density	Float_32	m –3	8x1022…5x1025	33	132
Ozone_Number_Density	Float_32	m –3	1x1017…1x1019	33	132
Temperature	Float_32	ºC	-120.0…60.0	33	132
Pressure	Float_32	mb	1.0…1086.0	33	132
Relative_Humidity	Float_32	No Units	0…150	33	132
Surface_Wind_Speeds	Float_32	m/sec	-80…80	2	8
Tropopause_Height	Float_32	km	4…22	1	4
Tropopause_Temperature	Float_32	°C	-100…-20	1	4
Noise_Scale_Factor_532_Perpendicular	Float_32	counts1/2	TBD	1	4
Noise_Scale_Factor_532_Parallel	Float_32	counts1/2	TBD	1	4
Noise_Scale_Factor_1064	Float_32	counts1/2	TBD	1	4
Perpendicular_Column_Reflectance_532	Float_32	NoUnits	0.0…TBD	1	4
Perpendicular_Column_Reflectance_Uncertainty_532	Float_32	No Units	0.0…TBD	1	4
Parallel_Column_Reflectance_532	Float_32	No Units	0.0…TBD	1	4

Table B.5 continued

Parallel_C column_Reflectance_Uncertainty_532	Float_32	NoUnits	0.0…TBD	1	4
QC_Flag	UInt_32	NoUnits	TBD	1	4
QC_Flag_2	UInt_32	NoUnits	TBD	1	4

Table B.6 5 km lidar cloud layer record summary

Record Name	**Reference Table**	**Individual Record Size**	**Records/ File**	**File Size (bytes)**
Core Metadata Record	Omitted	870	1	870
Archive Metadata Record	Omitted	4	1	4
Lidar cloud & aerosol metadata record	Table 2.11	22,632	1	22,632
5 km Column Descriptor Record: Clouds	Table 2.12	279	4,010	1,118,790
5 km Layer Descriptor Record: Clouds	Table 2.13	2,500	4,010	10,025,660
Total Size 5 km Cloud Layer Product (bytes)				**11,167,956**
Total Size 5 km Cloud Layer Product (Mbytes)				**10.651**

Table B.7 Lidar cloud & aerosol level 2 metadata record

Parameter	Data Type	Units	Range	Elem/ Rec	Bytes
Product_ID	Char	NoUnits	N/A	80	80
Date_Time_at_Granule_Start1	Char	NoUnits	1/1958…6/2137	27	27
Date_Time_at_Granule_End1	Char	NoUnits	1/1958…6/2137	27	27
Date_Time_of_Production1	Char	NoUnits	1/1958…6/2137	27	27
Number_of_Good_Profiles	Int_32	NoUnits	0…63,630	1	4
Number_of_Bad_Profiles	Int_32	NoUnits	0…63,630	1	4
Initial_Subsatellite_Latitude	Float_32	deg	-90.0…90.0	1	4
Initial_Subsatellite_Longitude	Float_32	deg	-180.0…180.0	1	4
Final_Subsatellite_Latitude	Float_32	deg	-90.0…90.0	1	4
Final_Subsatellite_Longitude	Float_32	deg	-180.0…180.0	1	4
Lidar_L1_Production_Date_Time	Char	NoUnits	N/A	27	27
Number_of_Single_Shot_Records_in_File	Int_32	NoUnits	0…63,630	1	4
Number_of_Average_Records_in_File	Int_32	NoUnits	0…63,630	1	4
Number_of_Features_Found	Int_32	NoUnits	0…63,630	1	4
Number_of_Cloud_Features_Found	Int_32	NoUnits	0…63,630	1	4
Number_of_Aerosol_Features_Found	Int_32	NoUnits	0…63,630	1	4
Number_of_Indeterminate_Features_Found	Int_32	NoUnits	0…63,630	1	4
Lidar_Data_Altitudes	Float_32	km	-2…40	583	2,332
GEOS_Version	Char	NoUnits	N/A	64	64
Production_Script	Char	NoUnits	N/A	20,000	20,000
Record Size (bytes)					**22,632**

Table B.8 Lidar 5 km column descriptor record: cloud

Parameter	Data Type	Units	Range	Elem/ Rec	Bytes
Profile_ID	Int_32	NoUnits	1…3,153,600,000	2	8
Latitude	Float_32	deg	-90.0…90.0	3	12
Longitude	Float_32	deg	-180.0…180.0	3	12
Profile_Time3	Float_64	sec	4.204E8…7.389E8	3	24
Profile_UTC_Time4	Float_64	NoUnits	60,426…160,601	3	24
Day_Night_Flag	Int_8	NoUnits	0…1	1	1
Off_Nadir_Angle	Float_32	deg	0.0…10.0	1	4
Solar_Zenith_Angle	Float_32	deg	-0.0…180.0	1	4
Solar_Azimuth_Angle	Float_32	deg	-180.0…180.0	1	4
Scattering_Angle	Float_32	deg	0.0…180.0	1	4
Spacecraft_Position#	Float_64	km	-8000.0…8000.0	9	72
Pal_Col_Reflectance_532	Float_32	NoUnits	0.0…20.0	1	4
Parallel_Column_Reflectance_Uncertainty_532	Float_32	NoUnits	0.0…TBD	1	4
Parallel_Column_Reflectance_RMS_Variation_532	Float_32	NoUnits	0.0…TBD	1	4
Per_Col_Reflectance_532	Float_32	NoUnits	0.0…20.0	1	4
Perpendicular_Column_Reflectance_Uncertainty_532	Float_32	NoUnits	0.0…TBD	1	4
Perpendicular_Column_Reflectance_RMS_Variation_532	Float_32	NoUnits	0.0…TBD	1	4
Column_Integrated_Attenuated_Backscatter_532	Float_32	sr -1	0.0…1.0	1	4
Column_IAB_Cumulative_Probability	Float_32	NoUnits	0.0…1.0	1	4
Tropopause_Height	Float_32	km	4.0…22.0	1	4
Tropopause_Temperature	Float_32	ºC	-120.0…-20.0	1	4

Table B.8 continued

IGBP_Surface_Type	Int_8	NoUnits	1…17	1	1
NSIDC_Surface_Type	UInt_8	NoUnits	0…255	1	1
Lidar_Surface_Elevation	Float_32	km	-1.0…9.0	8	32
DEM_Surface_Elevation	Float_32	km	-1.0…9.0	4	16
Surface_Elevation_Detection_Frequency	UInt_8	NoUnits	0…165	1	1
Normalization_Constant_Uncertainty_532	Float_32	NoUnits	0…1.0	2	8
Calibration_Altitude_532	Float_32	km	0.0…40.0	2	8
FeatureFinderQC	UInt_16	NoUnits	0…32767	1	2

Table B.9 Lidar 5 km layer descriptor record: layers

Parameter	Data Type	Units	Range	Elem/ Rec	Bytes
Layer_Top_Altitude	Float_32	km	-0.5…30.1	10	40
Layer_Base_Altitude	Float_32	km	-0.5…30.1	10	40
Opacity_Flag	Int_8	NoUnits	0…1	10	10
Horizontal_Averaging	Int_8	km	5…80	10	10
Attenuated_Backscatter_Statistics_532	Float_32	km-1 sr -1	N/A	60	240
Integrated_Attenuated_Backscatter_532	Float_32	sr -1	0.0…1.0	10	40
Integrated_Attenuated_Backscatter_Uncertainty_532	Float_32	sr -1	0.0…TBD	10	40
Attenuated_Backscatter_Statistics_1064	Float_32	km-1 sr -1	N/A	60	240
Integrated_Attenuated_Backscatter_1064	Float_32	sr -1	0.0…1.0+	10	40
Integrated_Attenuated_Backscatter_Uncertainty_1064	Float_32	sr -1	0.0…TBD	10	40
Volume_Depolarization_Ratio_Statistics	Float_32	NoUnits	N/A	60	240
Integrated_Volume_Depolarization_Ratio	Float_32	NoUnits	0.0…1.0	10	40
Integrated_Volume_Depolarization_Ratio_Uncertainty	Float_32	NoUnits	0.0…TBD	10	40
Attenuated_Total_Color_Ratio_Statistics	Float_32	NoUnits	N/A	60	240
Integrated_Attenuated_Total_Color_Ratio	Float_32	NoUnits	0.0…2.0	10	40
Integrated_Attenuated_Total_Color_Ratio_Uncertainty	Float_32	NoUnits	0.0…TBD	10	40
Overlying_Integrated_Attenuated_Backscatter_532	Float_32	sr -1	0…10	10	40
Layer_IAB_QA_Factor	Float_32	NoUnits	0…1	10	40
Feature_Classification_Flags *	UInt_16	NoUnits	0…98,298	10	20
ExtinctionQC_532	UInt_16	NoUnits	0…65,535	10	20
CAD_Score	Int_8	NoUnits	-100…100	10	10
Measured_Two_Way_Transmittance_532	Float_32	NoUnits	0.0…1.0	10	40
Measured_Two_Way_Transmittance_Uncertainty_532	Float_32	NoUnits	0.0…TBD	10	40
Two_Way_Transmittance_Measurement_Region	Float_32	km	0.0…30.0	20	80

Table B.9 continued

Feature_Optical_Depth_532	Float_32	NoUnits	0.0…5.0	10	40
Feature_Optical_Depth_Uncertainty_532	Float_32	NoUnits	0.0…TBD	10	40
Initial_532_Lidar_Ratio	Float_32	sr	0.0…100.0	10	40
Final_532_Lidar_Ratio	Float_32	sr	0.0…250.0	10	40
Lidar_Ratio_532_Selection_Method	Int_8	NoUnits	0.0…5.0	10	10
Layer_Effective_532_Multiple_Scattering_Factor	Float_32	NoUnits	0.0…1.0	10	40
Integrated_Particulate_Depolarization_Ratio	Float_32	NoUnits	0.0…1.0	10	40
Integrated_Particulate_Depolarization_Ratio_Uncertainty	Float_32	NoUnits	0.0…TBD	10	40
Particulate_Depolarization_Ratio_Statistics	Float_32	NoUnits	N/A	60	240
Midlayer_Temperature	Float_32	ºC	110.0…60.0	10	40
Cirrus_Shape_Parameter	Int_16	NoUnits	0…550	40	80
Cirrus_Shape_Parameter_Uncertainty	Int_16	NoUnits	0…550	40	80
Cirrus_Shape_Parameter_Invalid_Points	Int_16	NoUnits	0…550	10	20
Ice_Water_Path	Float_32	NoUnits	TBD	10	40
Ice_Water_Path_Uncertainty	Float_32	NoUnits	0.0…TBD	10	40
Record Size (bytes)					2,500

Table B.10 IIR/lidar track product summary

Record Name	Reference	Record Size	Records/File	File Size (Bytes)
Core Metadata Record	Omitted	870	1	870
Archive Metadata Record	Omitted	4	1	4
IIR Track Metadata Record	Table B.11	285	1	285
IIR/Lidar Track Science Record	Table B.12	220	20,048	4,410,560
Total Size Profile Data Product (Bytes)				**4,411,719**
Total Size Profile Data Product (Mbytes)				**4.207**

Table B.11 IIR/Lidar track metadata record

Parameter	Data Type	Units	Range	Elem/ Rec	Bytes
Product_ID	Char	NoUnits	N/A	80	80
Date_Time_at_Granule_Start1	Char	NoUnits	1/1958…6/21 37	27	27
Date_Time_at_Granule_End1	Char	NoUnits	1/1958…6/21 37	27	27
Date_Time_of_Production1	Char	NoUnits	1/1958…6/21 37	27	27
Initial_IIR_Scan_Center_Latitude	Float_32	deg	-90.0…90.0	1	4
Initial_IIR_Scan_Center_Longitude	Float_32	deg	-180.0…180.0	1	4
Ending_IIR_Scan_Center_Latitude	Float_32	deg	-90.0…90.0	1	4
Ending_IIR_Scan_Center_Longitude	Float_32	deg	-180.0…180.0	1	4
Number_of_IIR_Records_in_File	Int_16	NoUnits	0…20,048	1	2
Number_of_Valid_08_65_Pixels	Int_16	NoUnits	0…20,048	1	2
Number_of_Valid_12_05_Pixels	Int_16	NoUnits	0…20,048	1	2
Number_of_Valid_10_60_Pixels	Int_16	NoUnits	0…20,048	1	2
Number_of_Invalid_08_65_Pixels	Int_16	NoUnits	0…20,048	1	2
Number_of_Invalid_12_05_Pixels	Int_16	NoUnits	0…20,048	1	2
Number_of_Invalid_10_60_Pixels	Int_16	NoUnits	0…20,048	1	2
Number_of_Rejected_08_65_Pixels	Int_16	NoUnits	0…20,048	1	2
Number_of_Rejected_12_05_Pixels	Int_16	NoUnits	0…20,048	1	2
Number_of_Rejected_10_60_Pixels	Int_16	NoUnits	0…20,048	1	2
Number_of_Rejected_08_65_Pixels_Location	Int_16	NoUnits	0…20,048	1	2
Number_of_Rejected_12_05_Pixels_Location	Int_16	NoUnits	0…20,048	1	2
Number_of_Rejected_10_60_Pixels_Location	Int_16	NoUnits	0…20,048	1	2
Number_of_Rejected_08_65_Pixels_Radiance	Int_16	NoUnits	0…20,048	1	2
Number_of_Rejected_12_05_Pixels_Radiance	Int_16	NoUnits	0…20,048	1	2
Number_of_Rejected_10_60_Pixels_Radiance	Int_16	NoUnits	0…20,048	1	2
Mean_08_65_Radiance_All	Float_32	Wm-2sr -1 µm -1	TBD	1	4

Table B.11 continued

Mean_12_05_Radiance_All	Float_32	Wm-2sr -1 µm -1	TBD	1	4
Mean_10_60_Radiance_All	Float_32	Wm-2sr -1 µm -1	TBD	1	4
Mean_08_65_Radiance_Selected_Cases	Float_32	Wm-2sr -1 µm -1	TBD	1	4
Mean_12_05_Radiance_Selected_Cases	Float_32	Wm-2sr -1 µm -1	TBD	1	4
Mean_10_60_Radiance_Selected_Cases	Float_32	Wm-2sr -1 µm -1	TBD	1	4
Mean_08_65_Brightness_Temp_All	Float_32	K	0.0…400.0	1	4
Mean_12_05_Brightness_Temp_All	Float_32	K	0.0…400.0	1	4
Mean_10_60_Brightness_Temp_All	Float_32	K	0.0…400.0	1	4
Mean_08_65_Brightness_Temp_Selected_Cases	Float_32	K	0.0…400.0	1	4
Mean_12_05_Brightness_Temp_Selected_Cases	Float_32	K	0.0…400.0	1	4
Mean_10_60_Brightness_Temp_Selected_Cases	Float_32	K	0.0…400.0	1	4
Number_of_Valid_LIDAR_Pixels	Int_16	NoUnits	0…20,048	1	2
Number_of_Invalid_LIDAR_Pixels	Int_16	NoUnits	0…20,048	1	2
Number_of_Rejected_LIDAR_Pixels	Int_16	NoUnits	0…20,048	1	2
Number_of_Identified_Pixels_Upper_Level	Int_16	NoUnits	0…20,048	1	2
Percent_of_Identified_Pixels_Upper_Level	Float_32	%	0.0…100.0	1	4
Number_of_Identified_Pixels_Lower_Level	Int_16	NoUnits	0…20,048	1	2
Percent_of_Identified_Pixels_Lower_Level	Float_32	%	0.0…100.0	1	4

Table B.12 IIR/lidar track science record

Parameter	Data Type	Units	Range	Elem/ Rec	Bytes
Latitude	Float_32	deg	-90.0...90.0	1	4
Longitude	Float_32	deg	-180.0...180.0	1	4
LIDAR_Shot_Time	Float_64	sec	N/A	1	8
IIR_Image_Time_12_05	Float_64	sec	N/A	1	8
Brightness_Temperature_08_65	Float_32	K	0.0…400.0	1	4
Brightness_Temperature_12_05	Float_32	K	0.0…400.0	1	4
Brightness_Temperature_10_60	Float_32	K	0.0…400.0	1	4
Effective_Emissivity_08_65	Float_32	No Units	-0.1…1.1	1	4
Effective_Emissivity_12_05	Float_32	No Units	-0.1…1.1	1	4
Effective_Emissivity_10_60	Float_32	No Units	-0.1…1.1	1	4
Eff. Emissivity_Uncertainty_0865	Float_32	No Units	TBD	1	4
Eff. Emissivity_Uncertainty_1205	Float_32	No Units	TBD	1	4
Eff. Emissivity_Uncertainty_1060	Float_32	No Units	TBD	1	4
Emissivity_08_65	Float_32	No Units	0.0…1.0	1	4
Emissivity_12_05	Float_32	No Units	0.0…1.0	1	4
Emissivity_10_60	Float_32	No Units	0.0…1.0	1	4
Emissivity_Uncertainty_0865	Float_32	No Units	TBD	1	4
Emissivity_Uncertainty_1205	Float_32	No Units	TBD	1	4
Emissivity_Uncertainty_1060	Float_32	No Units	TBD	1	4
Particle_Shape_Index	Int_8	No Units	TBD	1	1
Particle_Shape_Index_Conf.	Int_8	No Units	0…100	1	1
g	Int_8	No Units	TBD	1	1
g_confidence	Int_8	No Units	0…100	1	1
Eff. Particle_Size	Float_32	μm	0.0…300.0	1	4
Eff. Particle_Size_Uncertainty	Float_32	μm	TBD	1	4
Clear_Sky_Radiance_08_65	Float_32	Wm-2sr -1 μm -1	TBD	1	4
Clear_Sky_Radiance_12_05	Float_32	Wm-2sr -1 μm -1	TBD	1	4
Clear_Sky_Radiance_10_60	Float_32	Wm-2sr -1 μm -1	TBD	1	4
Optical_Depth_12_05	Float_32	No Units	TBD	1	4

Table B.13 Name, function, output file name, and data format

Name	Function	Name of output file	Format of output file
Onefile.pro	1. Process half-orbit file, identify ice clouds		
Oneday.pro	2. Combine processed half-orbit files into one-day file	yyyy-mm-dd-ZD[N].dat	Table 3.2
Grid_lon_lat_reiwc.pro	3. Produce grid file in lon-lat grid, calculate effective diameter and IWC	yyyy-mm-dd-ZD[N]-lon-lat-f-reiwc.dat	Table 3.3
adddatagrid_lon_lat_reiwc.pro	4. Produce one-month grid file	yyyy-mm-ZD[N]-lon-lat-f-reiwc.dat	Table 3.3
Grid_lat_hgt_reiwc.pro	Convert lon-lat grid into lat-hgt grid file	yyyy-mm-ZD[N]-lon-lat-f-reiwc-lat-hgt.dat	Table3.4
Grid_lat_hgt_reiwc_calheat.pro	Calculate heating rate of one-month lat-hgt grid	yyyy-mm-ZD[ZN]-lon-lat-f-reiwc-lat-hgt-calheat.dat	Table 3.4
griddraw_xxx_lon_lat.pro	5. Draw longitude-latitude plot	yyyy-mm-ZD[N]-lon-lat-f-reiwc.ps	
griddraw_xxx_lat_hgt.pro	5. Draw latitude-height plot	yyyy-mm-ZD[N]-lon-lat-f-reiwc-lat-hgt.ps	

Table B.14 Data record structure in file yyyy_mm_dd_ZD[N].dat

Latitude(0)	Longitude(1)	time(2)	ProfID0(3)	ProfID1(4)
ProfID2(5)	Top_height(6)	Top_temp(7)	(8)	(9)
BT0865(10)	BT1205(11)	BT1060(12)	E0865(13)	E1205(14)
E1060(15)	EF-P-size(16)	Clrrad0865(17)	Clrrad1205(18)	Clrrad1060(19)
Opt0532ll(20)	Opt0532hl(21)	Dep_ll(22)	Dep_hl(23)	Bksct_ll(24)
Bksct_hl(25)	Toph_ll(26)	Toph_hl(27)	Botm_ll(28)	Botm_hl(29)
Toptll(30)	Topthl(31)	Opt1205(32)	Iwc(33)	SE0865(34)
SE1205(35)	SE1060(36)	sene(37)	Rhflg(38)	Iirdataflg(39)
G(40)	(41)	Solarzen(42)	Solarazm(43)	Scatangle(44)
Surfelv(45)	Clnintgbact(46)	Igbpsurftype(47)	Offnadir(48)	Daynightflg(49)
Topha(50)	Topta(51)	Baseha(52)	Baseta(53)	Numlyra(54)
Ldr(55)	(16)	(17)	(18)	(19)
Tophf(60)	Toptf(61)	Basehf(62)	Basetf(63)	Numlyrf(64)
Ldrf(65)	(66)	(67)	(68)	(69)
Topht(70)	Toptt(71)	Baseht(72)	Basett(73)	Numlyrt(74)
Ldrt(75)	(76)	(77)	(78)	(79)
Tophe(80)	Topte(81)	Basehe(82)	Basete(83)	numlyre(84)
Ldre(85)	(86)	(87)	(88)	(89)
(90)	(91)	(92)	(93)	(94)
(95)	(96)	(97)	(98)	(99)
Toph1(100)	Topt1(101)	Baseh1(102)	Baset1(103)	Ldr(104)
Intgldr(105)	C5fkflg1(106)	Optics5321(107)	Midtemp1(108)	Hrzavg1(109)
(110)	Ext1(111)	Transmit1(112)	Region11(113)	Regin12(114)
Shpp1(115)	Iwp1(116)	Iwpync1(117)	Colorratio1(118)	Cirrflg1(119)
120-139, layer2 information with the same structure as 100-119				
140-159, layer3 information with the same structure as 100-119				
160-179, layer4 information with the same structure as 100-119				
180-199, layer5 information with the same structure as 100-119				
200-219, layer6 information with the same structure as 100-119				
220-239, layer7 information with the same structure as 100-119				
240-259, layer8 information with the same structure as 100-119				
260-279, layer9 information with the same structure as 100-119				
280-299, layer10 information with the same structure as 100-119				
300-899, total attenuated backscatter profile(583)				
900-1499, perpendicular attenuated backscatter profile(583)				
1500-2099, number of valid total attenuated backscatter values added (583)				
2100-2699, temperature profile(583)				
Note: The file yyyy_mm_dd.dat consists of one head record and many data records. Head record has 2700 double type elements. It includes only one field named altitude (300:882). Each data record has length of double type elements. The structure of data record is indicated above. Each data record includes one ice cloud column and its layer information.				

Table B.15 Data sumary in a lon-lat grid file

Num_overpass(0)	Num_cld_col(1)	(2)ldr	Cld_top_hgt(3)	Cld_top_temp(4)
Cld_bs_hgt(5)	Cld_bs_temp(6)	Cld_mid_temp(7)	Optic_depth(8)	(9)
(10)	(11)	(12)	(13)	(14)
(15)	(16)	(17)	(18)	(19)
(20)-(582)				
Total_bksct_profile (*,*,1, 583)				
Per_bkscat_profile (*,*,2, 583)				
Cnt_profile (*,*,3, 583)				
Temperature_profile (*,*,4, 583)				
Humidity (*,*,5, 583)				
Supersaturation density (*,*,6, 583)				
Supersaturaton ratio (*,*,7, 583)				
Ldr profile (*,*,8, 583)				
Heating rate profle (*,*,9, 583)				
Cnt_heat_profile (*,*,10,583)				
Note: one-day lon-lat grid file is named as yyyy-mm-dd-ZD[ZN]-lon-lat-?.dat. One-month lon-lat grid				

Table B.16 Data summary in a lat-hgt grid file

Num_over(0)	Num_cld_col(1)	(2)	Cld_top_hgt(3)	Cld_top_temp(4)
Cld_bs_hgt(5)	Cld_bs_temp(6)	Cld_mid_temp(7)	Optic_depth(8)	(9)
(10)	(11)	(12)	(13)	(14)
(15)	(16)	(17)	(18)	(19)
(20)-(49), (50)-(582)				
Tot_profile, (*,1,583)				
Per_profile, (*,2,583)				
Cnt_profile, (*,3,583)				
Temp_profile, (*,4,583)				
Humidity_profile, (*,5,583)				
Heatingrate_cloud_profile, (*,7,583)				
Ldr_profile, (*,8,583)				
Heatingrate_profile (*,9,583)				
Cnt_heatingrate_profile (*,10,583)				
Note: one-month lat-hgt grid file is named as yyyy-mm-ZD[N]-lon-lat-reiwc-lat-hgt.dat.				

Appendix C

This appendix includes the copy of the article. The copy is cited from: Sassen, K., and J. Zhu, A global survey of CALIPSO linear depolarization ratios in ice clouds: Initial findings, J. Geophys. Res., 114, D00H07, doi:10.1029/2009JD012279, 2009.

JOURNAL OF GEOPHYSICAL RESEARCH, VOL. 114, D00H07, doi:10.1029/2009JD012279, 2009

A global survey of CALIPSO linear depolarization ratios in ice clouds: Initial findings

Kenneth Sassen[1] and Jiang Zhu[1]

Received 18 April 2009; revised 11 August 2009; accepted 18 August 2009; published 14 November 2009.

[1] Linear depolarization ratio (δ) data from the summer/winter seasons over the first 2 years of Cloud-Aerosol Lidar and Infrared Pathfinder Satellite Observations (CALIPSO) satellite operations in the green (0.532 μm) laser channel are analyzed and interpreted in terms of ice cloud microphysical properties. That is, we use variations in δ as a proxy of cloud formation and environmental conditions that affect ice crystal shape and orientation. The cloud detection algorithm is tuned mainly to cirrus clouds, but also includes polar stratospheric clouds (PSC) and optically thin, low and midlevel ice clouds at high latitudes. As anticipated from ground-based polarization lidar studies, δ increase with increasing height/decreasing temperature, and the effects of horizontally oriented plate crystals in lowing δ are evident by comparing data obtained close to the nadir (0.3°) and off-nadir (3.0°) pointing directions. These differences in δ average 0.01–0.03, although this anisotropic scattering effect is particularly apparent at low altitudes in the mid and high latitudes. Unexpected findings include decreasing δ with increasing latitude, and δ in detected PSC that are usually similar to cirrus clouds. However, δ in PSC are lower in a belt in the lower stratosphere in the Southern Hemisphere and generally lower in the Northern Hemisphere, but higher in lower stratospheric nacreous clouds in both hemispheres. There are also significant differences in the ice cloud δ measured at night and day, but this is assumed to result from factors associated with day/night differences in CALIPSO data collection. Global average δ are 0.34–0.36 for day, and 0.23–0.26 for night.

Citation: Sassen, K., and J. Zhu (2009), A global survey of CALIPSO linear depolarization ratios in ice clouds: Initial findings, *J. Geophys. Res.*, *114*, D00H07, doi:10.1029/2009JD012279.

1. Introduction

[2] Every electromagnetic wave at any instant of time can be characterized by a state of polarization [*Swindell*, 1975]. This state of polarization involves an instantaneous plane of polarization that can be invariant with time (linearly polarized in some arbitrary direction), or undergoing rotation (circular polarization, or elliptical polarization in the general sense). A state of random polarization can be considered as a jumble of waves doing a near infinite number of their individual things.

[3] The capricious nature of polarized waves is readily apparent during the scattering of light by hydrometeors in the atmosphere, which tend to have dimensions much larger than the incident (visible) wavelengths. This is the realm of geometrical optics, where Mie theory offers a precise solution to scattering in all directions provided that the scatterer is spherically symmetrical, while approximate theories must be relied on for irregular particles [*Liou et al.*, 2002]. Excluding the forward-scattering diffraction process, which does not depolarize the light in the shadows edge, scattering that involves internal skew rays (i.e., nonnormal to the surface) will alter the polarization state of the scattered light. Reducing the problem to pure backscattering at 180°, the case for lidar, we find that spheres only have raypaths that preserve the incident polarization properties, while according to ray tracing the backscattering from nonspherical particles create depolarization in the backscatter except in the case of normal, or specular, reflections [*Liou and Lahore*, 1974; *Sassen*, 1991]. This is important because some ice crystals such as plates display large flat faces that are effective in creating nondepolarizing reflections, which also tends to orient them uniformly in space as a result of aerodynamic drag forces, such that backscatter depolarization can depend significantly on the lidar pointing angle [e.g., *Platt*, 1978; *Noel and Sassen*, 2005].

[4] Ray-tracing findings show that when randomly arrayed, the basic ice crystal habits generate different amounts of backscatter depolarization [*Takano and Liou*, 1995]. The linear depolarization ratio δ is commonly used in the lidar field to quantify changes in the backscattered polarization state, and is defined as the ratio of returned laser energies in the perpendicular to parallel planes of polarization relative to that transmitted. (Note that these two lidar signals can contain contributions from air molecules, aerosols, and clouds, such that the term *total* linear depolarization ratio is appropriate.) In going from thin hexagonal

[1]Geophysical Institute, University of Alaska Fairbanks, Fairbanks, Alaska, USA.

0148-0227/09/2009JD012279

plates to long column ice crystals, the predicted δ increase from 0.34 to 0.56, suggesting that lidar signals can be used to infer ice crystal shape.

[5] Since polarization lidars have been around [*Schotland et al.*, 1971], cirrus clouds have been under their scrutiny. As a matter of fact, polarized photons and cirrus cloud particles are an ideal match [*Sassen*, 1991, 2005a], while the need to better understand high cloud properties for climate studies is well established [e.g., *Liou*, 1986; *Stephens et al.*, 1990]. Up to recently, much of what we know about the properties of these high clouds has come from extended ground-based polarization lidar studies from various parts of the world. However, the results have not always been in good agreement, which could be attributed either to experimental uncertainties or to valid regional differences in ice crystal shapes caused by the cloud formation processes or local aerosol effects. For example, in the comparison of the temperature dependencies of δ given by *Sassen and Benson* [2001], although similar trends from midlatitude sites in the Northern and Summer Hemispheres were found, tropical cirrus results differed by up to $\delta \approx 0.2$. All climatological lidar studies, however, reveal an increasing trend in δ with increasing height/decreasing temperature.

[6] With the April 2006 launch of the Cloud-Aerosol Lidar and Infrared Pathfinder Satellite Observations (CALIPSO) satellite, however, the situation has changed dramatically, because Cloud-Aerosol Lidar with Orthogonal Polarization (CALIOP) depolarization data in the green (0.532 um) laser channel are now available globally. The data commenced on 15 June 2006, including measurements collected in both the nadir and off-nadir viewing directions, at a vertical resolution of 60 m in the upper troposphere and with a ground footprint of 333 m [*Winker et al.*, 2007; *Hunt et al.*, 2009]. This unique data set is important because we assert that variations in laser depolarization contain information reflecting the basic cloud microphysical, environmental, and formation processes in ice clouds.

[7] We have begun the analysis of this extended data set by examining the nature of the surprisingly large δ variations in ice clouds as functions of geographic location, season, height, and day versus night overpass data. CALIPSO and other members of the A-train constellation of satellites fly in a Sun-synchronous 705 km orbit, with repeated 01:30 and 13:30 local mean times for crossing the equator [*Stephens et al.*, 2002]. As of the time of this writing, CALIOP has emitted approximately 1.8 billion laser shots into the Earth's atmosphere.

2. Data Analysis

[8] The data analysis algorithm uses both CALIPSO Level 1 and 2 cloud data products to calculate suitably averaged, ranged-resolved δ. (Note that the Level 2 depolarization data product involves the vertical integration of the signals through each identified cloud layer [see *Cho et al.*, 2008].) The Level 1 data used here include the attenuated parallel and perpendicular backscatter profiles for each recorded laser shot, and the corresponding temperature profile. To reduce the effects of signal noise on calculating δ, the backscatter data at each height are averaged over 15 consecutive shots. Depending on the height above mean sea level (MSL), this yi eight resolutions ranging from 30 to 180 m in our realm of interest: the data resolution is 30 m from the surface to 8.3 km, 60 m from 8.3 to 20.2 km, and 180 m up to 30.1 km MSL. The temperature profiles are similarly averaged. Next, Level 2 data are examined to obtain all identified cloud top and base heights: note that this data product is based on the same 15-shot averages as we apply to Level 1 data. This yields a repeated 5 km long cloud column data product.

[9] We next decide which of the Level 2 layers are to be included in the analysis based on criteria developed earlier for visually identified cirrus clouds [*Sassen*, 2002a; *Sassen et al.*, 2008], but also including in the current study polar stratospheric clouds (PSC) and likely some diffuse midlevel ice clouds. The criteria for identifying cirrus and other ice clouds are that they must be transparent to lidar probing (i.e., cloud optical depth $<\sim 3.0-4.0$), and have cloud top temperatures colder than -40°C according to *Sassen and Campbell* [2001]. This approximate optical depth limit is determined by searching for a lidar return, below the highest suitable cloud layer, either at the Earths' surface height, or the top of a lower cloud layer that attenuates the laser pulse (and thus is rejected from further analysis). In effect, this avoids the inclusion in our sample of dense ice, water, and mixed phase clouds, which may produce photon multiple scattering depolarization increases [*Hu et al.*, 2006; *Cho et al.*, 2008], and most aerosol layers. The δ are calculated using the integrated backscatter signals at each height within those cloud layers identified in Level 2 data and passing our criteria. The vertical δ profiles are saved along with temperatures and location. Each day of compiled data is gridded into 5.0° latitude by 5.0° longitude bins and then into monthly averaged data files.

[10] Currently, only selected time intervals have been analyzed using this algorithm. We have chosen the three month periods representing Northern and Southern Hemisphere summers and winters (i.e., JJA and DJF) for both the initial nadir and the subsequent off-nadir viewing periods. Separate analyses are made for day and night CALIPSO observations. The results are presented in terms of global latitude versus longitude plots to show geographical differences, and latitude versus height plots to reveal the effects of cloud height/temperature on laser depolarization, for the first time, on a global scale.

3. Nadir Results

[11] In Figures 1–6 are presented results for the months of JJA 2006 and 2007, and DJF 2006–2007 when the CALIPSO viewing angle of 0.3° was very close to the nadir direction. (Note that a brief period of off-nadir data collected after 21 August 2007 is excluded from this analysis.) In other words, if horizontally oriented planar ice crystals represented a significant fraction of the total crystals present at any location, δ could be considerably lowered in comparison to those collected a few degrees or more off the nadir (see next section), sometimes even approaching zero [*Sassen and Benson*, 2001]. Day and night three monthly seasonal averages are given in Figures 1 and 2 (for JJA in both 2006 and 2007) and 4–5 (for DJF in 2006–2007), and the corresponding monthly averaged results for the zonal height distributions in Figures 3 and 6. It is important to note that for the months selected, the data for high latitudes

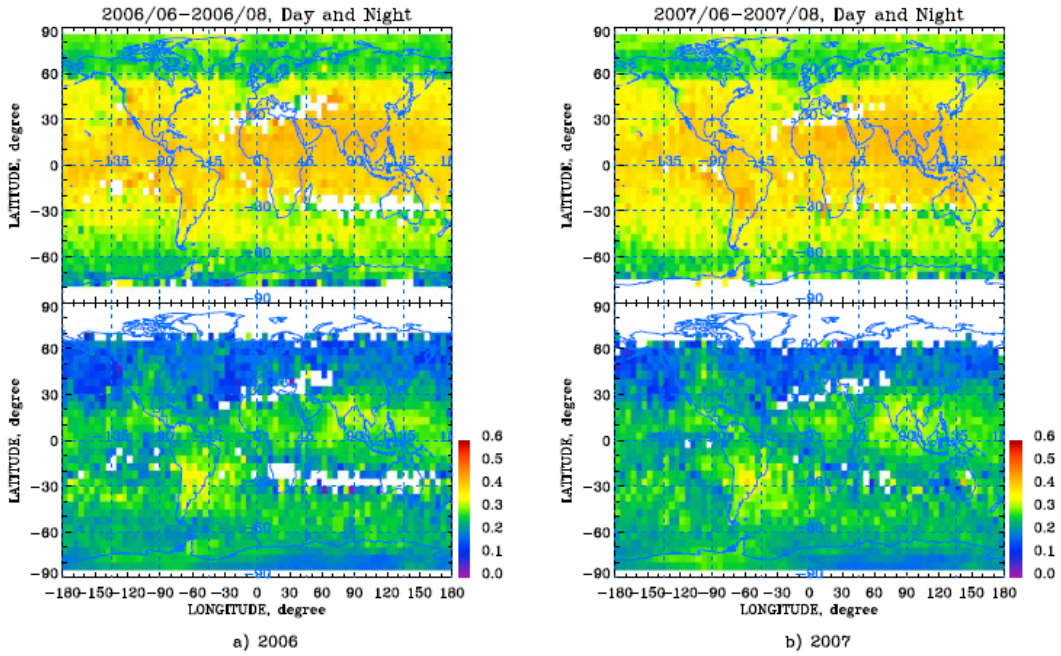

Figure 1. Latitude versus longitude displays of vertically averaged nadir CALIPSO ice cloud linear depolarization ratios (see color δ value scale at lower right). The data are for (top) day and (bottom) night, averaged over the months of JJA for (a) 2006 and (b) 2007.

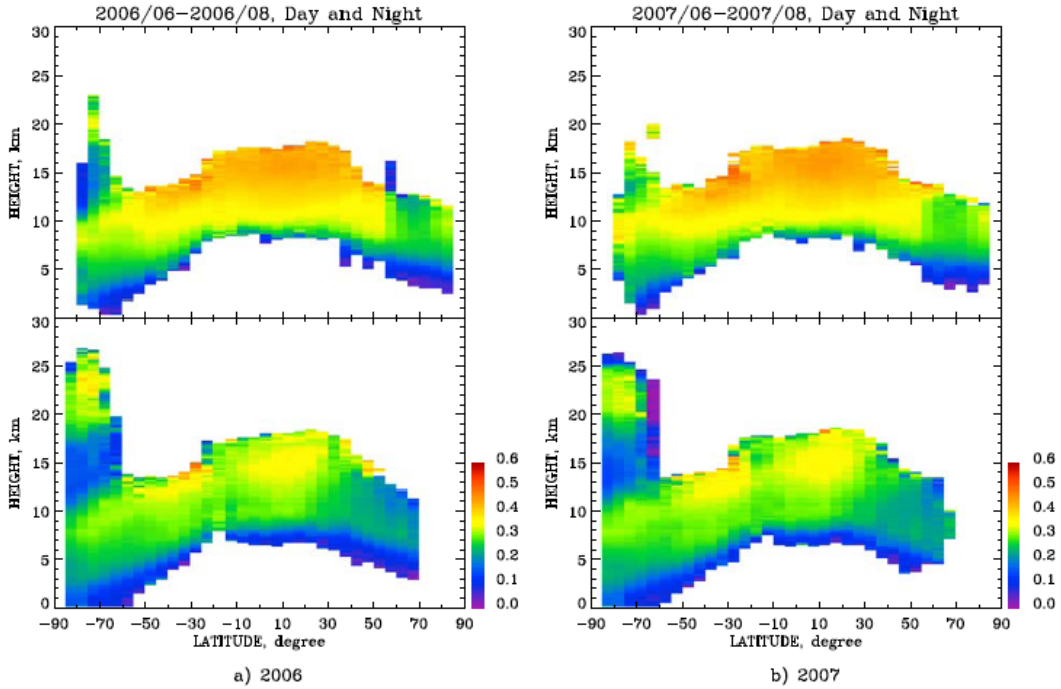

Figure 2. Latitude versus height displays of nadir CALIPSO ice cloud δ values for (top) day and (bottom) night aged over the months of JJA for (a) 2006 and (b) 2007.

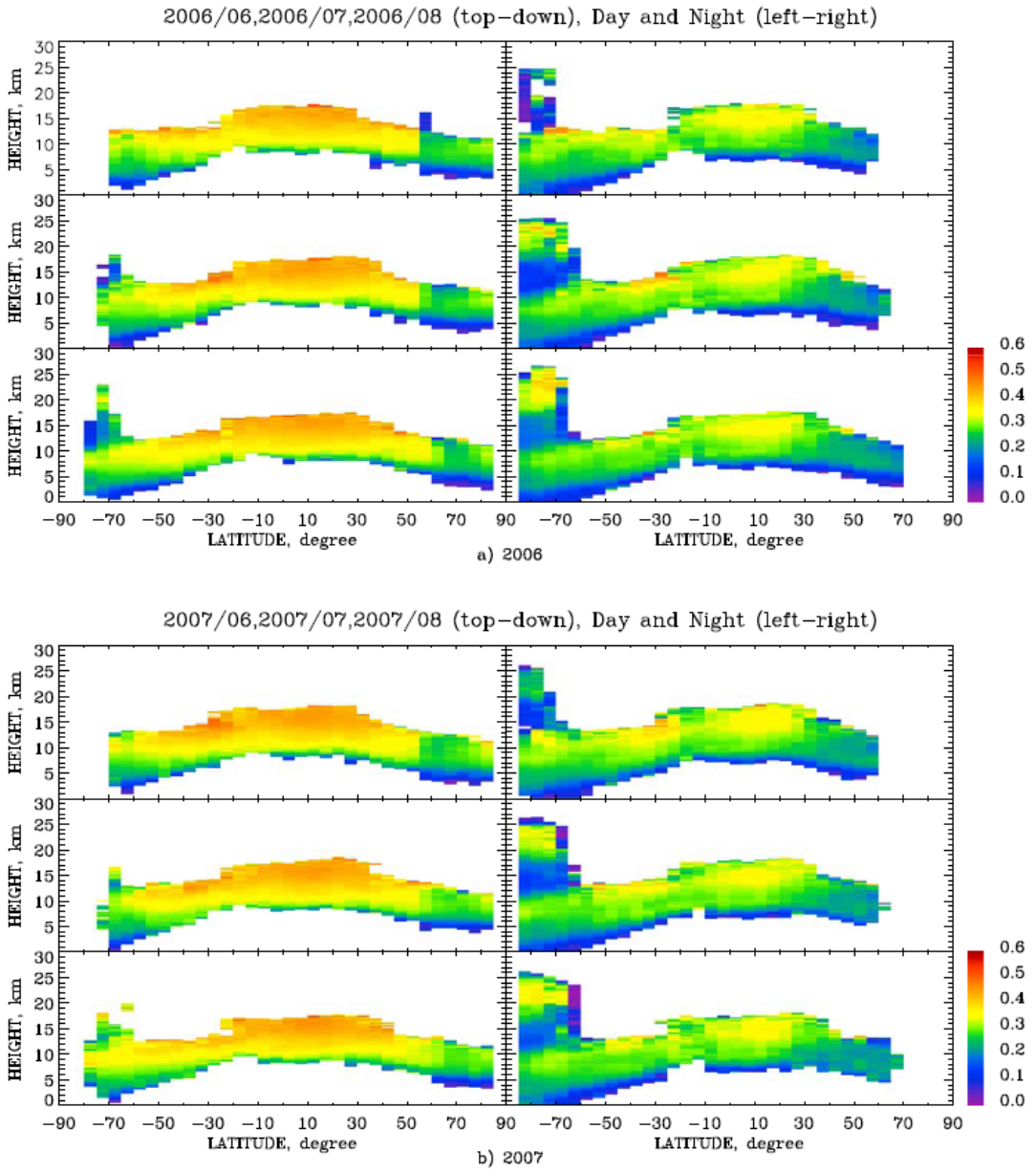

Figure 3. Single-month latitude versus height displays of nadir CALIPSO ice cloud δ values for (left) day and (right) night, for (a) 2006 and (b) 2007 for months June, July, and August.

correspond to summer/winter seasonal effects on cloud formation, as is particularly apparent in the varying presence of PSC extending up to 27 km MSL.

[12] In general, it is clear that the δ derived from CALIOP nadir data are on average significantly higher in tropospheric ice clouds a) during the day compared to night, and b) in the tropics and midlatitudes compared to higher (>∼50°) latitude local he possible effects of errors from signal noise caused by scattered sunlight and other causes will be discussed below.) Moreover, as expected from extended ground-based polarization lidar studies of cirrus clouds, δ tend to increase with increasing height, i.e., with decreasing temperature (Figures 2 and 5). The trend in the night data is similar, but some δ decreases are indicated as the tropical tropopause is approached.

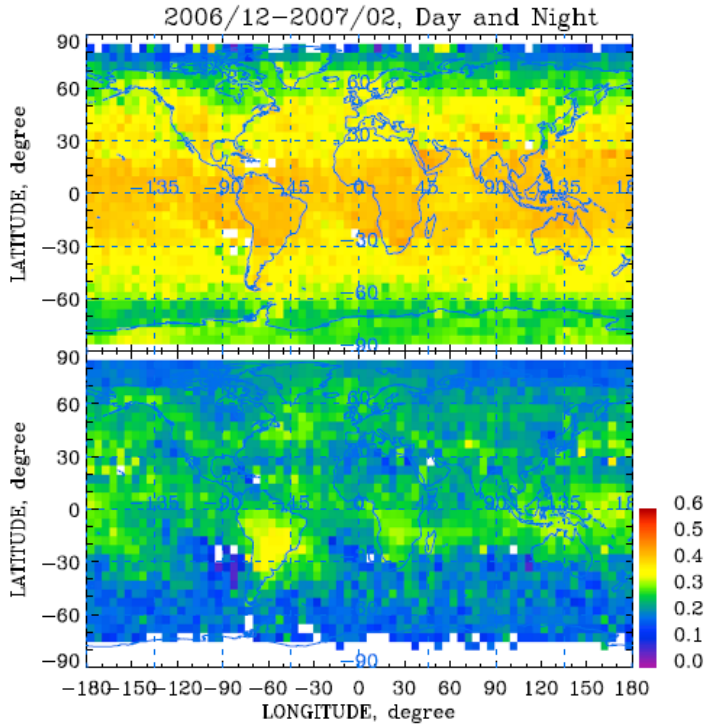

Figure 4. As in Figure 1 but for the months of December–January–February (DJF) 2006–2007.

[13] As for the basic effects of geography on the average δ, which are more readily apparent in the night plots in Figures 1 and 4, it appears that the highest δ (>∼0.25 at night) are generally confined to those areas in the tropics and subtropics that have the highest global frequencies of cirrus clouds in the corresponding months [see *Sassen et al.*, 2008, Figure 3], and which are indicated to generally be associated with deep convective clouds [*Sassen et al.*, 2009]. These areas include for DJF the Amazon Basin, southern Africa, the Malaysian region, and the central Pacific Ocean, and for JJA central America, the Indian Ocean Monsoon region, and the western Pacific Ocean. The strong depolarization generated in JJA over southern South America and its eastern coast, on the other hand, does not correspond to an area of significant cirrus cloud production. (It does correspond, however, to the location of the South Atlantic Anomaly, which produces a major increase in the green channel dark noise that may affect δ values [*Hunt et al.*, 2009]).

[14] The availability of results from two consecutive JJA seasons allows for the evaluation of interannual variations of ice cloud formation processes that are reflected by changes in lidar depolarization. In many respects the findings from the two seasons are surprisingly consistent. In Figure 1 (top), although the uniform drop in δ at a latitude of ∼+60° seems unrealistic, many details of the day and night δ variations are quite similar for the two years, such as the midlatitude regions showing lower depolarization and high latitude regions s g higher depolarization. The patterns in the latitude versus height displays in Figures 2 and 3 are also very similar, indicating a degree of year-to-year repeatability in both tropospheric and PSC ice cloud conditions. Apart from a few departures, like the July 2006 apparent aerosol peak at +60–65° latitude extending above the tropospheric cirrus, note the persistence of the two δ maxima in the upper troposphere at about +10° and −40° latitudes, and the similar PSC properties.

[15] In comparison, the plots for the 2007–2008 DJF nadir data reveal only some subtle seasonal differences in the geographic pattern of the average δ for tropospheric ice clouds (Figure 4). The latitude versus height displays in Figures 5 and 6 show stronger depolarization extending to higher latitudes in the winter hemisphere, and a tongue of low δ values in December extending into southern midlatitudes in the cloud top region (night only). PSC are nearly absent at this time in the Northern Hemisphere, but not entirely (see section 4).

[16] There are interesting δ variations with height and geographical location at high latitudes in connection with PSC, which are particularly evident in the one month averaged latitude-height displays (Figures 3 and 6). It is likely that Type II PSC, which have cirrus-like properties [*Palm et al.*, 2005], will be mainly detected, as indicated by the similar maximum lidar-derived PSC heights of ∼27 km MSL given by *Campbell and Sassen* [2008]. Over Antarctica, a region of $\delta \approx 0.1$ is generally present in the lower stratosphere before δ increase in the higher-altitude PSC, indicating a change in stratospheric particle shape, size or

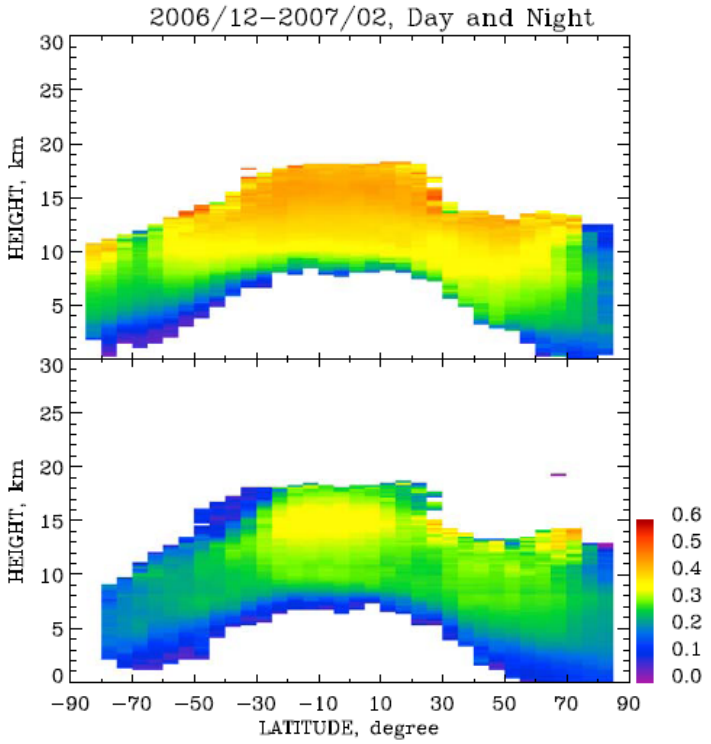

Figure 5. As in Figure 2 but for the months of DJF 2006–2007.

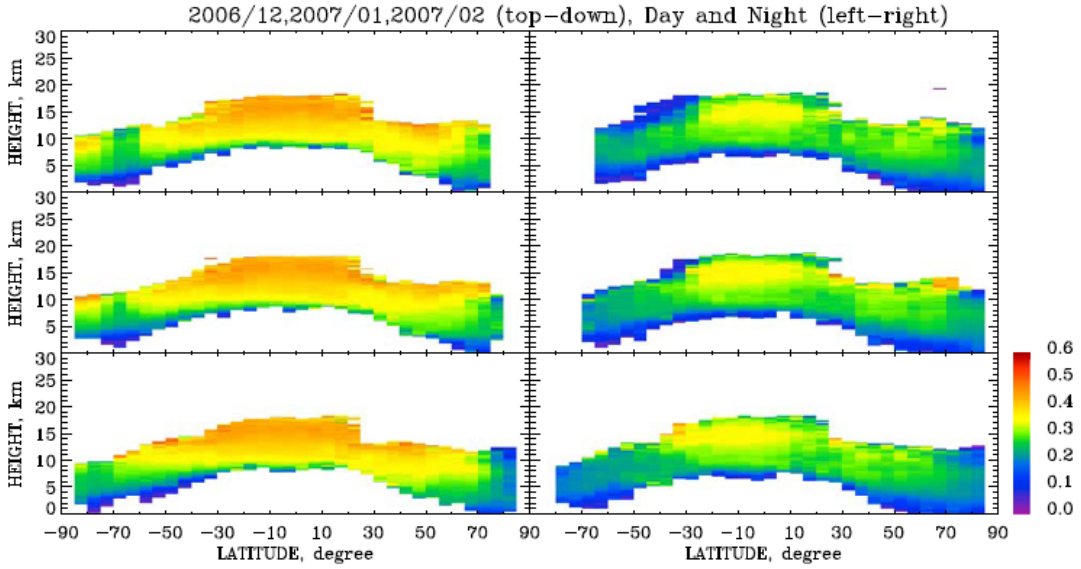

ure 6. As in Figure 3a but for the months of DJF 2006–2007.

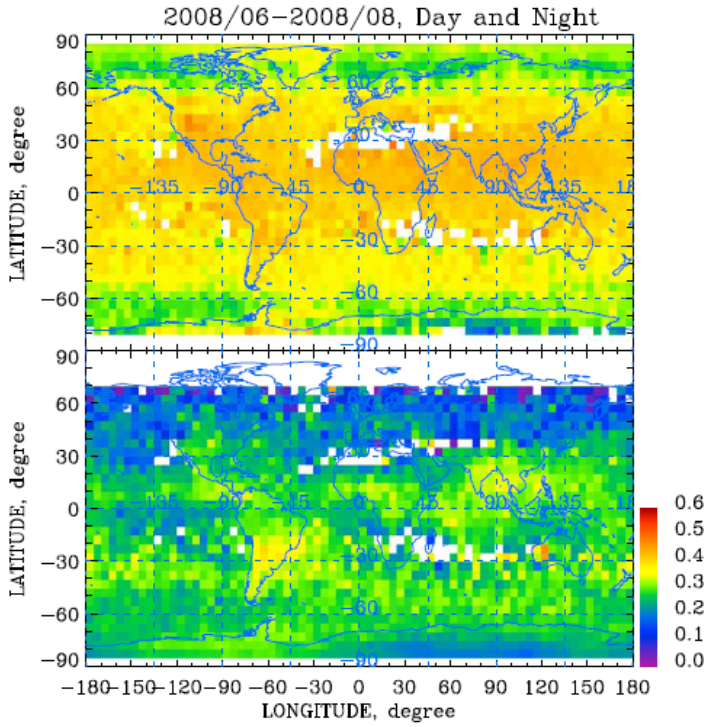

Figure 7. As in Figure 1 but for the months of 2008 June–July–August (JJA) and for off-nadir observations.

orientation with height. Moreover, there is evidence for relatively high δ of 0.45–0.55 associated with what we interpret as lower stratospheric nacreous clouds in both hemispheres. These regions are found in the night (i.e., winter) height-latitude displays between ~±65–75° latitude and 12–14 km height, particularly in the months of June (Figure 3a, top right) and January (Figure 6, right middle). What suggests that they are mountain-wave induced nacreous clouds is their association with mountainous regions such as the Antarctic Peninsula and Victoria Land, and Scandinavia and Greenland. Relatively strong depolarization is suggested in the vertically averaged δ within these areas in Figures 1 and 4, but similar plots giving data only for >12 km MSL (not shown) more clearly indicate their associations with elevated terrain. Interestingly, a similar occurrence of DJF-season 'cirrus' clouds is present in the *Sassen et al.* [2008] climatological study, but it is now apparent they these clouds generate unusually high δ at heights not far *above* the tropopause. The night height-latitude display in Figure 6 for December also shows the presence of a thin Northern Hemisphere PSC at a height of 19.5 km MSL.

4. Off-Nadir Results

[17] Operations after 28 November 2007 (and to date) have been conducted with the CALIOP system pointed 3.0° off the nadir directio rder to study the effects of horizontally oriented ice crystals on depolarization and any errors associated with the determination of cloud optical depth from the reflection-enhanced signal strengths. A viewing angle of 3.0° off the vertical direction is sufficient to greatly reduce the effects of specular reflections on lidar δ, except perhaps in the case of the larger flutter angles experienced by dendritic ice crystals at relatively warm temperatures [*Noel and Sassen*, 2005]. Thus, presented in Figures 7–12 are the results of the analyses analogous to Figures 1–6.

[18] A general comparison of the previous nadir to these off-nadir results shows that in every case the latter δ values are somewhat higher. The off-nadir latitude versus longitude displays of vertically averaged δ do not appear to be conspicuously higher, but the height-latitude displays show more dramatic differences. For both day and night data, areas with δ lower than ~0.15 are now nearly absent. These areas occurred previously mostly along the base of the ice clouds (i.e., at the warmest temperatures), and the off-nadir cloud 'bases' as a result are somewhat higher. In other words, these midlevel to low-level tropospheric ice clouds composed of oriented planar crystals appear to be optically thin, with an enhanced probability of detection when nadir data is collected. Given by *Sassen* [2002b, 2005b] are examples of the sensing by polarization lidar of similar thin ice clouds at relatively low altitudes (for cirrus) at both mid and high latitudes, which are often if not typically composed of oriented plate crystals. Ice crystal nucleation in

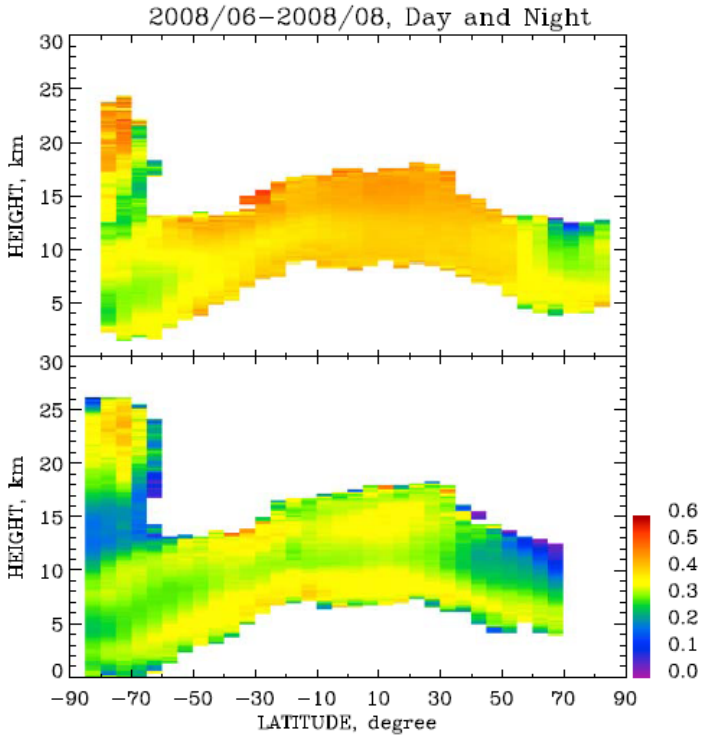

Figure 8. As in Figure 2 but for the months of 2008 JJA and for off-nadir observations.

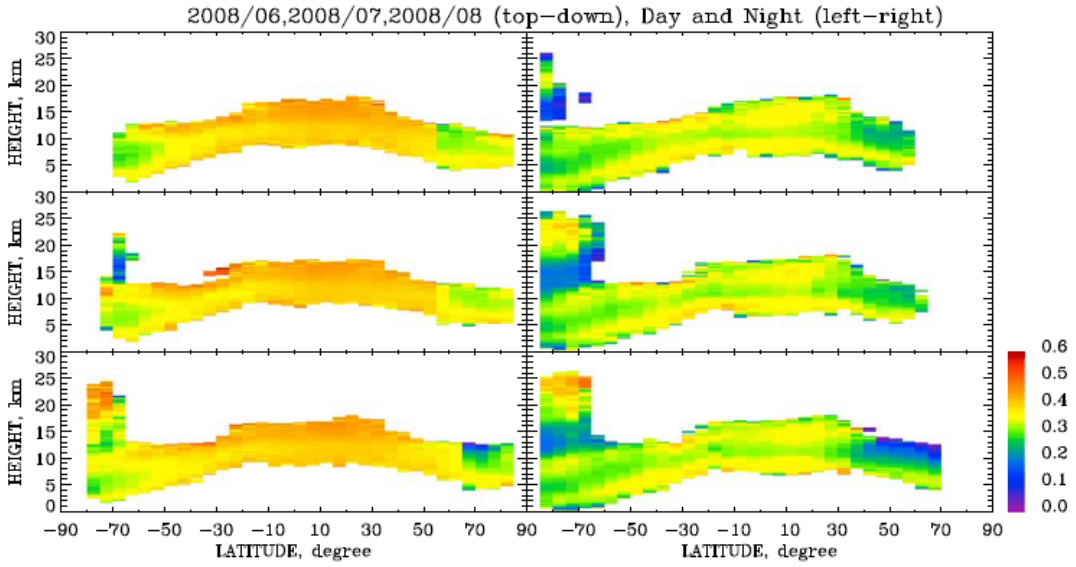

Figure 9. As in Figure 3a but for the months of 2008 JJA and for off-nadir observations.

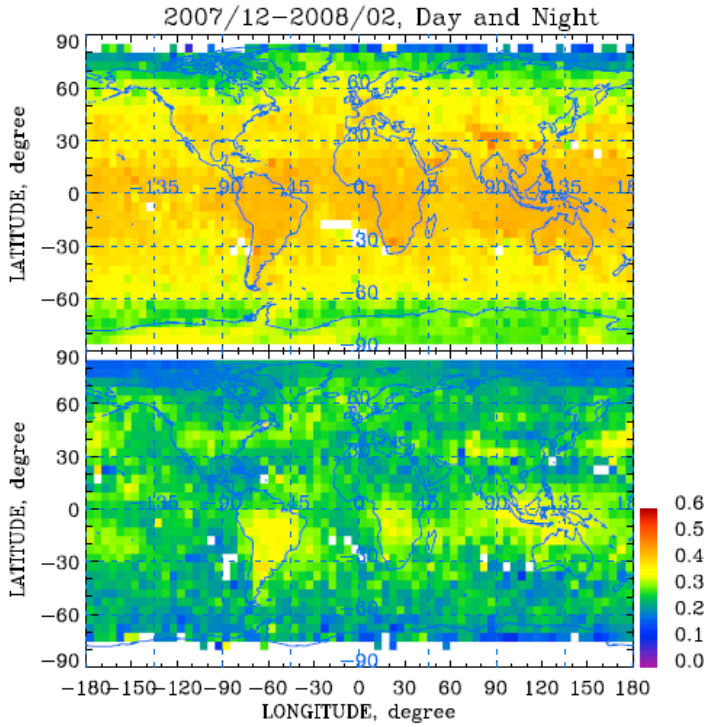

Figure 10. As in Figure 7 but for the months of DJF 2007–2008.

many cases may involve the deposition mode rather than the homogeneous freezing of haze particles typical of higher cirrus clouds.

[19] Other regions where oriented plate crystal returns are now absent or greatly reduced are at high altitudes in the southern midlatitudes (Figure 6, top right, versus Figure 9), which appear to extend into the lower stratosphere only at night, and at high latitudes in general. Even for the off-nadir data, however, it is clear that cirrus cloud δ are lower at high latitudes in both hemispheres, winter and summer. This is a consistent trend that shows that lidar depolarization in ice clouds tends to not only increase with height, but also to decrease with latitude. On the other hand, δ in the upper tropical atmosphere are similarly high in the nadir and off-nadir plots (compare Figures 2 and 8 and Figures 5 and 11), indicating that oriented plate crystals are not as common at these temperatures and locales.

[20] Also note that a measure of interannual variability in the presence of PSC is already indicated by the data. Comparing Figures 3 and 9 and Figures 6 and 12 reveals that although PSC are similarly abundant in the 2006, 2007, and 2008 Southern Hemisphere winters, it is only the 2007–2008 winter that shows evidence for significant Northern Hemisphere PSC. This strong Northern Hemispheric PSC occurrence is surprising, perhaps reflecting the dearth of lidar remote sensing sites in the vast Arctic region. PSC depolarization appears in Figure 8 to be somewhat higher in comparison to the nadir data, but interannual variations could be resp le for this. Note, however, that the band of relatively low δ from ~12–17 km MSL just above the tropopause does not appear to be due to oriented plates, but to different crystal shapes, perhaps as a result of evaporation effects on particle shape during sedimentation [*Nelson*, 1998], or to different particle compositions in these lower PSC.

5. Overview

[21] To quantify the regional and global differences in ice cloud depolarization described above, Tables 1 and 2 give the zonal and global averaged δ for the day, night, nadir, and off-nadir data sets, for both the JJA and DJF seasons, respectively. In terms of the global δ averages, it is apparent that day minus night differences are close to 0.11 regardless of season or CALIOP pointing direction. Global averages range from 0.34 to 0.36 for day, and 0.23 to 0.26 for night data. As discussed below, these day/night differences significantly exceed expectations based on ground-based polarization lidar studies. Differences between off-nadir and nadir δ range from 0.01 to 0.03, which is generally consistent with the results given by *Sassen and Benson* [2001], indicating that on average only a small amount of oriented plates are mixed in with randomly arrayed ice crystals. (Recall, however, that oriented plate crystals noticeably affect δ and cloud boundaries at low altitudes and high latitudes.) As far as latitudinal differences are concerned, off-nadir minus nadir δ are only ~0.01–0.02 in the tropics, but increase to 0.04–0.05 at higher latitudes,

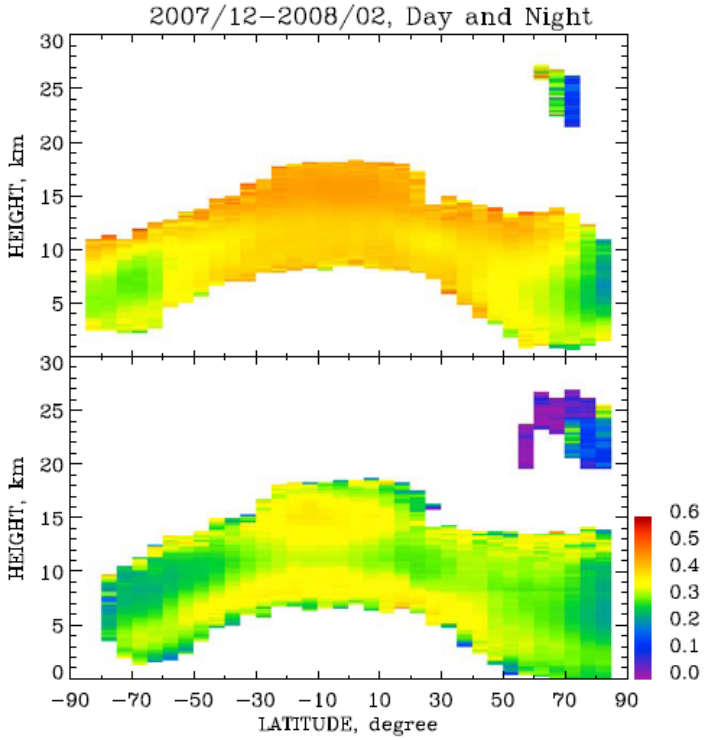

Figure 11. As in Figure 8 but for the months of DJF 2007–2008.

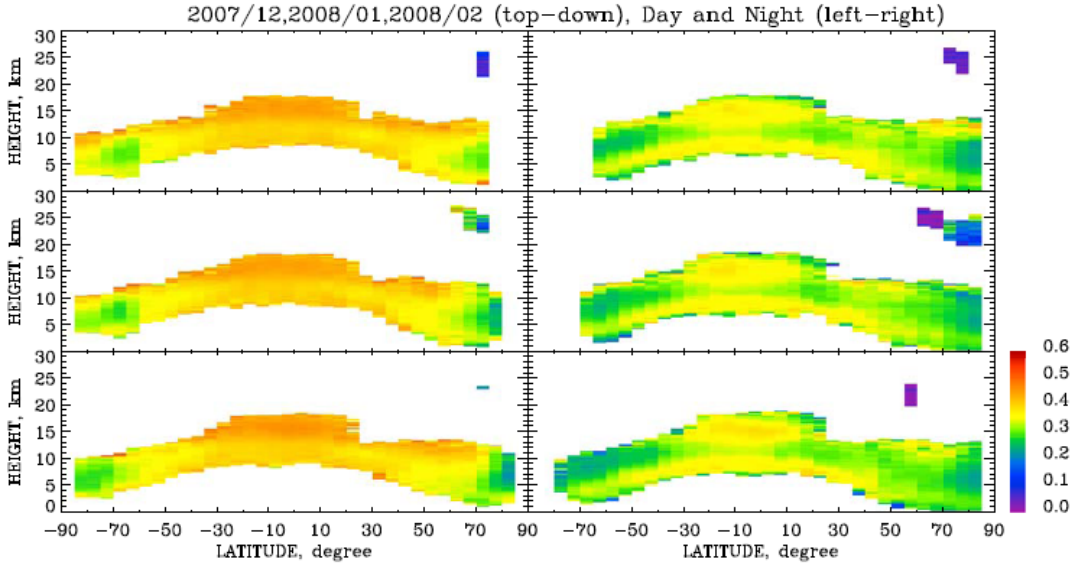

ure 12. As in Figure 9 but for the months of DJF 2007–2008.

Table 1. Vertically and Zonally Averaged δ Within the Indicated Latitude Belts for Various CALIPSO Polarization Lidar Operations for the Months of June–July–August[a]

Latitude	Nadir Day	Nadir Night	Off-Nadir Day	Off-Nadir Night
~−85 to −60°	0.26 (0.28)	0.23 (0.24)	0.30	0.26
−60 to −30°	0.31 (0.32)	0.25 (0.26)	0.35	0.28
−30 to −15°	0.36 (0.37)	0.25 (0.26)	0.38	0.29
−15 to +15°	0.40 (0.40)	0.27 (0.26)	0.41	0.28
+15 to +30°	0.40 (0.40)	0.26 (0.26)	0.41	0.27
+30 to + 60°	0.36 (0.35)	0.20 (0.20)	0.39	0.21
+60 to ~+85°	0.28 (0.30)	0.18 (0.18)	0.32	0.16
Global	0.34 (0.35)	0.24 (0.24)	0.36	0.25

[a]Nadir data were collected in 2006 (2007), and off-nadir data were collected in 2008.

suggesting that plate crystals are less common in the tropics, perhaps due to the effects of deep convection or the colder temperatures on ice crystal shape, size, and orientation.

6. Conclusions

[22] Now more than two years into the CALIPSO mission, sufficient data has accumulated to begin tackling some climatological aspects of this unique global data set, long awaited by polarization lidar researchers. The goal of this initial study has been to explore the ice cloud microphysical properties of the global CALIOP depolarization data set. We summarize our main findings below:

[23] 1. Depolarization in tropospheric ice clouds tends to increase with increasing height/decreasing temperature, as expected from various ground-based lidar studies.

[24] 2. Depolarization in tropospheric ice clouds tends to decrease with increasing latitude, an unexpected finding.

[25] 3. Depolarization in the PSC detected in the Southern Hemisphere is similar to tropospheric ice clouds, except it is lower in a band in the lower stratosphere. PSC occur less extensively in the Northern Hemisphere, and also seem to generate lower δ.

[26] 4. The depolarization decreases caused by sampling horizontally oriented ice plates during nadir observations are less in the high tropical atmosphere compared to mid and high latitudes at low altitudes. Global averages show only a 0.01–0.03 increase in δ in the off-nadir data.

[27] 5. Relatively strong depolarization seems to be associated with occasional lower stratospheric (nacreous) PSC in both hemispheres in regions where orographic effects are to be expected.

[28] 6. There are significant ($\delta \approx 0.11$) average differences between day and night data, which are inconsistent with earlier ground-based data. Average global δ values are 0.34–0.36 for day, and 0.23–0.26 for night.

[29] Unfortunately, the last finding indicates the presence of artifacts in the data set related to the effects of background signals from scattered sunlight in the green laser channel. Because of the vastly different background signal noise levels between day and night, it was recognized in the design of CALIPSO that on-board signal processing was needed to adjust the lidar receivers accordingly, as well as to reduce the backscatter data download rate [*Hunt et al.*, 2009]. In addition to t y and night receiver channel sensitivity selections, the mean background signal during daytime is monitored using signals measured from the upper atmosphere, where backscattered signals should be negligible, and subtracted electronically. Low and high gain digitizers are used for each channel, and tests performed to determine if signals are saturated at full scale. The abrupt δ changes often apparent at ~+60° latitude are considered to be an artifact of day versus night noise and gain selection effects (W. H. Hunt, personal communication, 2009). Interestingly, depolarization seems elevated near the location of the South Atlantic Anomaly, which produces a significant increase in the green channel dark noise.

[30] The evidence from extended ground-based polarization lidar research clearly contradicts the strength of the diurnal depolarization differences noted here. The mean δ from ruby (0.694 μm) lidar research at Salt Lake City, Utah (40° 49′ 00″ N, 111° 49′ 38″ W) was 0.33 for zenith measurements [*Sassen and Benson*, 2001]. Thus, the daytime CALIPSO data seem in compliance or slightly elevated, while those from the night are too low by about 0.10 (see Tables 1 and 2). More importantly, an examination of the mean diurnal δ variations from the same lidar data set [*Sassen et al.*, 2003] found only a 0.05 maximum difference between day and night values, with the minimum corresponding to a +45° solar elevation angle (i.e., opposite in solar phase to that noted here). The total day versus night difference in δ averaged only 0.02.

[31] On the other hand, because CALIPSO measures the total linear depolarization ratio at a 0.532 μm wavelength, molecular scattering effects on depolarization can be expected to lower nighttime δ to some degree. This is because optically thin ice clouds with weak lidar signals will be detected preferentially during night, and it is these clouds that will display lower δ due to the near-zero δ generated by the molecular backscattering component. Although *Sassen et al.* [2008] found only a 3.1% difference in the global average frequency of occurrence of cirrus clouds in day and night CALIPSO data, we find that in our sample the mean ice cloud base heights (not shown) are 0.5–1.0 km lower at night, especially at midlatitudes. Thus, those cloud regions that tend to show the lowest δ (see, e.g., Figures 3 and 12) are excluded from the daytime data set. Interestingly, mean cloud top heights are much more similar for day and night, differing by a few hundred meters in the tropics and subtropics. These findings reflect the fact that typical cirrus clouds display relatively strong signals at cloud top,

Table 2. Vertically and Zonally Averaged δ Within the Indicated Latitude Belts for Various CALIPSO Polarization Lidar Operations for the Months of December–January–February[a]

Latitude	Nadir Day	Nadir Night	Off-Nadir Day	Off-Nadir Night
~−85 to −60°	0.28	0.18	0.31	0.22
−60 to −30°	0.34	0.20	0.36	0.25
−30 to −15°	0.39	0.24	0.40	0.28
−15 to +15°	0.41	0.27	0.42	0.29
+15 to +30°	0.39	0.24	0.40	0.26
+30 to +60°	0.35	0.24	0.37	0.27
+60 to ~+85°	0.26	0.22	0.28	0.24
Global	0.34	0.23	0.36	0.26

[a]Nadir in 2007 and off-nadir in 2008.

where they are generated, but the signals generally fade away as cloud base is approached and molecular backscattering is enhanced [*Sassen*, 2002a]. We conclude that further research is needed to better understand the diurnal differences in the CALIPSO δ values.

[32] Despite these initial uncertainties, the global trends in δ must primarily reflect real cloud microphysical processes that affect ice crystal shape and orientation [*Sassen*, 1991]. For example, the depolarization decrease noted with increasing latitude may indicate ice cloud microphysical changes related to the warmer tropospheric temperatures generally experienced at high latitudes, and since these clouds are nearer to the Earth's surface, differences in the nucleation mechanisms of the ice particles. That is, the aerosol particles derived from the surface of the Earth that serve as ice nuclei will likely change with height [*Sassen*, 2005b], while the effects of deep convection, more prevalent in the tropics, could similarly have basic impacts on ice crystal shape and orientation. The fact that some of the highest depolarization found here is associated with apparent lower stratospheric polar nacreous clouds could reflect the effects of relatively strong orographic updrafts, which would modulate ice crystal concentration, size, and shape. It is also surprising that the boreal winter of 2007–2008 hosted a relatively large amount of PSC, a finding that may be due to a lack of Arctic lidar observing sites. These results suggest that additional CALIPSO depolarization studies will shed light on other basic ice cloud processes such as the impact of orographically induced cirrus, and the direct (contrail) and indirect effects of aircraft emissions on cirrus cloud content.

[33] In conclusion, this global lidar depolarization data set is an exciting development that will hopefully stimulate increased cloud microphysical/lidar research and further the likelihood of new, more advanced lidar satellite development.

[34] **Acknowledgments.** This research has been supported by NASA grant NNX08A056G (CALIPSO) and by NSF grant ATM-0630506. The authors thank the members of the CALIPSO science team, and especially W. H. Hunt and D. M. Winker for helpful discussions.

References

Campbell, J. R., and K. Sassen (2008), Polar stratospheric clouds at the South Pole from five years of continuous lidar data: Macrophysical and thermodynamic properties, *J. Geophys. Res.*, *113*, D20204, doi:10.1029/2007JD009680.

Cho, H.-M., et al. (2008), Depolarization ratio and attenuated backscatter for nine cloud types: Analyses based on collocated CALIPSO lidar and MODIS measurements, *Opt. Express*, *16*, 3931–3948, doi:10.1364/OE.16.003931.

Hu, Y., et al. (2006), Simple relation between lidar multiple scattering and depolarization in water clouds, *Opt. Lett.*, *31*, 1809–1811.

Hunt, W. H., D. M. Winker, M. A. Vaughan, K. A. Powell, P. L. Lucker, and C. Weimer (2009), CALIPSO lidar description and performance assessment, *J. Atmos. Oceanic Technol.*, *26*, 1214–1228.

Liou, K.-N. (1986), Influence of cirrus clouds on weather and climate: A global perspective, *Mon. Weather Rev.*, *114*, 1167–1199, doi:10.1175/1520-0493(1986)114<1167:IOCCOW>2.0.CO;2.

Liou, K.-N., and H. Lahore (1974), Laser sensing of cloud composition: A backscatter depolarization technique, *J. Appl. Meteorol.*, *13*, 257–263, doi:10.1175/1520-0450(1974)013<0257:LSOCCA>2.0.CO;2.

Liou, K.-N., Y. Takano, P. Yang, and Y. Gu (2002), Radiative transfer in cirrus clouds: Light scattering and spectral information, in *Cirrus*, edited by D. Lynch et al., pp. 265–296, Oxford Univ. Press, New York.

Nelson, J. (1998), Sublimation of ice crystals, *J. Atmos. Sci.*, *55*, 910–919, doi:10.1175/1520-0469(1998)055<0910:SOIC>2.0.CO;2.

Noel, V., and K. Sassen (2005), Study of ice crystal orientation in ice clouds from scanning polarization lidar observations, *J. Appl. Meteorol.*, *44*, 653–664, doi:10.1175/JAM2223.1.

Palm, S. P., M. Fromm, and J. Spinhirne (2005), Observations of antarctic polar stratospheric clouds by the Geoscience Laser Altimeter System (GLAS), *Geophys. Res. Lett.*, *32*, L22S04, doi:10.1029/2005GL023524.

Platt, C. M. R. (1978), Lidar backscattering from horizontally oriented ice crystal plates, *J. Appl. Meteorol.*, *17*, 482–488, doi:10.1175/1520-0450(1978)017<0482:LBFHIC>2.0.CO;2.

Sassen, K. (1991), The polarization lidar technique for cloud research: A review and current assessment, *Bull. Am. Meteorol. Soc.*, *72*, 1848–1866, doi:10.1175/1520-0477(1991)072<1848:TPLTFC>2.0.CO;2.

Sassen, K. (2002a), Cirrus clouds: A modern perspective, in *Cirrus*, edited by D. Lynch et al., pp. 11–40, Oxford Univ. Press, New York.

Sassen, K. (2002b), Indirect climate forcing over the western US from Asian dust storms, *Geophys. Res. Lett.*, *29*(10), 1465, doi:10.1029/2001GL014051.

Sassen, K. (2005a), Polarization in lidar, in *Lidar*, edited by C. Weitkamp, pp. 19–42, Springer, New York.

Sassen, K. (2005b), Dusty ice clouds over Alaska, *Nature*, *434*, 456, doi:10.1038/434456a.

Sassen, K., and S. Benson (2001), A midlatitude cirrus cloud climatology from the Facility for Atmospheric Remote Sensing: II. Microphysical properties derived from lidar depolarization, *J. Atmos. Sci.*, *58*, 2103–2112, doi:10.1175/1520-0469(2001)058<2103:AMCCCF>2.0.CO;2.

Sassen, K., and J. R. Campbell (2001), A midlatitude cirrus cloud climatology from the Facility for Atmospheric Remote Sensing: I. Macrophysical and synoptic properties, *J. Atmos. Sci.*, *58*, 481–496, doi:10.1175/1520-0469(2001)058<0481:AMCCCF>2.0.CO;2.

Sassen, K., K.-N. Liou, Y. Takano, and V. I. Khvorostyanov (2003), Diurnal effects in the composition of cirrus clouds, *Geophys. Res. Lett.*, *30*(10), 1539, doi:10.1029/2003GL017034.

Sassen, K., Z. Wang, and D. Liu (2008), The global distribution of cirrus clouds from CloudSat/Cloud-Aerosol Lidar and Infrared Pathfinder Satellite Observations (CALIPSO) measurements, *J. Geophys. Res.*, *113*, D00A12, doi:10.1029/2008JD009972.

Sassen, K., Z. Wang, and D. Liu (2009), Cirrus clouds and deep convection in the tropics: Insights from CALIPSO and CloudSat, *J. Geophys. Res.*, *114*, D00H05, doi:10.1029/2009JD011916.

Schotland, R. M., K. Sassen, and R. J. Stone (1971), Observations by lidar of linear depolarization ratios by hydrometeors, *J. Appl. Meteorol.*, *10*, 1011–1017, doi:10.1175/1520-0450(1971)010<1011:OBLOLD>2.0.CO;2.

Stephens, G. L., S. Tsay, P. W. Stackhouse Jr., and P. J. Flatau (1990), The relevance of the microphysical and radiative properties of cirrus clouds to climate and climate feedback, *J. Atmos. Sci.*, *47*, 1742–1753, doi:10.1175/1520-0469(1990)047<1742:TROTMA>2.0.CO;2.

Stephens, G. L., et al. (2002), The CloudSat mission and the A-train: A new dimension of space-based observations of clouds and precipitation, *Bull. Am. Meteorol. Soc.*, *83*, 1771–1790, doi:10.1175/BAMS-83-12-1771.

Swindell, W. (Ed.) (1975), *Polarized Light*, Dowden, Hutchison and Ross, Stroudsburg, Pa.

Takano, Y., and K.-N. Liou (1995), Solar radiative transfer in cirrus clouds. Part III: Light scattering by irregular ice crystals, *J. Atmos. Sci.*, *52*, 818–837, doi:10.1175/1520-0469(1995)052<0818:RTICCP>2.0.CO;2.

Winker, D. M., W. H. Hunt, and M. J. McGill (2007), Initial performance assessment of CALIOP, *Geophys. Res. Lett.*, *34*, L19803, doi:10.1029/2007GL030135.

K. Sassen and J. Zhu, Geophysical Institute, University of Alaska Fairbanks, 903 Koyukuk Dr., Fairbanks, AK 99775, USA. (ksassen@gi.alaska.edu)